Structural variations of feldspars at high pressure and high temperature

Lindsay Marie Kolbus

Dissertation submitted to the faculty of the Virginia Polytechnic Institute and State University in partial fulfillment of the requirements for the degree of

Doctor of Philosophy
In
Geosciences

Nancy Ross
Ross Angel
Richard Law
Carla Slebodnick
Fabrizio Nestola

April 24, 2012
Blacksburg, VA

Keywords: feldspar, structure, high-pressure, high-temperature, plagioclase

Structural variations in feldspars at high-pressure and high-temperature

Lindsay M. Kolbus

ABSTRACT

Feldspar minerals are framework aluminosilicates that comprise approximately 60 percent of the Earth's crust. The elastic and thermodynamic properties of this important mineral group are needed for the interpretation of seismic wave velocities, for understanding cation partioning patterns and for the determination of phase boundaries and reactions involving feldspars in the Earth's crust. Until recently, no systematic approach has been applied to describe the structural behavior of feldspars as a function of pressure, temperature and composition. In this thesis, high-pressure and high-temperature X-ray diffraction data were collected for feldspars over a range of compositions which has led to the development a structural model that allows one to predict the structural evolution of feldspars at depth in the Earth's crust. Specifically, the equations of state have been determined for two plagioclase feldspars (An20 and An78) with different states of Al/Si ordering using single-crystal X-ray diffraction. This study has shown that the introduction of Al,Si disorder into plagioclase structures at constant composition softens the structure by 4(1)% for An0, 2.5(9)% for An20 and is essentially zero for An78 compositions. The effect of pressure on the structure of an ordered An20 was also determined up to 9.15 GPa using single-crystal X-ray diffraction and it was found that the dominant compression mechanism involves tilting of the AlO_4 and SiO_4 tetrahedra. Similarly, high-temperature single-crystal X-ray diffraction data collected from an ordered An26 plagioclase and powder X-ray diffraction collected on a suite of Na-rich plagioclases that were refined using the Rietveld method indicate that the major

structural response to increased temperature involves tilting of the tetrahedra. Building on ideas originally proposed by Dr. Helen Megaw, the changes in the conformation of the tetrahedral framework of feldspars can be described in terms of four distinct tilt systems of rigid tetrahedra. This model demonstrates that the fundamental reason for the observed anisotropy and volume change of feldspars lies in the topology of the tetrahedral framework with the greatest contribution attributed to tilt systems 2 and 3.

Grant Information

The research in the dissertation was supported by the National Science Foundation grants EAR-0738692 to Dr. N.L. Ross and Dr. R.J. Angel and EAR-1118691 to Dr. R.J. Angel and N. L. Ross. Funding for travel, accommodation and equipment use in the crystallography lab at the University of Pavia, Italy was supplied by the Edward H. Kraus Crystallographic Research Fund through the Mineralogical Society of America. Travel grants to conferences were provided by the Geosciences Department at Virginia Tech, Geological Society of America and the Graduate Student Assembly Travel Fund Program.

Author Acknowledgments

The author would like to give her many thanks to Dr. Nancy L. Ross and Dr. Ross J. Angel for the assistance and guidance in completing this work.

Samples

The author would like to thank Dr. Fabrizio Nestola at the University of Padova for the analbite feldspar samples, Eleda Johnson for the previously collected data on an An37 plagioclase, and Dr. Ross J. Angel for the An20, An26, An27 and An78 plagioclase samples which were used in this research.

Experiments

Special thanks go to Dr. Fernando Camara, Dr. Chiara Domeneghetti and Francesco Pandolfo at the University of Pavia for the support of the research and use of the crystallography lab at the University of Pavia. Many thanks also go to the post-docs of the VTX lab for all of the help and support with the experiments with special thanks to Dr. Jing Zhao, Dr. Matteo Alvaro and Dr. Elinor Spencer.

Support

Thanks to go to all the fellow graduate students and my family for their self-less willingness to listen and support me throughout the completion of this dissertation.

Table of Contents

Abstract ii
Grant Information iv
Author's Acknowledgments v
Table of Contents vi
List of Figures viii
List of Tables xii

Chapter 1: Introduction

1.1 Occurrence and composition 1
1.2 Structure 2
1.3 Chapter Overviews 7
1.4 References 9

Chapter 2: The effect of Al,Si disorder on the bulk moduli of plagioclase feldspars

2.1 Opening Remarks 10
Abstract 11
Introduction 11
Experimental/sample description 12
Results 13
Discussion 15
Acknowledgements 17
References 17

Chapter 3: Tilts and tetrahedral: the origin of anisotropy seen in feldspars

3.1 Opening Remarks 19
Abstract 20
Introduction 20
Reference feldspar structure 21
Definition of Tilts 23
Tilting of the ideal structure 24
Methods 24
Limits to tilts 25
Tilt # 1 25
Tilt # 2 25
Tilt # 3 27
Tilt # 4 28
Volume changes in feldspars 28
Anisotropy of feldspars 29
Acknowledgments 32
References 32

Chapter 4: The effect of high-pressure on tetrahedral tilting in C-1 Ab-rich plagioclase feldspars

4.1 Introduction 34
4.2 Experimental 35
4.2.1 Sample Description 35
4.2.2 Experimental details 36
4.2.3 Data integration and refinement 38

4.3 Results …… 40
4.3.1 Refinement results for An20 and An37 …… 40
4.3.2 Cell parameter evolution for An20 and An37 …… 40
4.3.3 The volume change and elastic softening of Ab-rich plagioclase feldspars 41
4.3.4 Structural evolution with pressure for An20 and An37 ……..... 48
4.4 Discussion …… 55
4.4.1 Unit-cell strains …… 55
4.4.2 Linear strains and elastic softening ……..... 57
4.4.3 Tilts ……..... 59
4.4.4 The effect of O-O repulsion on tilt systems ……..... 60
4.5 Conclusions …….. 65
4.6 References ……. 67
Chapter 5: The effect of temperature on tetrahedral tilting in C-1 Ab-rich plagioclase feldspars
5.1 Introduction …… 69
5.2 Experimental ……..... 71
5.2.1 High-resolution high-temperature powder X-ray diffraction …… 71
5.2.2 High-temperature single-crystal X-ray diffraction on An27/An26 …… 72
5.2.3 Low-temperature single-crystal X-ray diffraction data collection on An26 76
5.2.4 Data analysis of the high- and low-temperature single crystal experiments on An26 76
5.2.5 Data analysis of the Rietveld refinements on albite ……. 77
5.3 Results ……. 79
5.3.1 Albite analysis: (comparison of single-crystal refinement and Rietveld refinement) 79
5.3.2 An26/An27 analysis (comparison between Rietveld refinements and single crystal data for a non-end-member feldspar) 86
5.3.3 Tilt system analysis of the Rietveld results of An35 and An46 …… 93
5.4 Discussion ……. 95
5.4.1 Comparing tilt systems for C-1 plagioclase with alkali feldspars at high-temperature 95
5.4.2 The effect of short M-O bonds on tilt system evolution ……. 97
5.4.3 A structural reasoning for negative thermal expansion in albite ……. 100
5.5 Conclusions …….. 105
5.6 References ……. 106
Chapter 6: Concluding Remarks
6.1 Conclusion ……. 109
6.2 References ……. 114
Appendix A: Structural Data ……. 115
Appendix B: Unit Cell Parameters ……... 160
Appendix C: Citations ……... 167

List of Figures

Chapter 1

Figure 1.1	A compositional phase diagram of feldspars	2
Figure 1.2	A portion of the feldspar structure showing the 4-membered tetrahedral rings and the bonding environment of the M-site	3
Figure 1.3	A portion of the feldspar structure showing the souble-crankshaft chains along the a-axis	4
Figure 1.4	Proposed sub-solidus equilibrium phase diagram from Carpenter (1994) at room pressure with structural phase transitions	7

Chapter 2

Figure 1	A pressure-volume plot with measured P-V data in chapter 2	14
Figure 2	An f-F plot of the data measured in chapter 2	14
Figure 3	A plot of the difference in room pressure bulk moduli against the difference in room pressure volume for the data in chapter 2	15
Figure 4	A plot of the room pressure bulk moduli and measured volumes of the data in chapter 2.	16
Figure 5	A plot of the room pressure bulk moduli and calculated densities of the data in chapter 2	16

Chapter 3

Figure 1	The framework of an ideal un-tilted feldspar viewed down the [104] direction	20
Figure 2	The variation of the lengths of three mutually perpendicular directions in $AlSi_3$ feldspars at room conditions, high-temperatures and high-pressures	21
Figure 3	Two views of the 4-ring of tetrahedra that forms the fundamental building block of the feldspar structure	22

Figure 4	The four tilt patterns of the tetrahedra in a 4-ring	23
Figure 5	The variation of the T-O-T angles with individual tilts of the ideal feldspar structure	26
Figure 6	The changes in the monoclinic unit cell parameters and unit-cell volume induced by the individual tilts of the ideal feldspar structure	27
Figure 7	The change in volume of the monoclinic unit-cell volume induced by individual tilts	28
Figure 8	Contoured maps showing the variation of unit-cell volume and shortest O-O distance between oxygens on different tetrahedral induced by the combination of tilts 2 and 3	29
Figure 9	The variation of tilt angles for all published structures of $AlSi_3$ feldspars at ambient conditions, high-temperature and pressures up to 4 GPa	30
Figure 10	The variation of the lengths of three mutually perpendicular directions in the ideal monoclinic feldspar as a function of combined effects of tilts 2 and 3	30
Figure 11	The variation of the unit-cell parameters a,b,c and d(100) as a function of tilts 2 and 3 of the ideal model feldspar	31
Figure 12	The variation of T-O-T bond angles with the value of tilt 2	32

Chapter 4

Figure 4.1	Fractional cell edge length change and volume change at high-pressure for An20 and An37	43
Figure 4.2	Unit cell angle changes at high-pressure for An20 and An37	44
Figure 4.3	A pressure-volume plot with the measured P-V data for low albite, analbite, An20 and An37	45
Figure 4.4	F-f_E plots of the volume data for low albite, analbite, An20, and An37	46
Figure 4.5	The bulk moduli versus pressure for low albite, analbite,	47

	An20 and An37	
Figure 4.6	The T-O-T angles at high-pressures for An20, An37, low albite and analbite	49-50
Figure 4.7	The four tilting systems at high-pressures for low albite, analbite, An20 and An37	52-53
Figure 4.8	Linear strain X,Y and Z from chapter 3 with the added values for An20 and An37 from chapter 4	54
Figure 4.9	Variation of tilts with unit-cell volume	58
Figure 4.10	Two of the shortest non-bonded O-O distances at high pressures for low albite, analbite, An20 and An37	63
Figure 4.11	A portion of the tilt system 2 and tilt system 3 model from Chapter 3 contoured to the unit-cell volume and *d(100)*	64
Chapter 5		
Figure 5.1	A custom-made high-temperature furnace	75
Figure 5.2	Fractional change for cell edge lengths at high-temperatures for the Rietveld refinement and single-crystal refinement results of An0	80
Figure 5.3	Unit cell angle changes at high-temperatures for the Rietveld refinement and single-crystal refinement results of An0	81
Figure 5.4	The four tilt systems for the Rietveld refinement and single-crystal refinement results of An0	82
Figure 5.5	T-O-T angles at high-temperatures for the Rietveld refinement and single-crystal refinement results of An0	84
Figure 5.6	The 7 shortest Na-O distances for the Rietveld refinement and single-crystal refinement results of An0	85
Figure 5.7	Fractional change of the cell edge lengths at high-temperatures for the Rietveld refinement and single-crystal refinement results of An26	89

Figure 5.8	Unit cell angle changes at high-temperatures for the Rietveld refinement and single-crystal refinement results of An26	90
Figure 5.9	The four tilting systems at high-temperature for the Rietveld refinement and single-crystal refinement results of An26	92
Figure 5.10	The four tilt systems for the Rietveld refinement and single-crystal refinement results of An35 and An46	94
Figure 5.11	The tilt system 2 and tilt system 3 model from chapter 3 contoured to cell parameter a, d(100),b,c and unit cell volume with added data from chapter 5	98
Figure 5.12	The Ca-Oa2, Ca-Oa1, Na-Oa2 and Na-Oa1 bond lengths for the results of the Rietveld refinements (An0, An27, An35 and An46)	99
Figure 5.13	The T1o tilt versus temperature , T1m tilt versus temperature , T1o tilt versus c-axis length and T1m tilt versus c-axis length for the Rietveld refinement results of albite , An27, An35, An46 and the single-crystal refinements of An26	102-103
Figure 5.14	The difference between the value for T1o and T1m versus c-axis length and T2o tilt and T2m tilt versus c-axis length for the Rietveld refinement results of albite ,An27, An35 and An46 and the single-crystal refinements of An26	104

Chapter 6

Figure 6.1	Two of the shortest non-bonded O-O distances for plagioclase at high-temperature and high-pressure	112-113

List of Tables

Chapter 2

Table 2.1	Sources for structural determinations, sources for equations of state determinations and equation of state parameters for Low Albite, Analbite, Hawkb, Hawkb/1, 101377a, and 101377a/1.	12
Table 2.2	Measured volumes at pressures for samples Hawkb, 101377a and 101377a/1.	13

Chapter 3

Table 3.1	Fractional coordinates of the ideal un-tilted feldspar, space group *C2/m*	23

Chapter 5

Table 5.1	Temperature calibration for the high-pressure furnace	73
Table 5.2	Model comparisons for the albite Rietveld results	77
Table 5.3	The single-crystal refinement results for An26 from 303K – 1023K	88

Chapter 1: Introduction

1.1 Occurrence and composition

Feldspars comprise about 60 percent of the Earth's crust and occur in a wide variety of geological environments ranging from igneous magmatic rocks to authengenic sedimentary rocks. The elastic and thermodynamic properties of this important mineral group are needed for the interpretation of seismic wave velocities in the Earth's crust, for understanding cation partioning patterns in the Earth's crust, and for the determination of phase boundaries and reactions involving feldspars. Feldspar minerals are aluminosilicates with the general chemical formula MT_4O_8 in which the tetrahedral T site can be occupied by Al^{3+} or Si^{4+} and the inter-framework M-site can be occupied by Ca^{2+}, Ba^{2+}, K^{1+} or Na^{1+}. As shown in Figure 1.1, two solid-solution series exist and include the naturally occurring plagioclase feldspars with mixing between $NaAlSi_3O_8$ (albite: Ab) and $CaAl_2Si_2O_8$ (anorthite: An) and the alkali feldspars with mixing between $NaAlSi_3O_8$ and $KAlSi_3O_8$ (K-feldspar: Or). For alkali feldspars, both end-members have the same Al:Si ratio of 1:3 while for plagioclase feldspars, one end-member (albite) has an Al:Si ratio of 1:3 while the other end-member (anorthite) has an Al:Si ratio of 2:2. The chemical formula of a ternary feldspar within these two solid solution series can be described by: $K_xNa_yCa_{1-(x+y)}Al_{2-(x+y)}Si_{2+(x+y)}O_8$ where $0 < (x+y) < 1$ in which x is the mole fraction of K-feldspar, y is the mole fraction of Na-feldspar, and 1-(x+y) is the mole fraction of Ca-feldspar.

Figure 1.1. A compositional phase diagram of feldspars.

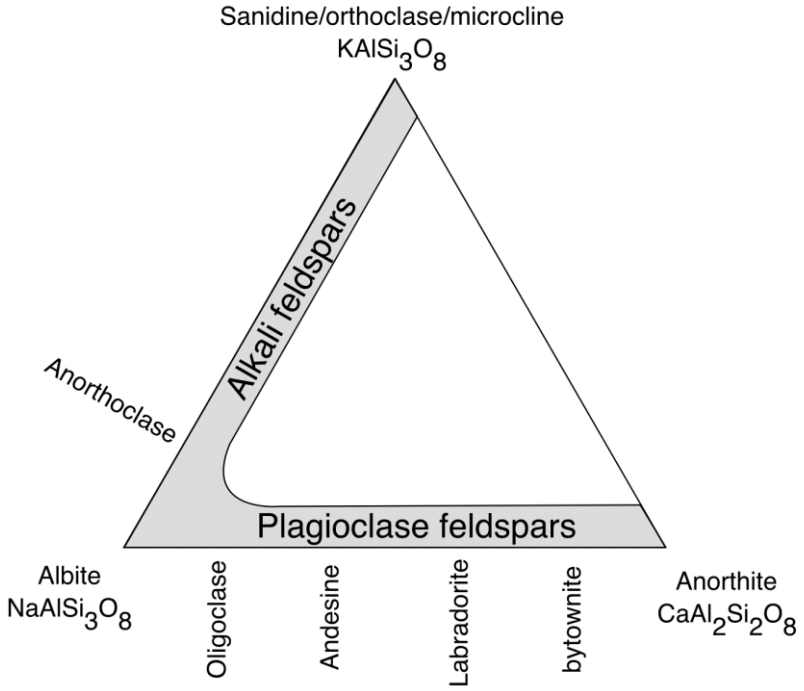

1.2 Structure

The feldspar structure consists of a three-dimensional framework of strongly-bonded TO_4 tetrahedra formed by the sharing of oxygen atoms between tetrahedra (Figure 1.2). The tetrahedra are arranged in four-membered rings that share corners with others to form a double crankshaft-like chain (see Figure 1.3). There are two double-crankshaft like chains in the structure; one parallel to *a* and the other parallel to *b*. The *M*-cations are located between the two double crankshaft chains in the unit cell. Changes in the state of Al,Si order amongst the *T*-sites can change the space group of the feldspar structure. For alkali feldspars with an Al:Si ratio of 1:3, the highest symmetry achievable is *C2/m* which is the space group for K-feldspar with complete disorder amongst the *T*-sites with two symmetrically distinct T-sites (T1 and T2) of which each site contains 25% aluminum and 75% silicon. Al,Si ordering causes the T1 and T2 sites to no longer be equivalent and causes the aluminum to preferentially occupy the T-site

Figure 1.2. A portion of the feldspar structure showing the 4-membered tetrahedral rings and the bonding environment for the *M*-site.

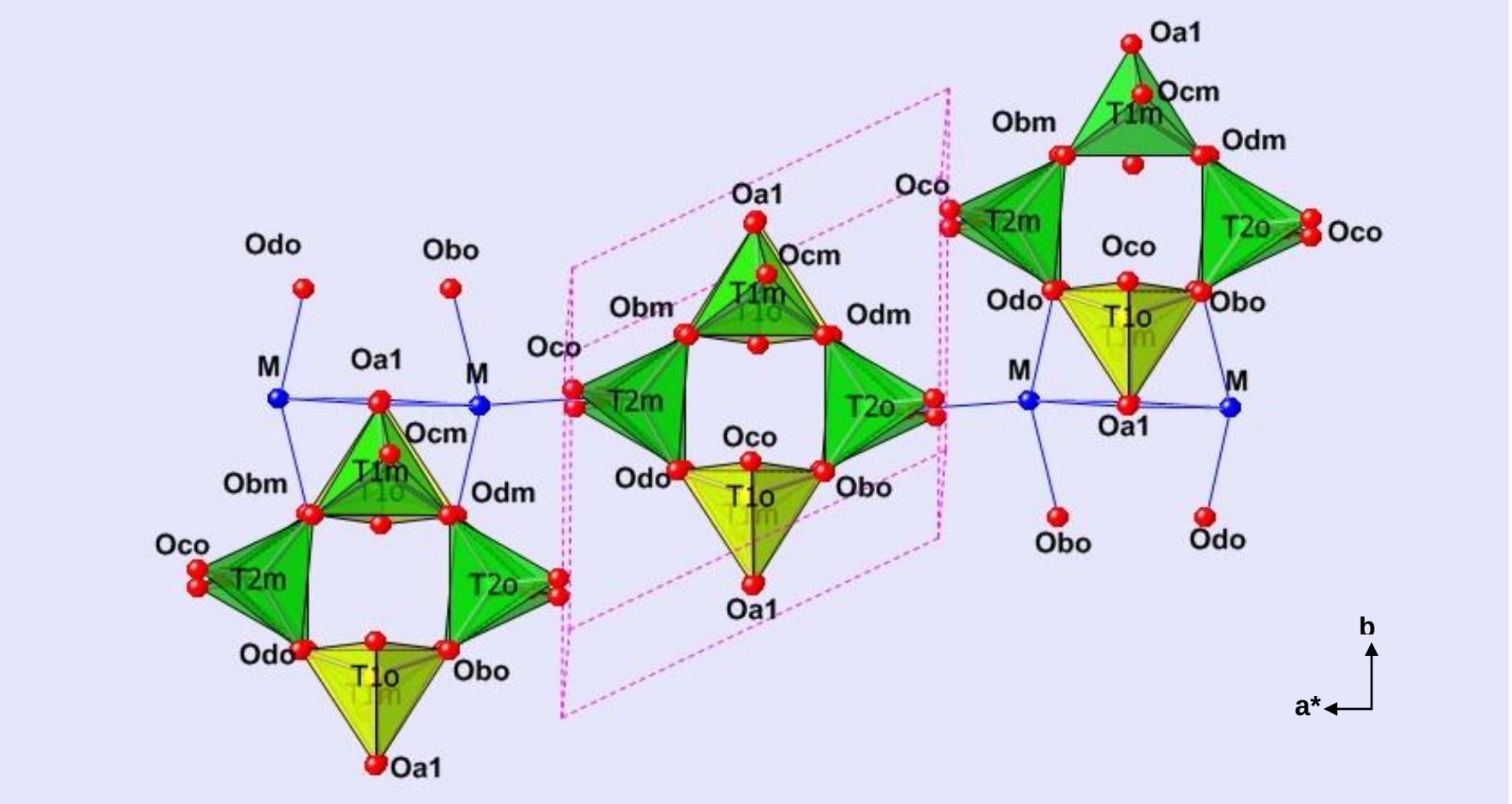

Notes. The crystallographic information file used to generate this image is of a low albite (Al,Si ordered) *C-1* structure from Downs *et al.* 1994. The yellow tetrahedra represent the AlO_4 and green represent SiO_4. Outlined in pink dashed lines is the unit cell for low albite.

Figure 1.3. A portion of the feldspar structure showing the double-crankshaft chain along the *a*-axis.

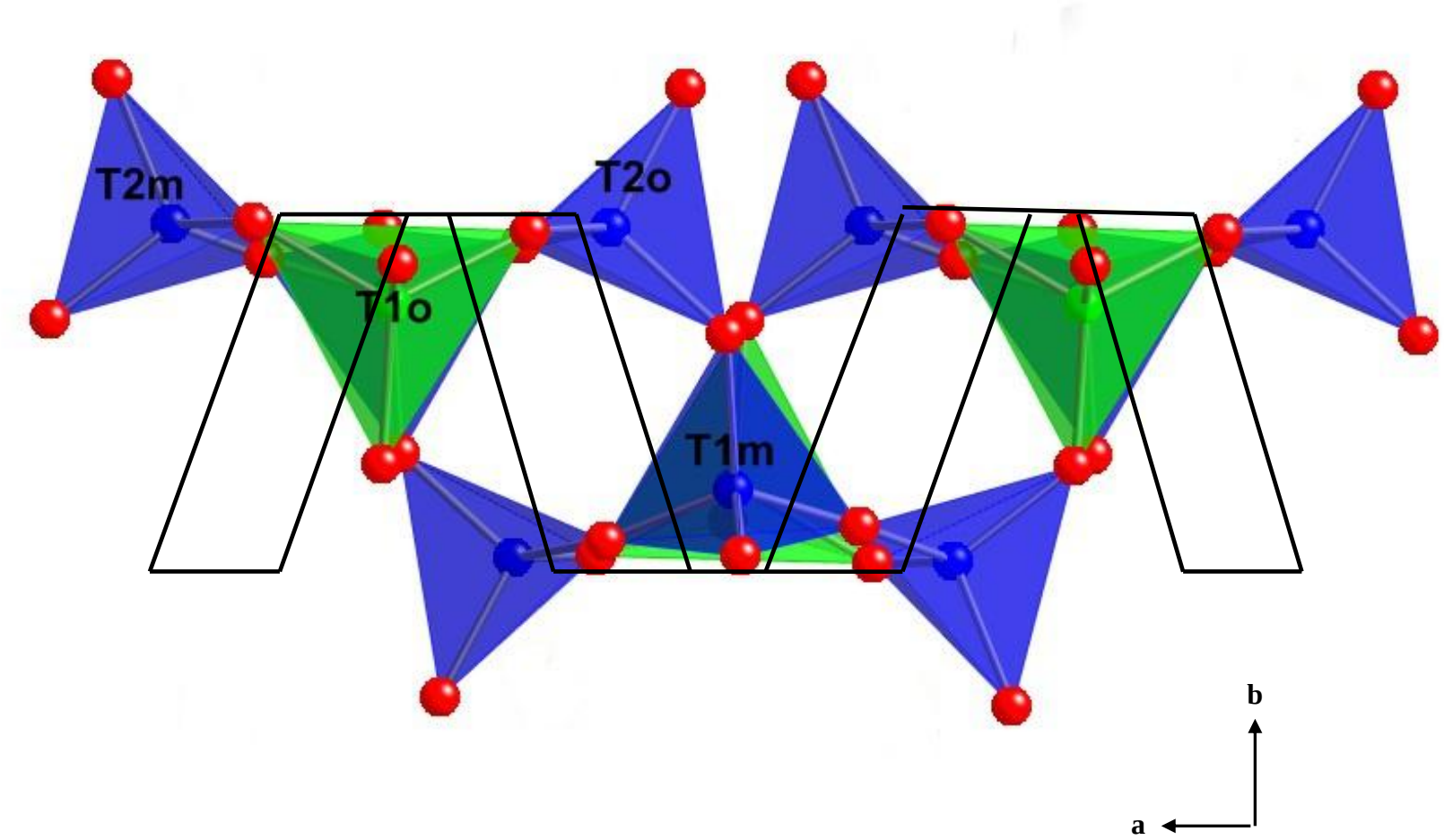

labeled “T1o” and the silicons to occupy the *T*-sites labeled “T1m”, “T2o”, and “T2m” (see Figure 1.2) which lowers the symmetry from *C2/m* to *C-1*. For plagioclase feldspars, the order-disorder phase transition is more complex because of resulting non-integer ratios between aluminum and silicon for intermediate compositions. For albite-rich plagioclase up to approximately An50Ab50, the structure is closer to the aluminum to silicon ratio of 1:3 and the space group is C-1 with a *c*-axis of 7Å but for any plagioclase composition of An greater than 50%, the Al:Si becomes closer to that of anorthite (2:2) in which the resulting space group becomes *I-1* and the *c*-axis doubles to 14 Å. Anorthite-rich plagioclases with more than 90% Ca^{2+} undergo a displacive phase transition to a structure with P-1 symmetry but the pattern of Al:Si ordering remains the same as the I-1 structures, and natural anorthites are close to being completely ordered with respect to their Al:Si distributions (e.g. Angel *et al.*, 1990; Carpenter *et al.*, 1990). Figure 1.4 below shows a proposed phase diagram for the plagioclase feldspars from Carpenter 1994. In this dissertation, I will focus will on the *C-1* feldspars.

The stability of feldspars and phase boundaries are dependent upon their compressibility and presence of other components within the bulk chemistry. The boundaries for the reactions of minerals in P-T-X space are dependent on thermodynamic properties such as thermal expansion and compressibility. Recent developments in X-ray diffraction at high-pressure and high-temperature have provided the means by which to study the feldspar structures with great precision from which then thermodynamic properties can be derived. Although plagioclase feldspars have been extensively studied, the systematics involved with respect to the structural changes with pressure, temperature, and composition are still not completely understood. Unit-cell parameter changes upon pressure, temperature, and compositional changes were previously used to infer the mechanisms of structural responses to these changes. This includes the use of 3

different trends with respect to plotting the *c*-axis versus *b*-axis and alpha versus gamma (Brown *et al.*1984). While this system worked well for alkali feldspars at high-temperatures and varying composition, the trends seen in terms of the evolution with unit-cell angles are more variable for feldspars at high pressure (Angel 1994). Cell parameter changes are generally poor indicators of structural change with pressure, temperature, and composition. Parameters such as polyhedra tilt angles and metal-anion-metal bond angles should be used to characterize structural behavior in framework structures (Taylor 1983). In addition, it is difficult to study plagioclase feldspars which are not end-member compositions due to the structural complications that arise from albite –like and anorthite-like structural mixing. The purpose of this dissertation is to provide a model and a systemic approach to describing plagioclase feldspar structures with varying composition at high-pressure and high-temperature to be able to predict the thermodynamic properties. Of special interest is the Na-rich *C-1* plagioclases which display anomalous behavior in their anisotropy and elasticity.

Figure 1.4. Proposed sub-solidus equilibrium phase diagram from Carpenter (1994) at room pressure with structural phase transitions.

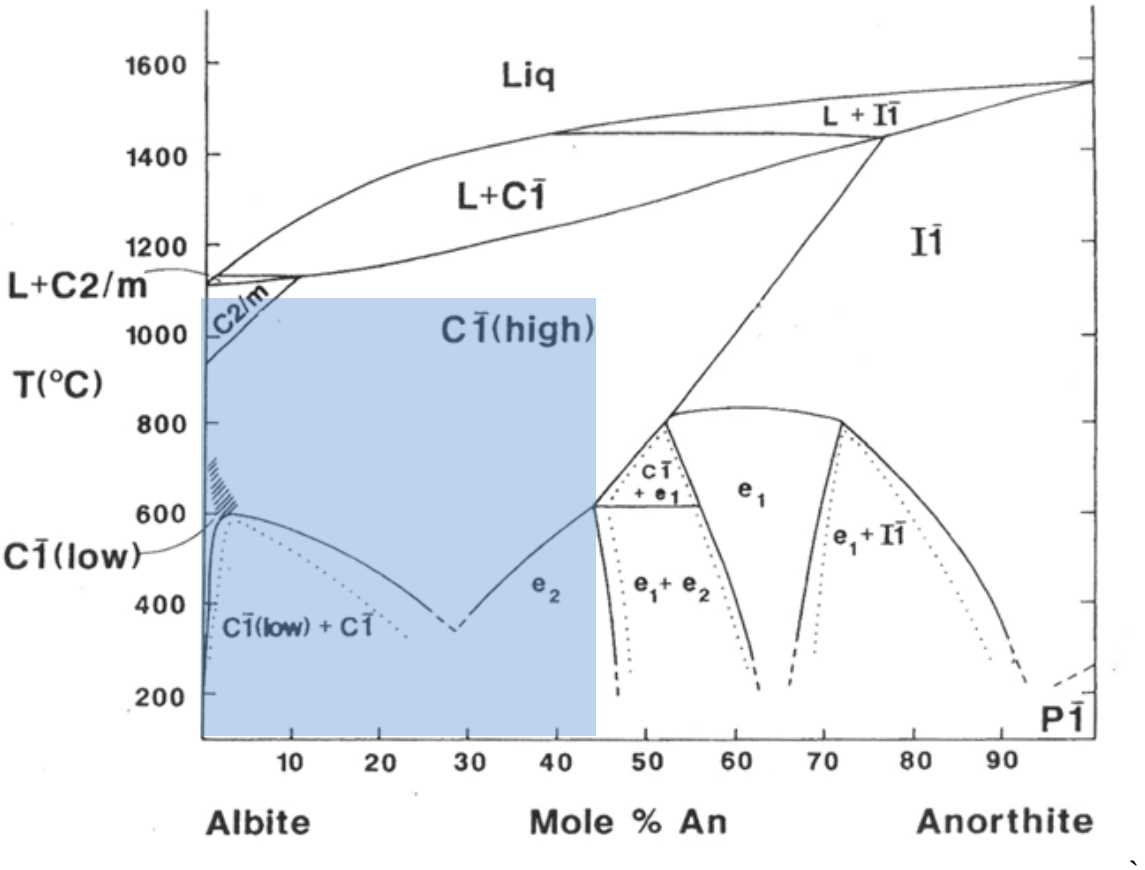

Notes. The highlighted region is that of the C-1 feldspars on which most of this dissertation will focus on.
Citation: Carpenter, M.A. (1994) Subsolidus phase relations of plagioclase feldspar solid solution. *In* Parsons I. (ed) Feldspars and Their Reactions. Kluwer Academic Publishers, Netherlands: 221-269.

1.3 Chapter Overviews

Chapter 2 describes how Al,Si disorder in the *T*-sites affects the bulk moduli for plagioclase feldspars. The recent developments in single-crystal high-pressure diffraction have allowed the observation of small changes in the structures of minerals and therefore provide the opportunity to see small but significant change in the bulk moduli of plagioclase feldspars as Al,Si disorder is induced in the plagioclase structure. The results from this study along with previous studies on albite and analbite (Benusa *et al.* 2005; Curetti *et al.* 2010) provide the framework for looking for consistent structural reasons for the anomalous behavior of Na-rich

feldspars at high pressure and the reason for the difference seen in the bulk moduli of plagioclase feldspars with changing state of Al,Si order with constant composition.

An elegant and systematic approach to describing the feldspar structure is described in Chapter 3. This chapter uses the idea of the feldspar tilting model from Megaw (1972) and significantly extends it. The tilting systems are applied to an idealized monoclinic feldspar model described in this chapter and investigated in terms of the changes seen in cell parameters, bond lengths and bond angles. In addition, the tilt systems are applied to previously collected single-crystal data on alkali feldspars at room conditions, low pressures and high temperatures. The tetrahedral tilting model in this chapter provides a systematic explanation for the anisotropy in the cell parameter evolution seen in alkali feldspars at low pressure and high-temperature and with changing composition.

The structures of Na-rich plagioclase feldspars at high pressure are investigated in Chapter 4. This chapter includes new data collected on an An20 plagioclase along with previously collected data from the literature. With the tilting model established in Chapter 3, it is possible to explain the anomalous elastic behavior seen in the Na-rich plagioclase feldspars including the elastic softening seen at higher pressures and the trends seen in the anisotropy with pressure.

Na-rich plagioclase feldspars at high-temperature were more extensively studied than at high-pressure but are still not completely understood. In Chapter 5, the results of high-temperature single-crystal X-ray diffraction are presented in addition to the Rietveld refinements on the Na-rich plagioclase feldspar powders that were previously analyzed in Tribaudino *et al.* 2010. Single-crystal refinement results and Rietveld refinement results are compared to provide a proof for the validity of Rietveld refinements on powdered mineral samples as means to study

small changes in the structures. The tetrahedral tilting model proposed in Chapter 3 is used to describe the Na-rich plagioclase feldspar structural changes at high-temperatures.

Chapter 6 concludes this study with brief comparison of the tetrahedral tilting model with respect to the Na-rich plagioclase structures at high pressures and high temperatures.

1.4 References

Angel, R.J., Carpenter, M.A., Finger, L.W. (1990) Structural variation associated with compositional variation and order-disorder behavior in anorthite-rich feldspars. *American Mineralogist*, **75**: 150-162.

Angel, R.J. (1994) Feldspars at high-pressure. *In* Parsons, I (ed.) Feldspars and their reactions. Kluwer Academic Publishers, Netherlands: 271-312.

Benusa, M., Angel, R.J., Ross, N.L. (2005) Compression of albite: $NaAlSi_3O_8$. *American Mineralogist*. **90**: 1115-1120.

Brown, W.L. (1984) Feldspars and Feldspathoids. Reidel Publishing co. Dordrecht.

Carpenter, M.A., Angel, R.J., and Finger, L.W. (1990) Calibration of Al/Si order variations in anorthite. *Contributions to Mineralogy and Petrology*, **104**: 471-480.

Carpenter, M.A. (1994) Subsolidus phase relations of the plagioclase feldspar solid solution. *In* Parsons I (ed) Feldspars and their reactions. Kluwer Academic Publishers, Netherlands: 221-269.

Curetti, N., Sochalski-Kolbus, L., Angel, R.J. , Benna, P., Nestola, F., Bruno, E. (2011) High-pressure structural evolution and equation of state of analbite. *American Mineralogist*, **96**: 383-392.

Downs, R.T., Hazen, R.M. and Finger, L.W. (1994) The high-pressure crystal chemistry of low albite and the origin of the pressure dependency of Al-Si ordering. *American Mineralogist*, **79**: 1042-1052.

Megaw, H.D. (1972) Tilts and tetrahedra in feldspars. *The Feldspars: Chapter 6.* P. 87-113.

Taylor, D. (1983) The structural behaviour of tetrahedral framework compounds – a review. Part I. structural behaviour. *Mineralogical Magazine*, **47**: 319-326.

Tribaudino, M., Angel, R.J., Camara, F. Nestola, F., Pasqual, D and Margiolaki, I. (2010) Thermal expansion of plagioclase feldspars. *Contributions to Mineralogy and Petrology,* **160**: 899-908.

Chapter 2: The effect of Al,Si disorder on the bulk moduli in plagioclase feldspars

2.1 Opening remarks

This chapter is a journal article that was published in The Mineralogical Magazine in the December 2010 issue. The ideas behind the research were discussed between Lindsay Sochalski-Kolbus, Dr. Ross J. Angel and Dr. Fabrizio Nestola. The annealed analbite sample used in the study was provided by Dr. Fabrizio Nestola. The experiments were conducted by Lindsay Sochalski-Kolbus with guidance from Dr. Ross J. Angel. The text was put together by Lindsay Sochalski-Kolbus and Dr. Ross J. Angel. This chapter is an isothermal equation of state study on plagioclase feldspars at high-pressure to determine what effect the Al,Si ordering and disordering has on the bulk modulus. It was found in this study that the increase of Al,Si disorder in plagioclase feldspars at constant composition softens the structure and thus the bulk modulus is lower. These findings serve as a precursor for investigating a systematic structural reason for the anomalous elastic behavior in Na-rich plagioclase feldspars as well as other strange structural behavior seen in feldspars.

Mineralogical Magazine, December 2010, Vol. 74(6), pp. 943–950

The effect of Al/Si disorder on the bulk moduli of plagioclase feldspars

L. M. Sochalski-Kolbus[1], R. J. Angel[1] and F. Nestola[2]

[1] Virginia Tech Crystallography Laboratory, Department of Geosciences, Virginia Tech, Blacksburg, VA 24060, USA
[2] Dipartimento di Geoscienze, Università di Padova, Via Giotto 1, I-35137 Padova, Italy

[*Received 24 August 2010; Accepted 24 November 2010*]

ABSTRACT

The volumes of a disordered An_{20} (Q_{od} = 0.15), a disordered An_{78} (Q_{od} = 0.55) and an ordered An_{78} (Q_{od} = 0.81) were determined up to 9.569(10) GPa, 8.693(5) GPa and 9.765(10) GPa, respectively, using single-crystal X-ray diffraction. The volume variations with pressure for these samples are described with 4th-order Birch Murnaghan equations of state with V_0 = 669.88(7) Å^3, K_0 = 59.7(7) GPa, K' = 5.7(5), K'' = −0.8(2) GPa^{-1} for disordered An_{20}, V_0 = 1340.48(10) Å^3, K_0 = 77.6(5) GPa, K_0' = 4.0(3), K'' = −0.59(9) GPa^{-1} for disordered An_{78} and V_0 = 1339.62(6) Å^3, K_0 = 77.4(6) GPa, K' = 4.2(4), and K'' = −0.7(1) GPa^{-1} for ordered An_{78}. Along with data from previous studies (An_0 ordered, An_0 disordered and An_{20} ordered), the volumes for the disordered samples were found to be up to ~0.3% larger than the ordered samples of the same composition. The disordered samples are softer than the ordered samples of the same composition by 4(1)% for An_0, 2.5(9)% for An_{20} and essentially zero for An_{78}. The relationship between volume increase, density decrease, and decreasing bulk modulus with increasing disorder is in accordance with Birch's Law.

Keywords: Burch-Murnaghan equation, Al,Si disorder, plagioclase.

Introduction

Feldspars are framework aluminosilicates that can contain monovalent or divalent cations in their extra-framework cation sites. This mineral group makes up ~60% of the Earth's crust and is an important constituent of metamorphic reactions. The plagioclase feldspars are a solid solution between albite ($NaAlSi_3O_8$) and anorthite ($CaAl_2Si_2O_8$). The naturally occurring end-members are found to be completely ordered with respect to their Al/Si distributions in the framework (e.g. Wainwright and Starkey, 1971; Ferguson *et al.*, 1958). The different Al:Si ratios of these two end-members result in them having fundamentally different ordering patterns of the Al and Si amongst the tetrahedral sites. In end-member albite, the Al only occupies one of the four symmetrically distinct tetrahedra and this kind of ordering results in space-group symmetry $C\bar{1}$ with a c unit-cell parameter of ~7 Å. The plagioclase solid solution is based on the coupled exchange of Ca^{2+}+Al^{3+} for Na^{+}+Si^{4+}. The substitution of Ca^{2+} for Na^{+} in the albite structure therefore changes the Al:Si ratio away from 1:3, because of the substitution of Al for Si, and thus induces partial Al/Si disorder in natural intermediate plagioclases. Up until ~50% Ca^{2+} substitution for Na^{+}, the pattern of Al/Si ordering remains the same as the pattern in albite, and the space group remains $C\bar{1}$. At Ca^{2+} contents >50%, the Al:Si ratio becomes closer to 2:2 and the ordering pattern changes to one in which the Al-rich and Si-rich tetrahedra alternate. This results in a doubling of the c unit-cell parameter to ~14 Å and space group $I\bar{1}$. Anorthite-rich plagioclases with >90% Ca^{2+} undergo a displacive phase transition to a structure with $P\bar{1}$ symmetry but the pattern of Al/Si ordering remains the same as the $I\bar{1}$ structures, and

* E-mail: lsochals@vt.edu
DOI: 10.1180/minmag.2010.074.6.943

natural anorthites are close to being completely ordered with respect to their Al/Si distributions (e.g. Angel *et al.*, 1990; Carpenter *et al.*, 1990).

There are thus two ways in which partial Al/Si disorder can be induced in the plagioclase feldspars. The first is the addition of Na into anorthite or Ca into albite which causes the Al:Si ratio to change away from integer ratios, as discussed above. The second is that high-temperature annealing followed by quenching can be used to induce partial or complete Al/Si disorder without changing the composition (e.g. Carpenter *et al.*, 1985, 1990; Prewitt *et al.*, 1976).

The effects that Al/Si disorder has on the structure of plagioclases and some of their thermodynamic properties have been determined. The introduction of Al/Si disorder induces significant changes in the unit-cell parameters (Kroll, 1978; Kroll and Ribbe, 1980) and an increase of up to ~2 Å^3 (~ 0.3%) in the volume (Kroll, 1983) at room conditions. Apart from the increase in configurational entropy, the change in enthalpy due to Al/Si disorder is small but measurable and ranges from ~4 to 16 kJ/mol (Carpenter *et al.*, 1985). It was shown that Al/Si disorder results in a ~4% softening of albite (Curetti *et al.*, 2010), and a slight softening of anorthite (Hackwell and Angel, 1992). By contrast, recent ultrasonic wave velocity measurements (Kono *et al.*, 2008) on a bulk specimen of a Bøggild intergrowth suggest that Al/Si disorder stiffens plagioclases of intermediate composition. Therefore, we have determined the effect of Al/Si disorder by a series of single-crystal high-pressure diffraction measurements of ordered and disordered intermediate plagioclases.

Experimental/sample description

The three pairs of plagioclase crystals discussed in this paper were chosen in order to represent the range of structural states found across the plagioclase join. Each pair of samples comprises a natural sample with the maximum state of Al/Si order possible for the composition, with a second sample of the same composition in which Al/Si disorder has been induced by high-temperature annealing. Details of the annealing procedures for samples Hawkb/1 and 101377a/1 are reported by Carpenter *et al.* (1985) and Curetti *et al.* (2010) for analbite. Bulk compositions of all six samples (Table 1) were determined by electron microprobe analysis and all samples have <3% Or content (Carpenter *et al.*, 1985; Curetti *et al.*,

TABLE 1. Sources for structural determinations, sources for equation of state determinations and equation of state parameters for Low Albite, Analbite, Hawkb, Hawkb/1,101377a, and 101377a/1. The numbers in parentheses represent the standard deviations.

Sample	Composition	Space group	Q_{od}*	Structural source	V_o†	K_o (GPa)†	K' (GPa)†	K'' (GPa^{-1})†	EoS source†
Low Albite	An_0	$C\bar{1}$	1	Downs *et al.* (1994)	664.76(9)	52.3(9)	8.8(6)	−2.8(2)	Benusa *et al.* (2005)
Analbite	An_0	$C\bar{1}$	0.09	Curetti *et al.* (2010)	667.09(8)	50.3(5)	8.9(5)	−2.4(3)	Curetti *et al.* (2010)
Hawkb	An_{20}	$C\bar{1}$	0.68	This study	667.88(7)	61.2(5)	5.6(4)	−0.94(14)	Angel (2004)
Hawkb/1	An_{20}	$C\bar{1}$	0.15	This study	669.32(9)	59.7(7)	5.7(5)	−0.8(2)	This study
101377a	An_{78}	$I\bar{1}$	0.81	Angel *et al.* (1990)	1339.62(6)	77.4(6)	4.2(4)	−0.7(1)	This study
101377a/1	An_{78}	$I\bar{1}$	0.55	Angel *et al.* (1990)	1340.48(10)	77.6(5)	4.0(3)	−0.59(9)	This study

* Defines the state of Al/Si order relative to completely ordered albite for $C\bar{1}$ and completely ordered anorthite for $I\bar{1}$. The equation is from Salje (1985) and is defined by (t1o−t1m)/(t1o+t1m). Site occupancies (ti) are determined from the average *T*–O bond lengths using the equation: ti = 0.25(1+nAn) + (<Ti–O>–<<T–O>>)/0.135 (Kroll and Ribbe, 1980; the coefficient 0.135 comes from Angel *et al.*, 1990).

† 4th-order Birch-Murnaghan EoS parameters refined using *EoSFit 5.2* (Angel, 2000)

2010). The state of Al/Si order of all of the samples was determined, by single-crystal diffraction, from the mean $T-O$ bond lengths within the structures (Table 1). The structure of Hawkb/1 was determined by single crystal X-ray diffraction using a Gemini diffractometer with Mo-$K\alpha$ radiation. Data were collected on an Atlas area detector up to 60º2θ. The data for the structure of Hawkb/1 were collected using a Super Nova diffractometer. Both structures were refined using *SHELX* (Sheldrick, 2007) in *WinGX* (Farrugia, 1999).

Single crystals of the three samples measured in this study were loaded separately in an ETH-designed diamond-anvil cell (Miletich *et al.*, 2000). The stainless steel gaskets used were all drilled to a diameter of 300 μm. For each sample, a ruby chip was used to measure approximate pressure, and the pressure-volume equation of state of quartz (Angel *et al.*, 1997) was used to determine the precise pressure for each data point. The cell was loaded with a 4:1 methanol/ethanol mixture to ensure hydrostatic conditions. The unit-cell parameters of the samples and the quartz were refined to the positions of reflections determined by 8-position centering (King and Finger, 1979) on a Huber 4-circle diffractometer using the *SINGLE* software (Angel *et al.*, 1997; Angel and Finger, 2011). The three data sets taken from the literature were collected using the same diffractometer with the same methods and were analysed using the same methodology.

TABLE 2. Measured volumes at pressures for samples Hawkb/1, 101377a and 101377a/1. The numbers in parentheses represent the standard deviations.

Sample	Pressure	Volume
Hawkb/1	0	669.32(9)
	0.314(4)	665.87(10)
	1.319(5)	655.52(9)
	2.489(5)	644.57(6)
	2.948(7)	640.41(6)
	4.248(6)	629.61(8)
	4.435(7)	628.05(9)
	5.148(8)	622.51(7)
	5.618(7)	618.78(7)
	6.207(8)	614.35(8)
	7.083(9)	607.96(9)
	8.204(11)	600.06(6)
	8.950(11)	594.76(7)
	9.569(10)	590.44(9)
101377a	0	1339.62(6)
	0.0725(4)	1338.34(10)
	0.711(3)	1327.57(6)
	1.219(4)	1319.40(7)
	1.969(5)	1307.61(8)
	2.624(6)	1297.70(6)
	3.259(5)	1288.03(7)
	3.412(6)	1285.57(9)
	4.699(7)	1266.79(9)
	6.077(9)	1247.72(7)
	6.805(9)	1237.80(5)
	7.096(8)	1234.09(6)
	7.425(8)	1229.62(8)
	8.428(20)	1216.16(9)
	8.624(10)	1213.08(7)
	9.440(10)	1201.20(8)
	9.765(10)	1196.41(9)
101377a/1	0	1340.4(1)
	0.054(5)	1339.5(2)
	0.069(4)	1339.2(2)
	0.364(4)	1334.32(11)
	0.669(4)	1329.13(9)
	1.142(4)	1321.5(2)
	1.339(4)	1318.2(2)
	1.446(5)	1316.62(11)
	1.968(5)	1308.2(9)
	2.425(5)	1301.3(1)
	2.679(5)	1297.5(2)
	2.804(6)	1295.54(9)
	3.355(5)	1287.5(2)
	3.778(5)	1281.03(11)
	3.853(5)	1280.3(2)
	4.644(7)	1269.0(2)
	5.152(5)	1262.0(2)
	5.395(8)	1258.5(2)
	5.780(5)	1253.22(11)
	6.196(9)	1247.7(1)
	6.787(5)	1239.4(2)
	7.089(5)	1235.7(2)
	7.289(5)	1232.9(2)
	7.855(5)	1225.3(2)
	8.227(5)	1219.8(2)
	8.693(5)	1214.3(2)

Results

The unit-cell volumes of the three samples (Hawkb/1, 101377a and 101377a/1) measured at various pressures (Table 2) and those of the previously measured samples [analbite (Curetti *et al.*, 2010), low albite (Benusa *et al.*, 2005) and Hawkb (Angel, 2004)] are plotted in Fig. 1. The volumes for 101377a and 101377a/1 are plotted as $V/2$ because they have $I\bar{1}$ symmetry with a doubled c unit-cell parameter of ~14 Å whereas

the remaining samples have a *c* unit-cell parameter of ~7 Å. The volumes of the natural samples increase ~0.8% from albite to An_{78} in agreement with Angel *et al.* (1988). The room-pressure volume increases up to ~0.3% with disorder at fixed composition, also in agreement with the literature (Prewitt *et al.*, 1976; Angel *et al.*, 1990). In fact, at all pressures, the volumes of the disordered samples remain larger than the volumes of the ordered samples of the same composition. It is clear from Fig. 1 that there is softening in albite (Benusa *et al.*, 2005) at pressures above 5 GPa. This trend is also present for the other samples, but is not obvious in the *P-V* plot.

Figure 2 is an $F-f_E$ plot of all of the data and the corresponding 4th-order Birch-Murnaghan equations of state (EoS) (Birch, 1947):

$$P = 3K_o f_E(1+2f_E)^{5/2}(1+\tfrac{3}{2}(K'-4)f_E+ \tfrac{3}{2}(K_oK''+(K'-4)(K'-3)+(35/9))f_E^2 \quad (1)$$

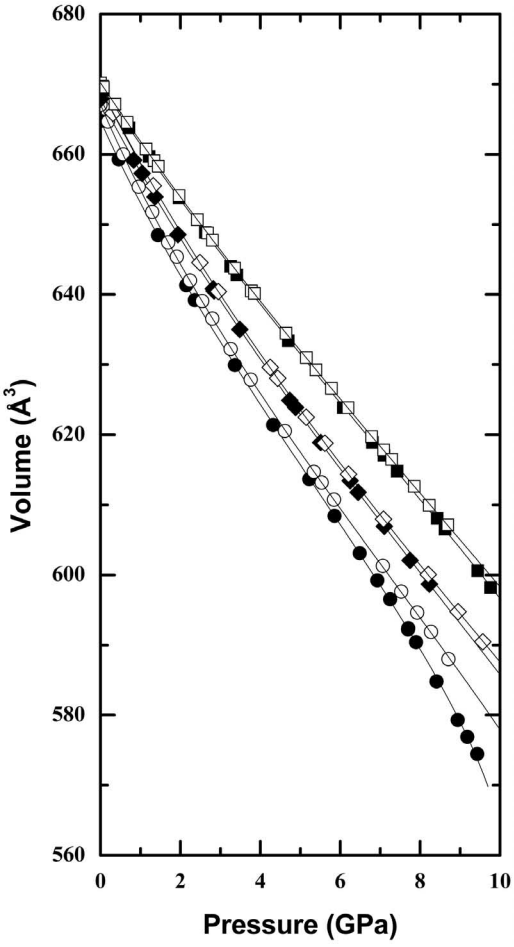

FIG. 1. A pressure-volume plot with the measured *P-V* data for analbite (open circles), low albite (filled circles), Hawkb/1 (open diamonds), Hawkb (filled diamonds), 101377a/1 (open squares) 101377a (filled squares). All lines plotted to fit the data are 4th order Birch Murnaghan equations of state.

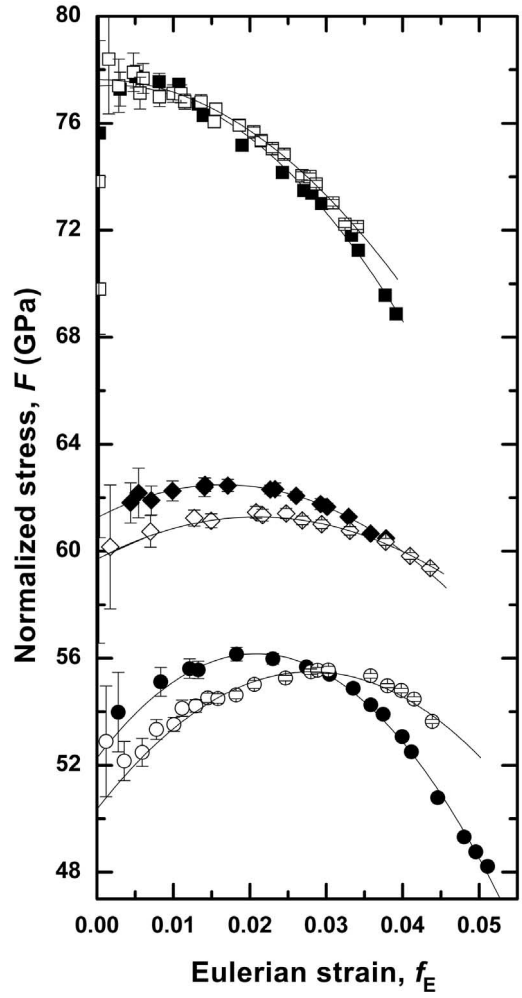

FIG. 2. An $F-f_E$ plot of the data for analbite (open circles), low albite (filled circles), Hawkb/1 (open diamonds), Hawkb (filled diamonds), 101377a/1 (open squares) and 101377a (filled squares). All lines plotted to fit the data are 4th-order Birch Murnaghan equations of state.

This 4th-order Birch-Murnaghan EoS is derived in terms of the Eulerian strain (f_E):

$$f_E = [(V_0/V)^{2/3}-1]/2 \quad (2)$$

in which V_0 is the zero-pressure unit-cell volume, and V is the unit-cell volume at a given pressure. The resulting definition of the normalized stress (F) is:

$$F = P/3f_E(1+2f_E)^{5/2} \quad (3)$$

and the 4th-order Birch-Murnaghan EoS can then be expressed by:

$$F = K_0(1+\tfrac{3}{2}(K'-4)f_E+ \tfrac{3}{2}(K_0K''+(K'-4)(K'-3)+(35/9))f_E^2 \quad (4)$$

The normalized stress (F) is therefore a simple polynomial in f_E, and a plot of F *vs.* f_E therefore shows the appropriate truncation of the EoS as well as an indication of the parameter values K_0, K' and K''. The y intercept of the plot is the room-pressure bulk modulus (K_0), the slope of the line is given by $\frac{3}{2}K_0(K'-4)$ and the curvature of the plot is an indication of the sign of K''. If the data fall on a horizontal line in the F–f_E plot, then they can be described by a 2nd-order EoS with $K' = 4$. If the data appear as a sloping line, then a 3rd-order truncation is sufficient to describe the data with a slope of $3K_0(K'-4)/2$ and an implied value of K''. If the F–f_E data lie on a curve, then a 4th order EoS must be used and K'' differs significantly from its implied value. All six datasets exhibit curvature. Therefore, 4th order equations of state were fitted to the data using the *EosFit* 5.2 program (Angel, 2000). All of the refined values of V_0 agree with the respective measured values for V_0 within the estimated uncertainties. Note that previous data for samples 101377a and 101377a/1 were fitted with a 3rd order equation of state (Angel, 2004) because of a lack of data at higher and lower pressures.

Values for the bulk moduli of all of the samples are given in Table 1. The bulk modulus for the naturally occurring ordered samples (low albite, Hawkb, and 101377a) increases by ~32% from An_0 to An_{78} which is in agreement with Angel (2004) and Johnson (2007). For the synthetically disordered samples (analbite, Hawkb/1 and 101377a/1), the bulk modulus increases by ~35% across the same compositional range. The bulk moduli of the disordered An_0 and An_{20} samples are less than that of the ordered samples of the same composition. This can be understood simply in terms of a volume effect. The disordered samples of An_0 and An_{20} have significantly larger unit-cell volumes (and hence lower density) than their ordered counterparts (Fig. 3). By contrast, at the An_{78} composition, the Al:Si ratio of 1.78:2.22 does not allow anything like full ordering in the nominally 'ordered' natural sample 101377a, and thus the change in the state of order upon high-temperature annealing is far less than in the other two samples (Table 1). Consequently, the volume change on disordering is smaller at An_{78} and there is no significant difference between the room-pressure bulk moduli of the An_{78} ordered and disordered samples.

Discussion

This general effect of decreasing bulk modulus with increasing volume at constant composition is the opposite of that seen for natural ordered plagioclases, in which increasing anorthite content leads to larger volumes and stiffer, not softer, bulk moduli (Fig. 4). However, the substitution of $Ca^{2+}+Al^{3+}$ for $Na^{+}+Si^{4+}$, while increasing the volume of the feldspar slightly also significantly increases the density, so the bulk moduli of the ordered plagioclases follows a smooth increasing trend with density (Fig. 5), in line with Birch's Law (Birch, 1961). The trend for plagioclases is clearly non-linear due to the lower bulk moduli for the albite-rich samples than would be expected by extrapolation from the data for compositions richer in Ca^{2+} (Fig. 5). In this context, the softening associated with

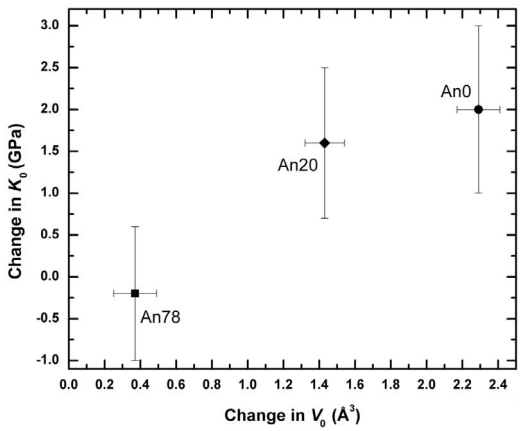

FIG. 3. A plot of the difference in room-pressure bulk moduli *vs.* difference in room-pressure volume between ordered and disordered samples for each of the pairs of samples with the same composition.

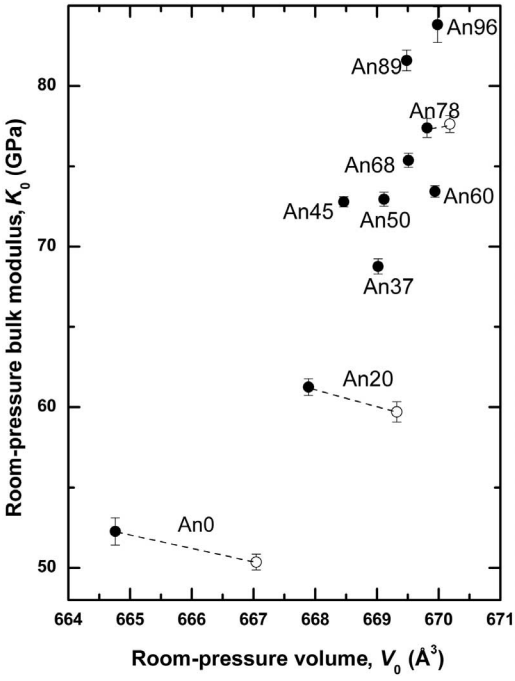

FIG. 4. A plot of the room-pressure bulk moduli and measured volumes of plagioclase from this work (An_0, An_{20} and An_{78}) and from Johnson (2007). The filled circles represent ordered samples while the open circles represent disordered samples.

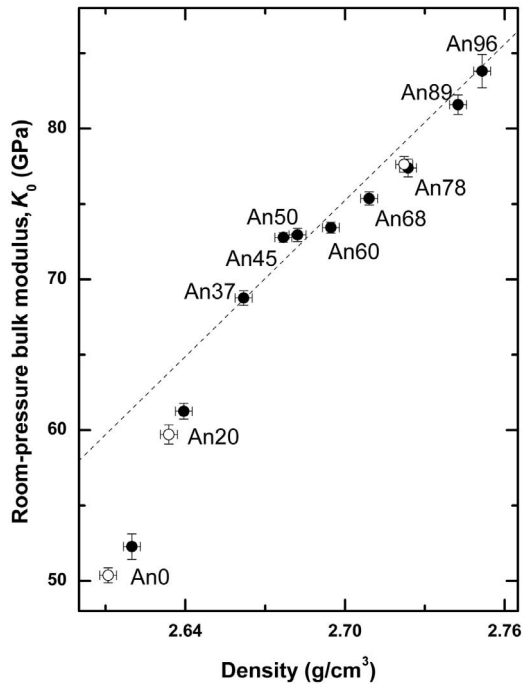

FIG. 5. A plot of the room-pressure bulk moduli and calculated densities of plagioclase from this work (An_0, An_{20} and An_{78}) and from Johnson (2007). The filled circles represent ordered samples while the open circles represent disordered samples.

disordering at constant composition is thus a consequence of decreasing density and is completely consistent with the general elastic properties of plagioclase feldspars.

The only other measurement of the effect of disorder on plagioclase bulk moduli is provided by Kono *et al.* (2008) who measured the compressional and shear-wave velocities of a bulk sample of An_{51} plagioclase with 0.2% chlorite and 0.5% opaques at a pressure of 1 GPa. After heating to 900ºC their sample became Al/Si disordered and exhibited apparently greater wave velocities than the original ordered sample. By using the equation of state parameters for An_{50} from Johnson (2007), room-temperature bulk moduli of 81.7 GPa and 85.3 GPa can be obtained from the velocities of Kono *et al*. (2008) for their ordered and disordered samples, respectively. The value for the ordered sample is >5 GPa higher than the value obtained from compressional data at 1 GPa (Johnson, 2007). The difference cannot be due to the trace mineral content because there is not enough of it within the bulk sample to effect the bulk modulus of the whole sample. Nor does the increase in bulk modulus upon disordering inferred from the velocities of Kono *et al.* (2008) make physical sense as they also report a normal (Kroll, 1978; Carpenter *et al.*, 1985) increase in the unit-cell volume of the recovered sample as a result of disordering. Apart from some experimental effect, the only other possibility is that there was a change in the microstructure of the An_{51} plagioclase which started as a coherent lamella Bøggild intergrowth.

In conclusion, the general effect of Al/Si disordering in plagioclase feldspars is to slightly soften the structure as a consequence of the increase in volume resulting from disordering. This is entirely consistent with the general trend of increasing bulk modulus with increasing density across the plagioclases from albite to anorthite. The amount of softening therefore scales with the volume changes and thus with the change in the degree of order. Therefore, the maximum possible change in elastic properties of

natural plagioclases is for end-member albite because the Al/Si arrangement can range from completely ordered to completely disordered. With increasing An content, natural $C\bar{1}$ feldspars annealed at low temperatures are less well ordered as a result of the substitution of Al for Si (Table 1), and thus the range of possible order is less. Thus, as we have demonstrated, while end-member albite is softened by 4(1)% by complete disordering, the An_{20} sample was only softened by 2.5(9)%. Similarly, as demonstrated by the An_{78} data, changes in the bulk moduli of the intermediate plagioclases with An content >50% are small because the best ordered samples still retain considerable compositionally induced disorder. The elasticity of plagioclases of An_{85}–An_{100} is complicated by the influence of the $P\bar{1}$ to $I\bar{1}$ transition, their resulting complex modulated microstructures (Nemeth *et al.*, 2007), and the interplay between Al/Si ordering and the transition (Angel, 1992). The latter probably explains why the softening associated with Al/Si disorder in anorthite appears stronger than in albite but this only occurs in anorthites annealed experimentally near the melting point and is probably not relevant for natural anorthites which exhibit very high degrees of Al/Si order (e.g. Angel *et al.*, 1990; Carpenter *et al.*, 1990).

Acknowledgements

This work was supported by NSF grant EAR-0738692 to N.L. Ross and R.J. Angel. The authors thank J.M. Brown for discussions and R. Miletich and P. Comodi for helpful reviews.

References

Angel, R.J. (1992) Order-disorder and the high-pressure $P\bar{1}$–$I\bar{1}$ transition in anorthite. *American Mineralogist*, **77**, 923–929.

Angel, R.J. (2000) Equations of state. Pp. 101–139 in: *High-temperature and High-pressure Crystal Chemistry* (R.M. Hazen and R.T. Downs, editors). Reviews in Mineralogy and Geochemistry, **41**, The Mineralogical Society of America, Washington D.C. and the Geochemical Society, St. Louis, Missouri, USA.

Angel, R.J. (2004) Equations of state of plagioclase feldspars. *Contributions to Mineralogy and Petrology*, **146**, 506–512.

Angel, R.J. and Finger, L.W. (2011) Single: a program to control single-crystal diffractometers. *Journal of Applied Crystallography*, **44**, DOI: 10.1107/S0021889810042305.

Angel, R.J., Hazen, R.M., McCormick, T.C., Prewitt, C.T. and Smyth, J.R. (1988) Comparative compressibility of end-member feldspars. *Physics and Chemistry of Minerals*, **15**, 313–318.

Angel, R.J., Carpenter, M.A. and Finger, L.W. (1990) Structural variation associated with compositional variation and order-disorder behavior in anorthite-rich feldspars. *American Mineralogist*, **75**, 150–162.

Angel, R.J., Allan, D.R., Miletich, R. and Finger, L.W. (1997) The use of quartz as an internal pressure standard in high-pressure crystallography. *Journal of Applied Crystallography*, **30**, 461–466.

Benusa, M., Angel, R.J. and Ross, N.L. (2005) Compression of albite, $NaAlSi_3O_8$. *American Mineralogist*, **90**, 1115–1120.

Birch, F. (1947) Finite elastic strain of cubic crystals. *Physical Reviews*, **71**, 809–824.

Birch, F. (1961) The velocity of compressional waves in rocks to 10 kilobars, Part 2. *Journal of Geophysical Research*, **66**, 2199–2223.

Carpenter, M.A., McConnell, J.D.C. and Navrotsky, A. (1985) Enthalpies of ordering in the plagioclase feldspars. *Geochimica et Cosmochimica Acta*, **49**, 947–966.

Carpenter, M.A., Angel, R.J. and Finger, L.W. (1990) Calibration of Al/Si order variations in anorthite. *Contributions to Mineralogy and Petrology*, **104**, 471–480.

Curetti, N., Sochalski-Kolbus, L., Angel, R.J., Benna, P., Nestola, F. and Bruno, E. (2010) High-pressure structural evolution and equation of state of analbite. *American Mineralogist*, in press.

Downs, R.T., Hazen, R.M. and Finger L.W. (1994) The high-pressure crystal chemistry of low albite and the origin of the pressure dependency of Al-Si ordering. *American Mineralogist*, **79**, 1042–1052.

Farrugia, L.J. (1999) *WinGX* suite for small-molecule single-crystal crystallography. *Journal of Applied Crystallography*, **32**, 837–838.

Ferguson, R.B., Traill, R.J. and Taylor, W.H. (1958) The crystal structures of low-temperature and high-temperature albites. *Acta Crystallographica*, **11**, 331–348.

Hackwell, T.P. and Angel, R.J. (1992) The comparative compressibility of reedmergnerite, danburite and their aluminum analogues. *European Journal of Mineralogy*, **4**, 1221–1227.

Johnson, E. (2007) *The Elastic Behavior of Plagioclase Feldspar at High Pressure*. MS Thesis, Virginia Polytechnic and State University, USA.

King, H.E. and Finger, L.W. (1979) Diffracted beam crystal centering and its application to high-pressure crystallography. *Journal of Applied Crystallography*, **12**, 374–378.

Kono, Y., Miyake, A., Ishikawa, M. and Arima, M. (2008) Temperature derivatives of elastic wave

velocities in plagioclase ($An_{51+/-1}$) above and below the order-disorder transition temperature. *American Mineralogist*, **93**, 558–564.

Kroll, H. (1978) Structures of heat-treated plagioclases An28, An52, An69 and estimation of Al,Si order from lattice-parameters. *Physics and Chemistry of Minerals*, **3**, 76–77.

Kroll, H. (1983) Lattice parameters and determinative methods for plagioclase and ternary feldspars. Pp. 101–139 in: *Feldspar Mineralogy* 2nd edition (P.H. Ribbe, editor). Reviews in Mineralogy **2**, The Mineralogical Society of America, Washington D.C., USA.

Kroll, H. and Ribbe, P.H. (1980) Determinative diagrams for Al,Si order in plagioclases. *American Mineralogist*, **65**, 449–457.

Miletich, R., Allan, D.R., and Kuhs, W.F. (2000) High pressure single-crystal techniques. Pp. 445–519 in: *High-temperature and High-pressure Crystal Chemistry* (R.M. Hazen and R.T. Downs, editors). Reviews in Mineralogy and Geochemistry, **41**, The Mineralogical Society of America, Washington D.C. and the Geochemical Society, St. Louis, Missouri, USA.

Nemeth, P., Tribaudino, M., Bruno, E., and Buseck, P.R. (2007) TEM investigation of Ca-rich plagioclase: structural fluctuations related to the $P\bar{1}-I\bar{1}$ phase transition. *American Mineralogist*, **92**, 1080–1086.

Prewitt, C.T., Sueno, S. and Papike, J.J. (1976) The crystal structures of high albite and monalbite at high temperatures. *American Mineralogist*, **61**, 1213–1225.

Salje, E.K.H. (1985) Thermodynamics of sodium feldspar I: order parameter treatment and strain induced coupling effects. *Physics and Chemistry of Minerals*, **12**, 93–98.

Sheldrick, G.M. (2007) A short history of *SHELX*. *Acta Crystallographica*, **64**, 112–122.

Wainwright, J.E. and Starkey, J. (1971) A refinement of the structure of anorthite. *Zeitschrift für Kristallographie*, **133**, 75–84.

Chapter 3. Tilts and tetrahedra: the origin of anisotropy seen in feldspars

3.1 Opening Remarks

This chapter has been accepted by The American Mineralogist and will appear in the May 2012 issue. The original idea of the initial analysis of the feldspars with respect to tetrahedral tilt systems is attributed to Lindsay Sochalski-Kolbus and Dr. Ross J. Angel. The scientific meanings of the initial results were discussed between Lindsay Sochalski-Kolbus, Dr. Ross J. Angel and Dr. Mario Tribaudino. The computer code for performing the calculations of the tilts values of structures was written by Dr. Ross J. Angel and extensively tested by Lindsay Sochalski-Kolbus. The idea for structures generated using the idealized model for feldspars was discussed between Dr. Ross J. Angel and Lindsay Sochalski-Kolbus for which the code was written by Dr. Ross J. Angel and tested by Lindsay Sochalski-Kolbus. The coordinates for the idealized structures were then generated and analyzed by Lindsay Sochalski-Kolbus. Guidance on the elements to focus on with respect to the results was provided by Dr. Mario Tribaudino. The manuscript was written, edited, revised and re-written over a period of two years by all authors. The content in this chapter provides a systematic model with which to describe the structural variations of plagioclase feldspars that I report in chapters 4 and 5, as well as explain the fundamental causes of the extreme anisotropy of feldspar minerals.

American Mineralogist, Volume 97, pages 765–778, 2012

DANA MEDAL LECTURE

Tilts and tetrahedra: The origin of the anisotropy of feldspars†

ROSS J. ANGEL,[1,*] LINDSAY M. SOCHALSKI-KOLBUS,[1] AND MARIO TRIBAUDINO[2]

[1]Crystallography Laboratory, Department of Geosciences, Virginia Polytechnic Institute and State University, Blacksburg, Virginia 24061, U.S.A.
[2]Dipartimento di Scienze della Terra, Università di Parma, Viale G.P. Usberti 157/A, I-43100 Parma, Italy

ABSTRACT

Following the ideas of Helen Megaw, we describe the changes in the conformation of the tetrahedral framework of feldspars in terms of just four distinct tilt systems of rigid tetrahedra. These systems are based on the four allowed tilts of a ring of four corner-linked tetrahedra with point symmetry 2. Of the four tilt systems, only two result in significant volume change of the unit cell. We show that all of the essential features of the structures, unit-cell parameters and volumes of the $AlSi_3$ feldspars, and their expansion and compression induced by changes in pressure, temperature, and composition at crustal pressures, are generated by the simultaneous application of these two tilts to an un-tilted framework of regular tetrahedra. In combination these two tilts impose significant anisotropy upon the expansion of the unit cell of the feldspar with the majority of the expansion accommodated by the expansion of *d*(100). This demonstrates that the fundamental reason for the anisotropy of feldspars lies in the topology of the tetrahedral framework. A comparison of the actual tilts observed in alkali feldspars with the model shows that the tilts maximize the shortest O-O distances in the structure, and therefore O-O repulsions along with the volume requirement control the values of the tetrahedral tilts in alkali feldspars and thus the anisotropy of the structure. Therefore, the bonding requirements of the bridging O atoms and the directionality of the bonding to the extraframework cations only play a secondary role in modifying this basic pattern of anisotropy, which is intrinsic to the common topology of the framework of all feldspars.

Keywords: Feldspars, elasticity, anisotropy, structure, compressibility, thermal expansion

INTRODUCTION

The elastic properties of a mineral are not only an extremely sensitive probe of the structure and bonding, but are intimately related to its thermodynamic behavior, structural phase transitions, and the cation partitioning between it and other phases. Because feldspars are the dominant minerals in the Earth's crust, the relationship between their elastic properties and structure is especially crucial for understanding geophysical observations and for determining which aspects of crustal processes are really recorded by the cation partitioning patterns observed in feldspars. The feldspar structure consists of a three-dimensional framework of strongly bonded TO_4 tetrahedra formed by the sharing of oxygen atoms between tetrahedra (Fig. 1), with T being dominated by Al^{3+} and Si^{4+} in natural feldspars. Low-charge cations M occupy the larger voids in the tetrahedral framework to provide charge balance. Given that the tetrahedral framework of feldspars is truly three-dimensional and has no obvious layering, it is initially very surprising that feldspars respond extremely anisotropically to changes in pressure, temperature, and the extraframework cation. Figure 2 shows that 60–70% of the volume change of all $AlSi_3$ feldspars, both monoclinic and triclinic, induced by compositional change (Fig. 2a) and temperature (Fig. 2b) is accommodated by changes in the length of the *d*(100) plane normal. The same anisotropy is shown in any other feldspars series in which the framework composition remains constant (e.g., within $AlGe_3$, or within Al_2Si_2 or $GaSi_3$; see Table 7.1 in Smith and

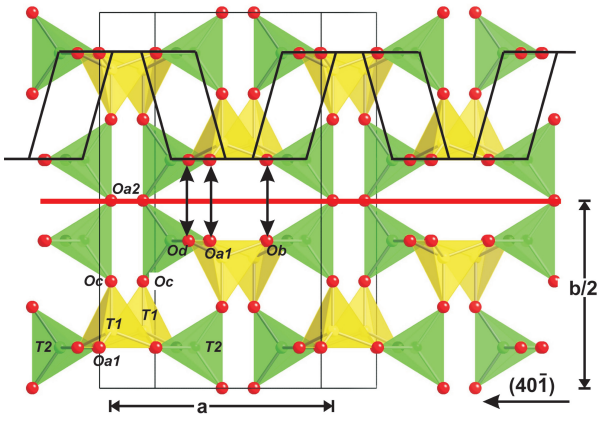

FIGURE 1. The framework of an ideal un-tilted feldspar, comprised of regular tetrahedra, viewed down the [104] direction. The trace of the mirror plane parallel to (010) is indicated by the thick horizontal line. The portion of the structure shown above the mirror forms one crankshaft chain of tetrahedra, as indicated schematically by the black frames, as does the portion of the structure shown below the mirror. These crankshaft chains extend along [100], which runs slightly into the plane of the drawing toward the left. The vertical arrows highlight the short O-O distances across the mirror plane that are equal to the tetrahedral edge length in this un-tilted structure. (Color online.)

* Present address: Dipartimento di Geoscienze, Via G. Gradenigo 6, I-35131 Padova, Italy. Email: rossjohnangel@gmail.com
† The content of this manuscript was presented as the Dana Medalist's lecture of the Mineralogical Society of America in Prague, Czech Republic, on August 19, 2011.

0003-004X/12/0506–765$05.00/DOI: http://dx.doi.org/10.2138/am.2012.4011

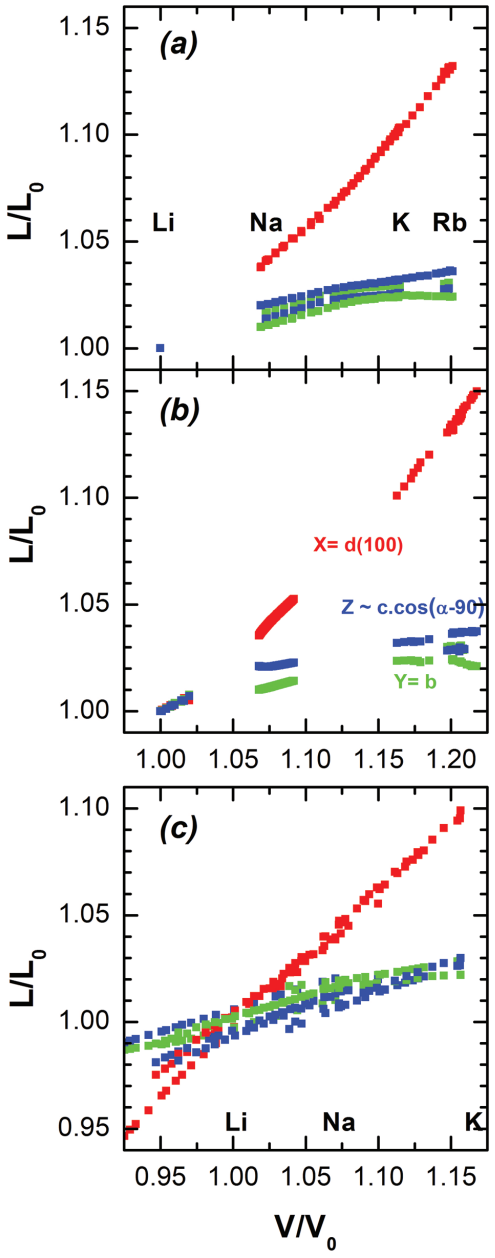

FIGURE 2. The variation of the lengths of three mutually perpendicular directions in $AlSi_3$ feldspars at (**a**) room conditions, (**b**) high temperatures and room pressure, (**c**) high pressures scaled to the values for Li-feldspar (Baur et al. 1996). Data from both monoclinic and triclinic feldspars are included. The greater slope of the line for the strain in the Cartesian X direction, parallel to the (100) plane normal, than for the two perpendicular directions indicates that *d*(100) accommodates between 60 and 70% of the volume changes of alkali feldspars. The element labels indicate the volumes of the corresponding end-member feldspar at room temperature and pressure. The ranges of both the x- and y-axes are the same in **c** as in **a** and **b** but the origin is shifted. Data in **a** from Kroll et al. (1986) and Hovis and Roux (2008); data in **b** from Hovis and Graeme-Barber (1997), Hovis et al. (2008), and Tribaudino et al. (2011); data in **c**, albite (Benusa et al. 2005), analbite (Curetti et al. 2010), Or37 anorthoclase (Nestola et al. 2008), Or82 sanidine (Angel, unpublished) and Or98 microcline (Allan and Angel 1997). (Color online.)

Brown 1987). This degree of anisotropy is as great as that of the sheet silicates, where the anisotropy clearly results from the bonding between the layers being significantly weaker than the strong bonding within the layers. But this cannot be the case for feldspars in which the directions of the T-O bonds are distributed more or less isotropically (Fig. 1). It has long been known that the feldspar structure is relatively soft due to the intrinsic flexibility of the crankshaft chains of tetrahedra within the framework (see Smith and Brown 1987, who describe the softness of a physical model of the framework). However, the crankshafts are aligned along [100] or **a**, so this does not explain the reason why the (100) plane normal, or **a***, exhibits the greatest strains with changes in temperature or extraframework cation. Megaw (1970, 1974a) suggested that the extraframework cations play the crucial role in modifying the anisotropy of the structure. In particular, she suggested that the shortest M-O bonds, M-Oa2, form part of a "strut" of atoms Oa2-M-M-Oa2 that lies along the [201] direction, almost parallel to **a***. She argued that this strut appears to force the crankshaft chain of tetrahedra open so as to provide M-Oa2 distances suitable for the M cation and to minimize the mutual repulsion of the M cations. This idea is certainly consistent with the observation that *d*(100) shows the greatest expansion with increasing temperature and M cation size (Figs. 2a and 2b). However, with the advent of high-pressure studies of feldspar it became apparent that the *d*(100) direction is also the direction of greatest compressibility in feldspars (Fig. 2c, e.g., Angel et al. 1988; Angel 1994) under hydrostatic compression. Subsequent determinations of the elastic tensors of feldspars (e.g., Brown et al. 2006; Brown and Angel in preparation) confirm that **a*** is the softest direction. It is then obvious that the M-Oa2 bonds and the associated "strut" cannot be the reason for the anisotropy of feldspars (Angel et al. 1988), because such a strut would be expected to make **a*** the stiffest direction, not the softest. The reason for the anisotropy must therefore lie elsewhere.

In this paper, we implement the suggestion of Megaw (1974a) to study the detailed consequences of the topology of the tetrahedral framework of feldspars by computer simulation. We start with a presentation of the idealized un-tilted structure derived by Megaw (1974a), and the patterns of tilts of rigid tetrahedra that are allowed by the topology. We then use a simple geometric model of the feldspar tetrahedral framework to explore the effects on the lattice parameters and volumes of each of the possible individual tilt systems of rigid tetrahedra. The results explain why only two of the four possible tilt systems dominate the structural variation of the alkali feldspars with pressure, temperature and composition. We go on to show that the anisotropy of the feldspar structure is a consequence of the topology of the tetrahedral framework as has been suggested (e.g., Winter et al. 1977; Brown et al. 1984), but not proven, in the past. The interactions of the framework with the extraframework cations and the distortions of the tetrahedra therefore have only secondary effects on the anisotropy.

REFERENCE FELDSPAR STRUCTURE

The basic building block from which the feldspar structure is constructed is a 4-ring of corner-sharing tetrahedra (Fig. 3). If the tetrahedra are perfectly regular and identical in size, then

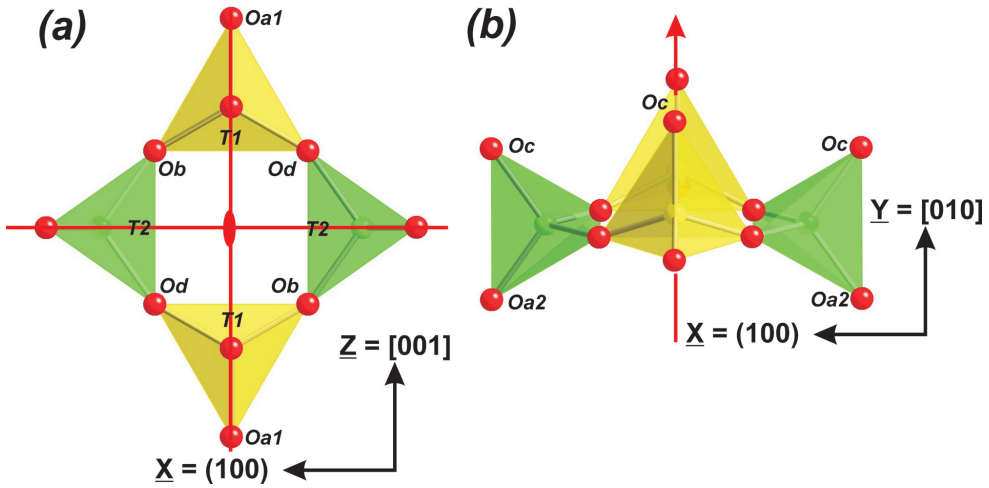

FIGURE 3. Two views of the 4-ring of tetrahedra that forms the fundamental building block of the feldspar structure. The diagrams show a ring comprised of perfectly regular tetrahedra with zero tilts and point symmetry *m2m* (indicated by the diad symbol and arrow, and the mirror lines). The view in **b** is slightly inclined from [001] so as to show both T1 tetrahedra. The directions **X**, **Y**, and **Z** are the Cartesian axes used to tilt the tetrahedra; the variation of the lengths of these vectors with unit-cell volume in $AlSi_3$ feldspars is shown in Figure 2. (Color online.)

there are three different conformations of such a 4-ring that have tetragonal point group symmetries, 4/*mmm*, $\bar{4}m2$, and 4*mm*. Each of these point symmetries imposes specific restraints on the mutual orientation of the tetrahedra. In all cases the common twofold axis perpendicular to the ring (and within the fourfold axes) makes the opposite pairs of tetrahedra tilt in the same way, while the remaining symmetry elements constrain the values of tilts or the relative tilts of the adjacent tetrahedra. However, the topology of the connections of the 4-rings within the feldspar structure reduces the point group symmetry of the 4-ring to a maximum of 2 (Fig. 1). This lower symmetry does not restrict the mutual orientations of the adjacent tetrahedra, nor their specific tilts, and thus the choice of exactly which configuration of tetrahedra to use as the un-tilted reference state is arbitrary; none of the subsequent tilts breaks the point symmetry 2. Note that this is in contrast to tilts in feldspathoids (e.g., Gatta and Angel 2007; Gatta et al. 2011) and perovskites (e.g., Glazer 1972; Howard and Stokes 1998; Wang and Angel 2011) in which tilting of polyhedra is symmetry-breaking, and thus the un-tilted configuration is unambiguously defined by its higher symmetry.

Megaw (1974a) chose as the "un-tilted" reference state a ring of four identical regular tetrahedra in which the bases of the two T1 tetrahedra lie in the same plane as the bridging O atoms within the ring, and the other pair of tetrahedra (T2) have their external edges aligned perpendicular to this plane (Fig. 3). This ring conformation has point symmetry *m*2*m*, but will be reduced to 2 by two of the four tilts. We use this same choice of reference structure because it offers computational convenience and the evolution through tilting of the structure to the configurations found in real feldspars is easy to follow. However, it does have the unfortunate property that tilting from this reference state generally leads to volume expansion of the structure, whereas symmetry-breaking tilts from a high-symmetry reference state in other frameworks such as perovskites (e.g., Wang and Angel 2011) or feldspathoids (e.g., Gatta and Angel 2007; Gatta et al. 2011) leads to volume reduction.

The ideal, un-tilted four-ring of tetrahedra is illustrated in Figure 3, with the atom positions labeled to follow the normal conventions applied to feldspars (Megaw 1974b). The bridging O atoms within the ring are denoted Ob and Od. The apices of the T1 tetrahedra that link the ring to other 4-rings are Oa1 (to another T1) and Oc (to T2). The Oc and Oa2 atoms form the outer edge of the T2 tetrahedron, with the Oa2 forming the link to the T2 tetrahedra of adjacent 4-rings within the feldspar structure.

Once the size of the tetrahedra is specified, the coordinates of these atoms can be calculated by simple geometry in an orthonormal Cartesian coordinate system whose origin lies at the center of the 4-ring in the Ob-Od-Ob-Od plane. The **X** axis is set parallel to the T2-T2 vector, the **Z** axis parallel to T1-T1, and the **Y** axis perpendicular to the plane of the ring and along the twofold symmetry axis. These Cartesian axes **X**, **Y**, and **Z** will become parallel to **a***, **b**, and **c** basis vectors of the conventional monoclinic cell of feldspars (Fig. 3). The fractional coordinates of the atoms comprising this ring can then be transformed into a monoclinic unit cell with *C*2/*m* symmetry operations that (apart from the twofold already present in the original 4-ring) generate the entire feldspar framework. The fractional coordinates of this ideal structure are given in Table 1, and are independent of the size of the tetrahedra. On the other hand, the unit-cell parameters do depend on the tetrahedral size and can be expressed in terms of the O-O edge length of the tetrahedron *l* (extended from Megaw 1974a) as

$$\begin{aligned} a &= \left(13/3 + 2\left(\sqrt{2} + 1/\sqrt{3}\right)\right)^{1/2} l \\ d(100) &= \left(1 + \sqrt{2}\right) l \\ b &= \left(3 + 2\sqrt{2/3}\right) l \\ c &= \left(1 + \sqrt{3}\right) l \\ \tan\beta &= -\left(1 + \sqrt{2}\right) \Big/ \left(1 + 1/\sqrt{3}\right) \end{aligned} \quad (1)$$

TABLE 1. Fractional coordinates of the ideal un-tilted feldspar, space group *C*2/*m*

Site	*x*	*y*	*z*
T1	0.00000	0.15198	0.78867
T2	0.35355	0.10792	0.70413
Oa1	0.00000	0.10792	0.00000
Oa2	0.50000	0.00000	0.78867
Ob	0.20711	0.10792	0.80259
Oc	0.00000	0.28416	0.78867
Od	0.20711	0.10792	0.43656

The unit-cell parameters can also be expressed in terms of the T-O bond length d by recalling that $d = l\sqrt{3/8}$ for a regular tetrahedron. The volume of the monoclinic unit cell is given simply as the product $b \cdot c \cdot d(100)$. Note that all of the unit-cell edges scale linearly with the size of the tetrahedra (Eq. 1), represented by the edge-length l. This confirms that the feldspar structure is fully three dimensional and isotropically scalable. If all of the cell edges are changed by the same percentage (i.e., subject to isotropic strain) then the T-O bond lengths increase by the same amount, and all interatomic distances increase by the same strain. The monoclinic unit-cell parameters of this un-tilted structure for a T-O bond length of d = 1.6500 Å characteristic of the average T-O bond length of $AlSi_3$ feldspars (and a corresponding tetrahedral edge-length l = 2.6944 Å) are a = 7.7703, b = 12.4830, c = 7.3613 Å. The β angle (Eq. 1) is independent of the size of the tetrahedra and is always equal to 123.159° for the un-tilted feldspar structure. The bond angles in the un-tilted structure are also independent of the size of the tetrahedra. All of the O-T-O bond angles have the ideal tetrahedral value of 109.47°, and the T-O-T angles are similar to those calculated by Megaw (1974a): Oa1 = 141.06°, Oa2 = 109.47°, Ob = 148.90°, Oc = 144.73°, Od = 148.90°. With the exception of the T2-Oa2-T2 angle all of these fall within the range of observed angles for feldspars. The small value of the T2-Oa2-T2 angle, across the mirror plane, results in the Oa1-Oa1, Ob-Ob, and Od-Od distances across this mirror plane being equal to the O-O distances that form the edges of the tetrahedra (Fig. 1). These short O-O distances have important consequences for the tilting that is allowed within this ideal structure, as we discuss below.

DEFINITION OF TILTS

In this section, we describe in detail the four possible tilt systems of the 4-ring that preserve the twofold axis of symmetry and do not distort the tetrahedra, and include our definitions of the tilt angles themselves. These definitions can be used both to impose tilts on a model structure and explore the consequences of tilting, as we do in the next section, and to calculate the tilts of the tetrahedra from the refined structures of real feldspars as we show in the following section.

We follow the labeling of the tilts and sign conventions established by Megaw (1974a) who first described structural distortions of the feldspars in terms of the tilting of the TO_4 groups with respect to one another, relative to the configuration of the four-ring having itself the *m*2*m* point symmetry described in the preceding section. The entire un-tilted structure has *C*2/*m* symmetry, set in the conventional orientation of the feldspar structure. In this un-tilted structure, the two apical O atoms of the T1 tetrahedra point along [010] from the tetrahedral bases that lie parallel to the (010) plane, and the T2 tetrahedra are set with an edge perpendicular to (010) as in Figure 3.

Tilt 1 is a rotation of the T1 tetrahedra around the Ob-Od edge (Fig. 4). Megaw (1974a) specified the tilt angle ϕ_1 in terms of the height of the Oa1 oxygen above the mid-point of the Ob-Od edge. For monoclinic feldspars this "height" is from the (010) plane in which the two Ob and two Od atoms lie. We have generalized this definition and make ϕ_1 the angle from the (010) plane of the vector from the mid-point of the Ob-Od edge to the Oa1 oxygen atom. Positive values of ϕ_1 correspond to the Oc apex of the T1 tetrahedron being tilted inward toward the ring (Fig. 4).

Tilt 2 is the tilting of the T2 tetrahedra that is equivalent to tilt 1 for the T1 tetrahedra (Fig. 4); Megaw described both of these as "hinge tilts." Tilt 2 is thus the rotation of the T2 tetrahedra around the Ob-Od edge. Megaw defined ϕ_2 in terms of the "height" of the mid-point of the Oc-Oa2 tetrahedral edge above or below the mid-point of the Ob-Od edge. We use the angle to the (010) plane of the vector between the mid-point of the Ob-Od edge and the mid-point of the Oc-Oa2 tetrahedral edge. This definition ensures that the value of ϕ_2 is independent of the values of the other tilts, especially tilt 3. Positive values of ϕ_2 correspond to tetrahedra being tilted so that the Oc atoms move outward from the 4-ring, and the Oa2 atoms inward (Fig. 4). Our values for the two "hinge" tilts, ϕ_1 and ϕ_2 are the same to those of Megaw (1974a) for real feldspars within the uncertainties (which can be estimated to be approximately half of the uncertainties in the T-O-T angles), and they are identical for tilts of the undistorted ideal structure.

Tilt 3 is the "wrinkle tilt." It is the mutual rotation of the two T2 tetrahedra by equal but opposite amounts around **a*** (i.e., a twist or torsion of the ring), which causes equal but opposite rotations of the T1 tetrahedra around **c** (Fig. 4). While it would

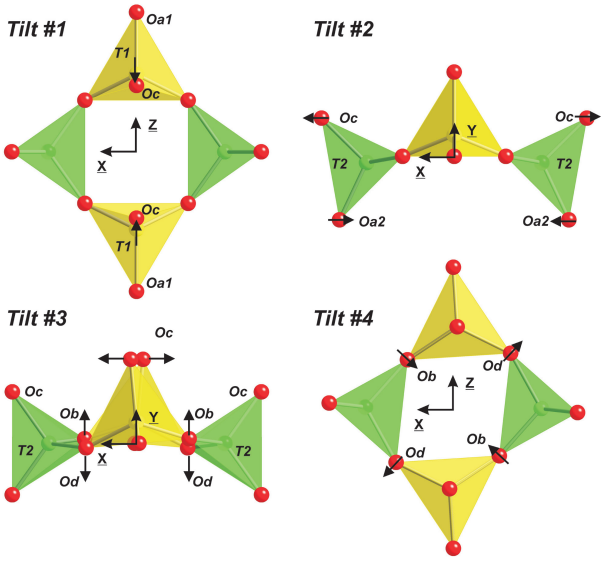

FIGURE 4. The four tilt patterns of the tetrahedra in a 4-ring that preserve the point symmetry 2, each drawn for a tilt angle $\phi = +10°$. The most significant displacements of oxygen atoms for each tilt are indicated by the small arrows. **X**, **Y**, and **Z** are the directions of the Cartesian axes, not the unit-cell axes. (Color online.)

seem more convenient to define ϕ_3 as the Oc-T1-T1-Oc torsion angle across the center of the 4-ring, this and similar definitions make the value of ϕ_3 sensitive to the internal distortions of both the T1 and T2 tetrahedra. Therefore we follow Megaw (1974a) and define the value of ϕ_3 in terms of the angle of the Ob-Od edge of the T1 tetrahedra from the (010) plane. In triclinic feldspars the distortions of the tetrahedra from ideality and equal size mean that values of ϕ_3 calculated from T1o and T1m are different. We deviate from Megaw's definition by making ϕ_3 the sum of the angles calculated for the two tetrahedra, rather than the average. There is a small effect of the ring shear (tilt 4) on the value of this torsion angle and hence ϕ_3; the measured torsion is reduced by increasing ring shear. The expression

$$\left(\frac{\phi_3\left(\text{Measured}\right)}{\cos\left(\phi_4\right)}\right)$$

provides a value for the ϕ_3 corrected to zero shear that is correct to within 0.01° for the range of shear and tilt angles found in alkali feldspars. The correction typically amounts to less than 0.2°, which is less than the uncertainty in ϕ_3 arising from a typical structure refinement.

Tilt 4 is the shear of the 4-rings within the (010) plane (Fig. 4). Megaw (1974a) defined it as one-half of the average deviation of the Ob-Od-Ob and Od-Ob-Od angles from 90°. This makes the value slightly dependent upon the value of ϕ_3, as tilt 3 makes the four oxygen atoms Od-Ob-Od-Ob non-coplanar and reduces the sum of the four angles at the corners of the ring to less than 360°. Therefore we define the ring shear as the average deviation of the four corner angles from their mean

$$\phi_4 = \frac{1}{4}\sum_{i=1,4}\left|\text{angle}_i\left(OOO\right) - \left\langle\text{angle}\right\rangle\right|.$$

This tilt is given a positive sign when the Od-Od diagonal of the ring is longer than the Ob-Ob diagonal, which is equivalent to the Ob-Od-Ob angles being smaller than the Od-Ob-Od angles.

While the various possible definitions of tilt angles are identical for the ideal structure of perfectly regular tetrahedra, as in other frameworks (e.g., Wang and Angel 2011) the introduction of distortions of the tetrahedra in real structures leads to ambiguities and different possible formulas to extract values of tilts from refined crystal structures. Therefore while our definitions and those of Megaw (1974a) yield identical values for tilts of the ideal structure with perfectly regular tetrahedra, they provide very slightly different absolute values for the tilt angles calculated from refined structures. Nonetheless, the sense of tilts and the trends in values from the two sets of definitions are the same, while a detailed exploration of several possible alternative definitions showed that the ones described here minimize the influence of the distortions on the values of the tilts calculated from real feldspars.

In triclinic feldspars with space group $C\bar{1}$ there are two independent T1 and T2 atoms in each 4-ring, so there are two independent tilts 1 and two tilts 2. We follow Megaw (1974a) in taking the average value of each as the tilt value, as it is the sum of the displacements of the oxygen atoms induced by the individual tilts that is related to the changes in lattice parameters. For feldspars in space groups $P\bar{1}$ and $I\bar{1}$ (e.g., Angel et al. 1990), $I2/c$ and $P2_1/c$ (e.g., Benna et al. 2007) in which there are more than one symmetry-independent 4-ring, appropriate averages can be taken of the tilt values calculated for the independent rings. The details of the structural evolution of these feldspars in terms of tilts will be examined in future papers, while we focus here on the common features of the structural evolution of all feldspars as illustrated by the $C\bar{1}$ and $C2/m$ feldspars with $AlSi_3$ as the tetrahedral cation content.

Tilting of the ideal structure

Methods

To apply a specific set of tilts to a feldspar model structure the coordinates of the atoms comprising one T1 and one T2 tetrahedron of the 4-ring are transformed back in to the orthonormal Cartesian coordinate system with the axial conventions of Brown et al. (2006)—that is, with **X**//**a***, **Y**//**b**, and **Z** perpendicular to both. Because the model structures are monoclinic, **Z** is parallel to **c**. The transformation matrix for the coordinates from the monoclinic unit cell to the orthonormal axial system is thus:

$$T = \begin{pmatrix} a\sin\beta & 0 & 0 \\ 0 & b & 0 \\ a\cos\beta & 0 & c \end{pmatrix}. \quad (2)$$

This is a special case of the general transformation matrix (for triclinic) of

$$T = \begin{pmatrix} a\sin\gamma\sin\beta^* & 0 & 0 \\ a\cos\gamma & b & c\cos\alpha \\ -a\sin\gamma\cos\beta^* & 0 & c\sin\alpha \end{pmatrix}. \quad (3)$$

The atom coordinates are then displaced so that the **Y** axis passes through the center of the 4-ring. The 1 and 2 tilts can then be applied as simple rotations of the atoms comprising the appropriate tetrahedra around the Ob-Od edges, and the 4 tilt as a simple shear of the coordinates in the **X-Z** plane. The wrinkle tilt (no. 3) is generated by an initial rotation of the T2 tetrahedron, followed by displacements of both T1 and T2 to preserve the connectivity at the Ob and Od atoms, and thus maintain both of the T-O bond lengths to each of these atoms. The result is an individual tilted 4-ring with atom positions described with respect to the Cartesian axial system. To generate the entire feldspar framework without imposing any distortions, the basis vectors of the unit-cell of the tilted structure are defined in terms of appropriate combinations of the interatomic vectors of the tilted 4-ring in the Cartesian coordinate system:

a = Twice the X plus Z components of the vector from the Oc on T1 to the Oc vector on T2 on adjacent tetrahedra within the 4-ring.

b = Twice the Y component of the Oa2-Oc edge vector of the T2 tetrahedron plus twice the Y component of the vector from Oa2 to Oc on T1.

c = Oa1 to Oa1 across the ring center.

The unit-cell edges and angles are then calculated from the scalar products between these basis vectors of the monoclinic unit cell expressed in the Cartesian orthonormal basis. The resulting monoclinic unit-cell parameters of the tilted structure can then be inserted in to the expression for the transformation matrix **T** (Eq. 2), and the coordinates of the atoms of the tilted 4-ring can then be transformed back in to the crystallographic unit cell with the matrix $\mathbf{T}^{-1}$. Following the application of this transformation the resulting coordinates and unit-cell parameters are combined with the $C2/m$ symmetry to generate the entire structure of the tilted feldspar in which the tetrahedra remain completely regular.

In principle, this method of defining the crystallographic basis vectors in terms of interatomic vectors in an orthonormal basis could be applied to any framework structure so as to calculate the unit-cell parameters arising from the tilting of rigid polyhedra. It has the advantage over methods such as distance-least-squares in

that it is geometrically exact rather than subject to convergence limits, it allows values of tilts (rather than bond angles) to be specified, and it is computationally trivial. Its disadvantage is that the transformation from the Cartesian coordinate system to the crystallographic one has to be specified explicitly for each structure type, as it depends upon (or indeed defines) the connectivity of the framework.

Limits to tilts

In the following we will use this method to explore how each of the individual tilt systems changes the T-O-T bond angles and the O-O distances of the idealized feldspar structure with perfectly regular tetrahedra, and how each affects the unit-cell parameters to precisely identify the origin of the anisotropy of the feldspar structure. From a purely geometrical perspective the tilts are not limited to any particular range of values. However, from a crystal-chemical perspective we will assume that tilts that reduce any O-O distance to less than that of the tetrahedral edge length are energetically unfavorable. Tilt angles are then limited to those values, which maintain all O-O distances equal to, or longer than, that of the tetrahedral edge. The un-tilted reference structure with $\phi_1 = \phi_2 = \phi_3 = \phi_4 = 0$ is therefore at the limit of some tilts because the Oa1-Oa1, Ob-Ob, and Od-Od distances across the mirror plane are equal to the tetrahedral edge length (Fig. 1). Because all of the unit-cell edges, and interatomic distances scale linearly with the size of the tetrahedra (Eq. 1) while all of the T-O-T and O-T-O bond angles are independent of the tetrahedral dimensions, the conclusions drawn in this section with respect to both the anisotropy of the feldspar structure and the limits to the tilt systems are independent of the size of the tetrahedra. Movie files illustrating the tilt systems have been deposited[1].

Tilt 1

In the un-tilted structure the Oa1-Oa1 distance across the mirror plane is equal to the tetrahedral edge length (Fig. 1). Negative values of ϕ_1 displace the Oa1 oxygen toward the mirror plane and reduce this Oa1-Oa1 distance, so ϕ_1 is restricted to being positive. Positive values of ϕ_1 directly increase the T1-Oa1-T1 bond angle from the value of 141.06° at zero tilt at approximately twice the rate of the tilt itself (Fig. 5a, and Table 5 in Megaw 1974a), so that with a tilt of $\phi_1 = 19.47°$ the T1-Oa1-T1 linkage becomes linear. At this tilt, the Oc-Oc distance across a 4-ring, and the Oa2-Oa2 distance between 4-rings simultaneously become equal to the tetrahedral edge length, so $0° < \phi_1 < 19.47°$.

In the ideal un-tilted ring, the Ob-Od tetrahedral edge that forms the axis of tilt 1 lies parallel to **a*** of the monoclinic cell, or X of the orthonormal basis. Therefore, tilt 1 might be expected to only change the cell parameters *b* and *c*. The *c* unit-cell parameter is decreased whatever the sense of the tilt because the monoclinic *c*-lattice repeat is defined by the Oa1-Oa1 vector across the entire 4-ring, and this distance is obviously decreased by either sense of tilt as the Oa1 atom is moved out of the plane defined by the Ob and Od atoms (Fig. 4). A positive value of ϕ_1 also raises the apical Oc atom further above this same Ob-Od plane, and will thus increase the length of the *b* unit-cell parameter. These are the senses of changes predicted by Megaw (1974a, Table 5). However, our full simulations of the structures (see Fig. 6a) suggest that her estimates for the rates of change of these two cell parameters are not correct. From Figure 6a it is clear that, at zero tilt, the rate of change of *c* must be zero, and it only becomes negative for finite tilts. It cannot have a single value as previously suggested. The rate of change of the *b* lattice parameter normalized by the length of the tetrahedral edge *l*, that is,

$$\frac{d\left(b/l\right)}{d\phi}$$

per radian, is 0.43 rad^{-1} compared to Megaw's value of 0.58 rad^{-1}. Furthermore, we see in Figure 6a that, although the *d*(100) plane spacing is not changed by tilt 1, as required because the axis of the tilt lies parallel to the (100) normal, both *a* and the β angle change, but in a complementary way to keep *d*(100) unchanged. The reason for the differences between the results of the current analysis and those of Megaw (1974a) is that she considered only the individual 4-ring, and not the consequences of its tilts on the position of its neighbors within the feldspar structure. As an example, the increase of ϕ_1 from 0° to 19.47° decreases the distance between the apical O atoms Oc on adjacent T1 and T2 tetrahedra within a 4-ring from 3.978 to 3.656 Å, while the component of this distance parallel to **a*** remains unchanged. Thus, the unit-cell undergoes a shear that maintains *d*(100) constant. This connectivity is also responsible for the changes of the T-Oc-T angle with ϕ_1 (Fig. 5a).

Since *d*(100) does not change with ϕ_1 the initial increase in volume with tilting arises from the greater rate of increase in *b* than decrease in *c* (Fig. 6a), which is a simple consequence of the initial orientation of the T1 tetrahedron with respect to the monoclinic unit-cell axes. As ϕ_1 becomes larger, the geometrical advantage changes and the volume decreases with further increases in tilt. The changes in the angles at the Ob and Od atoms, predicted by Megaw (1974a, Table 10) as being zero for tilt 1 merely follow directly from the tilting of the T1 tetrahedra (cf. Mihailova et al. 1994) in the ring and not from its external connectivity.

Tilt 2

Tilt 2, that applies only to the T2 tetrahedra naturally has the largest effect on the T2-Oa2-T2 bond angle between them; it changes at twice the rate of the tilt angle itself (Fig. 5b and Megaw 1974a). As noted above, in the un-tilted reference structure, the T2-Oa2-T2 bond angle is 109.47 and, as a consequence, the Oa1-Oa1, Ob-Ob, and Od-Od distances between mirror-related rings connected through Oa2 are equal to the length of the tetrahedral edges (Fig. 1). Negative values of ϕ_2 starting from the un-tilted reference structure are therefore forbidden because they further reduce these O-O distances across the mirror plane. Positive values of ϕ_2 increase the O-O distances across the mirror plane but lead to a reduction of the Od-Od distance across the inversion center to a value equal to the tetrahedral edge length at just above $\phi_2 = 29°$. This limit is lower than the value of $\phi_2 = 35.27°$ at which the T2-Oa2-T2 linkage becomes linear (Fig. 5b) and the Oc atom becomes co-planar with the Ob and Od atoms in the 4-ring making a perfect UDUD ring with $\bar{4}m2$ point

[1] Deposit item AM-12-042, movie files illustrating the tilt systems. Deposit items are available two ways: For a paper copy contact the Business Office of the Mineralogical Society of America (see inside front cover of recent issue) for price information. For an electronic copy visit the MSA web site at http://www.minsocam.org, go to the *American Mineralogist* Contents, find the table of contents for the specific volume/issue wanted, and then click on the deposit link there.

symmetry. The effective limits on tilt 2 are thus $0 < \phi_2 < +29°$.

Increasing positive values of ϕ_2 lead to an equal decrease in the T1-Oc-T2 angle, an increase at twice the rate of the T2-Oa2-T2 angle, and no change in the T1-Oa1-T1 angle (Fig. 5b), in agreement with Megaw (1974a). The small changes in the Ob and Od angles are again the consequence of the linkages within the 4-ring. The increase in the T2-Oa2-T2 angle, and the increase in the separation of the 4-rings across the mirror plane, causes a strong increase of the *b* unit-cell parameter with ϕ_2. As expected from the orientation of the rotation axis for tilt 2 parallel to [001], it has no effect on the *c* lattice parameter (Fig. 6b), in the same way that tilt 1 does not change *d*(100). But the connectivity of the feldspar framework makes the effect of tilt 2 on the third axis very different from tilt 1 as the shears of the unit cell required to maintain the connectivity between consecutive 4-rings along the crankshaft result in a strong expansion of *a* as well as a strong decrease in β, which combine to produce an even stronger expansion of *d*(100). The combined expansion of *d*(100) and *b* mean that tilt 2 has the largest effect on the unit-cell volume of any tilt (Fig. 6).

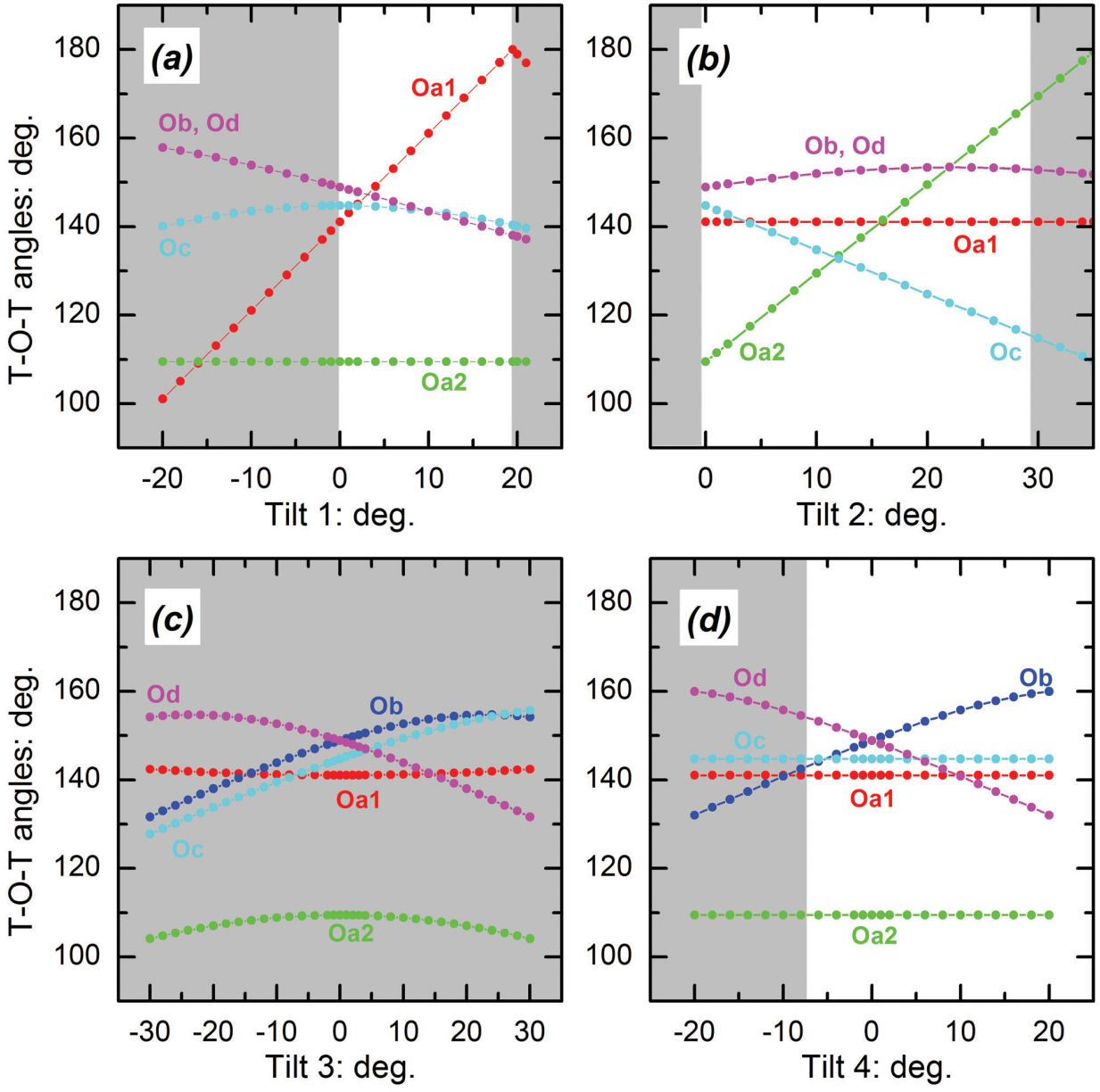

FIGURE 5. The variation of the T-O-T angles with individual tilts of the ideal feldspar structure. Grayed areas of the plots indicate tilt angles that generate O-O distances between O atoms on different tetrahedra that are shorter than the tetrahedral edge length. (Color online.)

Tilt 3

Because the wrinkle tilt involves opposite rotations of the T2 tetrahedra it displaces either a pair of Ob or a pair of Od atoms toward the mirror plane, which pair depending on the sign of ϕ_3. Because the distances from these atoms to their mirror-related equivalents is equal to the tetrahedral edge lengths in the un-tilted structure (Fig. 1) it therefore follows that non-zero values of ϕ_3 are forbidden unless ϕ_2 is positive, as that is the only tilt system that increases these O-O distances. Nonetheless it is useful to calculate the effect of tilt 3 on the unit-cell parameters and T-O-T bond angles as a basis for subsequent analyses. The changes in the T1-Ob-T2 and T1-Od-T2 angles are, as expected, symmetric about zero tilt, while the changes in the angles at Oa1 and Oa2 are much smaller (Fig. 5c). Note that the T1-Oc-T2 angle increases with tilt 3, whereas it decreases with tilt 2, but the rate of change of this angle with tilt 3 is just under half that with tilt 2 in agreement with Megaw (1974a, Table 10) when allowance is made for our definition of ϕ_3 giving values that are twice hers.

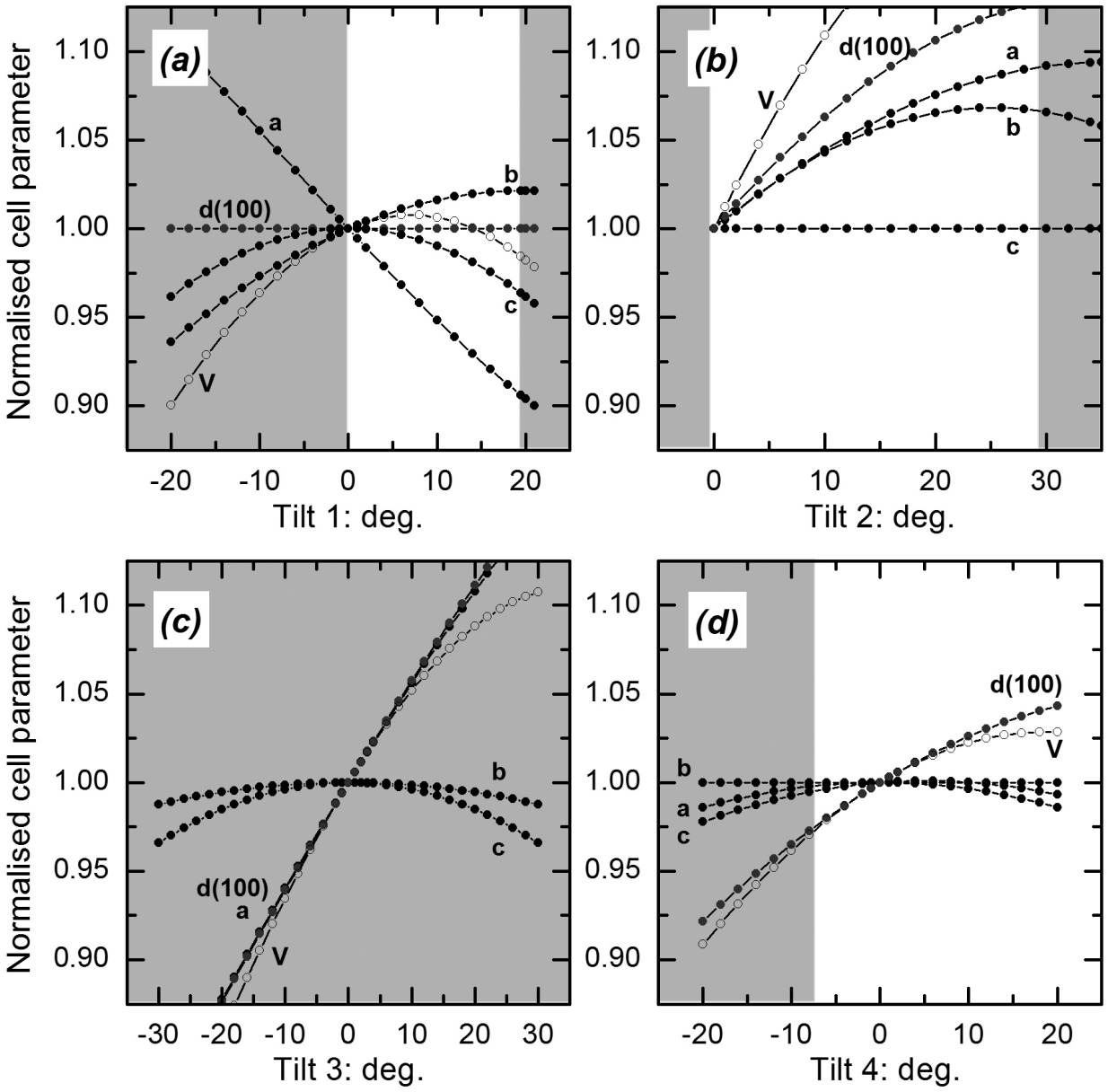

FIGURE 6. The changes in the monoclinic unit-cell parameters and unit-cell volume induced by the individual tilts of the ideal feldspar structure. Each unit-cell parameter is normalized to its value in the un-tilted structure, so the data points represent strains that are independent of the T-O bond length. For the monoclinic cell *d*(100), **b** and **c** are the repeat distances along the directions of the Cartesian axes **X**, **Y**, and **Z**, respectively. Grayed areas of the plots indicate tilt angles that generate O-O distances between O atoms on different tetrahedra that are shorter than the tetrahedral edge length.

Tilt 3 displaces the Oc apical atoms of the T1 tetrahedra of the ring in opposite directions along **a*** (Fig. 4), thus directly opening and closing the crankshaft chain of tetrahedra (Fig. 1) with an increase in ϕ_3 leading to expansion. Thus tilt 3 has the largest effect on the expansion of $d(100)$ and the a-axis, but either sign of ϕ_3 causes a small decrease in b and c. The expansion of $d(100)$ is, however, much greater than the shortening of either b and c, so that changes in ϕ_3 produce a volume change that is second only in magnitude to that induced by tilt 2 (Fig. 6).

Tilt 4

Because this tilt is a shear of the 4-ring entirely within the (010) plane (Fig. 4), there is no change in either the b unit-cell parameter, nor in the component parallel to [010] of any interatomic distance within the structure (Fig. 6d). Therefore tilt 4 will not change the O-O distances across the mirror plane. It only changes significantly the lengths of the Ob-Ob and Od-Od diagonals of the individual 4-rings, and the distances between adjacent [001] chains of 4-rings. Negative values of ϕ_4 decrease the shortest distances from the Ob atom in one ring to the Oa2 and Oc atoms forming the nearest vertical edge of the T2 tetrahedron in a neighboring chain. This limits ϕ_4 to values more positive than ~–7°. However, there is no corresponding limit to positive values of ϕ_4, because they only reduce the Ob-Ob diagonal of the ring, but do not bring any 4-rings closer together.

As a shear of the structure in the (010) plane, tilt 4 has a small effect on the a and c unit-cell parameters, but leads to an increase in $d(100)$ as a consequence of the strong decrease of the β unit-cell angle with increasing tilt (Fig. 6d). None but the T1-Ob-T2 and T1-Od-T2 angles are changed by the shear of the 4-ring (Fig. 5d).

Volume changes in feldspars

Because the feldspar framework is three dimensional and fully connected, expansion of the feldspar unit cell must be accompanied by the same volume change of the tetrahedral framework. The analysis presented above shows that there are two fundamental types of structural mechanism that can change the volumes of feldspars, deformation of the tetrahedra being excluded because the small shear strains that describe deformations of the tetrahedra have (to first order) no volume effects. Therefore, the first mechanism is the expansion of the tetrahedra, which Equation 1 shows should lead to an isotropic expansion of the unit cell. This is confirmed by experimental data for series of structures in which the tetrahedral cations are exchanged without a change in the extraframework cation (e.g., $KAlSi_3O_8$-$KGaSi_3O_8$-$KFeSi_3O_8$-$KAlGe_3O_8$-$KFeGe_3O_8$). For these series the experimental data (e.g., Table 7.1 in Smith and Brown 1987) show approximately isotropic expansion, with $d(100)$ expanding slightly less than the perpendicular directions, indicating that the effects on the unit-cell parameters of changing the tetrahedral cations are actually slightly modified by either tetrahedral distortions, changes in tilts, or both.

However, the volume changes on changing temperature, pressure or M cation within a single series of feldspars with constant tetrahedral cation composition cannot be explained by expansion of the tetrahedra. For example, the volume change from albite to sanidine is ~9%, (e.g., Table 7.1 in Smith and Brown 1987), which would require an expansion of the average <<T-O>> bond length within the structure of ~3% or 0.05 Å, whereas no such expansion is observed (e.g., compare Harlow and Brown 1980; Scambos et al. 1987). Similarly, the volume expansions and contractions upon heating or cooling are significantly greater than can be explained by the measured changes in T-O bond lengths. Therefore the majority of the expansion of feldspars must come from changes in the tilts of the framework.

The alkali (Na, K) feldspars have average <<T-O>> bond lengths of 1.65 ± 0.01 Å at room conditions, while <<T-O>> = 1.638 Å is slightly less in "Rb-sanidine" (Kyono and Kimata 2001). Figure 7 is a compilation of the calculated volume changes for each of the individual tilt systems taken from Figure 6, and replotted as absolute volumes for a structure with perfectly regular tetrahedra with a bond length of 1.6500 Å. The un-tilted structure has a unit-cell volume of 597.7 Å^3. It is clear from Figure 7 that only tilts 2 and 3 lead to significant volume expansion but, as noted above, tilt 3 cannot operate on its own because it leads to shortened O-O distances across the mirror plane. Tilt 2 is not limited in this way, and Figure 7 shows that it can expand the structure of ideal tetrahedra to the volume of albite (~664 Å^3), but that it cannot alone expand the structure further to that of the K-feldspars (V_{cell} ≈ 722 Å^3) or Rb-feldspars (V_{cell} ~742 Å^3). However, tilt 2 increases the distances between the oxygen atom pairs related by the mirror plane within the structure, and thus allows tilt 3 to operate simultaneously. The simultaneous application of both tilts together to the ideal structure leads to a further volume increase beyond that achievable by either tilt alone (Fig. 8a). Together they are more than sufficient to expand the structure to volumes in excess of the 755 Å^3 found in Rb-microcline at high temperatures (Hovis et al. 2008). Analysis of all of the available refined crystal structures of $AlSi_3$ feldspars collected at pressures less than 4 GPa, including all high-temperature

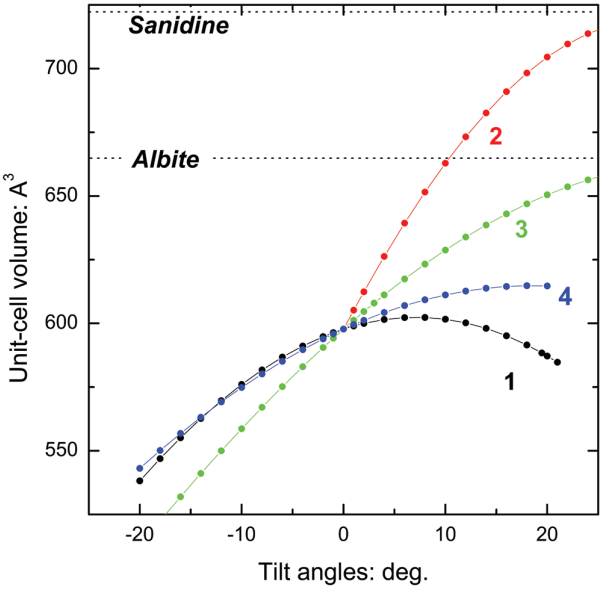

Figure 7. The change in volume of the monoclinic unit-cell volume induced by the individual tilts of the ideal feldspar structure with a T-O bond length of 1.650 Å. The observed unit-cell volumes of albite and sanidine are indicated. (Color online.)

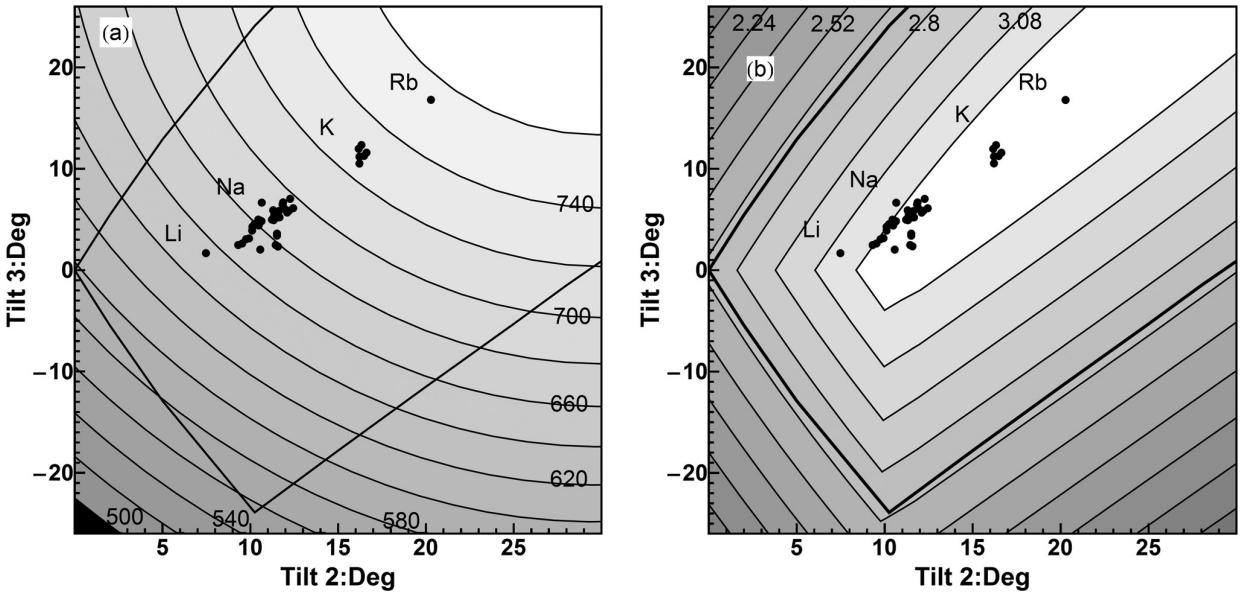

FIGURE 8. Contoured maps showing the variation of (**a**) unit-cell volume in cubic angstroms and (**b**) shortest O-O distance in angstroms between O atoms on different tetrahedra induced by the combination of tilts 2 and 3 of the ideal feldspar structure with a T-O bond length of 1.650 Å. The heavy lines indicate combinations of tilt angles that generate O-O distances between O atoms on different tetrahedra that are equal to the tetrahedral edge length. Black data points are the observed tilts in all available structures of $AlSi_3$ feldspars determined at ambient conditions, at high temperatures, and at pressures less than 4 GPa at room temperature.

determinations, confirms this picture. The values of tilts 1 and 4 show no significant variation (Fig. 9a), whereas both tilts 2 and 3 exhibit a uniform but non-linear increase with unit-cell volume (Fig. 9b), irrespective of whether the volume change is induced by changes in composition, temperature or pressure.

ANISOTROPY OF FELDSPARS

It is clear from Figure 8a that any given unit-cell volume can be achieved by a wide combination of values for the two tilts ϕ_2 and ϕ_3 while still keeping all of the O-O distances longer than the length of the edges of the tetrahedra; for example, a V_{cell} = 700 Å^3 could be achieved with tilts values ranging from $\phi_2 \sim 7.5°$ and $\phi_3 \sim 19°$ to $\phi_2 \sim 26°$ and $\phi_3 \sim -2°$. However, the values of ϕ_2 and ϕ_3 actually adopted by real alkali feldspars form a single approximately linear trend with $\phi_3 = 1.20\phi_2 - 8.09$ (data points on Fig. 8). This trend is perpendicular to the isochors of the model structure (Fig. 8a), which means that volume changes in real feldspars are achieved by the minimum possible change in the values of the tilts. But this does not explain why such values of the tilts are adopted. Analysis of the O-O distances in the tilted model feldspars shows that the tilts found in real feldspars approximately maximize the shortest distance between oxygen atoms that do not belong to the same tetrahedron (Fig. 8b). This strongly suggests that the conformation of feldspars is controlled by oxygen-oxygen repulsions and not by the bonded interactions between the O atoms and the extraframework cations.

Each of the two active tilts in alkali feldspars by themselves imposes significant anisotropy upon the expansion of the unit cell of the feldspar because tilt 2 expands *d*(100) significantly faster than *b* while not changing *c* (Fig. 6b), while tilt 3 actually leads to a contraction of *b* and *c* (Fig. 6c) while expanding *d*(100). In combination (Fig. 10) the effects of the two tilts thus produce a weak expansion in *b* and a very slight contraction in *c*, and most of the expansion of the model feldspar is then accommodated by the expansion of *d*(100). This demonstrates that the fundamental reason for the anisotropy of feldspars lies in the topology of the tetrahedral framework, with the exact values of tilts set by a volume requirement for the unit cell in combination with the requirement that distances between the non-bonded O atoms are maximized.

The model then allows several other structural features and trends that have been previously noted for the alkali feldspars to be explained. Examination of the evolution of the unit-cell parameters of model structures with the combination of tilts found in the real alkali feldspars (Fig. 11), shows in detail that with increasing unit-cell volume, both the *a* and *b* cell parameters expand together up to approximately the values of the tilts found in the end-member K-feldspars, while the change of the *c* cell parameter is much smaller (Fig. 11c). With further continuous increase in tilts beyond those in K-feldspars, the rate of increase of *b* due to tilt 2 decreases so that the decrease of *b* due to tilt 3 (Fig. 6) begins to dominate. This leads first to no further expansion in *b* (Fig. 11b), as seen in the K-Rb series at room temperature (Hovis and Roux 2008). If these trends in tilts continue beyond the values found in Rb feldspar at room temperature (Kyono and Kimata 2001), which is the most tilted feldspar for which structure data exists, then the model predicts an actual decrease in *b*, as seen in Rb feldspars at high temperatures (Hovis et al. 2008). Thus the model shows that the evolution of the unit-cell parameters of alkali feldspars that had previously been separated in to distinct "Trends" (Brown et al. 1984), and postulated to indicate structural changes or phase transitions between them,

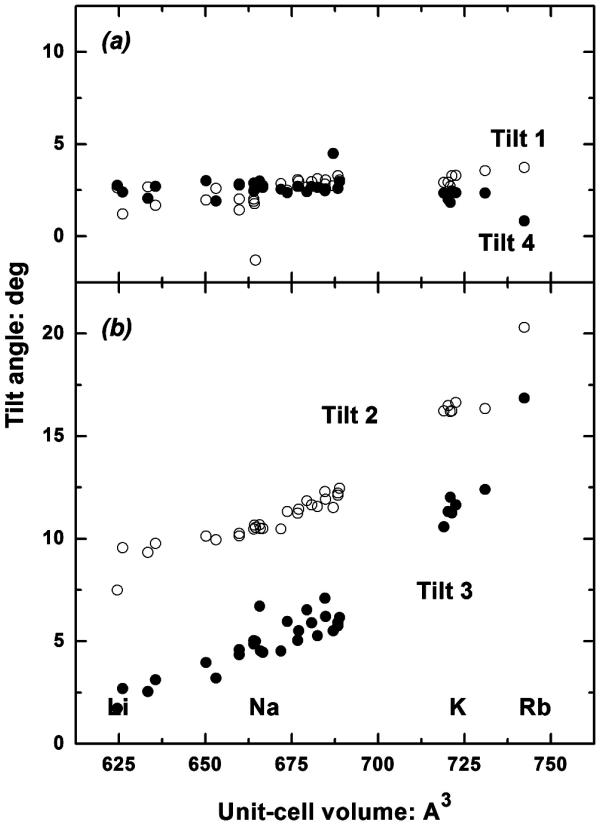

FIGURE 9. The variation of tilt angles for all published structures of $AlSi_3$ feldspars at ambient conditions, at room pressure and variable temperature, and at room temperature and pressures up to 4 GPa. The unit-cell volumes of end-member feldspars at room conditions are marked approximately by the element symbols for the corresponding M cation.

is in fact a simple consequence of a smooth and continuous increase in the magnitudes of the two dominant tilt systems of the framework. Similarly, the negative thermal expansion of the *c*-axis in albite (e.g., Tribaudino et al. 2011) is also seen to be a direct consequence of the topology of tilt 3, which shortens this axis with increasing cell volume (Figs. 6c and 11c). The fact that other alkali feldspars actually exhibit small and often zero thermal expansion of this axis (Hovis and Graeme-Barber 1997; Hovis et al. 2008) indicates that there are other, secondary, effects that modify the basic pattern of anisotropy imposed by the two dominant tilt systems as controlled by O-O mutual repulsions.

Figure 12 shows that the model structure with just tilts 2 and 3 with the values that follow those observed in the alkali feldspars (and that thus maximize the shortest O-O distances) also reproduces the relative magnitudes of the T-O-T bond angles, even for triclinic feldspars for which the average values of the symmetry-equivalent pairs of Ob, Oc, and Od atoms are plotted. The model also displays most of the trends in T-O-T angles observed within the real structures, with the strong increase in T2-Oa2-T2, the maximum in the T1-Ob-T2 and the weaker variation in the other three angles being clearly reproduced by the model. The fact that it predicts that T1-Oa1-T1 should also be invariant and that T1-Od-T2 should decrease with increasing unit-cell volume, while in real feldspars they, respectively, increase and remain constant, again indicates that secondary mechanisms operate in real feldspars to modify the intrinsic behavior of the framework imposed by its topology.

It is therefore clear that the model with just tilts 2 and 3 does reproduce the essential features of the evolution of the cell parameters and structures of the alkali feldspars, and in particular the anisotropy of the strain induced by pressure, temperature, or changes in the extraframework cation. However, this model does not provide a perfect match to all of the parameters of real feldspars, in part due to the omission of tilts 1 and 4. When average values from real alkali feldspars of $\phi_1 = \phi_4 = 2.6°$ (Fig. 9a) are added to the model structures with tilts 2 and 3, the effects on the cell parameters are small and as expected from Figures 6a and 6d; they produce a small increase in volume, no change in $d(100)$, an increase in b, and a small decrease in c. Together these result in no visible change in the pattern of anisotropy along the trend of the real alkali feldspars that is shown in Figure 9. As predicted from Figures 5a and 5d, they do however significantly change the predicted values of the T1-Oa1-T1 and T1-Od-T2 bond angles, but not their trends, and the discrepancies to real structures with the same tilts remains. These discrepancies can be attributed to the several distortions present in the real feldspars that are absent from the model. In a real feldspar individual T-O bond lengths differ from the average value for the structure as a

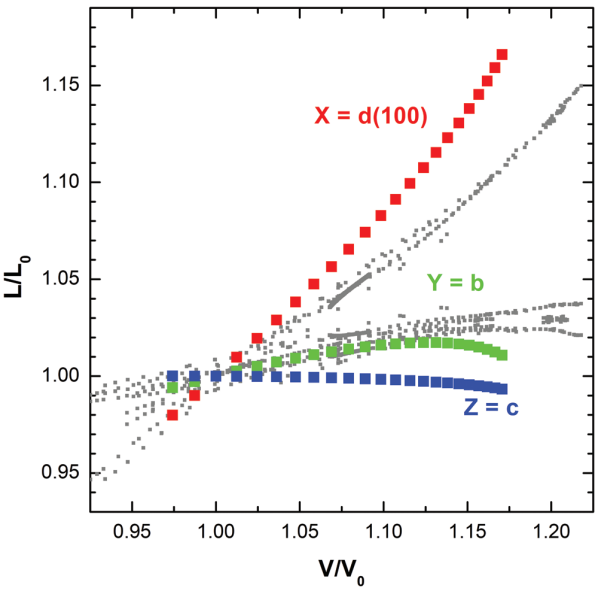

FIGURE 10. The variation of the lengths of three mutually perpendicular directions in the ideal monoclinic feldspar as a function of combined effects of tilts 2 and 3, with the values set to follow the evolution (see Fig. 8) of the tilts in $AlSi_3$ feldspars. All axial lengths are scaled to the values for a model ideal feldspar with tilts $\phi_2 = 8.4°$ and $\phi_3 = 2.0°$, close to the values for Li-feldspar. The small gray data points are experimental data previously shown in Figure 2 and scaled to the cell parameters of Li-feldspar (Baur et al. 1996). The model correctly predicts the sense of anisotropy and the magnitude of the strain along $\mathbf{Y} = b$, but overestimates the expansion along $\mathbf{X} = d(100)$ and underestimates that of c. (Color online.)

result of Al/Si ordering, variations in T-O-T angles, bonding to the extraframework cations and the occupancy of the neighboring tetrahedral site (e.g., Angel et al. 1990, and references therein). The changes induced by these factors in the T-O bond lengths together with the variations in O-T-O angles both contribute to shifts in the oxygen positions and, as a consequence, changes in the T-O-T angles from those of the model with ideal regular tetrahedra of equal sizes. These in turn contribute to making the T-T distances in the real structures generally shorter than those predicted by the model.

As a consequence of the over-estimation of T-T distances by the models, the volumes of the unit cells are over-estimated by the model as can be deduced by comparison of Figure 8a with the observed volumes of feldspars. Some of the differences can be ascribed to the fact that in some alkali feldspars the observed value of <<T-O>> is slightly less than in the model used to generate Figures 7, 8, and 11. After rescaling the model by the observed <<T-O>> (cf. Eq. 1) we find that the model still overestimates the unit-cell volumes for the alkali feldspars with smaller cations (~3% for albite and ~4% for Li-feldspar) with smaller discrepancies for those with larger cations. The addition of tilts 1 and 4 to the model reduces the discrepancy

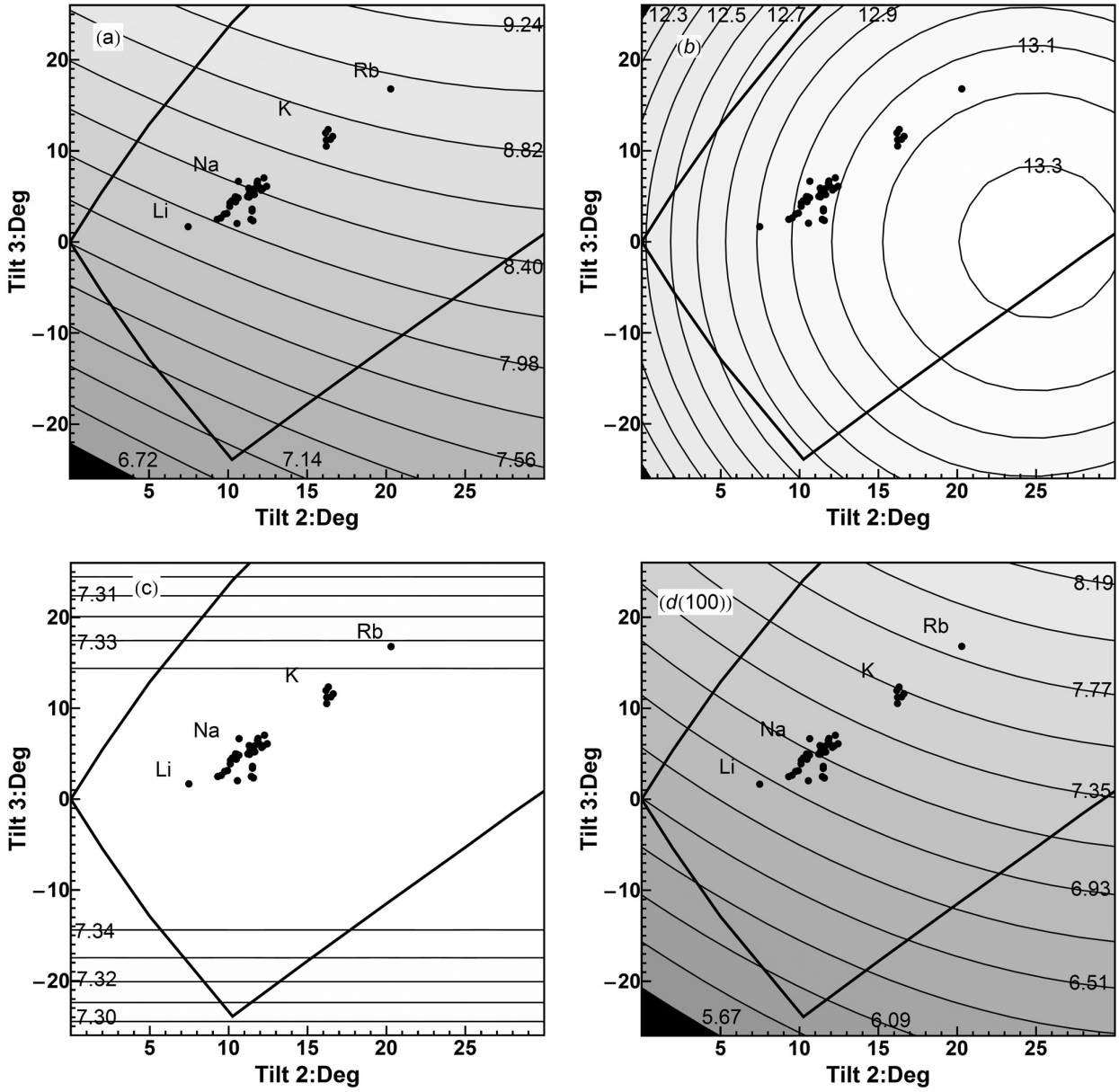

Figure 11. The variation of the unit-cell parameters *a*, *b*, *c*, and *d*(100) as a function of tilts 2 and 3 of the ideal model feldspar structure with a T-O bond length of 1.650 Å. The heavy lines indicate combinations of tilt angles that generate O-O distances between O atoms on different tetrahedra that are equal to the tetrahedral edge length. Black data points are the observed tilts in all available structures of $AlSi_3$ feldspars determined at ambient conditions, at high temperatures, and at pressures less than 4 GPa at room temperature.

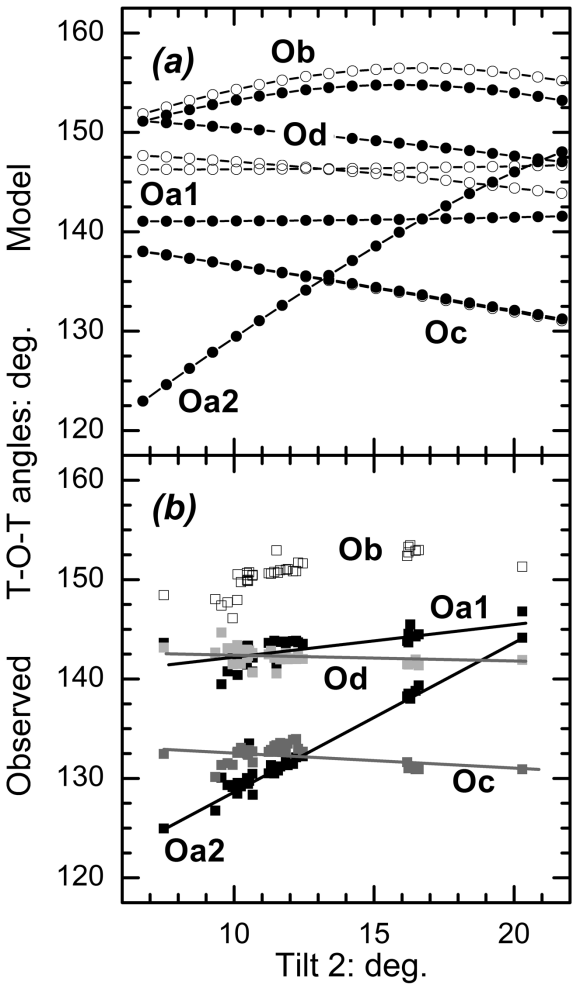

FIGURE 12. The variation of T-O-T bond angles with the value of tilt 2. In **a**, the closed symbols show the angles in the ideal model structure with the values of ϕ_2 and ϕ_3 set to follow the evolution of the tilts in $AlSi_3$ feldspars, but with $\phi_1 = \phi_4 = 0$. The small open symbols are the values in the model structures with the same values of ϕ_2 and ϕ_3 but with $\phi_1 = \phi_4 = 2.6°$. (**b**) The angles in the 33 feldspar structures plotted in Figures 8, 9, and 11. Lines are drawn to indicate trends.

in volume to ~3% for Li-feldspar and less than 1% for K- and Rb-feldspars. A comparison of the structures of the real feldspars with the corresponding models shows that, except for the very distorted structure of Li-feldspar, differences in the volume of the cavity containing the extraframework cation accounts for more than 50% of the volume difference between the model structures and the real feldspars. The uncoordinated "free space" between the tetrahedra accounts for the remaining difference in unit-cell volumes. Therefore, although the main contribution to the changes seen in feldspar structures with thermal expansion, compression, and change in composition can be explained by the response of the framework alone without the need to consider M-O bonding, the subtle discrepancies between the model and real feldspars indicate a secondary role of M-O bonds in modifying both the anisotropy and volume changes of feldspars. The exact role and behavior of the M-O bonds cannot, however, be predicted by this geometrical model of the tetrahedral framework because the position of the M cation within the cavity is not fixed but is free to change. The prediction of the position of the M site within the cavity of the framework and thus the prediction of M-O bond lengths would require the addition of a model for the M-O interactions.

In conclusion, we have shown that the essential features of the structures, unit-cell parameters and volumes of the $AlSi_3$ feldspars, and their expansion and compression induced by changes in pressure, temperature, and composition, can only be achieved by the simultaneous application of tilts 2 and 3 to an un-tilted framework of regular tetrahedra. This analysis is confirmed by a survey of the refined crystal structures of $AlSi_3$ feldspars that shows these two tilts are the only ones to change significantly and systematically (Fig. 9). In combination these two tilts impose significant anisotropy upon the expansion of the unit cell of the feldspar with the majority of the expansion accommodated by the expansion of $d(100)$. This demonstrates that the fundamental reason for the anisotropy of feldspars lies in the topology of the tetrahedral framework. The topology restricts the tilt patterns that result in significant volume change, and makes those that do generate volume change generate anisotropic expansion as a consequence of the linkages between the 4-rings. A comparison of the actual tilts observed in alkali feldspars with the model structures shows that the values of the tilts adopted by real feldspars are those that maximize the shortest O-O distances in the structure. Therefore the O-O repulsions along with the volume requirement control the values of the tetrahedral tilts in alkali feldspars and thus the anisotropy of the structure. Thus, we conclude that the bonding requirements of the bridging O atoms, the directionality of the bonding to the extraframework cations and the tilt systems 1 and 4 only play a secondary role in modifying this basic pattern of anisotropy. Because all feldspars exhibit the same framework topology, these conclusions will also apply to the plagioclases even though they exhibit lower symmetries.

ACKNOWLEDGMENTS

This work was supported by National Science Foundation grants EAR-0738692 and EAR-1118691 to Nancy Ross and Ross John Angel (R.J.A.), and the Deutsche Forschungsgemeinschaft in the form of a Mercator Professorship to R.J.A. (INST 152/526-1). R.J.A. thanks Boriana Mihailova for hosting his professorship in Hamburg and David Palmer for implementing the reading of multiple CIFs and the generation of crystal movies in CrystalMaker that enabled the visualization and consequent understanding of our results. Jim Langridge and Miles Gentry (Virginia Tech) provided essential IT support that allowed this project to be completed. We are grateful to Nancy Ross, Ralf Dohmen, Diego Gatta, Guy Hovis, Boriana Mihailova, Fabrizio Nestola, Ian Parsons, Daria Pasqual, and many others who provided discussion, suggestions, and reviews over the long period of gestation and preparation of this manuscript.

REFERENCES CITED

Allan, D.R. and Angel, R.J. (1997) A high-pressure structural study of microcline ($KAlSi_3O_8$) to 7 GPa. European Journal of Mineralogy, 9, 263–275.

Angel, R.J. (1994) Feldspars at high pressure. In I. Parsons, Ed., Feldspars and their Reactions, C421, p. 271–312. Kluwer, Dordrecht.

Angel, R.J., Hazen, R.M., McCormick, T.C., Prewitt, C.T., and Smyth, J.R. (1988) Comparative compressibility of end-member feldspars. Physics and Chemistry of Minerals, 15, 313–318.

Angel, R.J., Carpenter, M.A., and Finger, L.W. (1990) Structural variation associated with compositional variation and order-disorder behavior in anorthite-rich feldspars. American Mineralogist, 75, 150–162.

Baur, W.H., Joswig, W., and Muller, G. (1996) Mechanics of the feldspar framework; Crystal structure of Li-feldspar. Journal of Solid State Chemistry, 121, 12–23.

Benna, P., Nestola, F., Boffa-Ballaran, T., Balić-Žunić, T., Lundegaard, L.F.,

and Bruno, E. (2007) The high-pressure structural configurations of $Ca_{0.2}Sr_{0.8}Al_2Si_2O_8$ feldspar: The $I\bar{1}$-$I2/c$ and $I2/c$-$P2_1/c$ phase transitions. American Mineralogist, 92, 1190–1199.

Benusa, M., Angel, R.J., and Ross, N.L. (2005) Compression of albite, $NaAlSi_3O_8$. American Mineralogist, 90, 1115–1120.

Brown, J.M., Abramson, E.H., and Angel, R.J. (2006) Triclinic elastic constants for low albite. Physics and Chemistry of Minerals, 33, 256–265.

Brown, W.L., Openshaw, R.E., McMillan, P.F., and Henderson, C.M.B. (1984) A review of the expansion behavior of alkali feldspars: coupled variations in cell parameters and possible phase transitions. American Mineralogist, 69, 1058–1071.

Curetti, N., Sochalski-Kolbus, L., Angel, R.J., Benna, P., Nestola, F., and Bruno, E. (2010) High-pressure structural evolution and equation of state of analbite. American Mineralogist, 96, 383–392.

Gatta, G.D. and Angel, R.J. (2007) Elastic behavior and pressure-induced structural evolution of nepheline: implications for the nature of the modulated superstructure. American Mineralogist, 92, 1446–1455.

Gatta, G.D., Angel, R.J., Rotiroti, N., Zhao, J., Alvaro, M., and Carpenter, M.A. (2011) Phase-stability, elastic behavior and pressure-induced structural evolution of kalsilite: a ceramic material and high-*T*/high-*P* mineral. American Mineralogist, 96, 1363–1372.

Glazer, A.M. (1972) The classification of tilted octahedra in perovskite. Acta Crystallographica, B28, 3384–3392.

Harlow, G.E. and Brown, G.E. (1980) Low albite: an X-ray and neutron diffraction study. American Mineralogist, 65, 665–675.

Hovis, G.L. and Graeme-Barber, A. (1997) Volumes of K-Na mixing for low albite-microcline crystalline solutions at elevated temperature: A test of regular solution thermodynamic models. American Mineralogist, 82, 158–164.

Hovis, G.L. and Roux, J. (2008) Thermodynamic mixing properties of Rb-K feldspars. American Mineralogist, 93, 1597–1602.

Hovis, G.L., Morabito, J.R., Spooner, A., Mott, A., Person, E.L., Henderson, C.M.B., Roux, J., and Harlow, D. (2008) A simple predictive model for the thermal expansion of $AlSi_3$ feldspars. American Mineralogist, 93, 1568–1573.

Howard, C.J. and Stokes, H.T. (1998) Group-theoretical analysis of octahedral tilting in perovskites. Acta Crystallographica, B54, 782–789.

Kroll, H., Schmiemann, I., and von Coelln, G. (1986) Feldspar solid solutions. American Mineralogist, 71, 1–16.

Kyono, A. and Kimata, M. (2001) Refinement of the crystal structure of a synthetic non-stoichiometric Rb-feldspar. Mineralogical Magazine, 65, 523–541.

Megaw, H. (1970) Structural relationship between coesite and feldspar. Acta Crystallographica, B, 26, 261–265.

Megaw, H.D. (1974a) Tilts and tetrahedra in feldspars. In W.S. MacKenzie and J. Zussman, Eds., The Feldspars, p. 87–113. Manchester University Press, U.K.

——— (1974b) The architecture of feldspars. In W.S. MacKenzie and J. Zussman, Eds., The Feldspars, p. 2–24. Manchester University Press, U.K.

Mihailova, B., Zotov, N., Marinov, M., Nikolov, J., and Konstantinov, L. (1994) Vibrational spectra of rings in silicate glasses. Journal of Non-Crystalline Solids, 168, 265–274.

Nestola, F., Curetti, N., Benna, P., Ivaldi, G., Angel, R.J., and Bruno, E. (2008) Compressibility and high-pressure behaviour of $Ab_{63}Or_{27}An_{10}$ anorthoclase. Canadian Mineralogist, 46, 1433–1454.

Scambos, T.A., Smyth, J.R., and McCormick, T.C. (1987) Crystal-structure refinement of high sanidine from the upper mantle. American Mineralogist, 72, 973–978.

Smith, J.V. and Brown, W.L. (1987) Feldspar Minerals. Springer-Verlag, Berlin.

Tribaudino, M., Bruno, M., Nestola, F., Pasqual, D., and Angel, R.J. (2011) Thermoelastic and thermodynamic properties of plagioclase feldspars from thermal expansion measurements. American Mineralogist, 96, 992–1002.

Wang, D. and Angel, R.J. (2011) Octahedral tilts, symmetry-adapted modes and polyhedral volume ratios in perovskite structures. Acta Crystallographica, B67, 302–314.

Winter, J.K., Ghose, S., and Okamura, F.P. (1977) A high-temperature study of the thermal expansion and the anisotropy of the sodium atom in low albite. American Mineralogist, 62, 921–931.

Manuscript received September 26, 2011
Manuscript accepted February 7, 2012
Manuscript handled by Simon Redfern

Chapter 4: The effect of high-pressure on tetrahedral tilting in C-1 Ab-rich plagioclase feldspars

4.1 Introduction

Feldspar structures at high-pressures have been widely studied and analyzed in terms of the mechanisms that cause changes in the crystal framework. High-pressure feldspar structures are of particular interest because of the anisotropy of compression with 60-70 percent of the unit-cell attributed to the *d(100)* (or a* direction) and the elastic softening that occurs at higher pressures for more Ab-rich plagioclase feldspars (*e.g.* Angel 2004b; Chapter 2 of this thesis; Benusa *et al.* 2005; Johnson 2007). Previous structural studies on feldspars at high pressures attempted to use individual bond lengths or bond angles to describe the overall structural changes. Allan and Angel (1992) studied a single crystal of microcline up to 7.1 GPa and concluded that the structural mechanisms upon compression for microcline involves a link between the changes of the T-Obm-T and T-Obo-T angles, with the movement of the *M*-cation in the extra framework cavity via specific M-O bond lengths. Similarly, Downs *et al.* (1999) looked at reedmergerite at pressures up to 4.7 GPa and attributed the structural changes to the collapse around the M-site cavity via specific T-O-T angles. Down *et al.* (1994) looked at the compression mechanisms in low albite up to 3 GPa and attributed the changes to single T-O-T angles as well.

Although there are some apparent changes between various T-O-T angles with composition and increasing pressure in feldspars as described in recent publications, these changes are ambiguous. The structural changes that are attributed to T-O-T angle(s) differ for feldspars of various compositions over a range of pressures and temperatures. A less ambiguous approach to describing the structural change with pressure for feldspar minerals is the tetrahedral

tilting systems and model introduced in Chapter 3. The tilting of the rigid tetrahedra as a mechanism of compression has been discussed before (Nestola *et al.* 2008), but they did not analyze the changes in terms of the specific tilting modes. Therefore, to the best of the author's knowledge, there has not been any quantification of the tilting systems in feldspars at high pressures. It has already been shown in Chapter 3 of this thesis that there are systematic changes present with respect to the tilting systems for alkali feldspars with composition change of the *M*-site, increasing temperatures and pressures up to 4 GPa. The variation in tilts explains the variation in the unit-cell parameters and therefore, tetrahedral distortions and triclinic distortion are secondary effects. The aim of this study is to explore how these tilting systems change with pressure and whether the tilt 2 and tilt 3 model proposed in Chapter 3 applies for Na-rich plagioclase feldspars at high pressure. In addition, the tilt systems were explored for distinct patterns associated with elastic softening seen in Na-rich plagioclase feldspars through analysis of experimental data.

4.2 Experimental

4.2.1 Sample description

Four samples of Na-rich plagioclase samples were selected for the tilt system analysis; three of which are in the literature ; low albite (An0 ordered) (Benusa *et al.* 2005), analbite (An0 disordered) (Curetti *et al.* 2010), An37(Johnson 2007). Low albite, An20, An37 contain the maximum state of Al/Si order that is possible for each respective composition and both were chosen for this structural study because of the composition and quality of data. The provenance for An20 is a pegmatite located in Bakersville, North Carolina. The bulk composition of this plagioclase was determined by electron microprobe analysis and contains <3% Or content

(Carpenter *et al* 1985). The data for low albite and An37 were collected by previous authors (Benusa *et al.* 2005 and Johnson 2007) with the description of the data collection described therein. Analbite contains the maximum state of Al/Si disorder and is characterized in Curetti *et al.* (2010) with details discussed in chapter 2 of its unit-cell parameter variation this thesis.

4.2.2 Experimental details

The details of the experiments performed on An37 involved data collections with one crystal mounted inside of an ETH-designed diamond anvil cell and two crystals were mounted at lower pressures of which details are described in Johnson 2007. Although the data collections done on these An37 crystals were accurate and precise, I have been able to improve upon the previous protocol used to integrate and refine the data. The data have therefore been re-analyzed in the same way as I describe below for An20, and are presented here in this chapter. From this re-analysis, it was clear that the use of two crystals in different orientations within the DAC is superior to just one because the estimated standard deviations associated with the bond lengths and angles were much lower in the refinements than the refinements with only one crystal involved. Therefore, two crystals (Hawkb_A and Hawkb_B) of a well-characterized An20 plagioclase were chosen for high-pressure single-crystal X-ray diffraction. Sample Hawkb_A has the dimensions of 165μm X 90μm X 20μm and Hawkb_B had the dimensions of 150μm X 67.5 μm X 30μm. Intensity measurements on both crystals in air were performed on a Gemini diffractometer (Agilent Technologies) equipped with MoKα radiation and a graphite monochromator. The state of Al/Si order of the An20 plagioclase was confirmed using the refinements from the single-crystal X-ray diffraction data and the equation from Kroll and Ribbe (1980) that uses the mean T-O bond lengths to determine aluminum content of each individual tetrahedra.

An ETH-designed diamond-anvil cell was selected to perform the high-pressure single-crystal measurements on Hawkb_A and Hawkb_B. The culet sizes of the diamonds were 600 microns and were aligned optically with a polarized microscope. A stainless steel gasket was indented to a thickness of 100μm and a hole was drilled in the center of the indentation of a thickness of 80 microns and diameter of 300 microns. Both crystals were placed on one diamond culet in different orientation to maximize the number of accessible reflections during the high-pressure intensity data collections to use in the refinements. Hawkb_A was placed in a way so that the c*-direction was parallel with respect to the incident beam while Hawkb_B was placed in a way so that b*-direction was parallel with respect to the incident beam. In addition to the crystals, a ruby chip was mounted to determine the precise pressure for each data point. The cell was loaded with a 4:1 methanol/ethanol mixture to ensure hydrostatic conditions. The unit-cell parameters of the crystals were refined to the positions of reflections determined by 8-position centering (King and Finger 1979) on a Huber 4-circle diffractometer using the SINGLE software (Angel and Finger, 2011).

Intensity measurements were performed at the pressures of 0, 2.149, 5.717, 6.756 and 8.144 GPa on the crystals within the ETH-Designed Diamond anvil cell. This was done with an Agilent Xcalibur single-crystal diffractometer equipped with MoKα radiation, a graphite monochromator, and a point detector 'fixed phi-mode' setting was used on the omega scans which resulted in around 1500 reflections for each of the crystals from 2 to 40 degrees θ. The scan widths were set to 1.2° and scan steps set to 0.05° for each measurement for both crystals.

4.2.3 Data integration and refinement

To extract the actual intensities and correct for background and instrumental factors, the data for both crystals were integrated using WinIntegrStp v3.5 (Angel 2003). This program fits individual intensity peaks using pseudo-Voigt functions (Pavese and Artioli 1996). Each data set was then treated for absorption by the crystal and components of the DAC with Absorb v.6.2 (Angel 2004a). The intensity data was then merged with Average v.2.2 and processed with criteria for outlier rejection (Angel 2004c). The reflections for each dataset were then set to a different batch number (Hawkb_A set to 1 and Hawkb_B set to 2) to be treated as separate groups of reflections with unique scale factors for the refinement process and merged as a joint *hkl* file. This file, in addition to an instruction file, was used in the structure refinements. The very precise unit-cell parameters obtained from the Huber diffractometer were used in the refinements. The instruction file, in addition to the usual cards, contained a card that refines a relative scale factor and multiplies the reflections labeled with "1" by the scale factor and "2" with the scale factor and a factor 1/sqrt(BASF). This refined value of this relative scale factor (BASF) was used to re-scale the reflections from Hawkb_B after the absorption correction was applied. The re-scaled reflections were then merged with the reflections from Hawkb_A after the absorption correction. The new merged file of Hawkb_A reflections and re-scaled Hawkb_B reflections were merged via Average v.2.2 as was done to the individual reflections. The averaged merged file of Hawkb_A and Hawkb_b reflections was then refined in WinGX (Farrugia 1999) using Shelxl 97 (Sheldrick 2008) without the relative scale factor card. This method increases the number of reflections used in the refinement processes and thus greatly reduces the error on bond-lengths and angles.

Unfortunately, the gasket began to expand at 8.14 GPa and the Hawkb_B crystal was crushed. The DAC was then loosened and Hawkb_A and the ruby chip were recovered. A new gasket was made with the same indentation and diameter. Hawkb_A was placed on the DAC in the same orientation as the previous measurements and a new crystal (Hawkb_C) was used to complete the high-pressure structural determinations. This new crystal was selected from the same batch of powder as Hawkb_A and Hawkb_B. The dimensions of Hawkb_C are 120μm X 80μm X 30 μm and it was placed on the diamond culet next to Hawkb_A so that b*-direction was parallel to the incident beam. The remaining measurements (3.76 and 4.31 GPa) were carried out with these two crystals and the same methods were applied as for the Hawkb_A/Hawkb_B configuration.

The models used for the refinement is similar of both An20 and An37 were similar to those developed by Johnson 2007. All *T*-sites were set to isotropic displacement parameters. The aluminum and silicon occupancies on the *T*-sites were set to the values determined from the bond lengths through the equation in Kroll and Ribbe (1980). All oxygen's were set to have isotropic displacement parameters and refineable positions. The Na/Ca *M*-site was split in to two sites, with occupancies of the partial sites set to the composition from microprobe data with the minute amount of K being accommodated by the Ca-site. The two M partial sites were set to have anisotropic displacement parameters and their positions refined independently. Thus, the position of the Na and Ca sites are correlated and should not be taken as any more than providing an approximation to the overall scattering density of the *M-site.*

4.3 Results

4.3.1 Refinement results for An20 and An37

The refinement results for the merged and rescaled refinements of Hawkb_A/Hawkb_B, Hawkb_A/Hawkb_C and An37 are reported in Table A.4.1 and Table A.4.2 respectively in Appendix A. All refinements resulted in reasonable standard errors on the bond lengths and angles which are necessary for proper calculation of the tilt systems. Loss of reflections for each refinement as pressure increases in the diamond anvil cell is due to the movement of the reflections beyond the angle limit for the diamond cell window at higher pressures.

4.3.2 Cell parameter evolution for An20 and An37

The fractional change of the unit cell parameters *a*,*b*,*c* and *d(100)* and the unit-cell volume from room pressure to 9.45 GPa for An37 and room pressure to 9.15GPa for An20 are depicted in Figure 4.1. Unit-cell angles alpha beta and gamma are shown in Figure 4.2 (a), (b) and (c) respectively. The previous results generated for An20 (Angel 2004b) used in an equation of state investigation and the results generated for An20 for this study show consistency (Figure 4.1 and 4.2). All cell parameters in Figure 4.1a for An20 and An37 are decreasing with increasing pressure in agreement with Angel (2004c). The anisotropy in the evolution of the unit cell upon compression is obvious in Figure 4.1a as the *d(100)* spacing and *a*-axis show the greatest change from 0-9.15 GPa for An20 and 0-9.43 GPa for An37. This anisotropy is similar to the previous studies on low albite (Benusa *et al*. 2005) and analbite (Curetti *et al*. 2010), however the *d(100)* direction shows slightly greater softness with pressure for low albite and analbite than the *a*-direction for analbite and low albite. An20 and An37 show very similar responses to pressure with respect to the fractional change in the b- axis, c-axis and volume change. The *a*-axis and *d(100)* is softer for An20 than An37 and thus An20 shows greater

anisotropy than does An37. The unit cell angles (Fig. 4.2) for both An20 and An37 change similarly with increasing pressure. Alpha decreases with increasing pressure steadily with alpha being greater in value for An20 than for An37 at all pressures. Beta increases from room pressure to 3 GPa for both An37 and An20 with a more dramatic increase in the beta angle of An20. From 3 GPa to the maximum pressure measured for An20, the beta angle remains the same. From 3 GPa to around 5 GPa for An37, the beta angle remains the same and then begins to decrease slightly from 5 GPa to the maximum pressure. The gamma angle for both An20 and An37 increases from room pressure to the maximum pressure at which each sample was measured.

4.3.3 The volume change and elastic softening of Ab-rich plagioclase feldspars

The unit-cell volumes of all the samples represented in Figure 4.3a are previously measured samples including data from Figure 2.1. It is clear from Figure 4.3b that the compression of *d(100)* is similar to that of the volume compression and comprises 60-70 percent of the volume change upon compression. A 4^{th} order equation of state was fit to all data sets and is described in Equations 2,3 and 4 in Chapter 2 of this thesis. As such, the *f-F* plots of the respective *PV* and *Pd(100)* plots parabolic curves (Figure 4.4). This parabolic curve, as described mathematically in Chapter 2, is unlike most solids and indicates structural softening rather than stiffening at higher pressures. The point at which F_E reaches a maximum is the point at which the pressure derivative K' is reduced to 4; the further decrease in the slope to more negative values is indicative of the onset of elastic softening. The onset pressure of this behavior is different for all of the samples. In addition, the exaggeration of curvature becomes less as Ca-content is increased in the Na-rich plagioclase and becomes more and more 3^{rd} order in behavior (and thus without elastic softening) . In addition to the *f-F* plot for the volume, a parabolic curve's evident

for the *d(100)* direction (Figure 4.4b) which suggests that this direction in the lattice also shows elastic softening. In fact, the point of maximum F_E appears to be at lower pressures in the *d(100)* than with the volume plot.

A more direct way to see the elastic softening is to plot the pressure variation of the bulk and linear moduli that can be calculated from the refined EoS parameters. Figure 4.5 shows both the bulk moduli and the linear moduli for the *d(100)* as a function of pressure. Normal solids would exhibit a steady, almost linear increase in bulk modulus with pressure, especially over small pressure intervals (which is why the Murnaghan EoS which implies a linear variation of modulus with pressure can be used to describe the compression of crustal minerals at crustal pressures). As Ca content increases in the ordered feldspars, the pressure at which the bulk moduli reaches a maximum also increases (Figure 4.5). For these three samples, the onset of softening of *d(100)* precedes that of the volume, so it seems reasonable to attribute the volume softening to the softening of *d(100)*, and to conclude that the addition of Ca to the albite structure in some way results in a stiffening of the *d(100)* and thus to an increase in the pressure at which softening initiates and a decrease in the amount of softening. Analbite shows quite distinct behavior; although is softer than ordered low albite at low pressures, the softening is delayed until higher pressures and, further, the peak in the volume bulk modulus occurs before (rather than after) the pressure at which softening starts in *d(100)*. The reasons for this must lie in some differences in the response of the disordered structure from those of the ordered feldspars (even allowing for the fact that intermediate plagioclase are partially disordered as a result of the Al/Si exchange).

Figure 4.1. Fractional cell edge length change and volume change at high-pressure for An20 and An37.

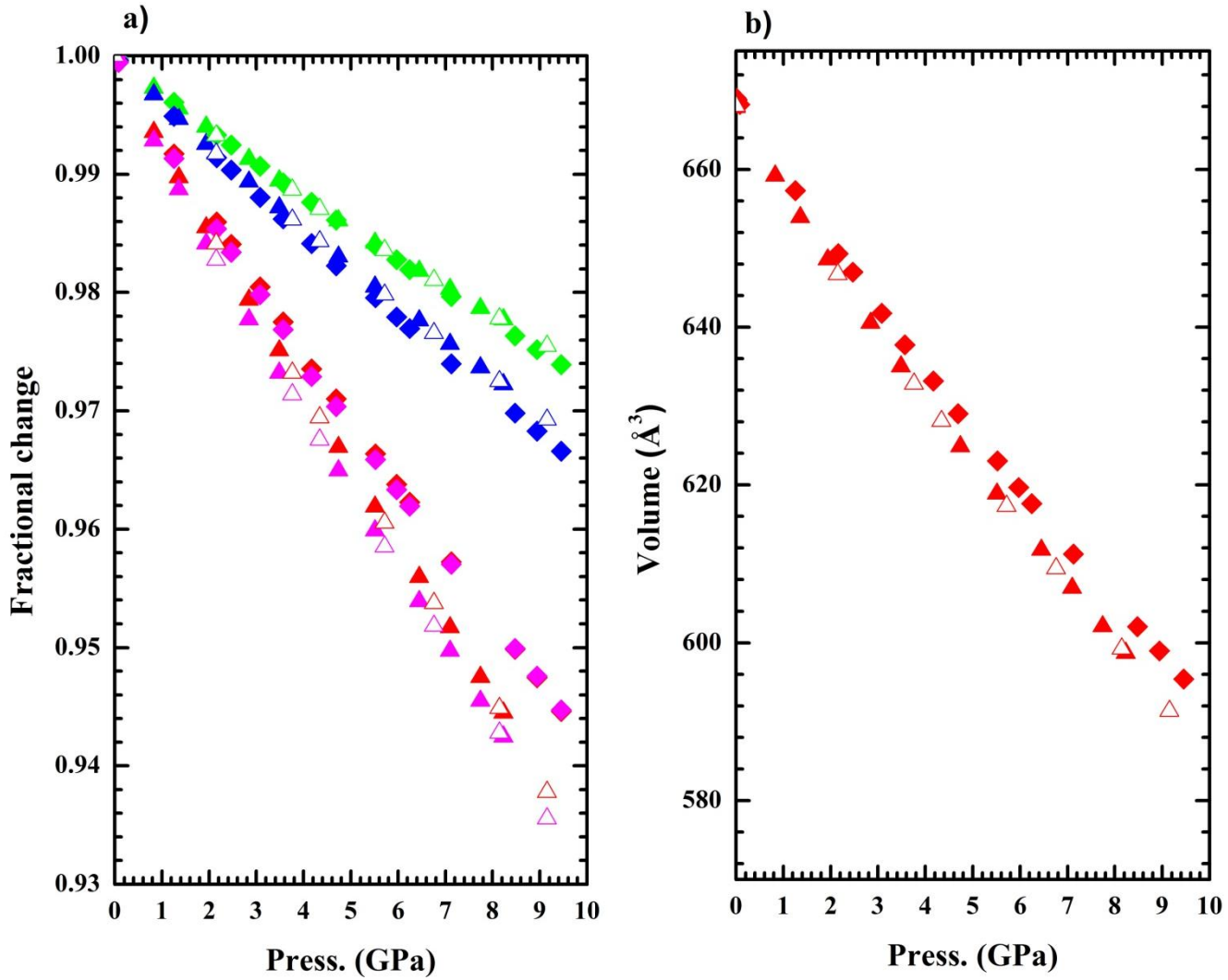

Notes. (a) The fractional change of *a* (red), *d(100)* (pink), *b*(green) and *c*(blue) versus pressure for An37 (solid diamonds) (Johnson 2007), An20 (Angel 2004b open triangles) and the Hawkb_A (An20) (solid triangles) .(b) The unit cell volume versus pressure An37 (Johnson 2007) (solid diamonds), An20 (Angel 2004b solid triangles) Hawkb_A (An20) (solid triangles). The estimated standard deviations on the unit cell volume are smaller than the symbols.

Figure 4.2. Unit cell angle changes at high-pressure for An20 and An37.

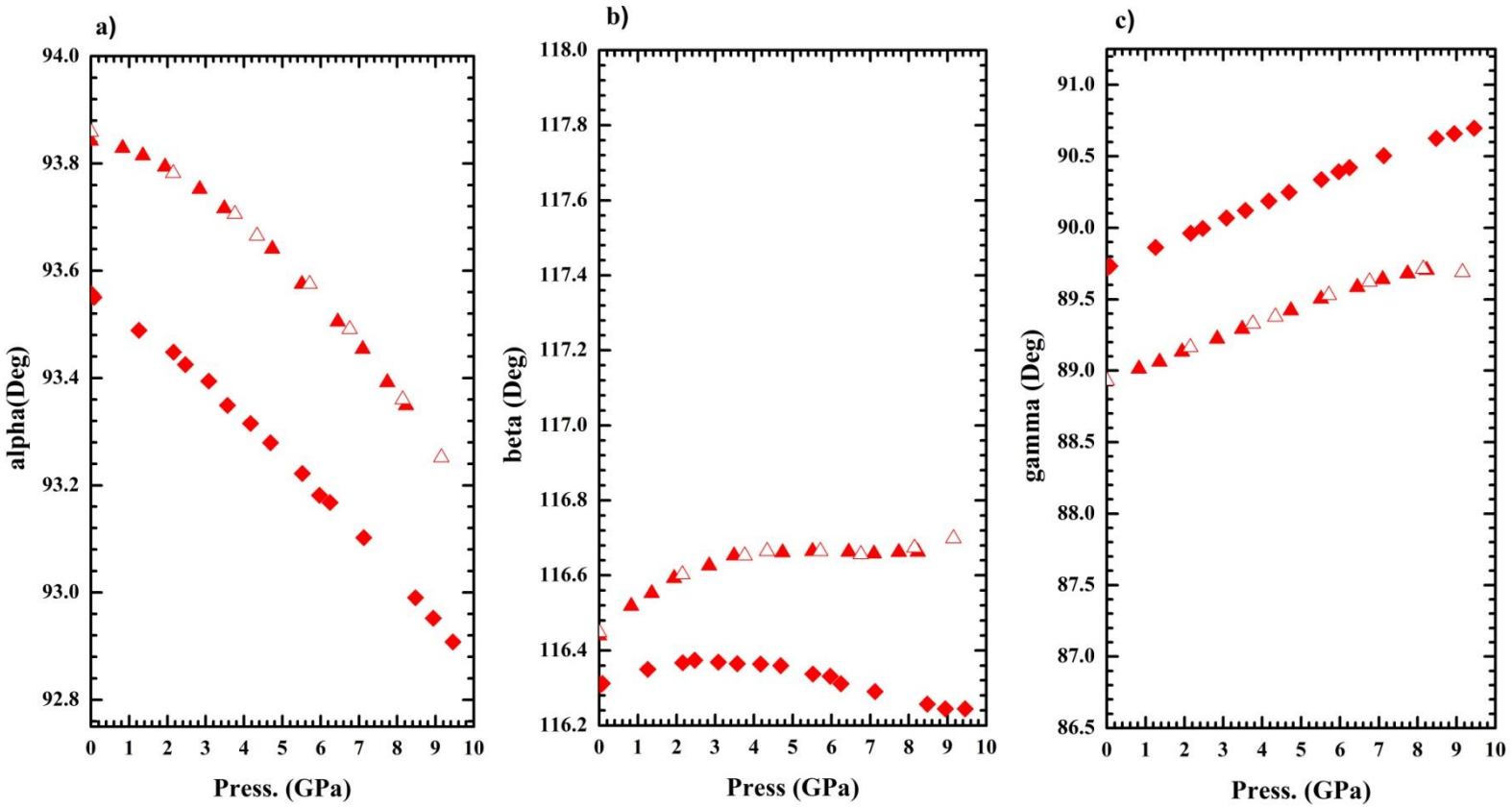

Notes. unit cell angles alpha (a), beta (b) and gamma (c) for An37 (Johnson 2007) with are the solid squares, An20 (Angel 2004b) which are the solid triangles, and the results of the experiment performed on Hawkb_A (An20) which are the open triangles. The estimated standard deviations on the unit cell volume are smaller than the symbols.

Figure 4.3. A pressure-volume plot with the measured *P-V* data for low albite, analbite, An20 and An37.

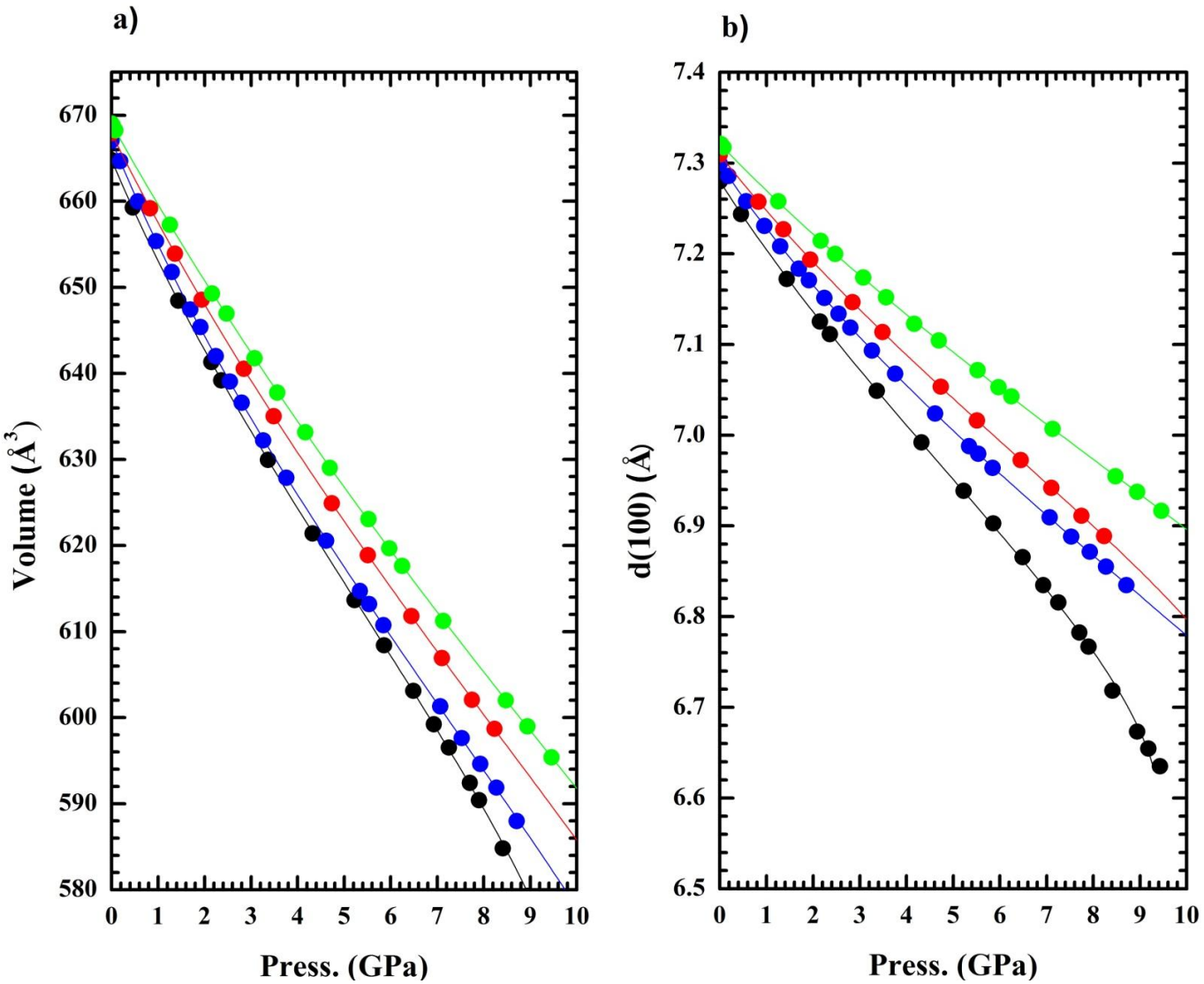

Notes. A pressure-volume plot with the measured *P-V* data (a) and calculated *d(100)* values (b) for low albite (Benusa *et al.* 2005) (black symbols), analbite (Curetti *et al.* 2010) (blue symbols), An20 (Angel 2004b) (red symbols) and An37 (Johnson 2007) (green symbols). All lines plotted in (a) and (b) are 4th order Birch Murnaghan equations of state fit to each data set. The values for *d(100)* for all samples were calculated using Cifreader.

Figure 4.4. *F*-f_E plots of the volume data for low albite, analbite, An20, and An37.

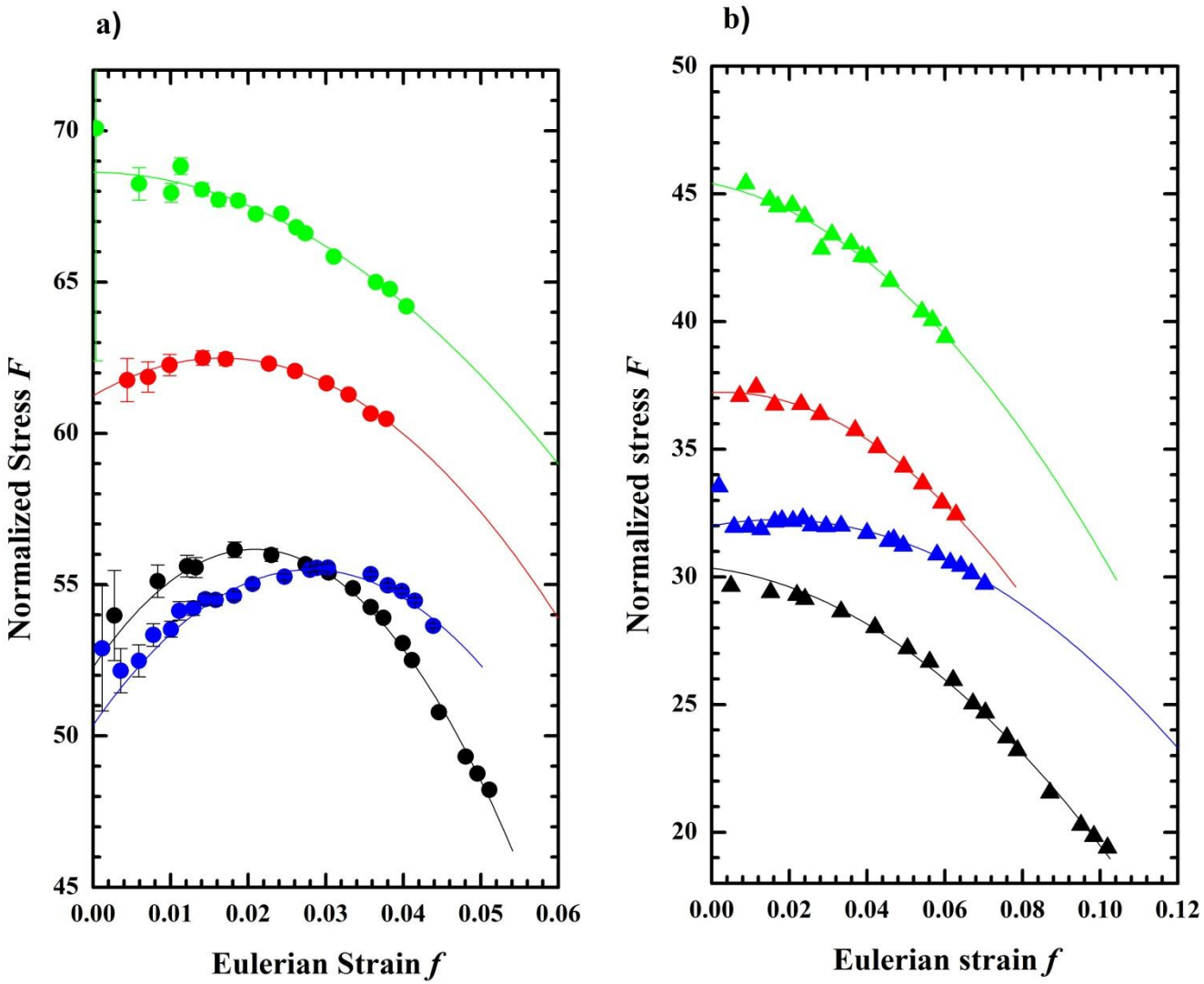

Notes. *F*-f_E plots of the volume data (a) and *d(100)* (b) for low albite (Benusa *et al.* 2005) (black symbols), analbite (Curetti *et al.* 2010), An20 (Angel 2004b) (red symbols) , and An37 (green symbols) (Johnson 2007). All lines are 4th-order Birch Murnaghan equations of state fit to the data.

Figure 4.5. The bulk moduli versus pressure for low albite, analbite, An20 and An37.

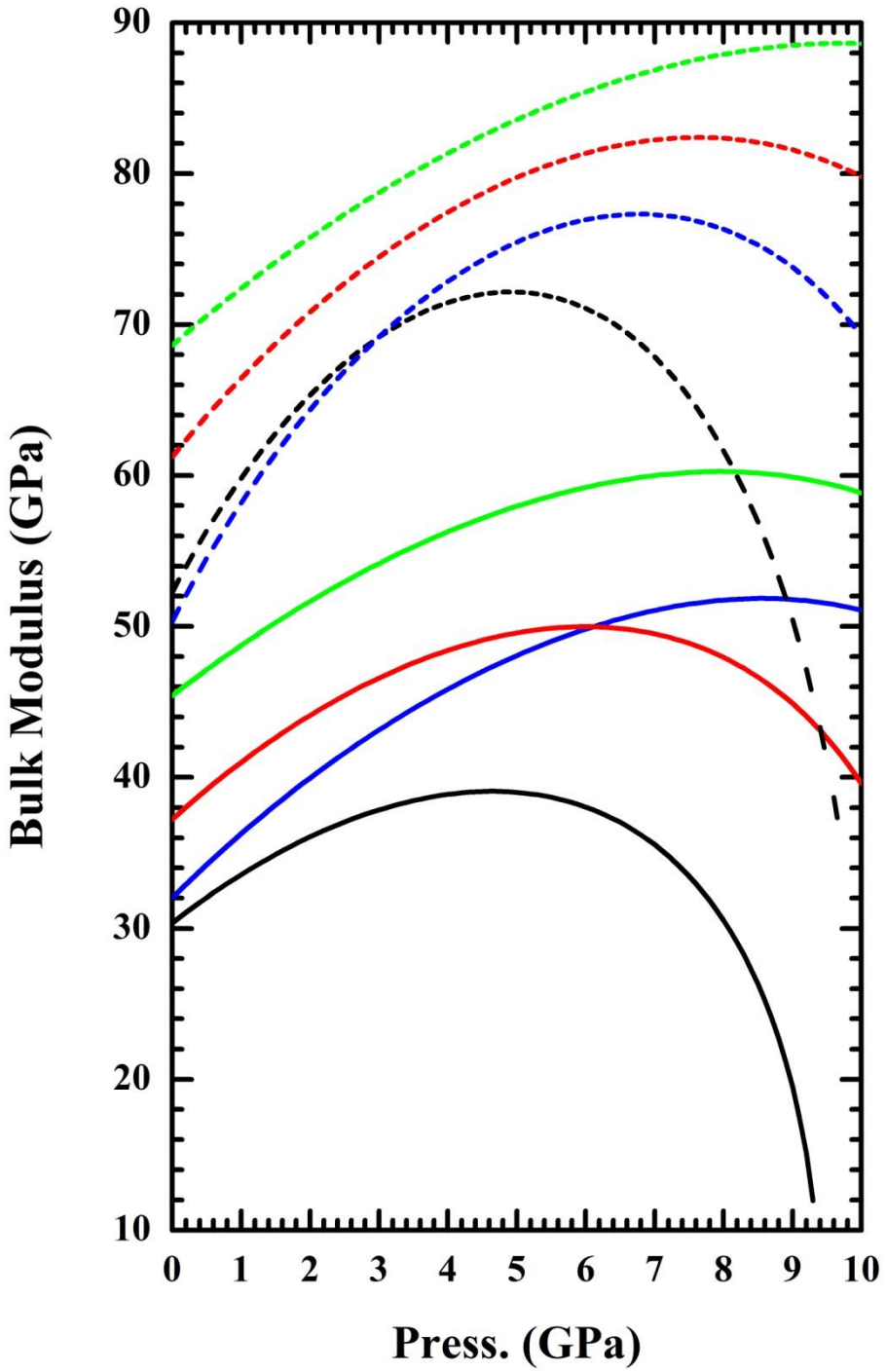

Notes. The bulk moduli versus pressure for low albite (black), analbite (blue), An20 (red), An37 (green) generated by EoSfitv5.2. The dashed lines represent the bulk moduli for volume and the solid lines represent the bulk moduli for d(100)

4.3.4 Structural evolution with pressure for An20 and An37.

The T-O-T angles for An20 and An37 behave similarly from room pressure to the maximum pressure measured for both samples (Figure 4.6). Some of the T-O-T show a significant change in angle with pressure (*e.g.* T-Obo-T and T-Oco-T) while others show very little change (*e.g.* T-Oa1-T and T-Oa2-T). The T-Oco-T shows the greatest change with a decrease in value as pressure increases for both An20 and An37 (Figure 4.6 a and b). This trend is also observed for low albite and analbite (Figure 4.6 c and d) but the change is much more drastic than with An20 and An37 in this study. Interestingly, the changes with respect to the T-O-T angles associated with the 4-ring parallel to the 010 plane (T-Obo-T, T-Obm-T, T-Odo-T, and T-Odm-T) behave differently for An37, An20, low albite and analbite. For analbite, the T-Obm-T and T-Odm-T show a convergence towards a common angle starting at 8GPa and the T-Obo-T and T-Odo-T both begin to show a slight decrease (Figure 4.6 c and d). For low albite, both T-Obm-T and T-Odm-T decrease dramatically at 6 GPa while the T-Odo-T begins to increase dramatically at this pressure and the T-Obo-T begins to have a dramatic decrease starting at 4 GPa. The T-Obm-T and T-Obo-T angle begins to decrease slightly and the T-Odm-T and the T-Odo-T begins to increase slightly with increasing pressure between 8-9 GPa for An20 and An37. While there is some evidence for unique evolution of structure with pressure for An20, An37, analbite and low albite seen in these T-O-T angles, there is no clear systematic change. Furthermore, the changes seen in these angles cannot account for the extreme anisotropy seem in Ab-rich plagioclase feldspars.

Figure 4.6. the T-O-T angles at high-pressures for An20(a), An37(b), low albite(c) and analbite(d).

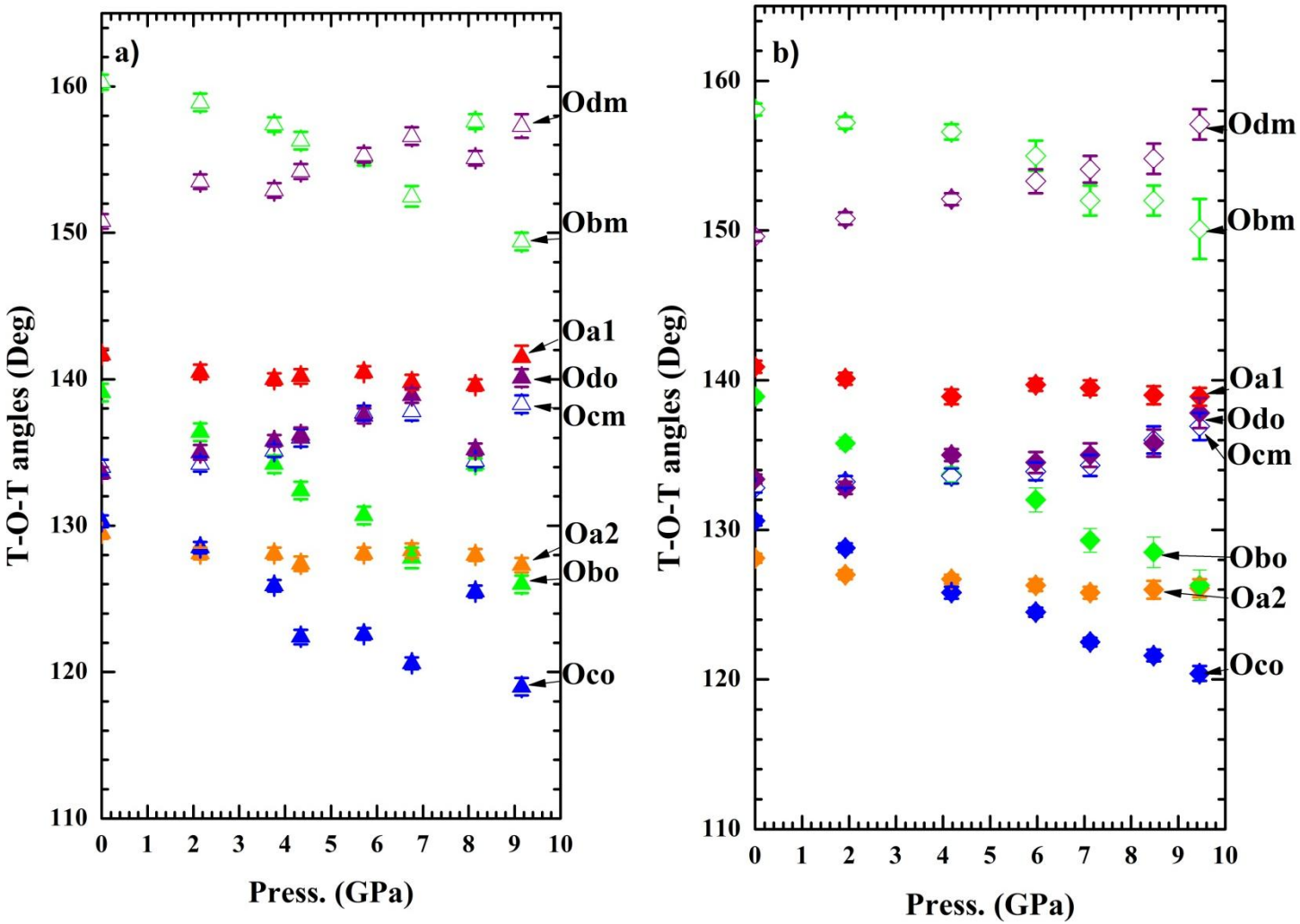

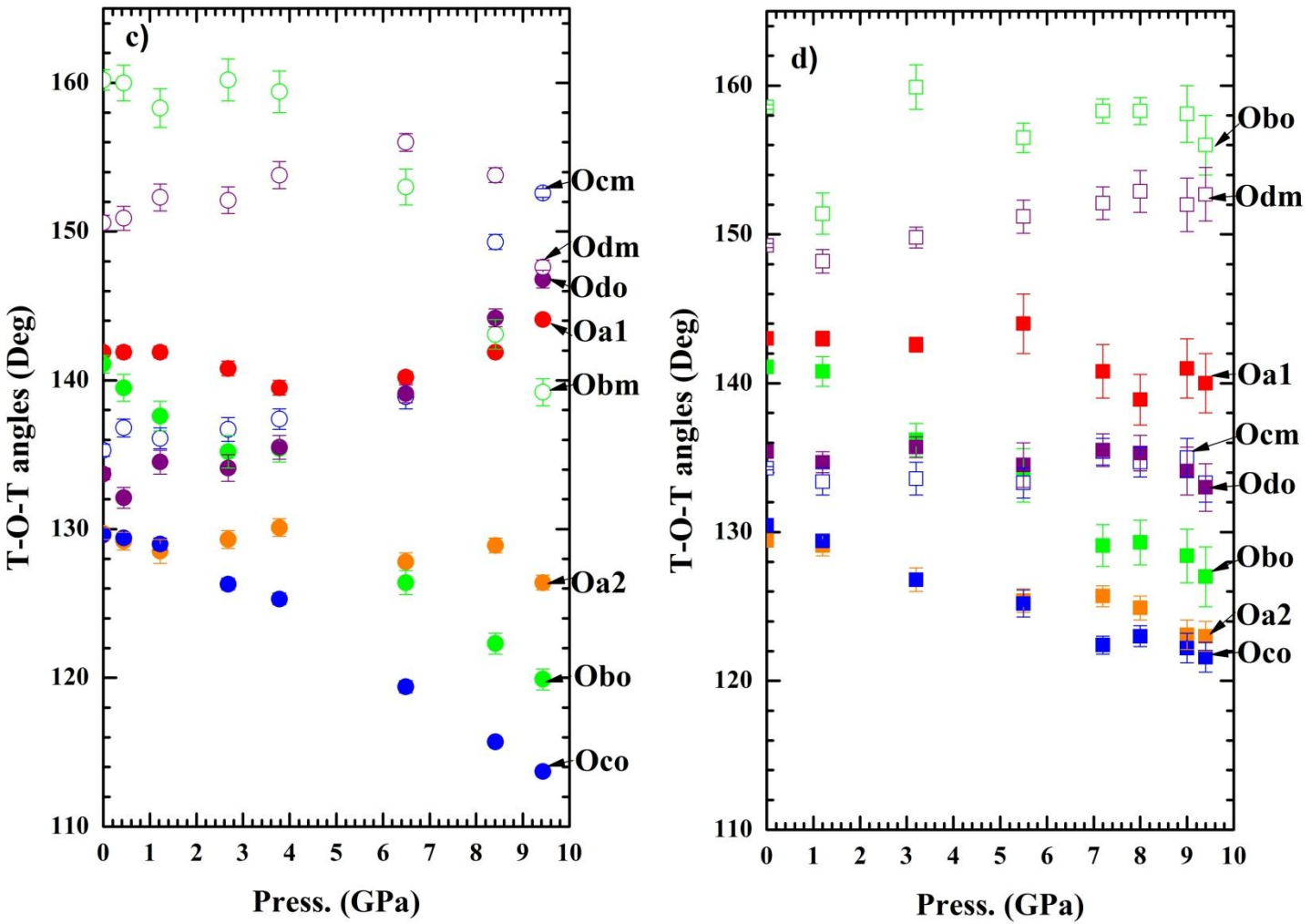

Notes. the T-O-T angles for An20(a) from room pressure to 9.15 GPa, An37 (b) from room pressure to 9.457 GPa, low albite (c) from room pressure to 9.43 GPa and analbite (d) from room pressure to 9 GPa.

A more systematic approach to describe the evolution of structure with pressure for feldspars involves the tetrahedral tilt system model described in detail in Chapter 3. Figure 4.7 shows the values of the four unique tilting systems calculated from the refined structures of low albite, analbite, An20 and An37 as a function of pressure. The evolution of tilt systems 1 and 2 are very similar to the changes seen in alkali feldspars as a function of P, T or change in composition; tilt 1 shows very little variation with pressure and only at the highest pressures does the albite structure exhibit a small increase in this tilt. Tilt system 2 (Figure 4.7b) shows a small decrease of tilt angle with increasing pressure for all of the samples with the greatest change seen in analbite. The evolution of tilt system 3 (Figure 4.7c) with increasing pressure for all compositions shows a uniform decrease in tilt angle (similar to that of tilt system 2 but it is more dramatic) from room pressure to around 6 GPa for all samples. Between 6-7 GPa there is an onset of significant change in this tilting angle for all compositions. Low albite and An20 both exhibit an increase in tilt 3with increasing pressure beyond 6-7 GPa with a larger increase for low albite. Analbite behaves like An37 with a decrease in tilting angle with pressure beyond 6 GPa. Up to ~4 GPa, tilt system 4 shows very little variation in any sample, consistent again with the pattern in alkali feldspars. But above 5 GPa albite, An20 and An37 all show a dramatic decrease in the value of this tilt to large negative values, while the tilt in analbite changes very little.

Figure 4.7. The four tilting systems at high-pressures for low albite, analbite, An20 and An37.

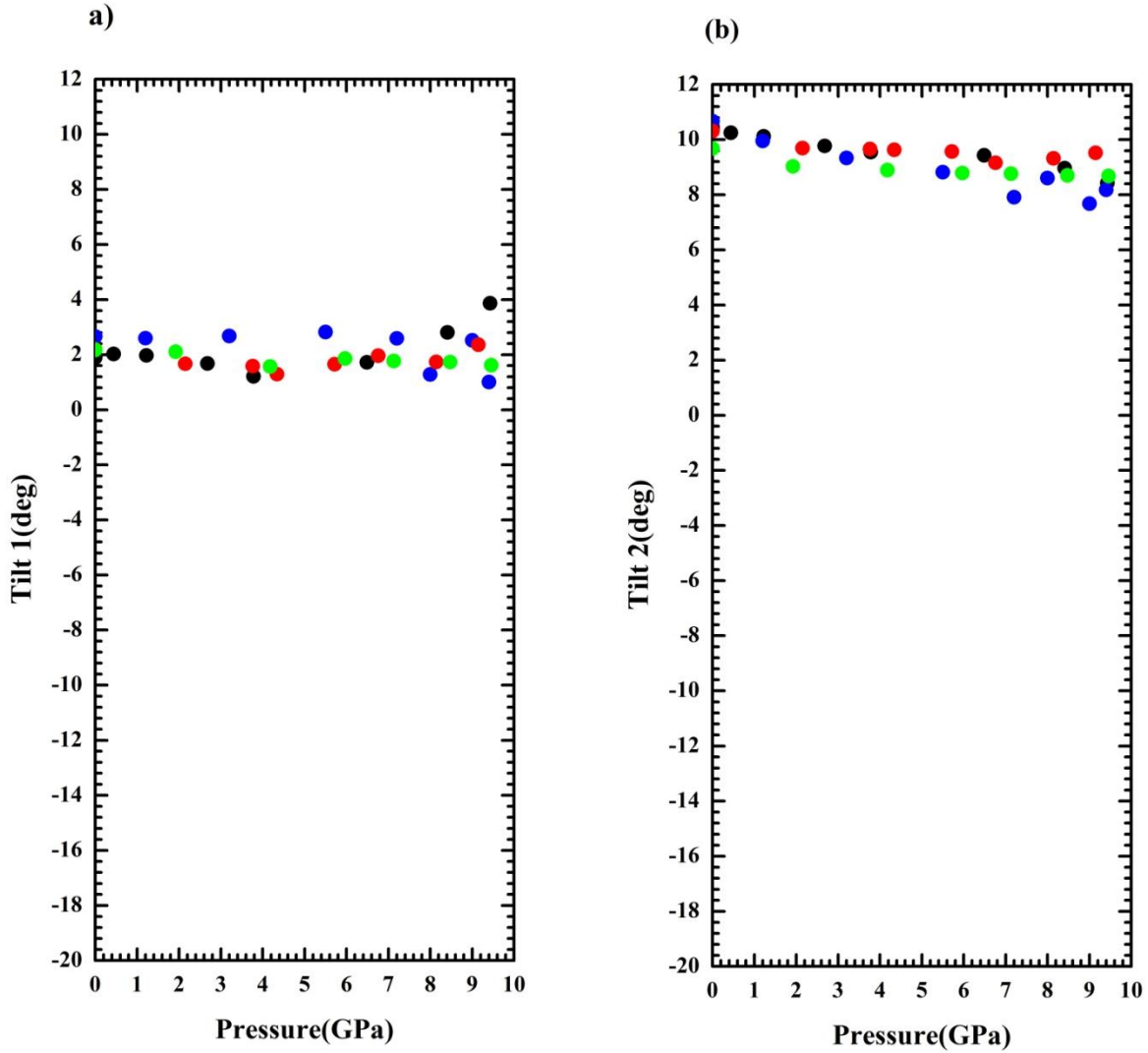

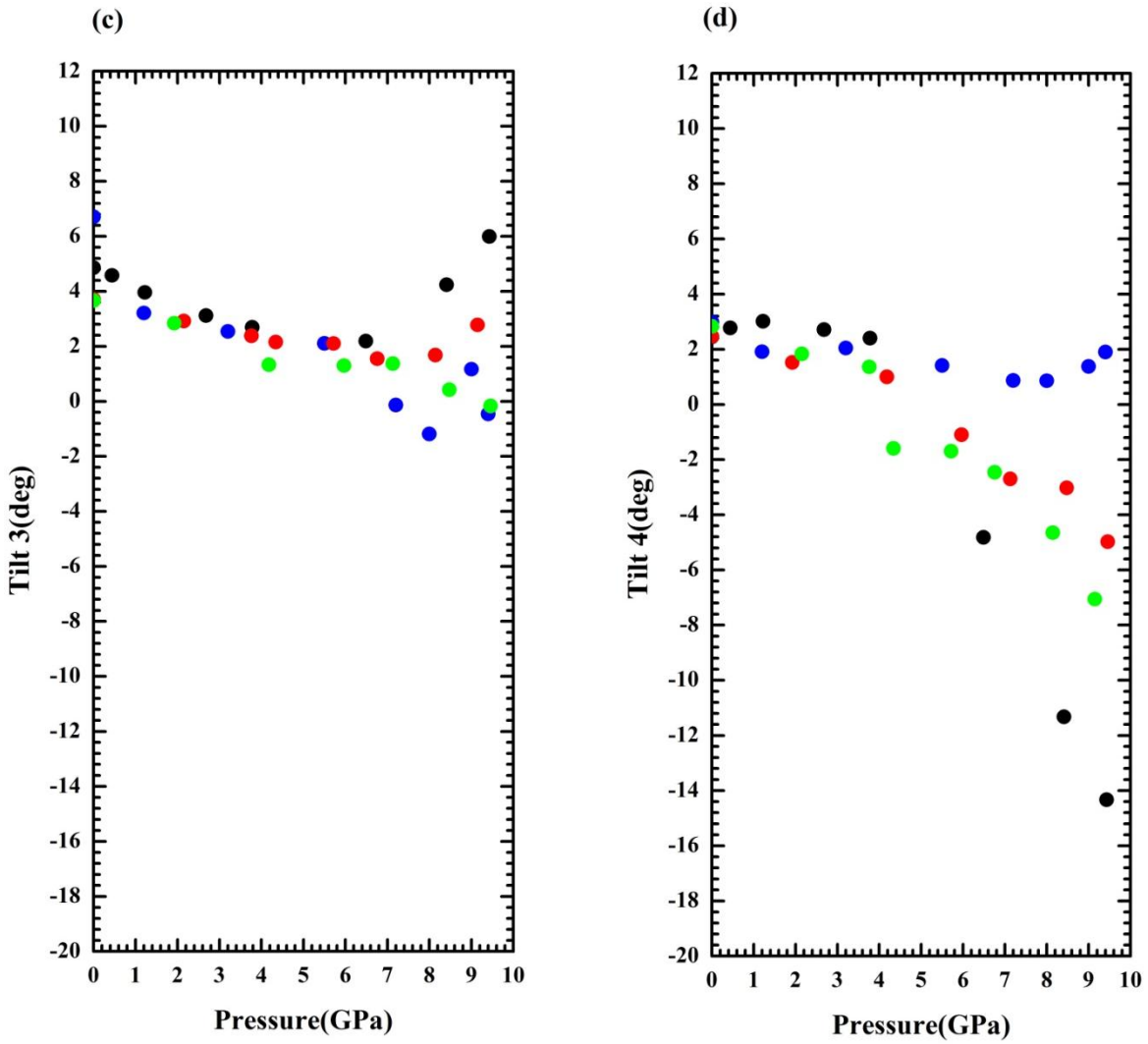

Notes. low albite = black symbols, analbite = blue symbols, An20 = red symbols and An37 = green symbols.

Figure 4.8. Linear strain in Cartesian directions X, Y and Z from chapter 3 of this thesis with the values for An20 and An37 added from this chapter.

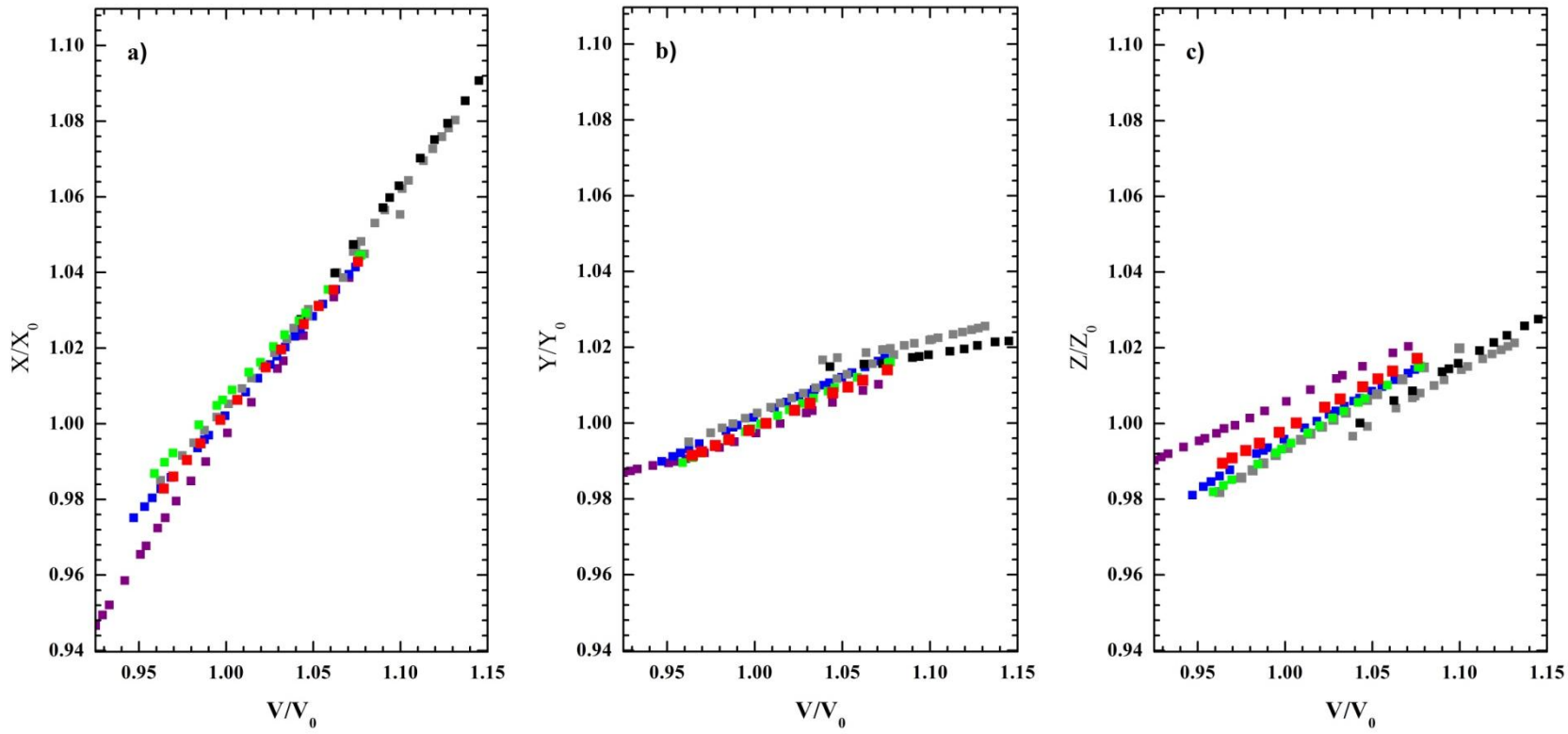

Notes. Black symbols = Al,Si ordered alkali feldspars from chapter 3, gray symbols = Al,Si disordered alkali feldspars from chapter 3, purple = low albite from this chapter, blue symbols = analbite from this chapter, red symbols = An20 from this chapter, green symbols = An37 from this chapter.

4.4 Discussion

The albite-rich feldspars at high-pressures presented in this chapter exhibit both similarities and differences compared to alkali feldspars presented in Chapter 3.

4.4.1 Unit-cell strains

While it is clear from Figures 4.1 and 4.2 that the general pattern of unit-cell compression of Na-rich plagioclase is similar to that of the alkali feldspars, as represented by albite, the anisotropy of the structure is better understood in terms of the linear strains in three perpendicular directions, as defined and plotted for the alkali feldspars in Figure 3.2c. Figure 4.8 is the same plot split in to three parts with the high-pressure data added. It can be deduced that the anisotropy seen in analbite, An20 and An37 is very similar to that of the alkali feldspars. Over the entire pressure range (from room pressure to 9 or 10 GPa) the strain of the *d(100)* or Cartesian *X*-axis is the greatest in magnitude indicating that the *d(100)* (*X*) is still the direction of greatest change upon compression. Despite this general trend, there are some differences in the linear strains in Figure 4.8. The strain for length *d(100)* (figure 4.8a) of An20 and An37 follows the same linear trend as that of the alkali feldspars described earlier in chapter three (this includes low albite and analbite). However, the strain of *d(100)* vs. the volume strain for low albite deviates from the general trend at values of V/V_o below 1.03 – 1.04 which corresponds to a pressure of about 2.1 GPa. The corresponding pressures for V/V_o = 1.03 in the other samples are approximately 2.2 GPa for analbite, 2.8 GPa for An20, 3.1 GPa for An37, 3.9 GPa for anorthoclase, 7.1 GPa for sanidine and 6.6 GPa for microcline, but these other compositions do not show the strong deviation seen for albite. This deviation may be related to the softening seen in albite, and that it is not apparent for other samples because either they do not soften (e.g.

microcline, sanidine) or the amount of softening is less and occurs at higher pressures (e.g. An20 and An37; see fig 4.5).

For the perpendicular directions *Y* (*b*-axis) and *Z* (length of *c*.cos(α-90)) there is again a uniformity of behavior between the samples, but there are differences in the detailed evolution, especially for albite. The *Y*-direction does show a uniform difference (Figure 4.8b) in the high-pressure data from the behavior of the alkali feldspars – even though the compressional data for the K-rich feldspars (e.g Allan and Angel 1997; Scambos *et al.* 1987) fall along the trends for the changes of the alkali feldspars with pressure and composition. So, it appears that there is a change in the strain pattern at around 1.07-1.08 of the Li-feldspar volume, which actually corresponds to the volume of the structure of albite at room conditions. Such a change is consistent with the data in figures 5.2a and 5.2b from chapter 5, although it could not be proven without data for feldspars with compositions along the $(Na,Li)AlSi_3O_8$ join. The increase in slope of Y/Y_o with decreasing volume represents a small increase in the amount of strain accommodated by this direction that is the same for all four samples studied at high pressure.

For *Z* (Fig 4.8c), the relative slopes of the linear strain versus the volume strain are the same, meaning that the amount of compression of the structure accommodated by this direction is the same as in the alkali feldspars. There are apparent offsets with respect to the c-axis (strain on the length of *Z*); for low albite, analbite, An20 and An37, this volume strain interval corresponds to room pressure while for anothoclase is corresponds to a pressure of 1.1 GPa, microcline to 5.2 GPa and sanidine to 4.5 GPa. The offset of albite can be better explained in terms of a volume offset – the thermal expansion data of Tribuadino *et al.* (2010) and the trends of bulk moduli with density (Chapter 2) show that albite has a smaller volume than would be expected by extrapolation with composition from the unit-cell volumes of the plagioclases.

4.4.2 Linear strains and elastic softening

The pressures at which there is a change in the linear strains does not match up with the maximum in the *f-F* plot (Figure 4.4). The approximate pressure at which the maximum of the *f-F* plot occurs is 3.9 GPa for albite, 5.3 GPa for analbite, 3.4 for An20 and room pressure for An37. While it is clear that Na-rich plagioclase feldspars behave like that of alkali feldspars at low pressure and high-temperature, there is no clear correlation between linear strains seen in Figure 4.8 and the maxima of the *f-F* plots seen in Figure 4.4. This is expected as the maxima in the *f-F* plot corresponds to the pressure at which K' becomes 4, not to the point of softening (Figure 4.5) which is when K' = 0.

Figure 4.9. Variation of tilts with unit-cell volume.

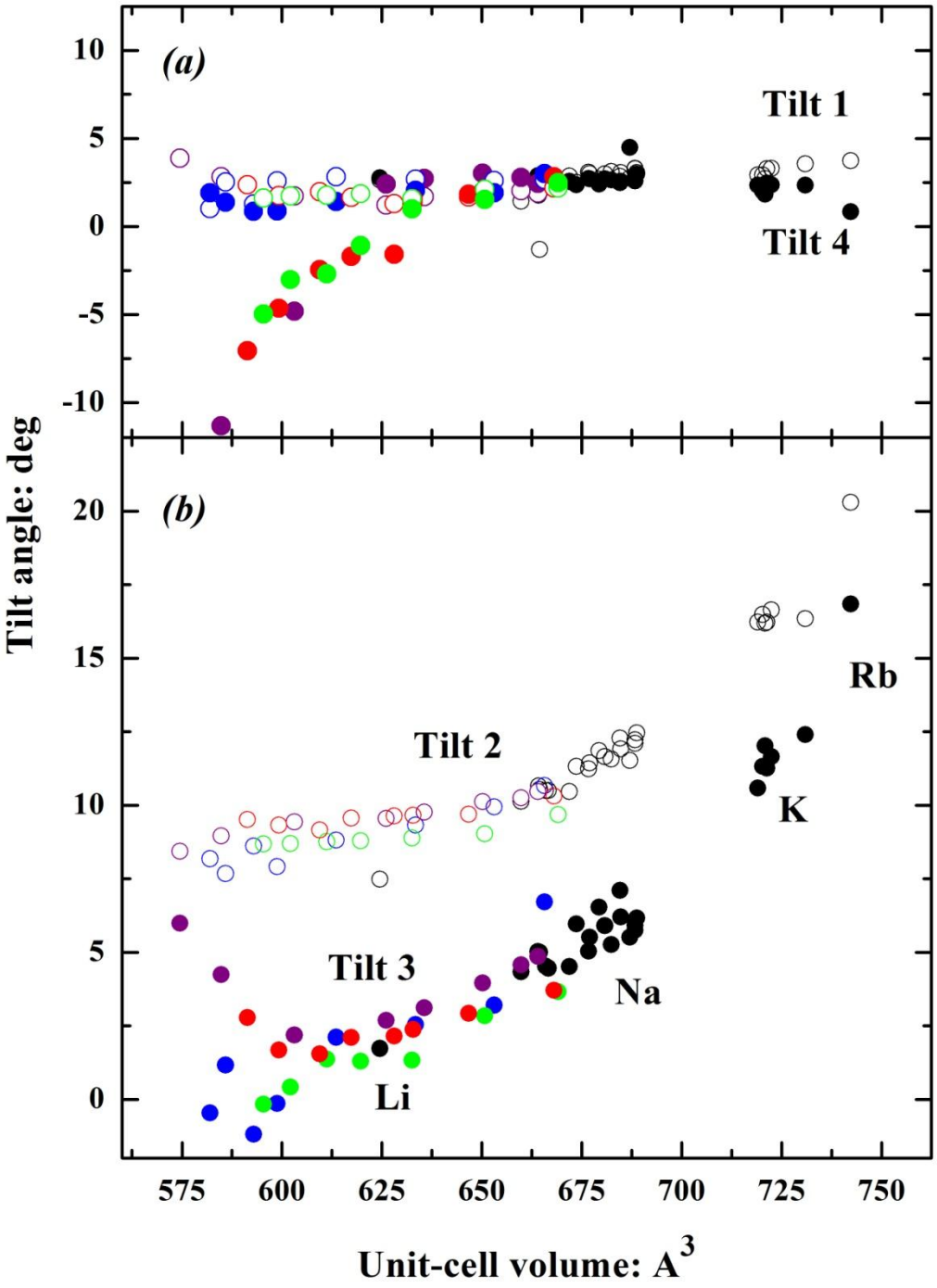

Notes. Black = alkali feldspars at low pressure taken from Figure 3.9, Purple = low albite,blue = analbite, red = An20 and green = An37.

4.4.3 Tilts

While it is clear from Figure 4.7 that there is some uniformity in the behavior of the albite-rich feldspars at high pressure, there are differences in the pressures at which the tilting patterns change. However, when the data are plotted against unit-cell volume, some clearer systematic changes are evident. Figure 4.9 is includes the data from Figure 3.9 with the added data points for the samples described in this chapter. Plotted in black are the alkali feldspars discussed in chapter 3 and the new plagioclase data are in colors. With the addition of high-pressure data (i.e. above 4 GPa), there are now two distinct intervals of tilting angles changing with volume. The achievement of the small volumes seen with the high pressure data appears to require additional mechanisms of compression. So, it is no surprise that the tetrahedral tilting behavior is different for the plagioclase samples with smaller volumes at higher pressures than with the alkali feldspars.

At unit-cell volumes at large volumes down to 625$Å^3$ (corresponding to about 4-5 GPa) tilt systems 2 and 3 dominate the structural change with a steady decrease in both tilt systems for both alkali feldspars and the Na-rich plagioclase feldspars from room pressure to about 4-5GPa. At volumes at 625 $Å^3$ and below, tilt systems 3 and 4 dominate the volume change. From 625$Å^3$ – 575$Å^3$, tilt system 4 starts off positive and progressively becomes more negative as volume decreases for low albite, An20 and An37. For analbite, this tilt remains constant. Tilt system 3 starts off positive and decreases with increasing volume for low albite and An20. For analbite and An37, tilt system 3 starts off at a small angle and becomes bigger as volume decreases for low albite and An20. For analbite and An37, this tilt angle decreases with decreasing unit-cell volume. Taking into account the volume requirement explained in Chapter 3, the trends described with respect to the volume and tilt system change makes sense. Tilt system 4 is at very

negative values for low albite, An20 and An37 at smaller volumes, exceeding the isolated tilt limit of -7° calculated for tilt 4 (Figure 3.5c). The -7 limit can be exceeded because tilt system 3 counters this effect. Tilt 4 decreases the Ob-Oa1 distance and Ob-Oco distance while the larger angles observed for tilt 3 at the small volumes increases these two distances.

For analbite and An37 in the 625-575 $Å^3$ regime, the story is a bit different; within the data scatter, tilt 3 does not show large deviations from the alkali trends. The slightly lower value of tilt 3 seen at high pressures (smaller volumes) in analbite and An37 is most likely due to the increased Al-content in the *T*-sites either due to compositionally induced Al,Si disorder (An37) or heat-induced Al,Si disorder (analbite). There is clearly a complex relationship with how tilt 3 behaves with respect the amount of Al in the *T*-sites because this tilt system involves a relative movement of all the symmetrically distinct *T*-sites.

The result shown in Chapter 3 demonstrates that the volume changes above 625 $Å^3$ are clearly dominated by tilt system 2 and 3 with little change in tilt system 1 and 4 for both the plagioclase samples analyzed in this chapter and the alkali feldspars from Chapter 3. So, it can be inferred that for feldspars at high pressure, the volume changes are mainly dependent on tilt system 3 and 4. This is in contrast to lower pressures and high-temperatures, where tilt systems 2 and 3 dominate. The common dominant tilt for both regions is tilt system 3, so there is a direct relation between the evolution of this tilt system with respect to activation of tilt system 4 and tilt system 2.

4.4.4 The effect of O-O repulsion on tilt systems

The limitations of the various tilting systems described in chapter 3 is dependent on non-bonded O-O repulsive forces and specific O-O distances get smaller with decrease in tilt systems 2 and 3. The Na-rich plagioclase feldspars show the same trends. For example, if the trends of

the alkali feldspar tilts are extended to tilt 3 = 0 and tilt 2 ~ 7.5, then this Ob-Ob distance would be reduced to 3.17 Å in the ideal model structure, significantly shorter than any non-bonded O-O distance in the alkali feldspars (except for Li-feldspar). The detailed evolution of the Obo-Obm and Odo-Odm distances in the real structures is complicated (Fig 4.10) and varies between the samples. In albite and An20 the Obo-Obm distance initially decreases rapidly and then becomes constant with pressure increase over 6 GPa, while in analbite and An37 the distances decrease to ~3.10 Å. The Odo-Odm distances across the pseudo-mirror remain more or less constant and do not decrease below 3.05 Å. Analbite is different from the other samples in that, the Odm-Odm distance across the inversion centre also decreases to 3.10 Å. Despite these variations, none of these O-O distances between different tetrahedra drop below 3.05 Å, and the specific behavior of Obo-Obm in albite and An20 (which show the most softening) strongly suggests that it must be these O-O repulsions that change the behavior of tilt 3 and activates tilt 4.

In fact, the behavior seen with respect to the Ob-Ob distance change with pressure is strikingly similar to that of the evolution of tilt system 3 with pressure. At 4 GPa, there is no further possibility of decreasing the tilt 3 without shortening the O-O distances rapidly, yet volume compression must be accommodated. Either a decrease in tilt 1 or tilt 4 could in principle accommodate this, but as noted in chapter 3 a decrease in tilt 1 reduces instead the Oa1-Oa1 distances, whereas the shear of the 4-ring represented by tilt 4 does not change any of the shortest distances. Therefore the activation of tilt 4 is a further consequence of the requirement of the structure to minimize the repulsions between the non-bonded oxygen atoms. The anisotropy of compression induced by tilt 4 alone (Figure 3.6d) is similar to that of tilts 2 and 3 together, so the overall pattern of anisotropy is maintained during further compression. Further, the fact that tilt 4 does not change the shortest O-O non-bonded distances means that tilt 4 does not

significantly increase the O-O repulsions, and there is no further increase in bulk modulus when it starts to operate. The fact that it leads to softening, along with a coupled change in the behavior of tilt system 3, must mean that the sum total of O-O repulsions, including those between more distant O-O pairs, must be slightly reduced compared to the lower-pressure regime.

Figure 4.11 shows these changes in a different way, as a plot of tilt 2 versus tilt 3 on the contour maps for volume and *d(100)* taken from Chapter 3. While the evolution of these tilts in An20 and an37 are close to the trends in the alkali feldspars, low albite diverts upwards to more positive tilt 3 than expected for the values of tilt 2 at higher pressures, while analbite deviates in the opposite direction.

Figure 4.10. Two of the shortest non-bonded O-O distances at high-pressures for low albite, analbite, An20 and An37.

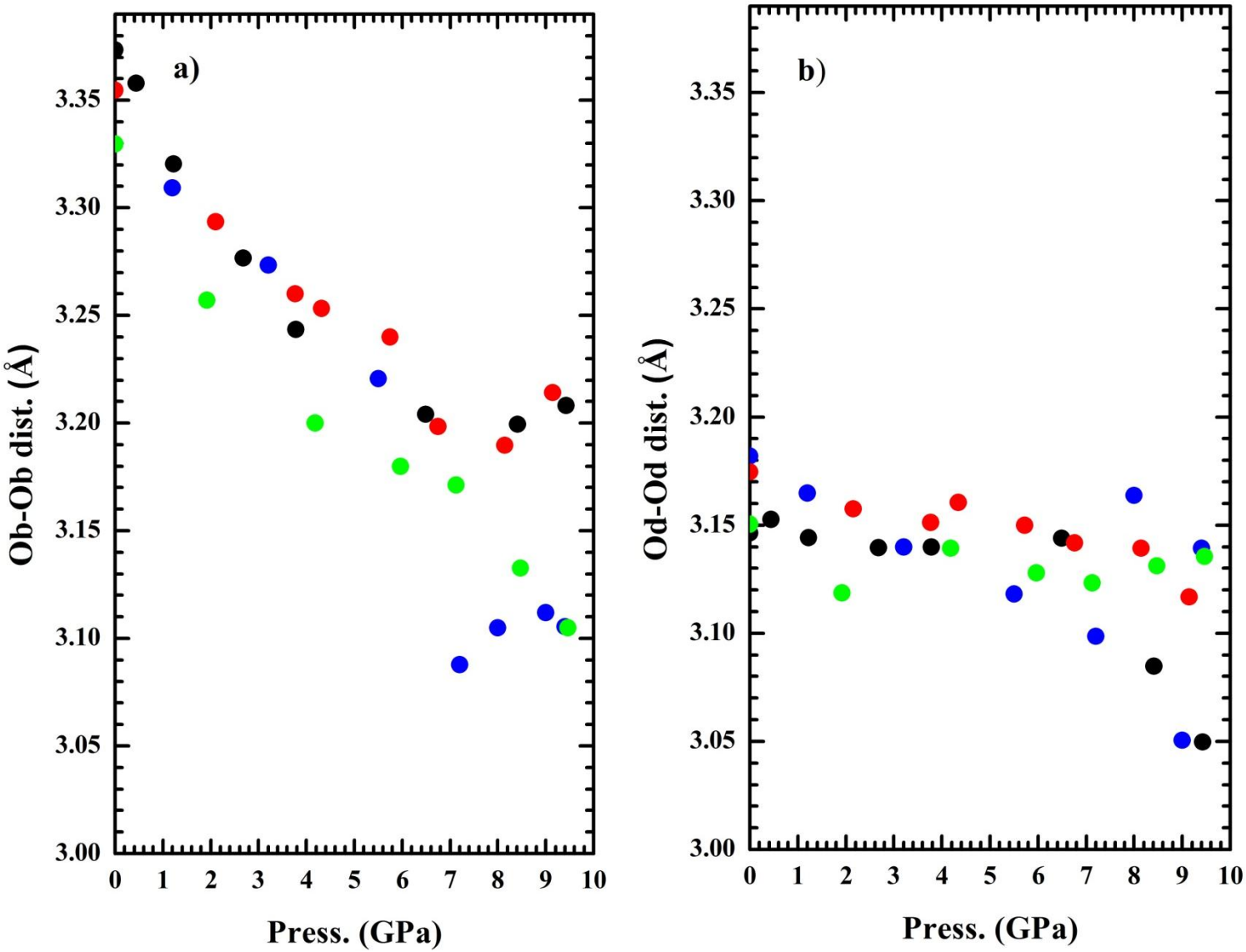

Notes. The Ob-Ob distances across the mirror plane (a) and the Od-Od distances across the pseudo mirror (b) versus pressure for low albite (black), analbite (blue), An20(red) and An37(green).

Figure 4.11. A portion of the tilt system 2 and tilt system 3 model from Chapter 3 contoured to the unit cell volume (a) and d(100) (b).

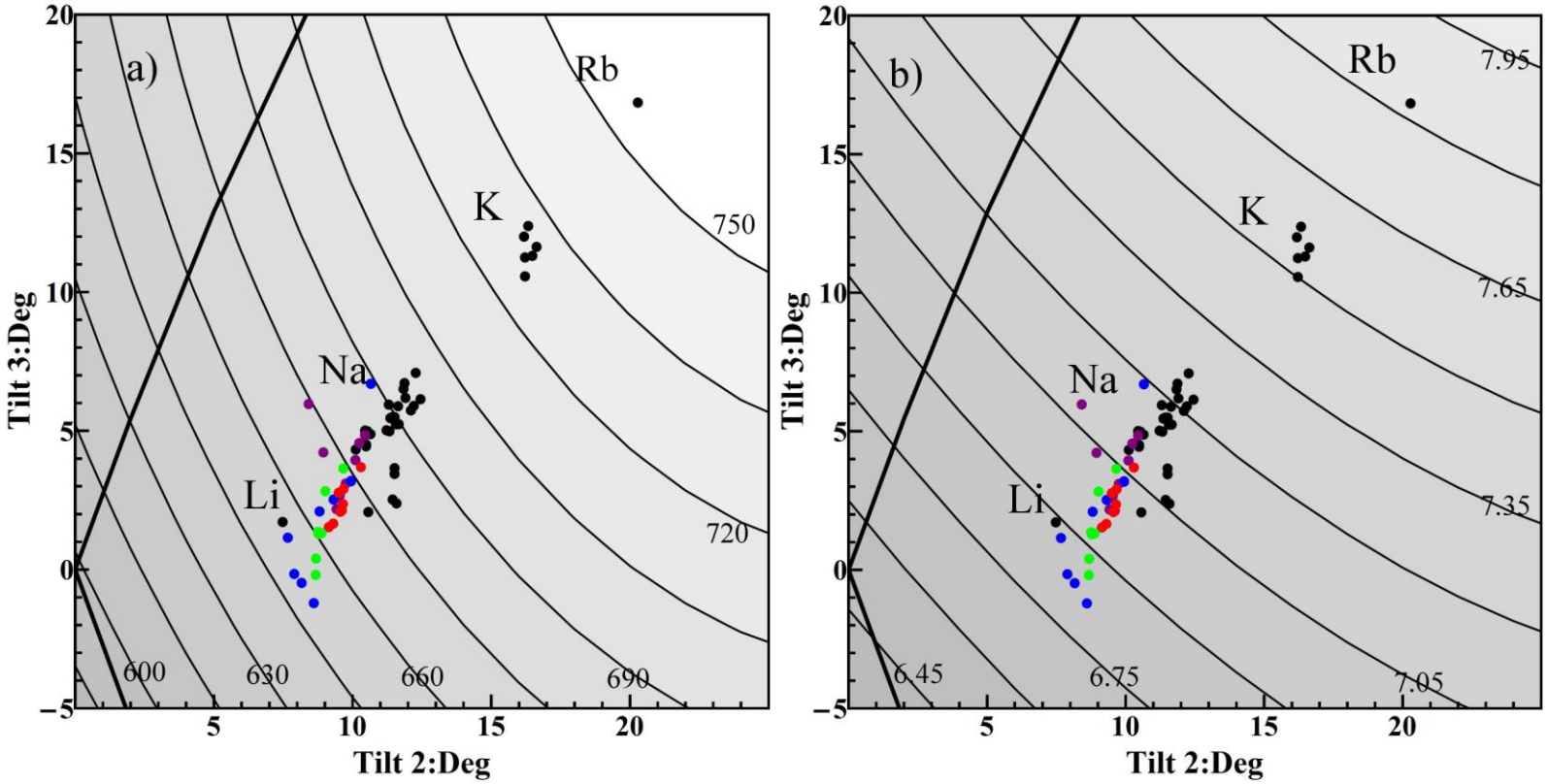

Notes. Black dots = low albite (Benusa *et al.* 2005), blue dots = analbite (Curetti *et al.* 2010), red dots = An20, green dots = An37 and purple dots = alkali feldspar results (also plotted in chapter 3).

4.5 Conclusions

The fact that we observe clear systematic trends in the tetrahedral tilting systems with pressure means that they are clearly a better means by which to describe the change of Na-rich plagioclase structures with pressure than with the changes of T-O-T angles. The analysis of the structural evolution of each of the samples in terms of tilts shows two distinct regimes that extend over different pressure ranges, and those pressure ranges are different for each sample. At low pressures and relatively large volumes, the dominant mechanism of compression is the reduction of tilts 2 and 3 at approximately the same rate with volume (Figure 4.9) as the alkali feldspars display. At about a cell volume of 625 $Å^3$ and below in the ordered samples tilt 4 decreases with decreasing volume. This does not happen in feldspars with significant disorder (analbite). For analbite, tilt 4 remains relatively unchanged up until 9 GPa and compression continues to be accommodated by a decrease in tilt 3 and tilt 2.

Therefore, the evolution of structure with pressure for Na-rich plagioclase and the anisotropy upon compression in the low-pressure regime can be predicted by the same analyses of tilts 2 and 3 used for the alkali feldspars. But the model just taking tilt system 2 and 3 into account does not properly predict the anisotropy of the structures at high pressures nor does it properly describe the structural reasons for elastic softening. It would also be a reasonable conclusion that the softening shown in albite and the plagioclase feldspars is associated with this change in tilting because the amount of change in tilt 4 decreases with increasing anorthite content, while the pressure at which softening initiates also increases with anorthite content.In addition, it is clear that shortening of the Obm-Obm and Odm-Odm distances across the mirror plane as a result of tilt systems 2 and 3 decreasing with increasing pressure for Na-rich

plagioclase provide a means for justifying the activation of tilt system 4 and change of behavior in tilt system 3 at higher pressures in the ordered samples.

Finally, the unique behavior of the analbite and, to some degree, An37 from the ordered samples, points to an influence of factors outside of our simple model of tilting of rigid tetrahedra under monoclinic symmetry. Clearly the redistribution of Al and Si affects both the detailed size and distortions of the tetrahedra and thus the O-O distances at a given value of tetrahedral tilt, and thus it is to be expected that the distortions accompanying Al/Si exchange will influence which tilt systems operate under high compression.

4.6 References

Allan, D.R. and Angel, R.J.(1997) A high-pressure structural study of microcline ($KAlSi_3O_8$) to 7 GPa. *European Journal of Mineralogy*. **9**: 263-275.

Angel, R.J. (2003) Automated profile analysis for single-crystal diffraction data. *Journal of Applied Crystallography*, **36**: 295-300.

Angel, R.J. (2004a) Absorption corrections for diamond-anvil pressure cells implemented in a software package Absorb-6.0. *Journal of Applied Crystallography*, **37**: 486-492.

Angel, R.J. (2004b) Equations of state of plagioclase feldspars. *Contributions to Mineralogy and Petrology*, **146**: 506-512.

Angel, R.J. and Finger, L.W. (2011) Single: a program to control single-crystal diffractometers. *Journal of Applied Crystallography*, **44**: DOI: 10.11007/S0021889810042305.

Benusa, M., Angel, R.J., Ross, N.L. (2005) Compression of albite, $NaAlSi_3O_8$. *American Mineralogist*, **90**: 1115-1120.

Curetti, N., Sochalski-Kolbus, L.M., Angel, R.J., Benna, P., Nestola, F., Bruno, E. (2010) High-pressure structural evolution and equation of state of analbite. *American Mineralogist*, **96**: X-X.

Downs, R.T., Hazen, R.M., Finger, L.W. (1994) The high-pressure crystal chemistry of low albite and the origin of the pressure dependency of Al-Si ordering. *American Mineralogist*, **79**: 1042-1052.

Downs, R.T., Yang, H. Hazen, R.M., Finger, L.W., Prewitt, C.T. (1999) Compressibility mechanisms of alkali feldspars: new data from reedmergnerite. *American Mineralogist*, **84**: 333-340.

Farrugia, L.J. (1999) *WinGX* suite for small-molecule single-crystal crystallography. *Journal of Applied Crystallography*, **32**, 837-838.

Johnson, E. (2007) *The elastic behavior of plagioclase feldspar at high-pressure*. MS thesis, Virginia Polytechnic and State University, USA.

King, H.E. and Finger, L.W. (1979) Diffracted beam crystal centering and its application to high-pressure crystallography. *Journal of Applied Crystallography*, **12**: 374-378.

Kroll, H. and Ribbe, P.H. (1980) Determinative diagrams for Al,Si order in plagioclases. *American Mineralogist*, **65**: 449-457.

Nestola, F., Curetti, N., Benna, P., Ivaldi, G., Angel, R.J., and Bruno, E. (2008) Compressibility and high-pressure behavior of $Ab_{63}Or_{27}An_{10}$ anorthoclase. *The Canadian Mineralogist*, **46**: 1443-1454.

Pavese, A., Artioli, G. (1996) Profile-fitting treatment of single-crystal diffraction data. *Acta Crystallographica*, **A52**: 890-897.

Scambos, T.A., Smyth, J.R. and McCormick, T.C. (1987) Crystal structure refinement of high-sanidine from the upper mantle. *American Mineralogist*, **72**: 973-978.

Chapter 5: The effect of temperature on tetrahedral tilting in C-1 Ab-rich plagioclase feldspars

5.1 Introduction

The structures of framework minerals typically respond to changes in temperature by the tilting of the strongly-bonded polyhedra, with little change in the internal geometry of the individual polyhedral (Ross, 2000). For example, high-quality powder structures at room temperature and high temperatures were obtained for other framework minerals such as sodalite –group minerals (Hassan and Grundy 1984; Hassan *et al.* 2004) and danalite (Antao *et al.* 2003) from Rietveld refinement. For danalite, Antao and authors looked at small changes in the relative tilting of the BeO_4 and SiO_4 tetrahedra defined in Hassan and Grundy (1984) from 33°C-1000°C. For sodalite, relative tilting of the SiO_4 and AlO_4 tetrahedra was observed and was accounted as the greatest factor in the volume expansion from 28°C – 982°C. Several other zeolites have been studied at high temperature as well to describe the effect of dehydration on the structural response to increasing temperature (Cruciani, Artioli *et al.* 1997; Fisher *et al.* 2008; Ori *et al.* 2009; Lee *et al.* 2011; Wadoski *et al.* 2011). Some of this involves several phases of structural response with the greatest change seen in the framework cavity and twisting of the tetrahedra once the structure is relatively dehydrated.

Similarly, feldspathoids have been studied at high and low temperature, with the observations on the structural change being particular T-O-T bond angles changing as a result of the tilting of the effectively rigid tetrahedra (*e.g.* Gatta *et al.* 2010; Angel *et al.* 2008). The changes in the structure of albite was originally described by relationships with the *M*-site cation environment with its surrounding oxygen atoms (Kroll *et al.* 1980). In addition, a framework "collapse" around this *M*-cation was characterized by the relative movements of the oxygen atoms surrounding the cavity with respect to one another (Winter *et al.* 1977; Kroll *et al.* 1980).

Other proposed factors involved in the structural change of albite with temperature included the isotropic displacement factors on the individual oxygen atoms around the *M*-cavity in relation to the distance to the *M*-cation (Prewitt *et al.* 1976). Although there are significant changes with the *M*-site geometry and displacement ellipsoid of the *M*-cation as temperature is increased, this does not provide an unambiguous explanation for the changes observed in the plagioclase structure with temperature. Recent work uses a model that involves the relative tilting of the individual tetrahedral in the four-ring parallel to the (010) direction to be able to predict the anisotropy seen in alkali feldspars at ambient conditions (*e.g.* Chapter 3 of this thesis). At non-extreme temperatures and pressures (up to 4GPa), the anisotropy of feldspars and other essential features of the framework can be predicted by the application of 2 of the 4 individual tilting systems (tilt system 2 and 3) while the other two (1 and 4) play a secondary role in modifying the basic pattern of the anisotropy. The use of models showed that the tilts seen in real structures maximize the shortest O-O distances in the structure and that O-O repulsion control of the tetrahedral tilting. These O-O short distances were analyzed in monalbite and analbite at high-temperature (Kroll *et al.* 1980) but the resulting responses of the structure were not systematically documented until the tetrahedral tilting systems were further quantified in Chapter 3 of this thesis.

Recent developments in X-ray diffractometry include high-resolution synchrotron radiation powder diffraction that enables the accurate detection and analysis of subtleties in volume expansion and detailed evolution of crystal structures with temperature, pressure and composition. Such data were used by Tribaudino *et al.* (2010) who determined the unit-cell parameters and thermal expansion coefficients of plagioclase feldspars from room temperature to 944K across the compositional join and that of Tribaudino *et al.* (2011) who used the data from

90-200K to model the low-temperature thermal expansion and determine the implications for the heat capacities of plagioclase feldspars.

It is clear from Tribaudino *et al*. (2010) that the anisotropy seen at low and high temperatures is more prevalent in *C-1* than *I-1* feldspars and the thermal expansion coefficient changes at a greater rate with composition for *C-1* feldspars for which the reasons are still unclear. Until now, no structural refinement on non-end-member *C-1* plagioclase feldspars has been performed on powdered mineral samples or single crystals at non-ambient temperatures. In this work, two studies were performed to analyze the tilt systems described in Chapter 3 with respect to Ab-rich plagioclase feldspars at high temperature in attempt to better understand the anisotropy in plagioclase feldspars at high temperature. The first was to use the Rietveld refinement method on high-resolution powder diffraction data from 90K to 944K on end-member and non-end-member Ab-rich *C-1* plagioclase feldspars (collected by Tribaudino *et al.* 2010). The second was single-crystal X-ray diffraction performed on a Ab-rich ordered plagioclase (An26) crystal from room temperature to 1023K. The single-crystal data is used as a cross-check for the high-resolution powder data of similar composition. These two studies are combined to investigate whether the tilt systems are a reliable model to describe the thermally-induced structural changes that *C-1* plagioclase undergoes at low and high temperatures.

5.2 Experimental

5.2.1 High-resolution high-temperature powder X-ray diffraction

High resolution powder diffraction was performed on 9 well-characterized plagioclase samples with compositions chosen to span the plagioclase join. The original data were reported by Tribaudino *et al.* (2010, 2011) and used to determine the evolution of the unit cell parameters of the samples with temperature, but not the structures. Experiments were done at the ESRF

beam line ID31 over a temperature range of 298K to 935K at steps of 3-5 K from 298-477 and 10K from 450-935. There were a total of 9 detectors present each covering 2° 2θ. To minimize the instrumental contributions to the widths of the diffraction lines, the measurements were carried out at a wavelength of 0.40006(4)Å using a 2.0 mm^2 incident beam size. Measurements between 298K and 477K were performed using Oxford Cryosystems 700-series nitrogen cryostream of which the temperature was continuously ramped at 2°K per minute. The measurements between 450K and 935K were performed using a hot air blower of which the temperature was continuously ramped at 1.4°K per minute. The samples were spun at high speed to ensure reasonable powder averaging. The nominal temperatures of the samples in the hot air blower were corrected by cross-calibration to a single-crystal measurement of albite. For details see Tribaudino *et al.* (2010) and Tribaudino *et al.* (2011).

5.2.2 High- temperature single crystal X-ray diffraction on An27/An26

The sample that was chosen for high-temperature single-crystal X-ray diffraction was a 27 percent anorthite plagioclase which was previously studied in Carpenter *et al.* (1985) for calorimetric studies. The sample's provenance is a pegmatite from the head of Little Rock Creek, North Carolina of which most samples were found to be homogeneous. The chemical mean composition is An27Or2Ab71 where An = %Ca, Or = %K and Ab = %Na as determined by electron microprobe analysis (Carpenter *et al.* 1985). A 150μm X 90μm X 30μm piece was chosen and was checked to make sure it was not twinned with a polarizing microscope. The crystal was mounted on an Agilent Gemini diffractometer with MoKα radiation and a graphite monochromator. This instrument is equipped with an EoS CCD detector. The crystal was screened for spot quality with exposure time set to 15 seconds at 50kV and 40mA and 96 percent of the resulting reflections were indexed.

The sample was then carefully placed in a 0.3 millimeter quartz capillary of which was sealed off at the tip (24 mm long from base of capillary to tip) with quartz-glass wool. The capillary was mounted on a Huber goniometer head of which was mounted onto a Phillips PW-1100 four-circle diffractometer with a graphite monochromator. A detachable furnace, which was built by Dr. Michael Carpenter and colleagues at the University of Cambridge (Figure 5.1), was placed over the mounted capillary and the crystal was aligned optically. An H-shaped resistance heater was placed so that the calibrated "hot spot" of the furnace was centered with respect to the crystal. This assembly allowed for the incident and diffracted beams to reach and leave the crystal, passing through the kapton window. This furnace used in the experiment to control the temperature contained Pt/Pt-rhodium R-type thermocouples. The furnace was powered by a control unit, equipped with a Eurotherm temperature controller. The geometrical restrictions allow for collection of data intensity up to +/- 28° in ω. Quartz has a low thermal conductivity as a result, the location of the crystal with respect to the thermocouple tip and the actual temperature imposed on the crystal is not what is reported by the controller. The "hot spot" area was calibrated by the melting points of a series of selected pure salts (Table 5.1) by Francesco Pandolfo at University of Pavia.

Table 5.1. Temperature calibration for the high-temperature furnace

Calibrant	$T_{MP,obs}$ (K)	T_{MP} (K)
Urea	398	407
Thiourea	429	444
$AgNO_3$	459.5	485
$NaNO_2$	517	524
ZnI_2	672	719
NaI	847.5	923
KCl	937	1043
Na_2SO_4	1052	1157

Notes. Observed melting points of published melting points for standard compounds. The values for the reference melting points of the various salts were taken from Weast *et al.* (1986).

The reflections used for the refinement of unit-cell parameters and full structure refinement were collected to $2\theta_{max} = 50°$. The scan time for each reflection was set to 20 seconds at 50kV and 30mA. Fifty-three reflections were used for least squares refinement of the cell parameters. Eight data sets at 25K intervals were collected up to 473K for determining the unit cell parameters. Five full intensity data sets were collected at 50K intervals up to 473K for structural refinements.

Due to complications with the generator, the experiment was switched to another Phillips diffractometer. The sensitivity on this diffractometer is less than that of the first diffractometer used in this experiment, so another a crystal was needed that was larger than the first for the experiment to maximize the amount of intensity and maximize the number of reflections to be used in the refinements. Due to the small size of the An27 samples, another sample of similar composition was used for the remainder of the experiment. The second crystal that was used in this experiment was an An26 plagioclase previously studied by Brown *et al.* (unpublished) of which the elastic moduli were determined. The sample is from a tonolitic body in the Monson Gneiss of Central Massachusetts. A piece of the sample was broken off (275μm X 150μm X 100μm) and was prepared for data collection in the same way that the previous sample was. On this diffractometer with the new sample, data was collected to perform unit cell refinements every 25K from 303K-1073K. Full intensity data collections for structural refinement were made at 50K intervals from 523K-1073K. The full intensity data collection made at 1073K was not good enough to refine the structure of An26 properly because the quartz vial had recrystallized (confirmed optically) and the peak overlaps from the quartz interfered with the reflections for An26.

Figure 5.1. A custom-made High-temperature furnace **.**

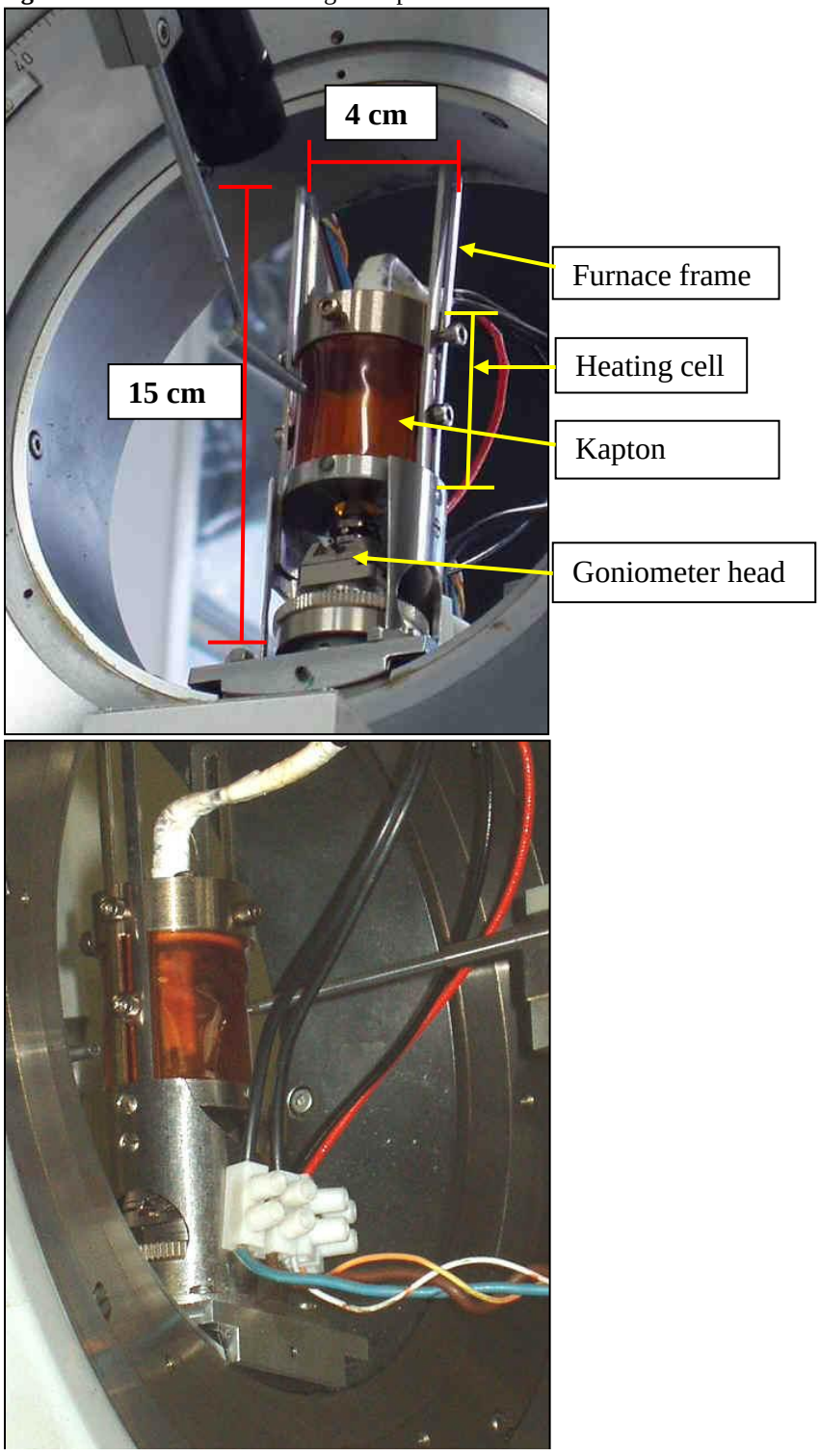

Notes. The detachable microfurnace used for high-temperature single-crystal X-ray diffraction used on a Phillips PW1100 diffractometer. It consists of a H-shaped Pt-Rh resistance heater and a Pt:Pt-Rh thermocouple inside a steel cylindrical cage 1 inch wide closed with a Kapton film.

5.2.3 Low-temperature single crystal X-ray diffraction data collection on An26

A different crystal of the An26 sample with the dimensions of 150μm X 100μm X 70μm was chosen for low-temperature single crystal X-ray diffraction. The crystal was mounted on a glass fiber using super glue which was mounted on a goniometer head and then mounted on an Agilent Gemini diffractometer with MoKα radiation (λ = 0.71073 Å) and a graphite monochromator. The crystal was cooled using a cryojet system and data collected at five different temperatures (100K, 150K, 200K, 250K, and 300K). Each data collection included intensity measurements out to 60° 2θ with the exposure times of 20 seconds.

5.2.4 Data analysis of the high- and low - temperature single crystal experiments on An26

The data integration for the high-temperature single-crystal experiment on An26 was done using the Lehmann-Larsen method (Lehmann and Larson, 1974). The number of reflections used for each refinement was between 1170 and1200. The raw intensities were not corrected for absorption because this absorption coefficient is minimal. The structural refinements against F^2 were done using SHELXL (Sheldrick, 2008).

CrysAlisPro (Oxford Diffraction) was used for the data integration on each of the low temperature experiments on An26. The refinements were performed using SHELXL (Sheldrick, 2008) with around 1900 reflections used in the refinements.

Table. 5.2. Model comparisons for the albite Rietveld results

patts. per bin	Temp. Interval (K)	lowest T - Highest T (K)	Uiso	2θ cutt-off	$wChi^2$
20	61	90 - 151 (stream)	Odiff	25	3.29
20	61	90 - 151 (stream)	Osame	25	3.3
5	42	902-944 (blower)	Odiff	25	8.94
5	42	902-944 (blower)	Osame	25	8.959
6	15	92 - 107 (stream)	Odiff	30	3.85
6	15	92 - 107 (stream)	Osame	30	3.852
6	15	92 - 107 (stream)	Odiff	25	3.292
6	15	92 - 107 (stream)	Osame	25	2.93
6	15	92 - 107 (stream)	Odiff	20	3.415
6	15	92 - 107 (stream)	Osame	20	3.417
2	10	934 - 944 (blower)	Odiff	30	9.204
2	10	934- 944 (blower)	Osame	30	8.934
2	10	934 - 944 (blower)	Odiff	25	8.915
2	10	934 - 944 (blower)	Osame	25	9.228
2	10	934 - 944 (blower)	Odiff	20	9.783
2	10	934- 944 (blower)	Osame	20	9.82

Notes. Details regarding the information for the different Rietveld refinements on An0.

5.2.5 Data analysis of the Rietveld refinements on albite

The availability of refined structures of albite as a function of temperature in the literature (Harlow and Brown (1980); Ribbe *et al.* (1969); Smith and Artioli (1986); Winter *et al.* (1979)) together with my own single-crystal refinements of the structure of An26 from 303K to 1023K provide an opportunity to verify the results of Rietveld refinements of the powder data and to determine the optimal refinement model. Structural information was obtained by constrained sequential Rietveld analysis of the diffraction patterns using automatic sequential routine implemented in the EXPGUI-GSAS software package (Toby 2001; Larson and Van Dreek2004). The data sets on their own at 2-5 Kelvin per data set are not good enough for a robust analysis of the structures by Rietveld refinement. To investigate the best model to use for sequential GSAS which should produce the most accurate model for the plagioclase structures, the datasets for albite have been binned at larger temperature intervals (10K, 20K, and 50K). Table 5.2 shows

the resulting $wChi^2$ for the various refinements. Two different sets were binned with a different number of patterns (first column in Table 5.2) based on which device was used for heating/cooling which is indicated next to the temperature interval in Table 5.2. All models used in the refinements for structural analysis were set to have anisotropic *Na*-sites and all the remaining atoms as isotropic. Two different structural models were used in this analysis; one where the oxygen atoms had isotropic displacement parameters constrained to be equal and the other where the oxygen atoms had isotropic displacement parameters refined independently (column 3 of Table 5.2). The unit cell parameters were refined independently for each pattern of which the starting cell parameters were taken from Tribaudino *et al*. (2010). For each temperature interval and oxygen model, three different 2θ cut-offs were chosen (20° (d_{min} = 2.31 , 25°(d_{min}=1.85) and 30° (d_{min}=1.55)) which are indicated in the fourth column of Table 5.2.

It was found that there is essentially no effect of 2θ cut-off, binning interval and oxygen model on the cell parameters, bond lengths and bond angles. In some cases, the $wChi^2$ differed by a small amount depending on the oxygen model. None-the-less, the $wChi^2$ value for the 25° 2θ cut-off was the lowest. The model with oxygen isotropic parameters set to being independent is preferred because this provides a model for the intensities in the diffraction pattern that is physically reasonable and allows for a stable automated refinement. In addition, the isotropic parameters for the oxygen differ by a significant amount within the esd's which is consistent with the single crystal data. The differences in these isotropic parameters stay relatively constant as temperature increases. The peak positions and unit-cell parameters did not change based on the binning interval. The results of the Rietveld for the An27 plagioclase will be compared to that of high-temperature single-crystal X-ray diffraction on a sample of the same composition of which intensity measurements were conducted at 50K intervals. The refinement model with the

50 K interval binning, a 25° 2θ cut-off and oxygen atoms set to having different isotropic temperature parameters was chosen for the analyses and comparisons to the single-crystal data.

5.3 Results

5.3.1 Albite analysis: (comparison of single-crystal refinement and Rietveld refinement)

A comparison of the results of the Rietveld refinements of the albite data to those of the single-crystal refinements of low albite at low and high temperature (Harlow and Brown (1980); Ribbe *et al.* (1969); Smith and Artioli (1986); Winter *et al.* (1979)) shows that, in general, all cell parameters from the Rietveld refinements agree well with the single crystal data (Figures 5.2 and 5.3). The spacing *d(100),* increases the most with increasing temperature, followed by *a*, *b* and then *c*. At low temperatures (below about 400 Kelvin), the *c*-parameter shows negative thermal expansion and then begins to increase with temperature This is also seen in the results from the refinements with finer binning of the data reported by Tribaudino *et al.* (2011). Alpha and gamma show a similar behavior with little to no change up to about 300 Kelvin and then both begin to decrease with increasing temperature (Figure 5.3). Beta shows a sharp decrease in value with temperature throughout the temperature range (Figure 5.3). There is large scatter for the single crystal data points for gamma, but the esds are larger than that of the scatter so it is not significant and this lattice parameter does not show much variation with temperature (less than 0.2°). As for the volume, there is a subtle but noticeable change in curvature below 200 Kelvin from the Rietveld refinements that reflects the beginning of low-temperature saturation of the thermal expansion that is required by thermodynamics, but this is apparent in the single crystal data, perhaps because the single crystal data are compiled from experiments using different instruments.

Figure 5.2. Fractional change for cell edge lengths at high-temperatures for the Rietveld refinement and single-crystal results of An0.

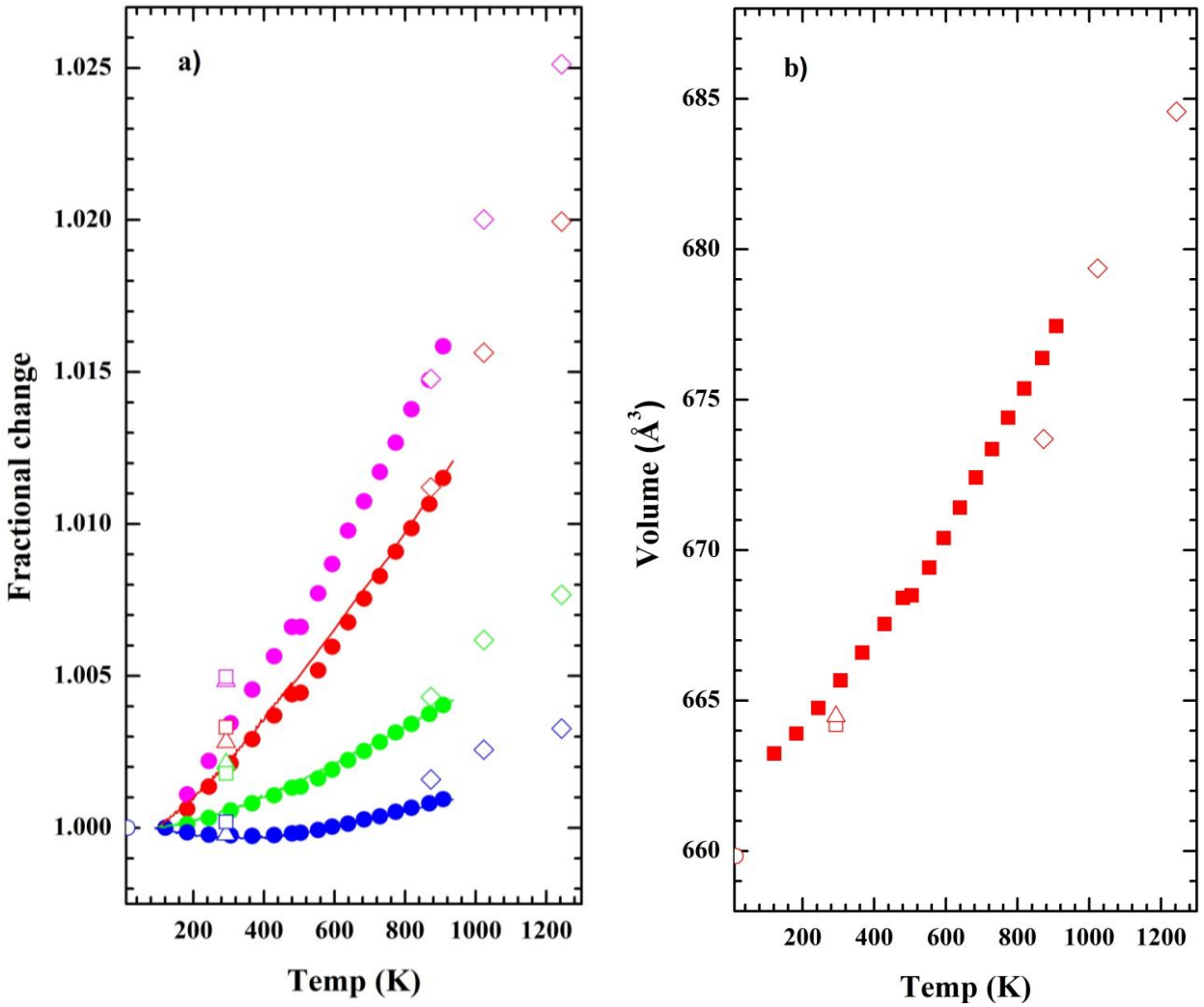

Notes. Fractional change for cell parameters (fig. a) and the unit cell volume (fig. b) for albite from 13K-1243K. Fig a: red = *a*, pink = *d(100)*, green = *b*, blue = *c*. In figure a, the solid lines represent the fractional changes of *a*,*b* and *c* at every temperature increment taken from Tribaudino *et al.* (2010). The solid symbols for both figures represent the results from the Rietveld refinements and the open symbols represent data from single-crystal work in the literature (circle = Smith and Artioli (1986), square = Harlow and Brown (1980), triangle = Ribbe et al. 1967 and diamond = Winter et al 1979). Estimated standard deviations are smaller than the symbols.

Figure 5.3. Unit cell angle changesat high-temperatures for the Rietveld refinements and single-crystal refinements of An0.

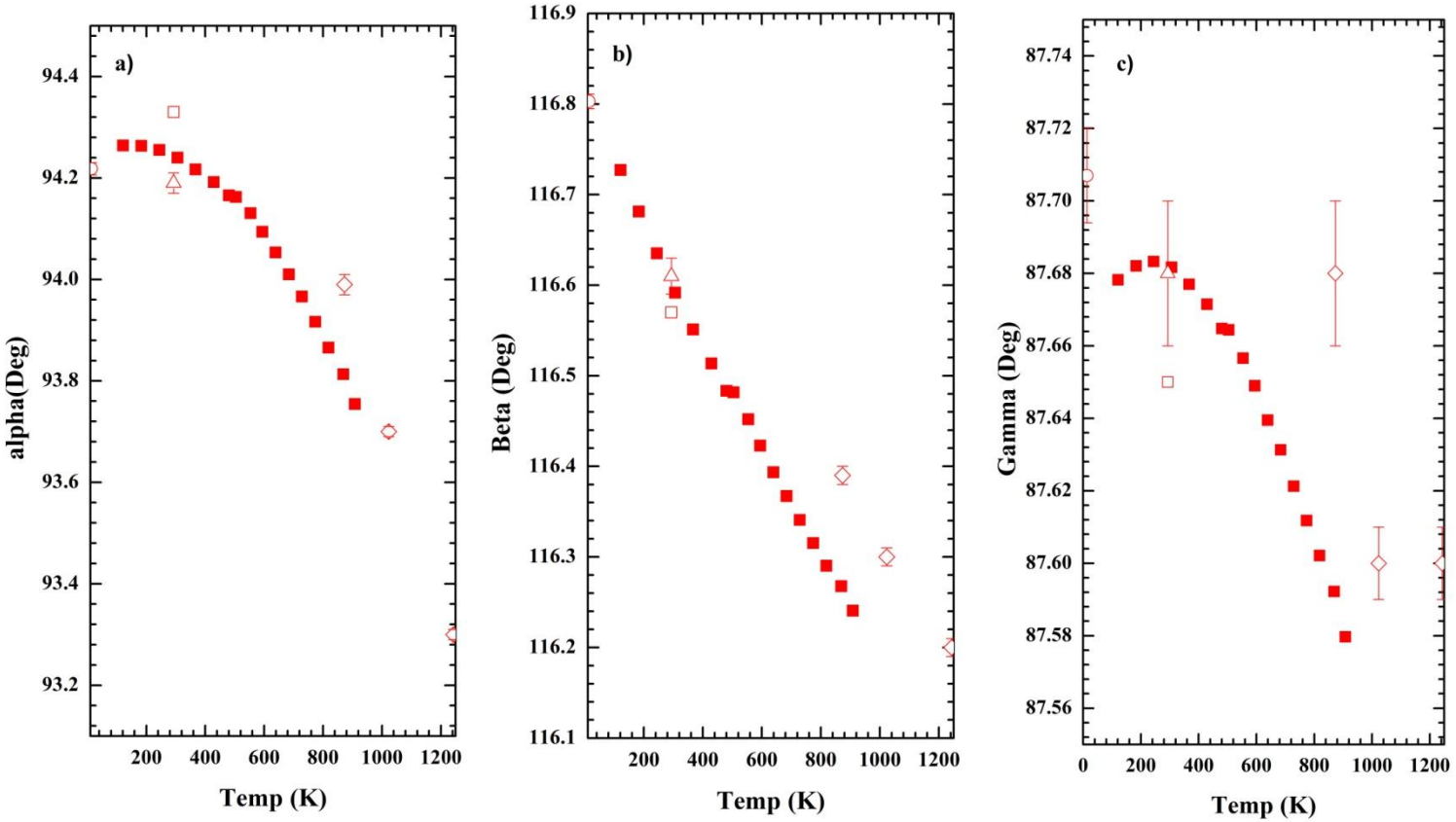

Notes. Unit cell angles alpha (fig. a), beta (fig. b), gamma (fig. c) for albite from 13K – 1243K. The solid symbols for all figures represent the results from the Rietveld refinements and the solid symbols with black outline represent data from single-crystal work in the literature (circle = Smith and Artioli (1986), square = Harlow and Brown (1980), triangle = Ribbe et al. 1967 and diamond = Winter et al 1979).

Figure 5.4. The four tilt systens at high-temperature for the Rietveld refinement and single-crystal refinement results of An0.

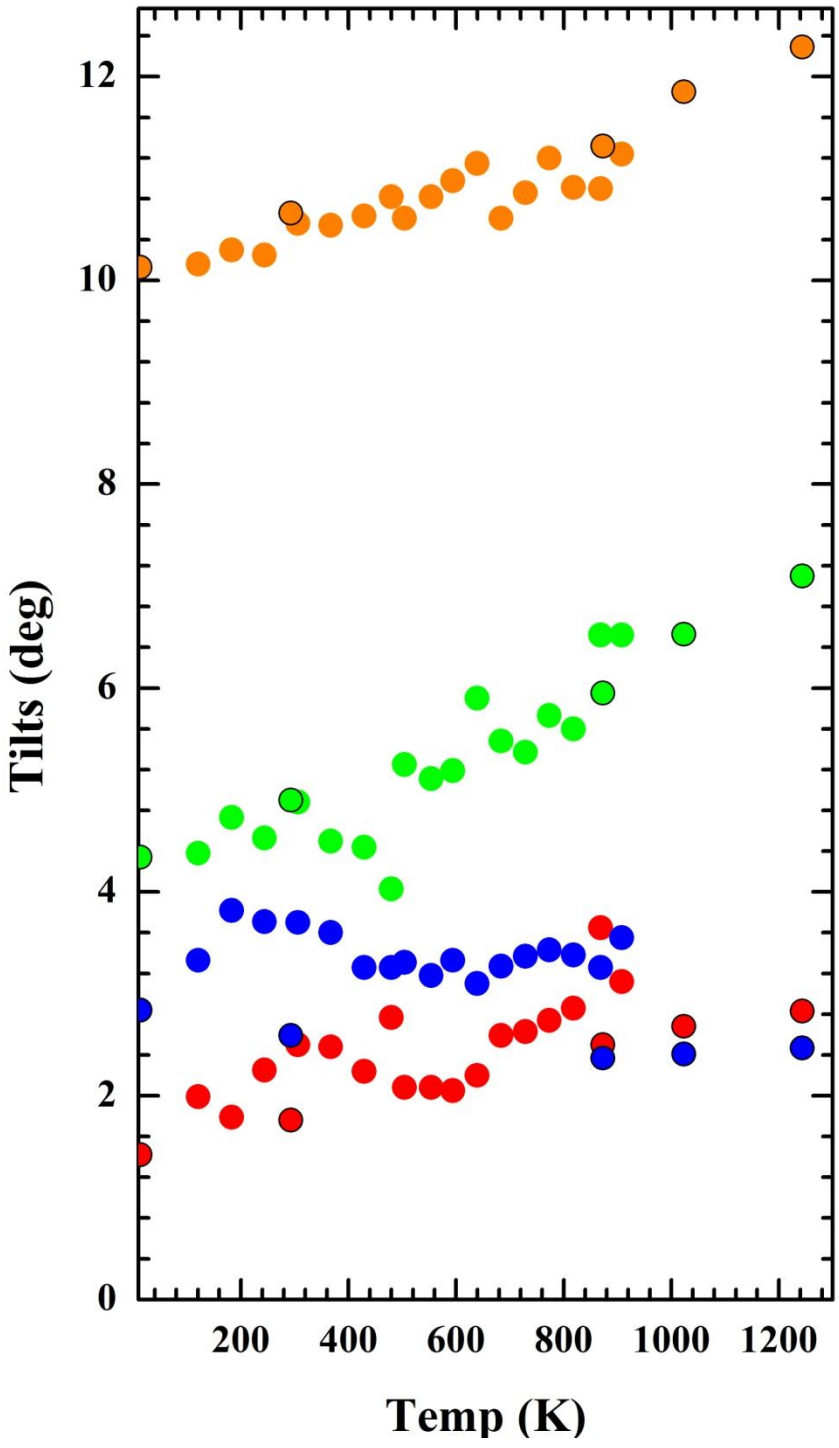

Notes. The four tilt systems for An0 Rietveld refinements (closed symbols) and low and high temperature single crystal data from the literature (closed symbols with black outline). Tilt 1 = red, Tilt 2 = green, Tilt 3 = pink, Tilt 4 = blue.

The powder and single-crystal structures were also analyzed using the 4 tilt system models. The values for Tilt systems 1,2 and 3 agree remarkably well when comparing the Rietveld refinement results and single-crystal refinement results (Figure 5.4). Tilt 2 starts at about 10° at lower temperature and by ~900 K there is a noticeable increase in tilt angle. Tilt 3 starts off at about 4° and gradually increases with increasing temperature. However, tilt system 1 starts off at 2° for lower temperatures and does not vary much with increasing temperature. The angles for tilt system 4 from the Rietveld refinements do not agree as well with the tilts derived from the single crystal refinements (Figure 5.4). The difference between the Rietveld refinements and single crystal refinements for tilt system 4 is about 1° which is outside the estimated error on the tilting systems (about 0.2-0.5 degrees). The estimated error on the tilting systems is difficult to calculate analytically from the least squares, but this error can be estimated by approximately half of the esd of the T-O-T angles. It is clear from Figure 5.4 that tilt system 2 and 3 change the most with increasing tilting angle as temperature increases.

The more traditional measures of feldspar crystal structures such as the T-O-T angles from the Rietveld refinements (Figure 5.5a) and the single crystal refinements (Figure 5.5b) agree quite well with each other. The Na-O distances from the Rietveld refinements and single crystal data (Figure 5.6) agree very well with the Oa2 being the shortest distance. Most of the Na-O distances shown in Figure 5.6 remain relatively unchanged in the temperature range for both single crystal and Rietveld refinements with the biggest change occurring for the Na-OA1$ distance.

Figure 5.5. T-O-T angles at high-temperatures for the Rietveld refinements and single-crystal refinements results of An0.

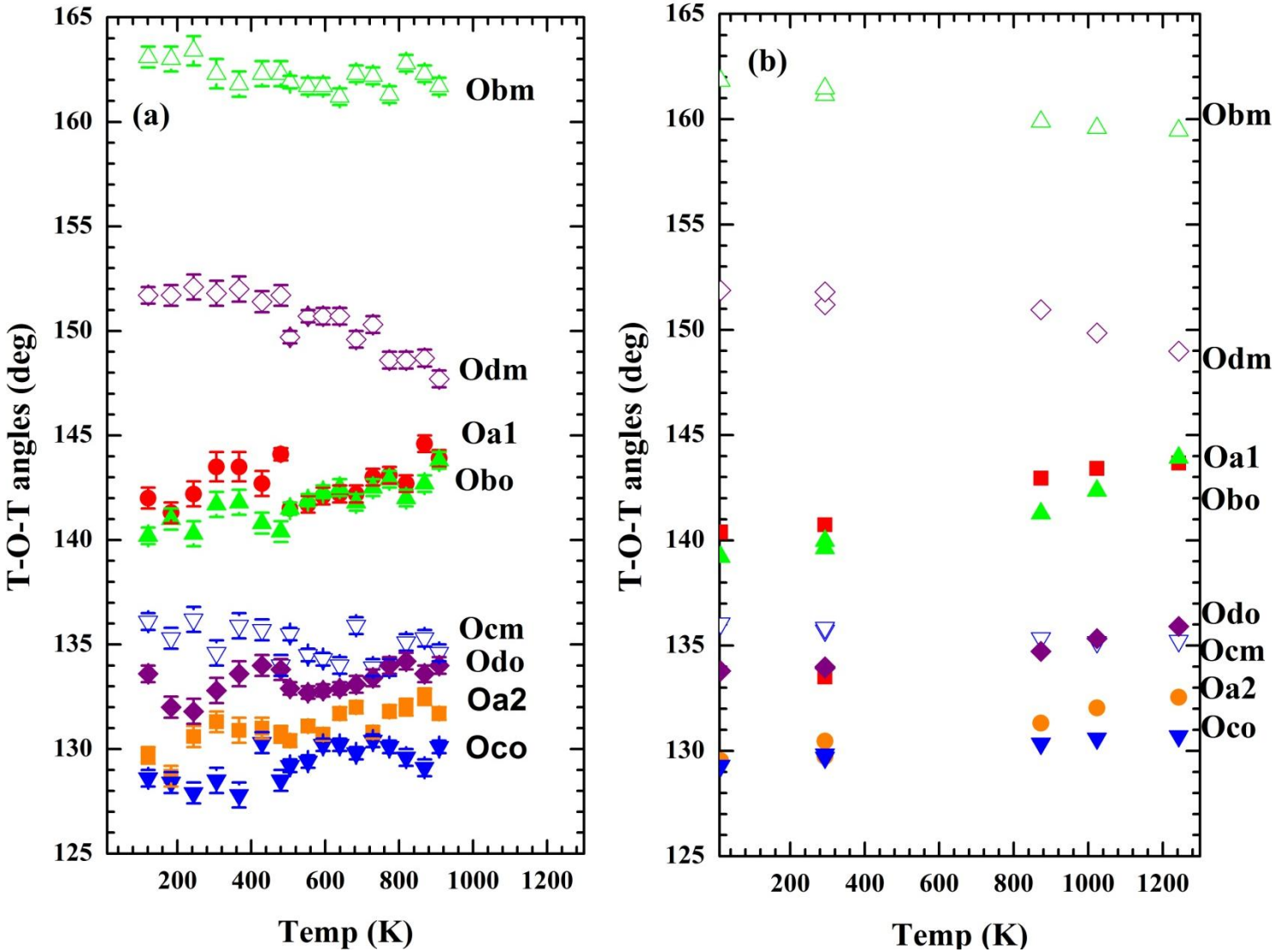

Notes. T-O-T angles for An0 Rietveld refinements (first image) and single crystal data from literature (second image). T-Oa1-T – red squares, T-Oa1$-T(longer) = orange circles, T-Oa2-T = closed green triangles, T-Obo-T = closed blue triangles, T-Oco-T = closed brown triangles, T-Odo-T = closed purple diamonds, T-Odm-T open purple diamonds.

Figure 5.6. The 7 shortest Na-O distances the Rietveld refinement and single-crystal refinement results of An0.

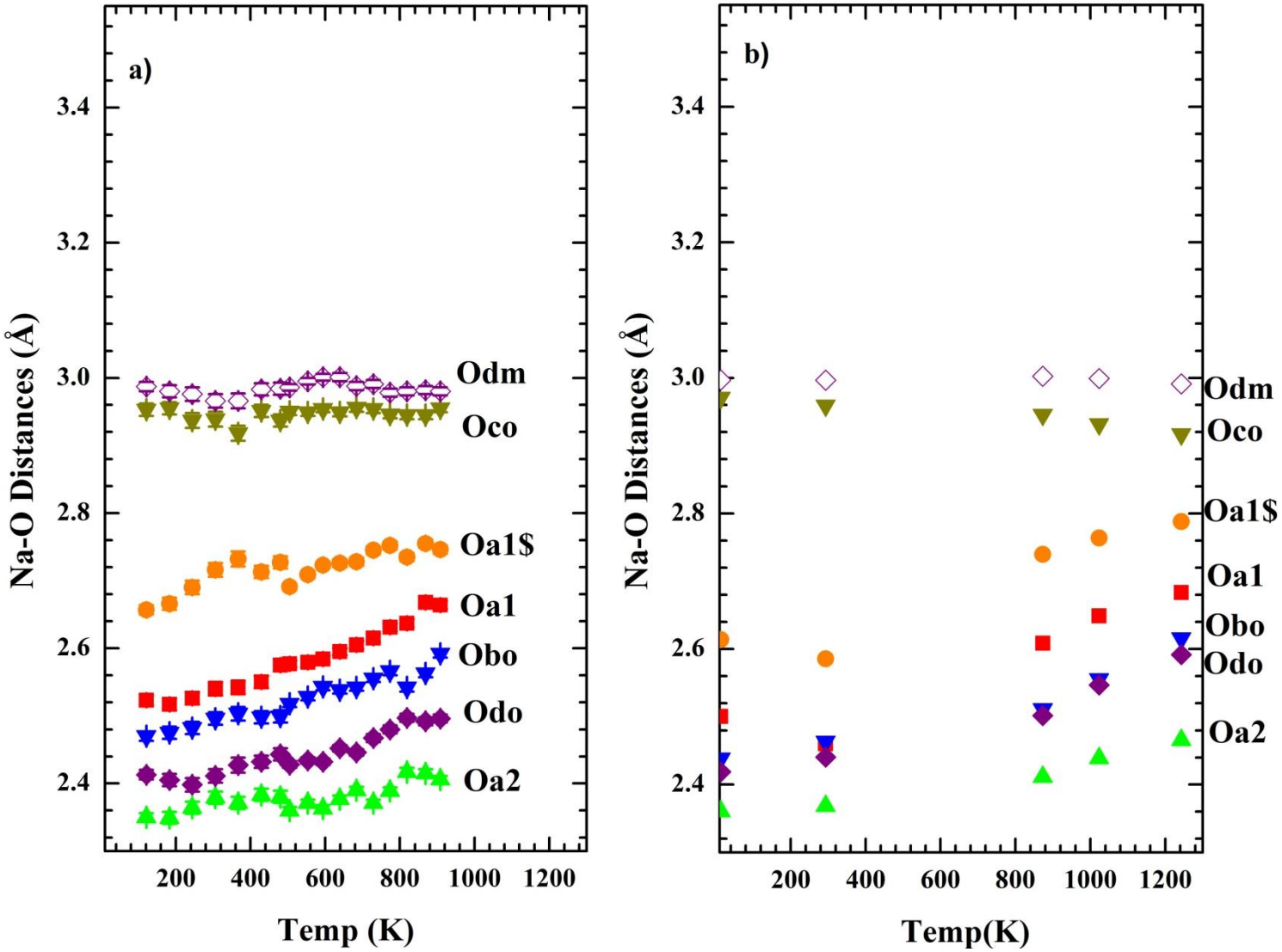

Notes. The 7 shortest Na-O distances for An0 from the Rietveld refinements (a) and the single-crystal refinements (b). The "$" symbol represents a second Oa1 oxygen that is symmetry-equivalent to the first.

It is obvious from these structural results that the powder data compares favorably with the single-crystal data. Therefore, it is feasible to use the powder data to study structural evolution versus temperature for *C-1* Na-rich feldspars.

5.3.2 An26/An27 analysis (comparison between Rietveld refinements and single crystal for a non-end member feldspar)

To investigate the reliability of the Rietveld refinements on a plagioclase, the data from the Rietveld refinement of the An27 sample of Tribaudino *et al*. (2010,2011) was refined in exactly the same way as the end-member albite with the addition of a second extra-framework *M*-site position to represent the Ca (and K content). As Ca and K have similar scattering factors and similar size, and the orthoclase content of plagioclase is typically only 1-2 mol%, a single Ca occupancy is used to represent Ca and K.

The model used for the single-crystal refinements pertaining to the experiments done on An27 and An26 at high- and low- temperatures involved extra-framework cation sites containing Na and Ca that were split and had occupancies fixed at the composition of An25Ab73Or2 based on the electron microprobe analysis (Brown *et al.* unpublished), with the Ca occupancy used to represent Ca and K. The *T*-site occupancies were split for Al and Si based on the refined average T-O bond lengths using the equation described in (Kroll and Ribbe, 1983). All atoms except Ca were set as anisotropic with the *T*-sites set to having the same anisotropic temperature factors and a fixed position. For consistency between the data for both diffractometers used on the high-temperature experiments in Pavia, all data sets from 303K - 1023 were cut off at 50° 2θ. Table 5.3 shows the refinement results for An26 from 303K-1023K. Structure refinements at high-temperature tend to underestimate the T-O bond lengths because the model of anisotropic but independent thermal motion does not correctly describe the ‘riding’ motion of the O on the T

atoms. As a consequence the ‘raw’ T-O bond lengths calculated directly from the refined fractional coordinates show a small decrease with increasing temperature.

Table 5.3. The single-crystal refinement results for An26 from303-1023K

Temp (K)	ρ_{calc}(g/cm^3)	meas. Ref.	unique ref	refl. $F_o > 4\sigma(F_o)$	GooF	R_1 (F) with $F_o > 4\sigma(Fo)$	wR_2 (F^2)	Weighting Scheme	Residuals (e$^-$/Å^3)
303	2.661	2712	1177	969	1.025	0.0292	0.0742	0.03,2.75	- 0.39/0.39
323	2.660	2698	1178	980	1.062	0.0304	0.0787	0.04,2.11	- 0.35/0.42
373	2.656	2703	1178	974	1.072	0.0307	0.0799	0.04,2.11	- 0.34/0.43
423	2.655	2708	1178	976	1.072	0.0339	0.0825	0.04,2.35	- 0.47/0.42
473	2.652	1183	1177	939	1.014	0.038	0.0953	0.03,8.10	- 0.47/0.44
523	2.649	1184	1177	927	1.164	0.0388	0.085	0.01,5.84	- 0.55/0.44
573	2.647	1185	1179	925	1.142	0.0397	0.087	0.02,6.08	- 0.48/0.51
623	2.644	1187	1182	918	1.197	0.0398	0.0953	0.02,5.42	- 0.41/0.52
673	2.641	1189	1181	923	1.114	0.0403	0.0833	0.01,6.17	- 0.46/0.40
723	2.638	1191	1184	916	1.136	0.0411	0.0928	0.02,6.22	- 0.59/0.47
773	2.635	1192	1183	931	1.133	0.0436	0.0888	0.01,6.04	- 0.45/0.45
823	2.632	1197	1189	903	1.138	0.0423	0.0957	0.02,5.77	- 0.48/0.50
873	2.629	1199	1190	910	1.114	0.0424	0.103	0.03,5.65	- 0.43/0.43
923	2.625	1200	1194	913	1.104	0.0427	0.0977	0.03,5.35	- 0.37/0.40
973	2.622	1200	1196	901	1.116	0.047	0.1022	0.02,6.65	- 0.56/0.45
1023	2.619	1200	1195	907	1.097	0.0447	0.0956	0.02,5.69	-0.39/0.41

Figure 5.7. Fractional change of the cell edge lengths at high-temperatures for the Rietveld refinement results and single-crystal results of An26.

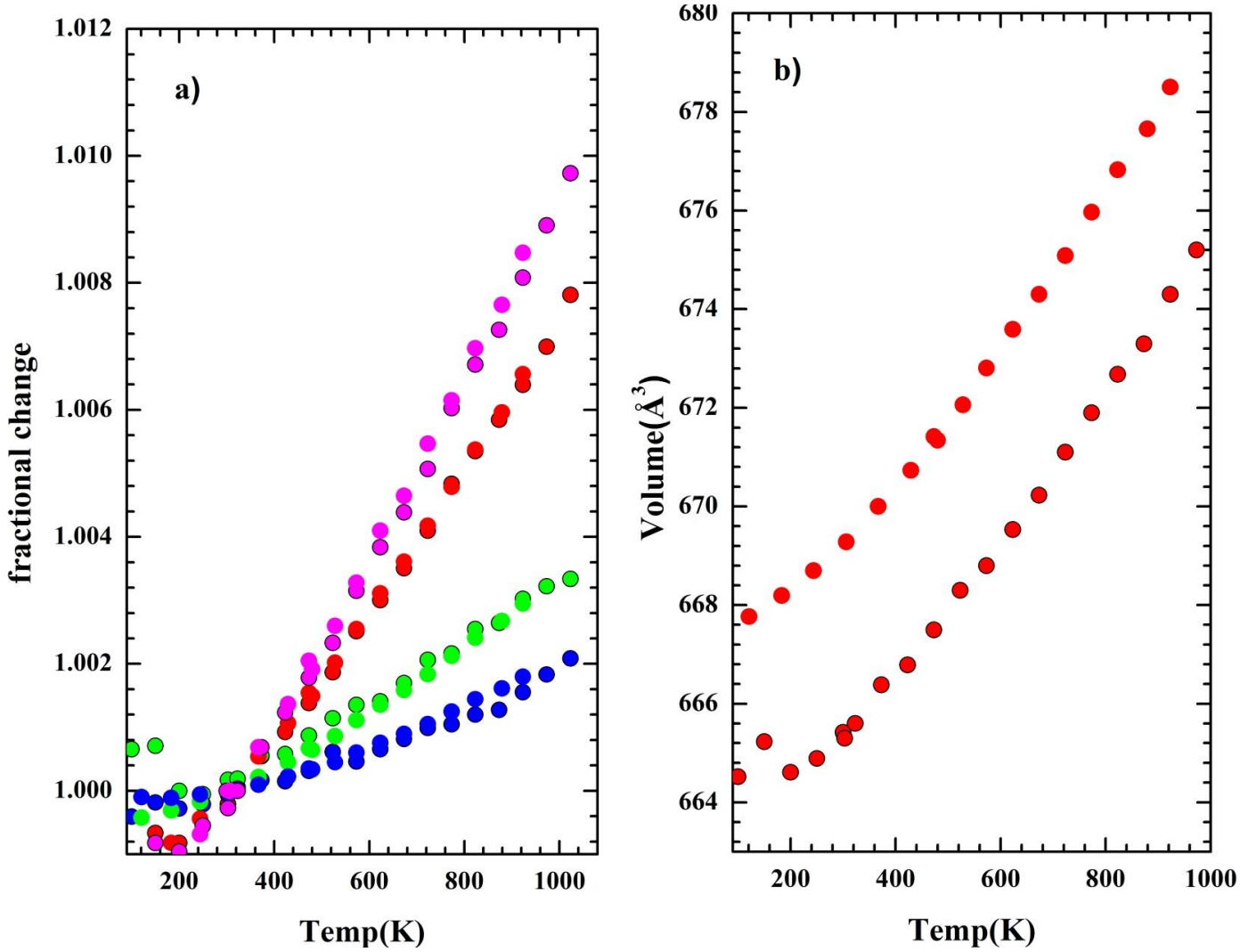

Notes. Fractional change for cell parameters (fig. a) and the unit cell volume (fig. b) for An26 from 100K -1023K and An27 from 90K-944K. Fig a: red = *a*, pink = *d(100)*, green = *b*, blue = *c*. The solid symbols for both figures represent the results from the Rietveld refinements and the solid symbols with black outline represent data from the single-crystal work. Estimated standard deviations are smaller than the symbols.

Figure 5.8. Unit cell angle changes at high-temperatures for the Rietveld refinements and single-crystal refinements of An0.

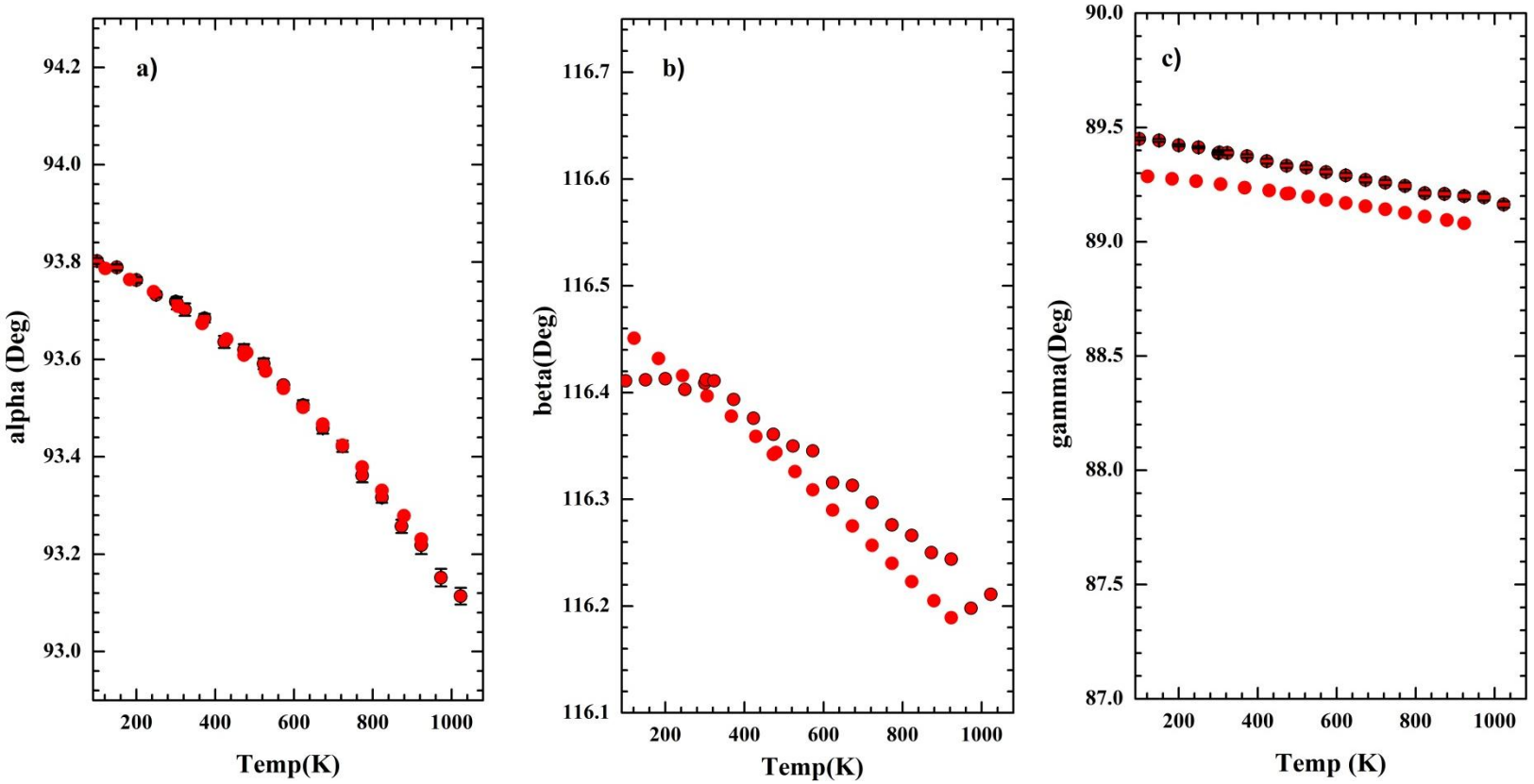

Notes. Unit cell angles alpha (fig. a), beta (fig. b), gamma (fig. c) for An26 from 100K – 1023K and An27 from 90K-944K. The solid symbols for all figures represent the results from the Rietveld refinements and the solid symbols with black outline represent data from the single-crystal work.

In general, the results from the An27 Rietveld refinements agree well with the single-crystal data of An26. The fractional change of *d(100)*, *a*, *b* and *c* between the An27 Rietveld refinement results and the An26 single-crystal results agree well with each other. Unit-cell angle alpha between the Rietveld refinement results of An27 and the single-crystal results of An26 agree remarkably well and this angle shows a decrease across this temperature range which is also what is seen in albite (Figure 5.8). Beta also agrees well between the Rietveld refinement results and the single-crystal refinement results, although there are some minor differences. For the An26 single-crystal refinement, beta stays the same until around 300 K where it begins to decrease with increasing temperature (Figure 5.8). For An27 Rietveld, beta decreases throughout the temperature range. Gamma behaves the same for both samples, but is a higher value for An26 which is expected because gamma is very sensitive to composition (Kroll and Ribbe 1980) (Figure 5.8). The volume, however, is lower than expected for An26 for reasons that are unclear, but probably a consequence of the method of fitting the peak profiles to determine Bragg angles in the high-temperature single-crystal diffraction experiment.

Figure 5.9 The four tilting systems at high-temperatures for the Rietveld refinement and single-crystal refinement results of An26.

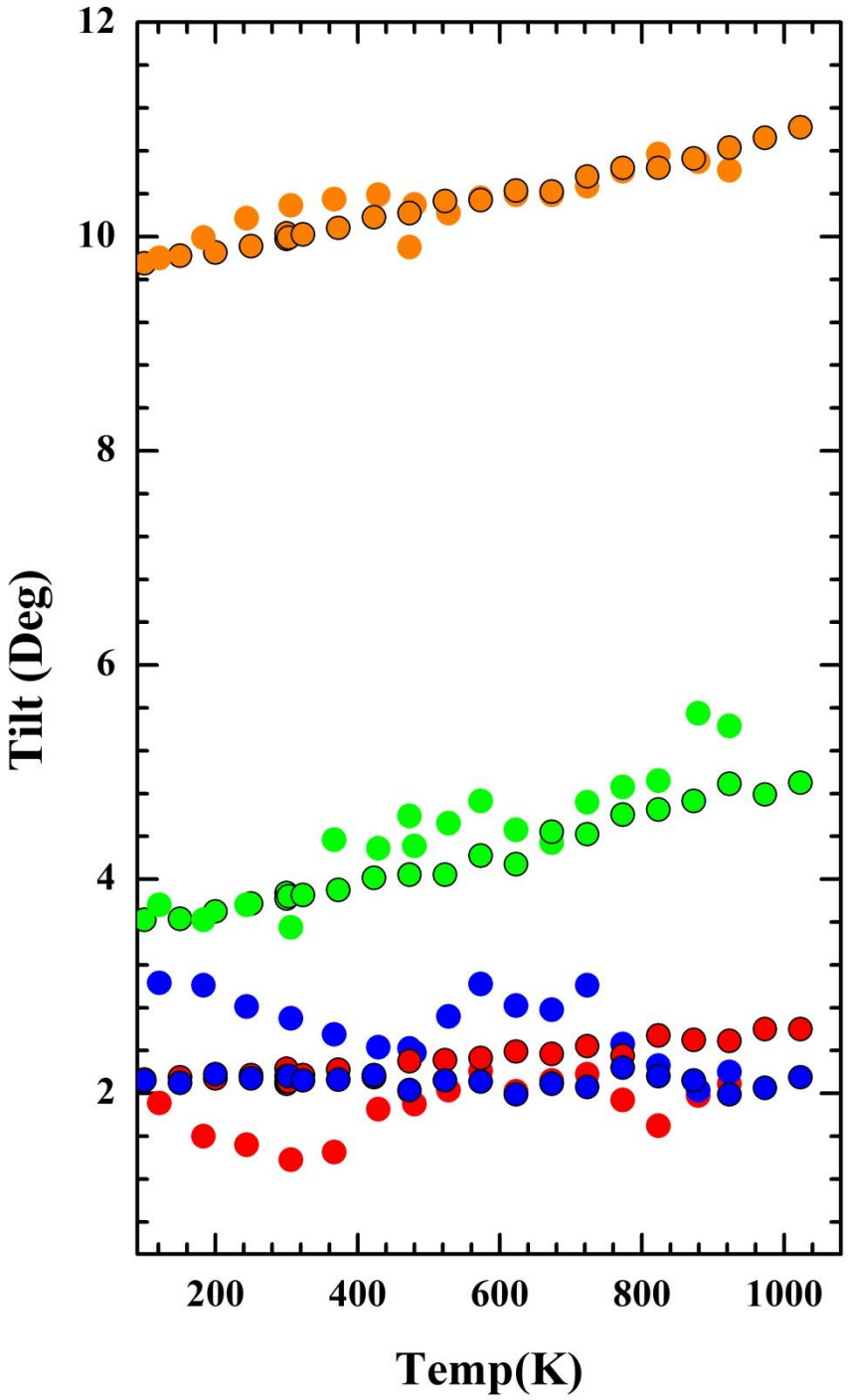

Notes. The four tilt systems for An27 Rietveld refinements (closed symbols) and low and high temperature single crystal data for An26 (closed symbols with black outline). Tilt 1 = red, Tilt 2 = orange, Tilt 3 = green, Tilt 4 = blue.

We see good agreement for the four tilt systems when comparing the An26 single-crystal refinement results with the An27 Rietveld refinement results. Referring to at Figure 5.9, it is obvious that tilt systems 2 and 3 dominate with respect to framework structural change over the entire temperature range. There is a noticeable difference between the single-crystal and powder refinement values of tilts 1 and 4, but the basic trends for these tilts with increasing temperature are the same. Tilt system 2 has the highest value (by far) starting off at about 10 degrees at 90K-100K and increases with temperature. Tilt system 3 behaves the same with a starting value of 3.5 degrees at 90-100K and increases with increasing temperature. Tilt systems 1 and 4 for the An27 Rietveld results oscillate a bit with no real defined trend towards an increase or decrease with increasing temperature. Tilt systems 1 and 4 from the single-crystal refinement results of An26 also remain relatively constant (within the error of a tilt) throughout the temperature interval.

Although there are complications due to the mixed occupancy of the *M*-site when dealing with constructing a model for the Rietveld refinements of An27, there are still good agreement with the An26 single-crystal results and the An27 Rietveld refinement results. It can therefore be deduced that Rietveld analysis on the remaining *C-1* plagioclase powders measured at ESRF is adequate to complete the tilt system analysis for Na-rich plagioclase feldspars.

5.3.3 Tilt system analysis of the Rietveld results of An35 and An46

The model from the An27 Rietveld refinements was used for the remaining re-binned datasets of plagioclase (An35 and An46) with some changes to accommodate for the change in composition. The *M*-site was split and set to the composition of the plagioclase based on the given stochiometry. Both the Na and Ca atoms in this split site were refined anisotropically while all other atoms were refined isotropically.

Figure 5.10. The four tilt systems for the Rietveld refinement results of An35 and An46.

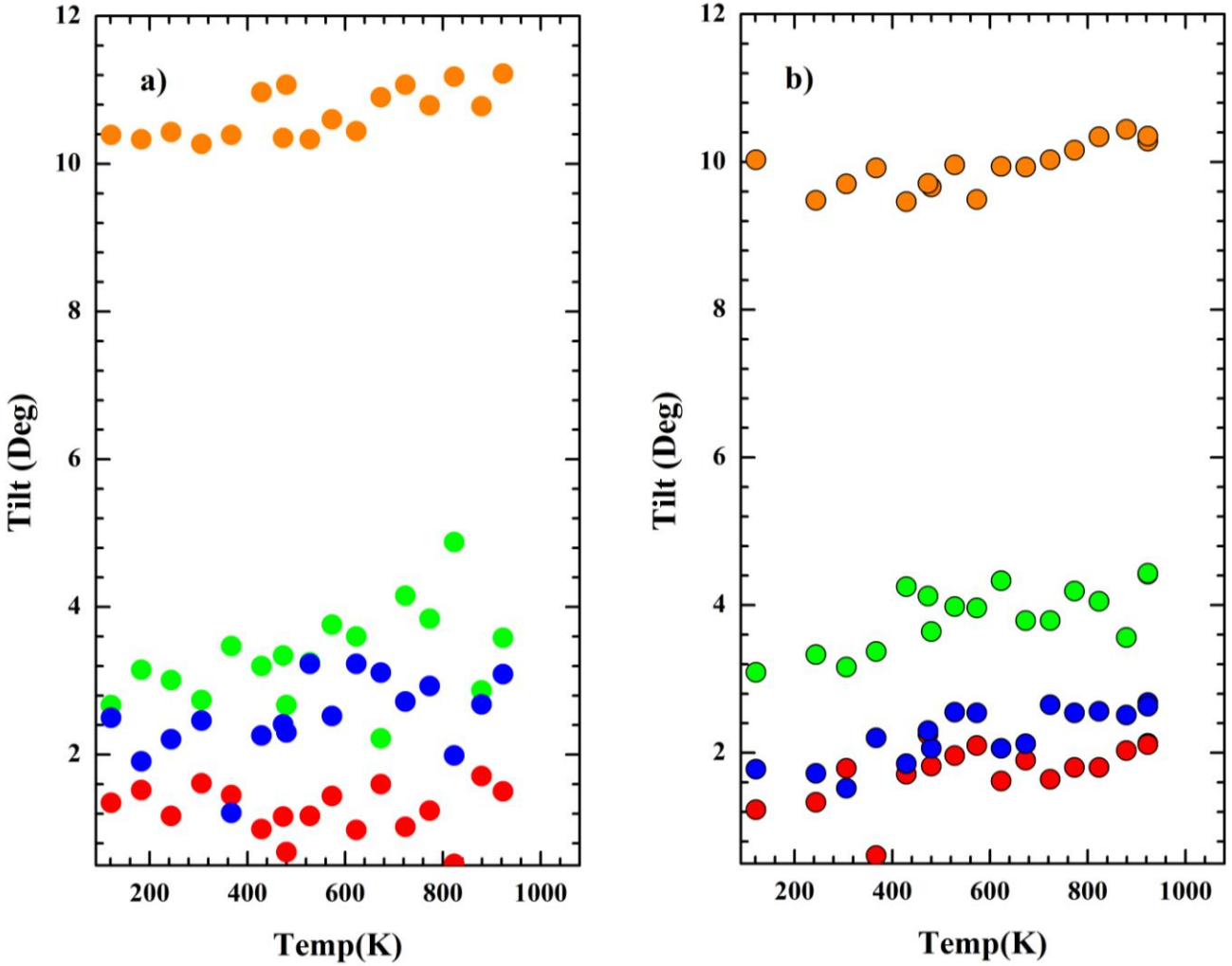

Notes. The four tilt systems for An35 Rietveld refinements (a) and Rietveld refinement results for An46 (b). Tilt 1 = red, Tilt 2 = orange, Tilt 3 = green, Tilt 4 = blue.

Figure 5.10 are the four tilting systems for the Rietveld refinement results of An35 and An46. These plots show the same tilt system trends as seen in albite (Figure 5.4) and An27 (Figure 5.7). With the following caveats; The tilts show more scatter for An35 than for An46. The dominance of tilt system 2 and tilt system 3 in terms of the framework structural evolution with temperature is not as prominent as was seen in albite and An27. Tilt system 2 still shows an increasing value as temperature is increased, but the effect is much more subtle for An35 and An46 than was seen for albite and An27. Tilt system 3 shows a subtle increase with increasing temperature, but this is more obvious for An46. Interestingly, Tilts 1 and 4 are a bit different for An35 and An46 than are for albite and An27. For An35, these tilts are much more scattered and appear to oscillate around a constant value with temperature. Tilts 1 and 4 for An46 on the other hand, show much less scatter and both show a slight increase with temperature (compared to the other Rietveld results).

5.4 Discussion

5.4.1 Comparing tilt systems for C-1 plagioclase with alkali feldspars at high-temperature

Looking at the tilting results for all samples (Albite Rietveld, An26 single crystal, An27 Rietveld, An35 Rietveld and An46 Rietveld), one can identify some general trends. The most obvious is that the rate of change of tilt 3 with temperature clearly decreases with increasing Ca content from about 2° per 1000K in end-member albite to about 1° per 1000K in An27 and An35 and significantly less than that in An45. These new results are consistent with the tilts that can be calculated from previous structure determinations of alkali feldspars at high-temperature. For example, Ohashi and Finger (1975) determined the crystal structure of sanidine at 1073K. This is actually one of the very few publications to previously calculate the tilts using the method of

Megaw (1974). Kimata *et al.* (1996) also determined the structure of a sanidine, at 1200K. Both of these studies show that in sanidine the same tilts 2 and 3 are the ones that change most with temperature, as in the *C-1* plagioclase, and as expected from the model described in Chapter 3. Henderson (1979) conducted a powder diffraction analysis of disordered albite (high albite) and sandine samples of varying composition from room temperature up to 1273K and showed that the dominant thermal expansion direction was found to be 22° from the direction of the double-crankshaft and approximately along the direction of *a**. Although he did not determine the structures, he deduced from these cell parameter measurements and Megaw's (1974) analysis that the structural mechanism of expansion was the tilt systems 2 and 3 and a subsequent increase of T2-OA2-T2. What is different between the *C-1* plagioclase and the alkali feldspars is the rate of change of tilt with temperature; the data of Kimata *et al.* (1996) show that tilt 3 increases by more than 3° per 1000K in sanidine, which is more than twice the rate measured for *C-1* plagioclase. It appears that the rate of change of tilts with temperature increases with the size of the extra-framework cation (from Ca to Na to K), the unit-cell volume, and the magnitude of the tilt itself. It cannot be determined which of these factors is controlling the tilt rate with temperature and thus in the structure whether the *M-O* bond distances (which generally increase with tilt system 3) or the O-O distances are the controlling structural parameter in determining tilt rate with temperature change and thus the thermal expansion.

Figure 5.11 below are Figures X and Y from Chapter 3 of this thesis with the added data from this chapter. As can be seen from this figure, all points for the Rietveld results cluster about the points corresponding to the results of several Na-feldspar studies from the literature, so the results from this study are consistent from what is expected from analyzing tilt systems 2 and 3 with respect to our model. Interestingly, the effect of calcium addition into a *C-1* feldspar

doesn't have nearly the effect on tilt systems 2 and 3 as the substitution of K^+ for Na^+ in the alkali feldspars. This isn't completely unexpected because the relative size of and Na^+ and Ca^{2+} in plagioclase feldspars cation are much more comparable than for a Na^+ and K^+ cation in alkali feldspars. Thus, there is a greater difference of an *M*-site change for the tilts of alkali feldspars compared to plagioclase feldspars.

5.4.2 The effect of short M-O bonds on tilt system evolution

While it is clear from this chapter and the previous chapter that the tilts dominate the structural changes with temperature and pressure, the *M*-site plays an important role with temperature. Ohashi and Finger (1975) connected the changes seen in tilt systems 2 and 3 to the strong anisotropy in favor of the *a** direction and the relative elongation of the K-polyhedra along this *a** direction. In supplement to this finding, the authors also mention the changes of the K-OA1 and K-OA2 distances and the O-K-O angle across the mirror plane as means for this polyhedral elongation. This idea can be extended into the plagioclase feldspars in this chapter at high-temperature. The M-Oa1 and M-Oa2 are also the two shortest bonds to both Na and Ca as with K for the sanidine studied by Ohashi and Finger, but not for the albite model for which the two shortest bonds are Na-Oa2 and Na-Odo. Figure 5.12 is a plot of these two shortest Ca-O and Na-O bonds at room temperature for An27, An35 and An46 and the Na-Oa2 bond for albite.

Figure 5.11. The tilt system 2 and tilt system 3 model from Chapter 3 contoured to cell parameter a , d(100), b, c and unit cell volume with data from this chapter (5).

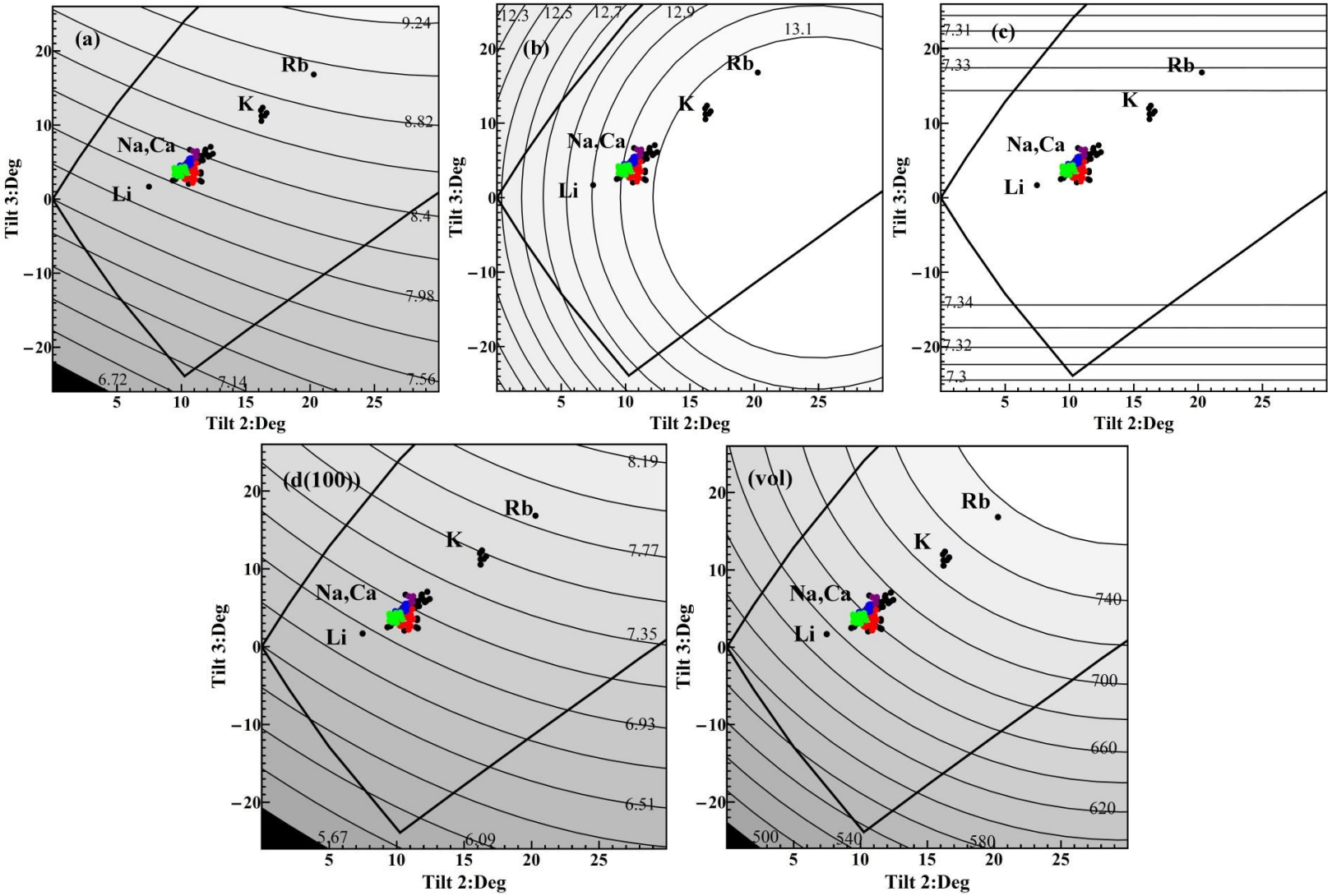

Notes. The tilt system 2 and tilt system 3 model from Chapter 3 contoured to cell parameter a (fig. a), d(100) (fig b), b (fig. c), c (fig d) and unit cell volume (fig. e). Purple dots = alkali feldspar results (also plotted in Chapter 3), black dots = albite Rietveld results, green dots = An27 Rietveld results, red dots = An35 Rietveld results, blue dots = An46 Rietveld results.

Figure 5.12. The Ca-Oa2, Ca-Oa1, Na-Oa2 and Na-Oa1 distances for the results of the Rietveld refinements (albite, An27,An35 and An46).

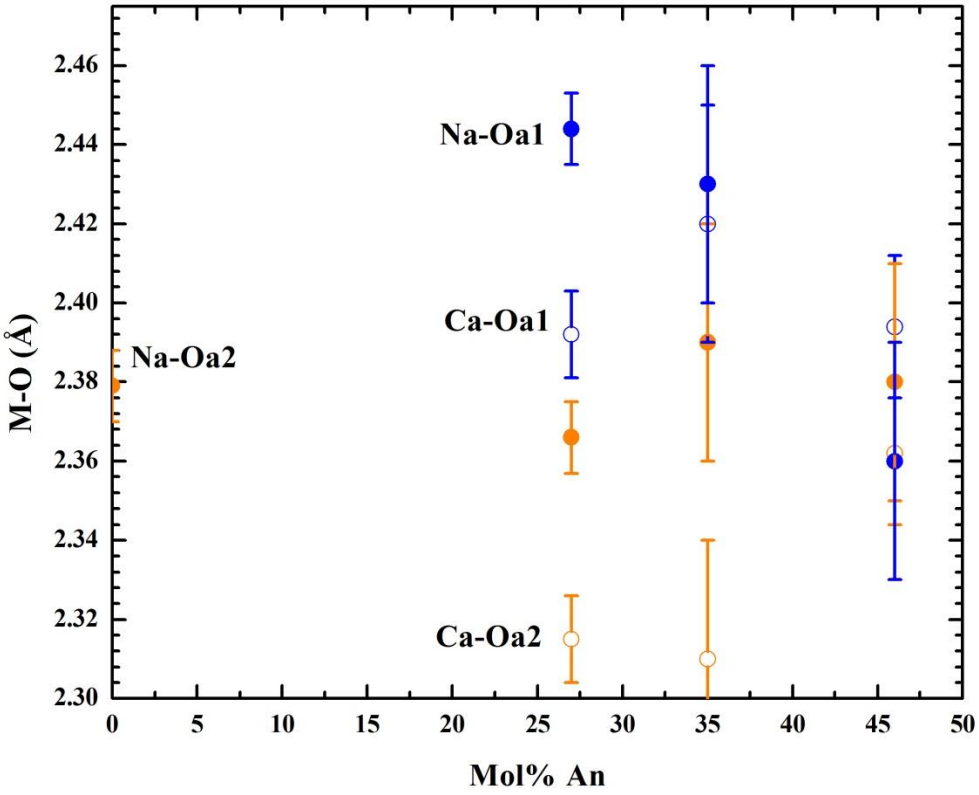

Notes. Closed blue = Na-Oa1, open blue = Ca-Oa1, closed orange = Na-Oa2 and open orange = Ca-Oa2.

From Figure 5.12, we can see the effect that splitting the *M*-site cation in separate Na and Ca position has on the short M-O bonds. This could be coupled to how the tilts affect the evolution of structure with temperature. What is particularly interesting about Figure 5.12 is the fact that the difference between the two shortest Ca-O and Na-O bonds converge towards a common bond-length as calcium content is increased in the structure. This could be a secondary effect as a result of the trends in the evolution of tilting systems for plagioclase at high temperatures and provide insight to the change in this trend with composition in terms of increasing Ca-content.

5.4.3 A structural reason for negative thermal expansion in albite

Unlike monoclinic feldspars, the values of tilt 1 and tilt 2 are averages in the triclinic structures, each over two symmetrically distinct tetrahedra. (Tilts 3 and 4 are cooperative tilts of all four tetrahedra in the 4-ring, so do not need to be considered as averages). Tilt system 1 as plotted above is the average of the two tilts of the T1o and T1m tetrahedra, which are significantly different in most *C-1* feldspar structures. The T1o tetrahedron, containing Al typically has a large positive value of tilt system 1, meaning that it is tilted inward towards the 4-ring, but T1m has a much smaller value, and is sometimes negative by a few degrees corresponding to an outwards tilt of the T1m tetrahedron. The idealized model presented in Chapter 3 has monoclinic symmetry, and therefore does not predict the effect of such a difference in tilt, so these high-temperature data provide the opportunity for its effects to be explored.

The effects of the differences in tilt systems 1 and 2 can be used as means of describing the structural mechanism responsible for the negative thermal expansion in the *c*-axis direction seen in albite and not seen in more Ca-rich *C-1* plagioclase feldspars. According the tetrahedral tilting model in Figure 3.6(a) in Chapter 3, the *c*-axis length should decrease with decreasing value of tilt 1. Figure 5.13 shows the values for the T1o tilt and T1m tilt versus *c*-axis length (a) and temperature (b). As can be seen from Figure 5.13 (a), T1o tilt pertaining to albite, An27, An35 and An46 is independent of temperature. An26 (single-crystal refinement results) however shows a decrease in tilt as temperature increases. The T1m tilt, however, decreases in magnitude with increasing temperature. With respect to the *c*-axis (Figure 13c and d), the T1o tilt and T1m tilt for all compositions approach 0 (no tilt) and the *c*-axis length increases which is in accordance with the tetrahedral tilting model (Figure 3.7a from chapter 3). Figures 5.13a and

5.13b both show magnitudes of individual tilts decreasing towards zero as temperature increases which causes the averaged tilt 1 to increase slightly. Figures 5.13c shows a decrease in the T1o tilt with increasing c-axis length while Figure 5.13d shows an decrease in negative tilt for T1m as c-axis length increases. Both are approaching zero tilt as c-axis length increases which is what the tilt model predicts in Figure 3.6a.

Figure 5.13. The T1o tilt versus temperature , T1m tilt versus temperature , T1o tilt versus *c*-axis length and T1m tilt versus c-axis length for the Rietveld refinement results of albite , An27, An35, An46 and the single-crystal refinements of An26.

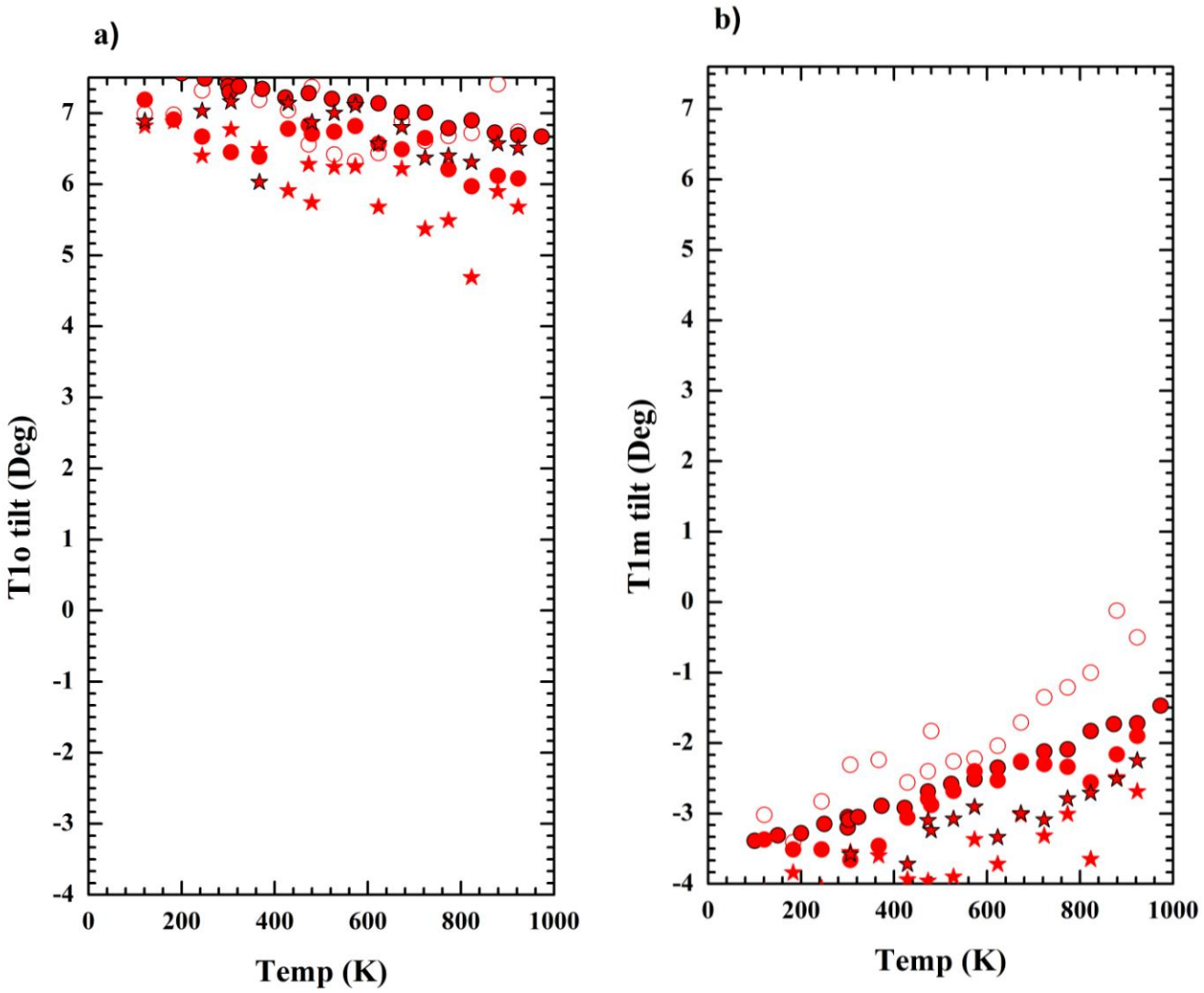

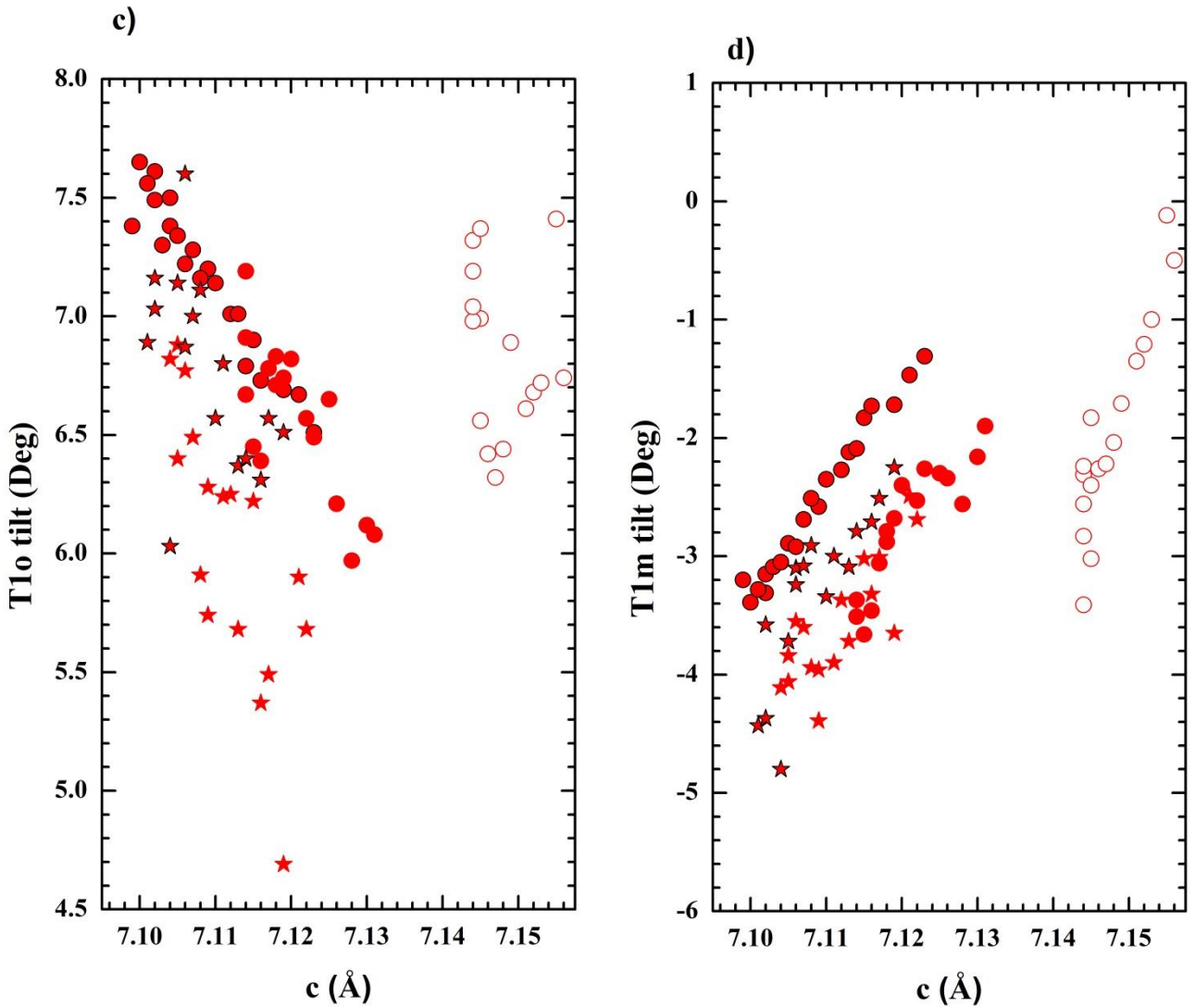

Notes. The T1o tilt versus temperature (a), T1m tilt versus temperature (b), T1o tilt versus c-axis length (c) and T1m tilt versus c-axis length (d) for the Rietveld refinement results of albite (open circles), An27 (solid circles), An35 (solid stars), An46 (starts with black outline) and the single-crystal refinements of An26 (solid circles with black outline).

Figure 5.14. The difference between the value for T1o and T1m versus c-axis length and T2o tilt and T2m tilt versus c-axis length for the Rietveld refinement results of albite ,An27, An35 and An46 and the single-crystal refinements of An26.

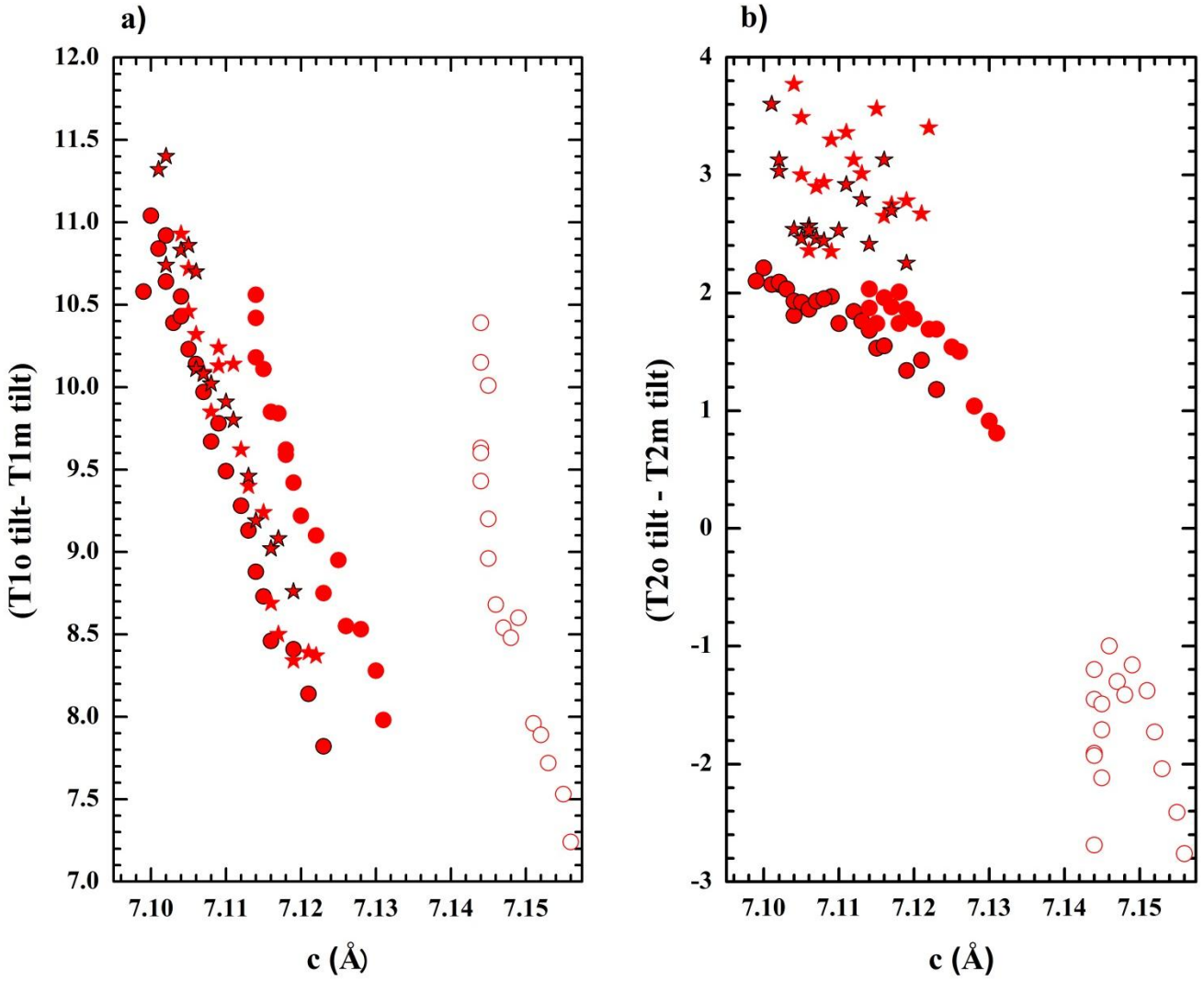

Figure 5.14. The difference between the value for T1o and T1m versus *c*-axis length (a) and T2o tilt and T2m tilt versus c-axis length (b) for the Rietveld refinement results of albite (open circles), An27 (solid circles), An35 (solid stars), An46 (starts with black outline) and the single-crystal refinements of An26 (solid circles with black outline).

As can be seen from Figure 5.14 (a), the difference between the values for the T1o tilt and T1m tilt is decreasing with increasing *c*-axis length and is thus approaching 0 (no tilting). The difference between the value for the T2o and T2m tilt is a different story however. An35 and An46 show scatter between this difference and their respective *c*-axis lengths while An26 and An27 both show a decrease in this difference at *c*-axis length is increasing. Albite, on the other hand, is showing a distinct evolution with respect to the other compositions and the temperature range of data collection. Interestingly, the difference between the T2o tilt and T2m tilt for albite is negative for all data points which are unlike the other compositions. In addition, the *c*-axis length increases steeply with decreasing T2o and T2m tilt difference, but this reaches a maximum around a difference of -1. The fact that this anomalous behavior is seen for albite with respect to the individual T1 and T2 tetrahedral tilting could provide a structural reasoning as to why negative thermal expansion in seen for the c-axis of albite but not that of more Ca-rich *C-1* plagioclase. Further work is required to work out all of the details, however.

5.5 Conclusions

Tilt systems 2 and 3 clearly dominate the evolution of structure with temperature of the Na-rich *C-1* feldspars and this is the same as seen in alkali feldspars. Chapter 3 shows that these two tilt systems affect the length of the *d(100)* plane normal more than other directions within the structure and thus the thermal expansion of Na-rich feldspars is very anisotropic. The anisotropy of thermal expansion decreases with increasing Ca content. The structural data described above in terms of the tilting systems shows that the decrease in anisotropy has its origin in the decrease in the rate at which tilt system 3 changes with temperature. The reason for tilt system 3 (and tilt system 2) changing less with temperature as the Ca content increases *must*

obviously be related to the Ca for Na substitution and the coupled Al for Si substitution in the framework. These two substitutions therefore have some 'opposite' effects on the structure – while Al enlarges the framework size (*e.g.* Angel *et al.,* 1990) and thus the cavities within it; the Ca atom requires a slightly smaller coordination than Na. And, at the same time the Ca forms stronger bonds with the framework oxygen atoms than Na, because it has a higher formal charge. The resulting structural changes to accommodate Ca substitution for Na are therefore complex, but include expansion of the average <<*T*-O>>, increased local distortions of the tetrahedra and changes in all four tilts. While the structural changes with composition would need further detailed analysis and comparison with the model predictions, this is not easy because of the change in size of the real framework (the increase in <<*T*-O>>). Nonetheless, this study has demonstrated that the behavior of *C-1* plagioclase with temperature is dominated by the same mechanisms of structural change as seen in the pure alkali feldspars.

5.6 References

Angel, R.J., Gatta, D.G., Boffa Ballaran, T., and Carpenter, M.A. (2008) The mechanism of coupling in the modulated structure of nepheline. *The Canadian Mineralogist*, **46**: 1465-1476.

Antao, S.M., Hassan, and Parise, J.B. (2003). The structure of danalite at high temperature obtained from synchrotron radiation and Rietveld refinements. *Canadian Mineralogist*, **41**: 1413-1422.

Carpenter, M.A., McConnell, D.C. and Navrotsky, A. (1985) Enthalpies of ordering in the plagioclase feldspar solid solution. *Geochimica et Cosmochimica Acta*, **49**: 947-966.

Cruciani, G., Artioli, G. Gualtieri, A. Stahl, K., Hanson, J.C. (1997) Dehydration dynamics of stilbite using synchrotron X-ray powder diffraction, *The American Mineralogist ,* **82**: 729-739.

Fisher, R. X., V. Kahlenberg, V., Lengauer, C.L., Tillmanns, E (2008) Thermal behavior and structural transformation in the chabazite-type zeolite willhendersonite, $KCaAl_3Si_3O_5H_2O$, *The American Mineralogist ,* **93**: 1317-1325.

Gatta, D.G., Ross, R.J. and Carpenter, M.A. (2010) Low-temperature behavior of natural kalsilite with P31c symmetry: An insitu single-crystal X-ray diffraction study. *American Mineralogist*, **95**: 1027-1034.

Harlow, G.E., Brown, G.E. (1980) Low albite: An X-ray and neutron diffraction study. *American Mineralogist*, **65**: 986-995.

Hassan, I, Antao, S.M. and Parise, J.B. (2004) Sodalite: High-temperature structures obtained from synchrotron radiation and Rietveld refinements. *American Mineralogist*, **89**: 359-364.

Hassan, I. and Grundy, H.D. (1984). The crystal structures of sodalite-group minerals. *Acta crystallographica*. **B40**: 6-13.

Henderson, C.M.B. (1979) An elevated temperature X-ray study of synthetic disordered Na-K alkali feldspars. *Contributions to Mineralogy and Petrology*, **70**: 71-79.

Kimata M., Shimizu M., Saito S. (1996) High-temperature crystal structure of sanidine Part II. The crystal structure of sanidine at 935 C, *European Journal of Mineralogy* **8**:15-24.

Kroll, H and Ribbe, P.H. (1983) Lattice parameters, composition and Al,Si order in alkali feldspars. Pp. 57-100 in: *Feldspar Mineralogy* 2nd edition (P.H. Ribbe, editor). Reviews in Mineralogy **2**, The Mineralogical Society of America, Washington D.C., USA.

Kroll, H., Bambauer, H.U. and Schirmer, U. (1980) The high albite-monalbite and analbite-monablite transitions. *American Mineralogist*, **65**: 1192-1211.

Kroll, H., Ribbe, P.H. (1980) Determinative diagrams for Al,Si order in plagioclases. *American Mineralogist*, **65**: 449-457.

Larson, A. and Von Dreele, R.B. (2004) General structure analysis system (GSAS). *Los Alamos Laboratory Report***, LAUR**: 86-748.

Lee, Y., Seoung, D., Jang, Y., Bai, J., Lee, Y (2011) Structural studies of NH_4-exchanged natrolites at ambient conditions and high temperature , *The American Mineralogist* ,**96**: 1308-1315.

Lehmann, M.S. and Larsen, F.K. (1974) A method for location of the peaks in step-scan-measured Bragg reflexions. *Acta Crystallographica* **A30**: 580-584.

Ohashi, F. and Finger, L.W. (1975) An effect of temperature on the feldspar structure: crystal structure of sanidine at 800°C. *Op. cit.* **74**: 569-572.

Ori, S.,Mazzucato, E., Vezzalini, G. (2009) Dehydration dynamics of barrerite: An insitu synchrotron XRPD study , *The American Mineralogist*, **94**: 64-73.

Prewitt, C.T., Sueno, S., and Papike (1976) Crystal-structures of high albite and monalbite at high temperatures. *American Mineralogist*, **61**: 1213-1225.

Ribbe, P.H., Megaw, H.D., Taylor, W.H. (1969) The albite structures. *Acta Crystallographia B*, **25**: 1503-1518.

Ross, N.L. (2000) Framework structures. In: Hazen, R.M., Downs, R.T. (eds) High-temperature and high-pressure crystal chemistry, Mineralogical Society of America, Washington DC.

Sheldrick, G.M. (2008) A short history of SHELX. *Acta Crystallographica*, **B64**: 112-122.

Smith, J.V., Artioli, G. (1986) Low albite, $NaAlSi_3O_8$: Neutron diffraction study of crystal structure at 13K. *American Mineralogist*, **71**: 727-733.

Toby, B. H. (2001) EXPGUI, a graphical user interface for GSAS. *Journal of Applied Crystallography*, **34**: 210-213.

Tribaudino, M., Bruno, M., Nestola, F., Pasqual, D. Angel, R.J. (2011) Thermoelastic and thermodynamic properties of plagioclase feldspars from thermal expansion measurements. *American Mineralogist*. **96**: 992-1002.

Tribaudino, M., Angel, R.J., Camara, F., Nestola, F, Pasqual, D., Margiolaki, I. (2010) Thermal expansion of plagioclase feldspars. *Contributions to Mineralogy and Petrology*, **160**: 899-908.

Wadoski, E., Armbruster, T., Lazic, B., Fisch, M. (2011) Dehydration of the natural zeolite goosecreekite CaAl2Si6O16 .5H2O upon stepwise heating: A single-crystal and powder X-ray study, *The American Mineralogist* , **96**:1070-1078.

Weast, R.C. (1986) Handbook of Chemistry and Physics: A ready-reference book of chemical and physical data 67th ed. (eds. Astle, M.J. and Beyer, W.H.), CRC Press, Boca Raton FL, USA.

Williams, P.P., Megaw, H.D. (1964) The crystal structures of low and high albites at -180°C. *Acta Crystallographica* **B17**: 882-890.

Winter, J.K., Ghose, S. and Okamura (1977) High-temperature study of thermal expansion and anisotropy of the sodium atom in low albite. *American Mineralogist*, **62**: 921-931.

Chapter 6: Concluding Remarks

6.1 Conclusion

Chapter 2 has shown that for C-1 feldspars at low-temperatures, the effect of Al,Si disorder on the bulk modulus is dependent on the amount of anorthite-component in the structure due to the induced compositional disorder or disorder induced by thermal annealing. The disorder causes the density to increase with increasing substitution of $Ca^{2+}+Al^{3+}$ for $Na^{+}+Si^{4+}$ for more albite-rich feldspars. The difference between the bulk modulus for the completely ordered state versus the completely disordered is greater than for more anorthite rich-feldspars. In addition, all samples from this study showed a parabolic curve in the *f-F* plot: indicative of elastic softening at higher pressures and therefore a 4^{th} order equation of state was fit to each dataset. The nature of elastic softening and the structural reasoning behind the elastic softening had not been successfully described to date.

The tetrahedral tilting model proposed in Chapter 3 provides a clear framework from which to derive the anisotropy and volume expansion seen in feldspars and thus show that the underlying topology of the tetrahedral framework is the main player. Tilt systems 2 and 3 work simultaneously to produce the anisotropy seen in alkali feldspars at pressures up to 4 GPa and at high-temperatures. However, tilt systems 2 and 3 alone do not provide a perfect match to the cell parameters of real feldspars which is partly due to the omission of tilt systems 1 and 4. For volume change requirement reasons, the O-O repulsions control the values of the tilting systems seen in alkali feldspars and the bridging oxygens, directionality of the bonding to the *M*-cation and tilt systems 1 and 4 play a secondary role in pattern of anisotropy.

Through the analysis of high-temperature single crystal X-ray diffraction and the Rietveld analysis of Na-rich plagioclase feldspars, it was possible to calculate the tetrahedral

tilting angles for these samples. The results from the study showed that the structural changes seen in Na-rich feldspars at high-temperature are dominated by the same mechanisms as alkali feldspars at low-pressure and high-temperature. However, the tetrahedral tilting model proposed in Chapter 3 involving tilts 2 and 3 cannot fully describe the structural change in Na-rich plagioclase feldspars (particularly with more Ca-content) at higher temperatures due to complications with the coupled substitution of Ca for Na in the *M*-site and Al for Si in the *T*-sites. The effect that Al has in the volume change is to expand the structure while Ca requires a smaller bonding environment so its effect is contraction. None-the-less, there are clear systematic changes present in the tetrahedral tilts with temperature of which to describe the structural change.

Through the implementation of high-pressure single crystal-ray diffraction on two different crystals of An20 and the re-analysis of an An37 plagioclase, it was possible to resolve the structures with great precision and therefore calculate the tetrahedral tilting systems for these samples. The structural changes at high-pressure of these samples were compared to that of previously collected data on low albite (Benusa *et al.* 2005) and analbite (Curetti *et al.* 2010). Systematic changes with respect to the tetrahedral tilting systems are clear with tilt systems 2 and 3 dominating the structural change in all of the samples up to 4 GPa which is similar to that of alkali feldspars at high-temperature and pressures up to 4 GPa. Tilt system 4 is activated at 4 GPa for all the ordered samples while for analbite this tilt system is not activated until around 8 GPa. The repulsive forces of the Obo-Obm and Odo-Odm non-bonded oxygen atoms play a key role in controlling the progression of tilt system 3 and the activation of tilt system 4. In order to satisfy electrostatic principles and keep the non-bonded oxygen atoms at favorable distances, the volume compression must be accommodated by tilting systems that satisfy this requirement.

The tetrahedral tilting systems clearly provide a systematic approach to describing the structural changes seen in feldspars at high-pressures and high-temperatures. As was described in Chapter 4, the O-O repulsions are players with respect to activation and deactivation of certain tilting systems. It is clear from Figure 6.1 that the roles that the shortest O-O distances play are different with pressure and with temperature. Figure 6.1a and 6.1c show a defined trend with pressure and the data tend to cluster around a more common value for the O-O distances than higher temperature (Figure 6.1b and 6.1d). Figure 6.1b and 6.1d show more scatter with the data and therefore show less of a dependence of these lengths with respect to high-pressure and high-temperature. In addition to this, the O-O distances for the plagioclase samples at high-temperatures are longer than that of the plagioclase samples that are at higher temperatures so it is no surprise that there are differences seen in the systematic changes of the tilt systems.

Figure 6.1. Two of the shortest non-bonded O-O distances for plagioclase at high-temperature and high-pressure.

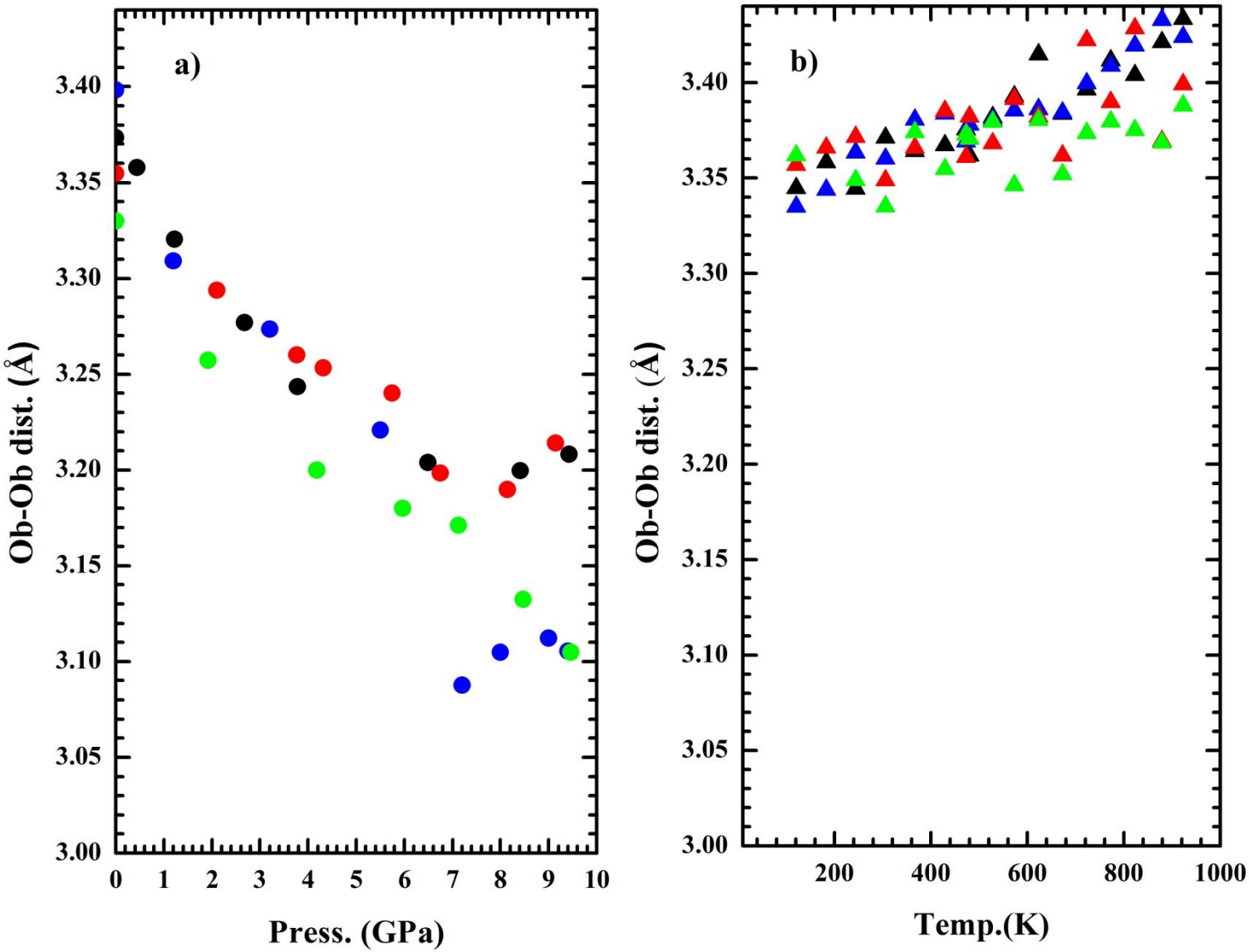

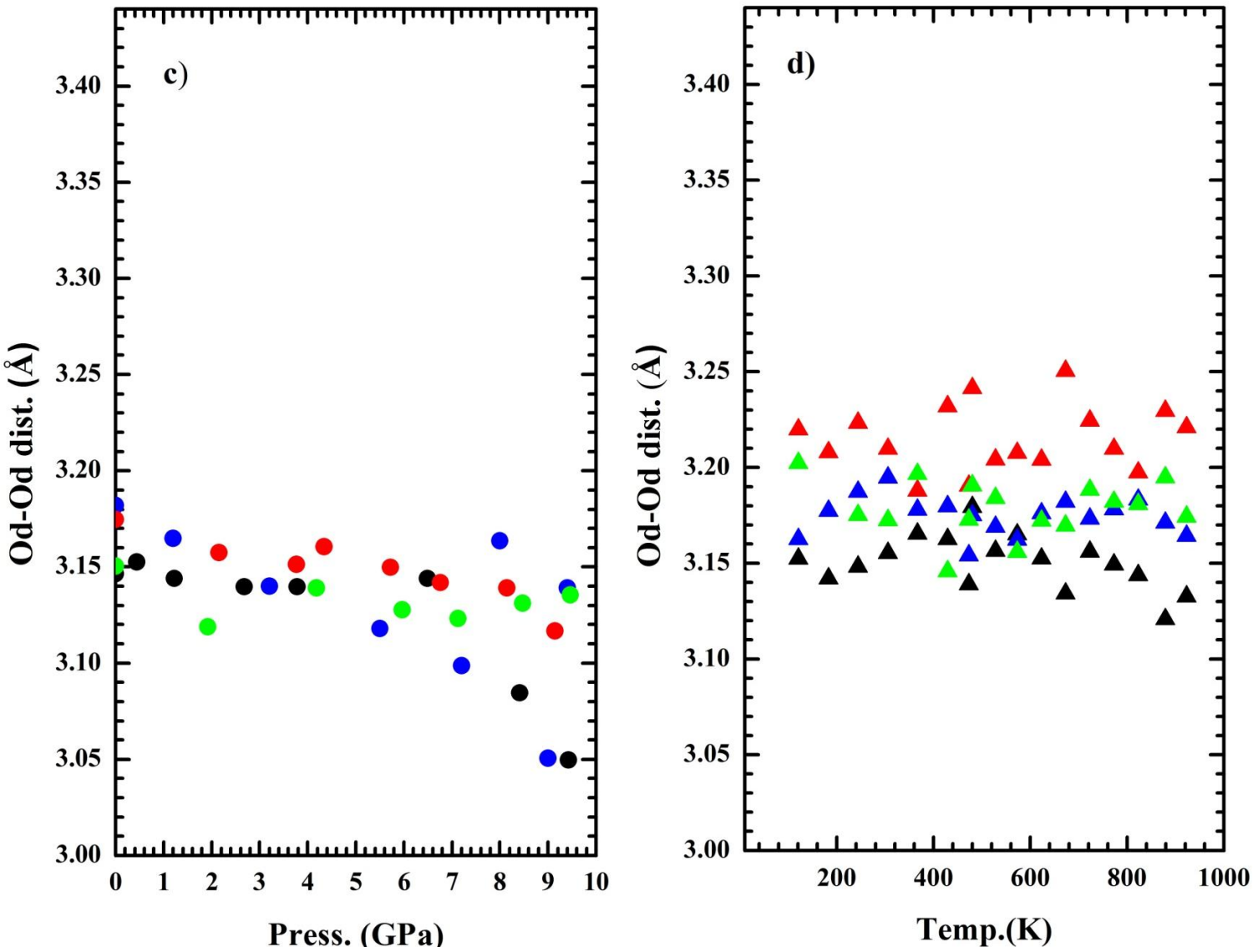

Notes. The short Obo-Obm distance across the mirror versus pressure for the plagioclase sample sin chapter 4 (a) and versus temperature for the plagioclase samples in the chapter 5 (b). Image (c) is the short Odo-Odm distance across the pseudo mirror versus pressure for the plagioclase samples in chapter 4 and in=mage (d) is the short Odo-Odm versus temperature for the plagioclase samples in Chapter 5.

6.2 References

Benusa, M., Angel, R.J., Ross, N.L. (2005) Compression of albite, $NaAlSi_3O_8$. *American Mineralogist*, **90**: 1115-1120.

Curetti, N., Sochalski-Kolbus, L.M., Angel, R.J., Benna, P., Nestola, F., Bruno, E. (2010) High-pressure structural evolution and equation of state of analbite. *American Mineralogist*, **96**: X-X.

Appendix A: Structural Data

Table A.4.1: The combined refinement results for An20 crystal A and (crystal B or crystal C) from room pressure to 9.150(10) GPa.

Press. (GPa)†	ρ_{calc}(g/cm^3)	meas. Ref.	unique ref	refl. $F_o > 4\sigma(F_o)$	GooF	R_1 (F) with $F_o > 4\sigma$(Fo)	wR_2 (F^2)	Weighting Scheme	Residuals (e$^-$/Å^3)
0.0001*	2.651	3151	1200	703	1.019	0.2273	0.1889	0.12,0	-0.80/0.86
2.149(9)*	2.737	3033	1036	622	1.048	0.0819	0.216	0.11,2.52	-0.71/0.65
3.764(9)*	2.797	2960	980	614	1.062	0.072	0.1911	0.1,0	-0.71/0.72
4.341(10)‡	2.818	2988	978	600	1.102	0.0726	0.1983	0.1,0	-0.78/0.99
5.757(10)*	2.868	2918	1224	698	1.45	0.1072	0.2764	0.2,0	-2.02/1.75
6.756(6)*	2.905	2859	1200	613	1.16	0.0948	0.2345	0.1,0	-0.79/0.84
8.144(9)*	2.954	2824	1143	573	1.169	0.0989	0.2355	0.15,0	-0.95/0.92
9.150(10)‡	2.994	2788	1009	512	1.029	0.1073	0.3148	0.19,0	-1.08/1.4

Notes.

† Pressures were calculated using the Equation of state for Quartz (Angel at el. 1999)

* Refers to results from experiments with crystal A and crystal B.

‡ Refers to results from experiments with crystal A and crystal C.

Table A.4.2: The combined refinement results for An37 from room pressure to 9.457(10) GPa.

Press. (GPa)†	ρ_{calc}(g/cm^3)	meas. Ref.	unique ref	refl. $F_o > 4\sigma(F_o)$	GooF	R_1 (F) with $F_o > 4\sigma(Fo)$	wR_2 (F^2)	Weighting Scheme	Residuals (e$^-$/Å^3)
0.0001‡	2.661	3192	1213	741	1.116	0.0696	0.1506	0.048,0.00	-0.58/0.57
1.92(3)‡	2.737	3030	1139	754	1.167	0.0773	0.1657	0.061,0.03	-0.62/0.64
4.18(3)‡	2.816	3380	1070	728	1.114	0.0777	0.1764	0.055,5.62	-0.82/0.7
5.967(9)*	2.874	1394	1153	819	1.095	0.0773	0.165	0.04,13.39	-0.53/0.50
7.128(9)*	2.914	1382	1014	808	1.038	0.0727	0.1617	0.04,10.67	-0.67/0.61
8.477(10)*	2.958	1385	794	657	1.115	0.0733	0.1688	0.02,24.65	-0.57/0.47
9.457(10)*	2.991	1383	944	760	1.118	0.096	0.219	0.05,32.52	-0.69/0.49

Notes.

† Pressures were calculated using the Equation of state for Quartz (Angel *at el.* 1999)

‡ Refers to results from experiments with two crystals in the DAC

*Refers to results from experiments with 1 crystal

Table A.4.3: Atomic positions and displacements parameters for An20 (T,M and O sites).

Atom	Pressure	x	y	z	Ueq	Atom	Pressure	x	y	z	Ueq
Na	0.0001	0.2688(9)	-.0128(6)	0.1566(14)	0.043(2)	**Ca**	0.0001	0.2746(18)	0.0267(11)	0.096(3)	0.024(3)
	2.149(9)	0.2626(8)	-.0104(6)	0.1545(14)	0.038(2)		2.149(9)	0.2744(18)	0.0282(11)	0.104(3)	0.020(4)
	3.764(9)	0.2585(9)	-.0097(6)	0.1542(12)	0.033(2)		3.764(9)	0.269(2)	0.0272(11)	0.099(3)	0.025(3)
	4.341(10)	0.2578(11)	-.0107(6)	0.1547(15)	0.034(2)		4.341(10)	0.269(3)	0.0274(11)	0.103(3)	0.021(3)
	5.717(10)	0.2540(11)	-.0098(6)	0.1547(15)	0.031(2)		5.717(10)	0.267(2)	0.0285(11)	0.104(3)	0.020(4)
	6.756(6)	0.2525(8)	-.0095(6)	0.1578(12)	0.027(2)		6.756(6)	0.2655(18)	0.0299(11)	0.104(3)	0.019(3)
	8.144(9)	0.2520(11)	-.0095(6)	0.1627(14)	0.027(2)		8.144(9)	0.258(3)	0.0287(12)	0.104(3)	0.019(4)
	9.150(10)	0.2501(14)	-.0091(11)	0.1678(16)	0.031(3)		9.150(10)	0.261(3)	0.028(3)	0.104(3)	0.026(5)

Atom	Pressure	x	y	z	Uiso	Atom	Pressure	x	y	z	Uiso
T1o	0.0001	0.0074(3)	0.1671(2)	0.2106(6)	0.017	**T1m**	0.0001	0.0042(3)	0.8186(2)	0.2342(6)	0.014
	2.149(9)	0.0052(4)	0.1655(2)	0.2101(6)	0.017		2.149(9)	0.0008(3)	0.8186(2)	0.2342(6)	0.014
	3.764(9)	0.0030(3)	0.1646(2)	0.2080(6)	0.017		3.764(9)	-.0016(3)	0.81819(18)	0.2337(6)	0.014
	4.341(10)	0.0022(3)	0.1645(2)	0.2081(6)	0.017		4.341(10)	-.0028(3)	0.8184(2)	0.2323(4)	0.014
	5.717(10)	0.0011(4)	0.1641(2)	0.2072(6)	0.017		5.717(10)	-.0046(4)	0.8176(2)	0.2332(6)	0.014
	6.756(6)	-.0013(4)	0.1638(2)	0.2060(6)	0.017		6.756(6)	-.0070(3)	0.8172(2)	0.2328(6)	0.014
	8.144(9)	-.0037(6)	0.1642(2)	0.2057(6)	0.017		8.144(9)	-.0095(4)	0.8168(2)	0.2321(6)	0.014
	9.150(10)	-.0062(6)	0.1655(4)	0.2070(6)	0.017		9.150(10)	-.0135(4)	0.8175(3)	0.2312(6)	0.014

Atom	Pressure	x	y	z	Uiso	Atom	Pressure	x	y	z	Uiso
T2o	0.0001	0.6895(3)	0.10969(18)	0.3164(6)	0.015	**T2m**	0.0001	0.6826(3)	0.88019(18)	0.3591(6)	0.015
	2.149(9)	0.6853(3)	0.1082(2)	0.3131(6)	0.015		2.149(9)	0.6758(3)	0.8793(2)	0.3571(6)	0.015
	3.764(9)	0.6828(3)	0.10690(18)	0.3112(6)	0.015		3.764(9)	0.6700(3)	0.87816(18)	0.3560(6)	0.015
	4.341(10)	0.6831(3)	0.1066(2)	0.3129(4)	0.015		4.341(10)	0.6681(3)	0.8776(2)	0.3556(4)	0.015
	5.717(10)	0.6819(4)	0.1059(2)	0.3116(6)	0.015		5.717(10)	0.6644(4)	0.8765(2)	0.3550(6)	0.015
	6.756(6)	0.6809(4)	0.1048(2)	0.3099(6)	0.015		6.756(6)	0.6606(4)	0.8759(2)	0.3543(6)	0.015

	8.144(9)	0.6807(4)	0.1041(2)	0.3098(6)	0.015		8.144(9)	0.6569(4)	0.8748(2)	0.3539(6)	0.015
	9.150(10)	0.6806(4)	0.1032(4)	0.3112(6)	0.015		9.150(10)	0.6523(6)	0.8740(3)	0.3520(6)	0.015

Atom	Pressure	x	y	z	Uiso	Atom	Pressure	x	y	z	Uiso
OA1	0.0001	0.0048(8)	0.1318(6)	-.0257(12)	0.02	**OA2**	0.0001	0.5898(8)	0.9950(6)	0.2809(12)	0.022
	2.149(9)	0.0042(9)	0.1292(6)	-.0273(13)	0.02		2.149(9)	0.5803(9)	0.9924(6)	0.2762(13)	0.022
	3.764(9)	0.0073(8)	0.1288(6)	-.0263(12)	0.02		3.764(9)	0.5754(8)	0.9928(6)	0.2798(12)	0.022
	4.341(10)	0.0068(8)	0.1281(6)	-.0257(11)	0.02		4.341(10)	0.5741(8)	0.9933(6)	0.2816(11)	0.022
	5.717(10)	0.0083(11)	0.1290(6)	-.0263(13)	0.02		5.717(10)	0.5695(11)	0.9925(6)	0.2838(13)	0.022
	6.756(6)	0.0085(9)	0.1293(6)	-.0267(13)	0.02		6.756(6)	0.5683(9)	0.9914(6)	0.2853(13)	0.022
	8.144(9)	0.0073(11)	0.1287(6)	-.0274(15)	0.02		8.144(9)	0.5663(11)	0.9919(6)	0.2872(15)	0.022
	9.150(10)	0.0099(12)	0.1310(9)	-.0266(14)	0.02		9.150(10)	0.5615(12)	0.9922(9)	0.2908(15)	0.022

Atom	Pressure	x	y	z	Uiso	Atom	Pressure	x	y	z	Uiso
Obo	0.0001	0.8140(8)	0.1086(6)	0.1907(13)	0.024	**Obm**	0.0001	0.8215(9)	0.8518(6)	0.2547(12)	0.025
	2.149(9)	0.8096(9)	0.1044(6)	0.1858(13)	0.024		2.149(9)	0.8136(9)	0.8505(6)	0.2503(13)	0.025
	3.764(9)	0.8082(9)	0.1002(6)	0.1814(13)	0.024		3.764(9)	0.8060(8)	0.8482(6)	0.2461(12)	0.025
	4.341(10)	0.8084(8)	0.0995(6)	0.1841(11)	0.024		4.341(10)	0.8046(8)	0.8471(6)	0.2452(11)	0.025
	5.717(10)	0.8044(11)	0.0970(7)	0.1806(14)	0.024		5.717(10)	0.7996(11)	0.8454(6)	0.2429(14)	0.025
	6.756(6)	0.8043(11)	0.0947(6)	0.1766(14)	0.024		6.756(6)	0.7965(11)	0.8454(6)	0.2390(13)	0.025
	8.144(9)	0.8003(11)	0.0919(6)	0.1731(16)	0.024		8.144(9)	0.7898(12)	0.8424(6)	0.2327(16)	0.025
	9.150(10)	0.7983(12)	0.0914(9)	0.1711(15)	0.024		9.150(10)	0.7794(12)	0.8389(9)	0.2258(15)	0.025

Atom	Pressure	x	y	z	Uiso	Atom	Pressure	x	y	z	Uiso
Oco	0.0001	0.0149(8)	0.2984(6)	0.2750(12)	0.024	**Ocm**	0.0001	0.0191(9)	0.6915(6)	0.2216(12)	0.023
	2.149(9)	0.0055(9)	0.2958(6)	0.2731(14)	0.024		2.149(9)	0.0139(9)	0.6907(6)	0.2175(14)	0.023
	3.764(9)	-.0028(8)	0.2959(6)	0.2744(12)	0.024		3.764(9)	0.0137(8)	0.6901(6)	0.2154(13)	0.023
	4.341(10)	-.0066(8)	0.2945(6)	0.2711(11)	0.024		4.341(10)	0.0112(8)	0.6898(6)	0.2147(11)	0.023
	5.717(10)	-.0148(11)	0.2941(7)	0.2728(14)	0.024		5.717(10)	0.0120(11)	0.6906(7)	0.2161(14)	0.023

	6.756(6)	-.0169(11)	0.2930(6)	0.2753(13)	0.024		6.756(6)	0.0130(9)	0.6901(6)	0.2179(13)	0.023
	8.144(9)	-.0244(11)	0.2932(6)	0.2725(15)	0.024		8.144(9)	0.0117(11)	0.6889(6)	0.2184(15)	0.023
	9.150(10)	-.0314(12)	0.2939(11)	0.2700(15)	0.024		9.150(10)	0.0102(12)	0.6884(11)	0.2194(15)	0.023

Atom	**Pressure**	**x**	**y**	**z**	**Uiso**	**Atom**	**Pressure**	**x**	**y**	**z**	**Uiso**
Odo	0.0001	0.2035(8)	0.1095(6)	0.3873(12)	0.023	**Odm**	0.0001	0.1871(9)	0.8659(6)	0.4307(13)	0.029
	2.149(9)	0.2038(9)	0.1101(6)	0.3874(13)	0.023		2.149(9)	0.1839(11)	0.8666(6)	0.4337(14)	0.029
	3.764(9)	0.2054(8)	0.1119(6)	0.3864(12)	0.023		3.764(9)	0.1850(9)	0.8679(6)	0.4347(14)	0.029
	4.341(10)	0.2074(8)	0.1115(6)	0.3870(11)	0.023		4.341(10)	0.1829(9)	0.8667(6)	0.4360(12)	0.029
	5.717(10)	0.2080(11)	0.1129(6)	0.3873(14)	0.023		5.717(10)	0.1810(12)	0.8679(7)	0.4341(15)	0.029
	6.756(6)	0.2091(9)	0.1144(6)	0.3883(13)	0.023		6.756(6)	0.1767(11)	0.8697(6)	0.4347(15)	0.029
	8.144(9)	0.2092(11)	0.1162(6)	0.3906(16)	0.023		8.144(9)	0.1711(12)	0.8710(7)	0.4347(18)	0.029
	9.150(10)	0.2076(12)	0.1184(9)	0.3903(15)	0.023		9.150(10)	0.1650(12)	0.8751(11)	0.4372(16)	0.029

Table A.4.4: Atomic positions and displacements parameters for An37 (T, M and O sites).

Atom	Pressure	x	y	z	Ueq	Atom	Pressure	x	y	z	Ueq
Na	0	0.2682(7)	-.0178(6)	0.1626(9)	0.0303(17)	**Ca**	0	0.2723(7)	0.0277(4)	0.1015(8)	0.0228(11)
	1.92	0.2634(8)	-.0149(6)	0.1626(11)	0.0291(18)		1.92	0.2678(7)	0.0265(4)	0.1012(9)	0.0216(12)
	4.18	0.2602(9)	-.0141(7)	0.1640(11)	0.027(2)		4.18	0.2649(8)	0.0261(6)	0.1018(11)	0.0214(14)
	5.97	0.2557(12)	-.0141(6)	0.163(3)	0.047(10)		5.97	0.2635(11)	0.0279(4)	0.104(3)	0.031(8)
	7.13	0.2550(13)	-.0137(6)	0.168(3)	0.044(11)		7.13	0.2625(13)	0.0271(6)	0.105(3)	0.039(10)
	8.48	0.2609(18)	0.0276(6)	0.103(5)	0.040(12)		8.48	0.254(3)	-.0142(8)	0.175(5)	0.068(13)
	9.46	0.262(2)	0.0267(6)	0.109(5)	0.042(13)		9.46	0.251(3)	-.0141(8)	0.171(5)	0.048(13)

Atom	Pressure	x	y	z	Uiso	Atom	Pressure	x	y	z	Uiso
T1o	0	0.0072(3)	0.16568(16)	0.2135(3)	0.0122(4)	**T1m**	0	0.0040(2)	0.81734(16)	0.2319(3)	0.0124(4)
	1.92	0.0053(3)	0.16447(18)	0.2136(4)	0.0130(4)		1.92	0.0015(3)	0.81716(16)	0.2313(3)	0.0131(4)
	4.18	0.0028(3)	0.1631(2)	0.2122(4)	0.0139(5)		4.18	-.0015(3)	0.8164(2)	0.2309(4)	0.0132(5)
	5.97	0.0011(4)	0.16252(15)	0.2111(11)	0.0191(5)		5.97	-.0039(4)	0.81601(14)	0.2304(11)	0.0175(5)
	7.13	0.0000(6)	0.16208(18)	0.2102(12)	0.0203(6)		7.13	-.0054(6)	0.81590(16)	0.2303(11)	0.0183(6)
	8.48	-.0031(6)	0.1621(2)	0.2082(15)	0.0251(8)		8.48	-.0085(6)	0.8152(2)	0.2298(13)	0.0235(8)
	9.46	-.0022(7)	0.1617(2)	0.2109(16)	0.0280(9)		9.46	-.0091(7)	0.8151(2)	0.2301(15)	0.0239(8)

Atom	Pressure	x	y	z	Uiso	Atom	Pressure	x	y	z	Uiso
T2o	0	0.6872(2)	0.10962(15)	0.3182(3)	0.0116(4)	**T2m**	0	0.6820(2)	0.87968(15)	0.3564(3)	0.0111(4)
	1.92	0.6838(3)	0.10853(16)	0.3159(3)	0.0115(4)		1.92	0.6766(3)	0.87848(16)	0.3554(3)	0.0117(4)
	4.18	0.6809(3)	0.1074(2)	0.3138(4)	0.0127(5)		4.18	0.6705(3)	0.8774(2)	0.3549(4)	0.0117(5)
	5.97	0.6810(4)	0.10559(14)	0.3149(11)	0.0152(5)		5.97	0.6669(4)	0.87598(14)	0.3564(11)	0.0154(5)
	7.13	0.6806(6)	0.10491(16)	0.3140(12)	0.0155(5)		7.13	0.6640(6)	0.87490(16)	0.3548(12)	0.0164(5)
	8.48	0.6798(6)	0.1040(2)	0.3128(15)	0.0212(8)		8.48	0.6618(7)	0.8742(2)	0.3567(15)	0.0214(8)
	9.46	0.6802(7)	0.1037(2)	0.3146(16)	0.0219(8)		9.46	0.6582(8)	0.8735(2)	0.3522(18)	0.0229(8)

Atom	Pressure	x	y	z	Uiso	Atom	Pressure	x	y	z	Uiso

OA1	0	0.0025(6)	0.1308(4)	-.0209(8)	0.0226(11)	**OA2**	0	0.5856(6)	0.9924(4)	0.2794(7)	0.0150(10)
	1.92	0.0027(7)	0.1292(6)	-.0224(9)	0.0249(13)		1.92	0.5776(6)	0.9924(4)	0.2800(8)	0.0168(11)
	4.18	0.0034(8)	0.1275(6)	-.0230(11)	0.0261(14)		4.18	0.5717(7)	0.9909(6)	0.2801(9)	0.0174(12)
	5.97	0.0028(12)	0.1283(6)	-.023(3)	0.0391(17)		5.97	0.5686(8)	0.9908(3)	0.280(3)	0.0166(11)
	7.13	0.0046(14)	0.1280(6)	-.022(3)	0.0398(19)		7.13	0.5653(11)	0.9909(4)	0.280(3)	0.0170(12)
	8.48	0.0044(18)	0.1277(7)	-.025(5)	0.044(2)		8.48	0.5637(12)	0.9892(6)	0.282(3)	0.0277(18)
	9.46	0.005(3)	0.1273(7)	-.026(5)	0.048(3)		9.46	0.5624(15)	0.9902(6)	0.287(3)	0.0246(18)

Atom	**Pressure**	**x**	**y**	**z**	**Uiso**	**Atom**	**Pressure**	**x**	**y**	**z**	**Uiso**
Obo	0	0.8147(6)	0.1078(4)	0.1927(8)	0.0199(11)	**Obm**	0	0.8181(7)	0.8525(4)	0.2476(8)	0.0265(12)
	1.92	0.8117(7)	0.1033(4)	0.1876(9)	0.0218(12)		1.92	0.8132(8)	0.8523(6)	0.2447(11)	0.0291(13)
	4.18	0.8099(8)	0.0986(6)	0.1858(11)	0.0250(14)		4.18	0.8066(9)	0.8505(6)	0.2424(11)	0.0294(15)
	5.97	0.8076(11)	0.0955(4)	0.184(3)	0.0262(13)		5.97	0.8004(11)	0.8476(4)	0.238(3)	0.0297(14)
	7.13	0.8040(12)	0.0934(4)	0.177(3)	0.0262(15)		7.13	0.7951(12)	0.8453(6)	0.230(3)	0.0292(15)
	8.48	0.8056(15)	0.0896(6)	0.181(3)	0.031(2)		8.48	0.7913(15)	0.8437(6)	0.232(3)	0.034(2)
	9.46	0.8024(18)	0.0894(6)	0.175(5)	0.036(2)		9.46	0.7868(18)	0.8450(6)	0.225(5)	0.033(2)

Atom	**Pressure**	**x**	**y**	**z**	**Uiso**	**Atom**	**Pressure**	**x**	**y**	**z**	**Uiso**
Oco	0	0.0133(6)	0.2933(4)	0.2760(8)	0.0198(11)	**Ocm**	0	0.0166(7)	0.6886(4)	0.2189(8)	0.0213(11)
	1.92	0.0063(7)	0.2924(6)	0.2764(11)	0.0233(12)		1.92	0.0138(7)	0.6885(6)	0.2154(11)	0.0244(12)
	4.18	-.0044(8)	0.2910(6)	0.2765(11)	0.0243(13)		4.18	0.0107(8)	0.6877(6)	0.2145(11)	0.0264(14)
	5.97	-.0097(11)	0.2897(4)	0.277(3)	0.0242(13)		5.97	0.0097(11)	0.6870(4)	0.211(3)	0.0298(14)
	7.13	-.0154(11)	0.2891(4)	0.277(3)	0.0256(15)		7.13	0.0089(13)	0.6868(6)	0.211(3)	0.0355(17)
	8.48	-.0205(14)	0.2892(6)	0.275(3)	0.032(2)		8.48	0.0099(16)	0.6858(7)	0.215(5)	0.044(2)
	9.46	-.0228(16)	0.2892(6)	0.278(3)	0.030(2)		9.46	0.0109(18)	0.6863(7)	0.219(5)	0.041(2)

Atom	**Pressure**	**x**	**y**	**z**	**Uiso**	**Atom**	**Pressure**	**x**	**y**	**z**	**Uiso**
Odo	0	0.1987(6)	0.1092(4)	0.3843(8)	0.0214(11)	**Odm**	0	0.1892(7)	0.8674(4)	0.4286(8)	0.0238(12)
	1.92	0.2015(7)	0.1085(4)	0.3846(9)	0.0223(12)		1.92	0.1878(8)	0.8678(6)	0.4293(11)	0.0263(13)

4.18	0.2026(8)	0.1120(6)	0.3838(11)	0.0255(14)	4.18	0.1858(9)	0.8684(6)	0.4312(11)	0.0282(15)
5.97	0.2021(12)	0.1119(4)	0.380(3)	0.0323(15)	5.97	0.1799(12)	0.8682(4)	0.427(3)	0.0316(14)
7.13	0.2025(14)	0.1131(6)	0.379(3)	0.0352(18)	7.13	0.1755(14)	0.8692(6)	0.426(3)	0.0345(17)
8.48	0.198(2)	0.1145(6)	0.374(5)	0.043(2)	8.48	0.175(2)	0.8696(7)	0.429(5)	0.045(2)
9.46	0.202(3)	0.1161(7)	0.382(5)	0.041(2)	9.46	0.175(3)	0.8703(7)	0.436(5)	0.044(3)

Table A.4.5: T-O bond lengths, M-O bond lengths and T-O-T angles for the single-crystal high-pressure refinement results for An20.

T1o-O Bonds (Å)	Press.†	Oa1	Obo	Oco	Odo	AVG*	AV*	QE*	Volume*
	0.0001	1.707(9)	1.705(6)	1.713(7)	1.727(6)	1.713	28.538	1.0074	2.551
	2.149(9)	1.709(9)	1.698(7)	1.692(9)	1.706(7)	1.7012	35.24	1.009	2.493
	3.764(9)	1.697(9)	1.688(6)	1.708(7)	1.697(6)	1.6975	42.063	1.0111	2.469
	4.341(10)	1.693(7)	1.684(6)	1.687(7)	1.709(7)	1.6933	42.793	1.011	2.452
	5.717(10)	1.690(9)	1.695(9)	1.696(10)	1.699(9)	1.695	46.077	1.012	2.456
	6.756(6)	1.688(9)	1.676(7)	1.688(9)	1.704(7)	1.689	51.339	1.0134	2.423
	8.144(9)	1.692(9)	1.686(9)	1.685(9)	1.702(9)	1.6912	57.184	1.0148	2.427
	9.150(10)	1.706(9)	1.679(10)	1.675(12)	1.687(10)	1.6868	58.493	1.0151	2.408

T1m-O bonds (Å)	Press.†	Oa1	Obm	Ocm	Odm	AVG*	AV*	QE*	Volume*
	0.0001	1.629(7)	1.609(6)	1.634(7)	1.619(9)	1.6227	4.909	1.0013	2.187
	2.149(9)	1.632(7)	1.603(7)	1.633(9)	1.608(9)	1.619	5.976	1.0017	2.172
	3.764(9)	1.628(7)	1.610(6)	1.630(7)	1.619(9)	1.6218	8.351	1.0022	2.182
	4.341(10)	1.628(7)	1.604(6)	1.633(7)	1.613(7)	1.6195	6.988	1.0019	2.173
	5.717(10)	1.622(7)	1.602(7)	1.609(9)	1.601(10)	1.6085	9.157	1.0023	2.129
	6.756(6)	1.619(7)	1.587(7)	1.609(7)	1.599(10)	1.6035	9.072	1.0023	2.108
	8.144(9)	1.620(9)	1.581(9)	1.615(9)	1.587(11)	1.6007	11.149	1.003	2.095
	9.150(10)	1.599(10)	1.591(9)	1.627(13)	1.601(10)	1.6045	10.752	1.0029	2.111

T2o-O bonds (Å)	Press.†	Oa2	Obo	Ocm	Odm	AVG*	AV*	QE*	Volume*
	0.0001	1.644(6)	1.627(7)	1.642(6)	1.638(9)	1.6377	8.414	1.0021	2.25
	2.149(9)	1.659(7)	1.616(7)	1.636(7)	1.633(9)	1.636	8.652	1.0021	2.239
	3.764(9)	1.641(6)	1.625(7)	1.619(6)	1.628(9)	1.6282	8.821	1.0022	2.208
	4.341(10)	1.634(7)	1.614(6)	1.630(7)	1.613(9)	1.6227	10.08	1.0025	2.185
	5.717(10)	1.642(9)	1.597(9)	1.623(7)	1.626(10)	1.622	9.433	1.0023	2.182

	6.756(6)	1.640(7)	1.608(9)	1.609(7)	1.633(10)	1.6225	8.838	1.0022	2.185
	8.144(9)	1.628(9)	1.594(9)	1.600(7)	1.633(11)	1.6137	11.522	1.003	2.147
	9.150(10)	1.631(12)	1.594(9)	1.600(11)	1.613(10)	1.6095	17.517	1.0044	2.125

T2m-O bonds (Å)	**Press.†**	**Oa2**	**Obm**	**Oco**	**Odo**	**AVG***	**AV***	**QE***	**Volume***
	0.0001	1.658(6)	1.635(7)	1.604(7)	1.622(9)	1.6298	7.377	1.0018	2.217
	2.149(9)	1.637(6)	1.622(7)	1.609(9)	1.621(9)	1.6223	8.007	1.002	2.186
	3.764(9)	1.638(6)	1.616(6)	1.598(7)	1.626(9)	1.6195	7.492	1.0019	2.175
	4.341(10)	1.642(7)	1.620(6)	1.610(7)	1.622(7)	1.6235	8.911	1.0022	2.188
	5.717(10)	1.640(9)	1.610(9)	1.616(9)	1.619(9)	1.6213	10.396	1.0026	2.178
	6.756(6)	1.620(7)	1.623(7)	1.603(9)	1.613(9)	1.6148	7.532	1.0019	2.155
	8.144(9)	1.626(7)	1.629(9)	1.601(9)	1.599(10)	1.6137	10.06	1.0025	2.148
	9.150(10)	1.627(12)	1.618(9)	1.593(10)	1.613(10)	1.6128	14.339	1.0037	2.142

Na-O bonds (Å)	**Press.†**	**Oa1**	**Oa1_$**	**Oa2**	**Obo**	**Odo**	**AVG**
	0.0001	2.504(9)	2.732(9)	2.365(9)	2.498(12)	2.421(11)	2.504
	2.149(9)	2.426(10)	2.634(9)	2.299(9)	2.441(12)	2.375(11)	2.435
	3.764(9)	2.397(9)	2.572(9)	2.264(9)	2.391(11)	2.347(10)	2.3942
	4.341(10)	2.370(9)	2.568(11)	2.249(9)	2.399(10)	2.338(9)	2.3848
	5.717(10)	2.352(11)	2.534(10)	2.220(10)	2.375(13)	2.319(12)	2.36
	6.756(6)	2.334(9)	2.522(9)	2.208(9)	2.357(11)	2.303(10)	2.3448
	8.144(9)	2.302(11)	2.512(10)	2.178(10)	2.354(12)	2.296(12)	2.3284
	9.150(10)	2.316(13)	2.506(17)	2.142(13)	2.375(13)	2.277(13)	2.3232

Ca-O bonds (Å)	**Press.†**	**Oa1**	**Oa1_$**	**Oa2**	**Obo**	**Ocm**	**Odo**	**AVG**
	0.0001	2.402(14)	2.935(13)	2.353(14)	2.447(18)	2.751(14)	2.555(17)	2.5738
	2.149(9)	2.346(14)	2.869(13)	2.256(15)	2.418(18)	2.675(13)	2.485(17)	2.5082

3.764(9)	2.280(15)	2.822(14)	2.238(15)	2.325(18)	2.679(15)	2.475(18)	2.4698	
4.341(10)	2.274(18)	2.802(13)	2.215(18)	2.351(18)	2.654(13)	2.438(17)	2.4557	
5.717(10)	2.238(15)	2.793(14)	2.187(17)	2.325(19)	2.647(15)	2.414(18)	2.434	
6.756(6)	2.207(14)	2.786(12)	2.186(14)	2.296(17)	2.626(13)	2.401(18)	2.417	
8.144(9)	2.162(14)	2.706(18)	2.196(17)	2.252(18)	2.638(18)	2.393(18)	2.3912	
9.150(10)	2.17(3)	2.73(2)	2.13(2)	2.22(2)	2.61(2)	2.42(2)	2.38	

T-O-T angles (°)	**Press.†**	**T-OA1-T**	**T-OA2-T**	**T-Obo-T**	**T-Obm-T**	**T-Oco-T**	**T-Ocm-T**	**T-Odo-T**	**T-Odm-T**
	0.0001	141.6(4)	129.4(4)	139.0(6)	160.5(5)	130.2(4)	134.0(5)	133.6(4)	150.7(5)
	2.149(9)	140.3(5)	128.0(4)	136.6(6)	159.0(6)	128.7(4)	133.9(5)	134.8(5)	153.1(5)
	3.764(9)	140.0(4)	128.1(4)	134.1(6)	157.5(6)	125.9(4)	135.1(4)	135.9(4)	152.7(5)
	4.341(10)	139.6(5)	128.0(4)	134.3(4)	157.6(5)	125.5(4)	135.8(5)	135.3(4)	155.0(5)
	5.717(10)	140.2(5)	127.4(5)	132.4(6)	156.4(6)	122.4(5)	136.1(6)	136.3(5)	154.2(5)
	6.756(6)	140.4(4)	128.1(4)	130.6(6)	155.2(6)	122.5(4)	133.5(4)	137.4(5)	155.2(5)
	8.144(9)	139.7(5)	128.3(5)	127.8(7)	152.6(7)	120.6(4)	132.7(5)	139.0(5)	156.5(6)
	9.150(10)	141.4(8)	126.4(9)	126.2(7)	149.5(6)	119.1(6)	133.0(7)	140.1(6)	157.2(8)

Notes.

* Calculated using CifReader

† Pressures were calculated using the Equation of state for Quartz (Angel *at el.* 1999)

$ The longer of the two OA1 bonds

Table A.5.1: T-O bond lengths, M-O bond lengths and T-O-T angles for the Rietveld refinement results for albite (An0).

T1o-O bonds (Å)	Binning[1] (K)	Ave (K)[2]	OA1	OBO	OCO	ODO	AVE.
	90 - 152	121	1.749(7)	1.743(6)	1.747(6)	1.726(6)	1.741
	153 - 213	183	1.767(9)	1.731(7)	1.745(7)	1.735(7)	1.745
	214 - 275	244	1.767(10)	1.733(9)	1.752(9)	1.727(9)	1.745
	279 - 336	306	1.761(10)	1.717(9)	1.753(9)	1.710(9)	1.735
	337 - 398	367	1.781(10)	1.709(9)	1.760(9)	1.698(9)	1.737
	399 - 459	429	1.770(9)	1.720(7)	1.754(7)	1.711(9)	1.739
	460 - 500	480	1.763(9)	1.727(7)	1.761(7)	1.708(9)	1.740
	452 - 494	473	1.770(5)	1.727(5)	1.747(5)	1.728(5)	1.743
	512 - 544	528	1.776(5)	1.724(5)	1.746(5)	1.722(5)	1.742
	552- 594	573	1.780(5)	1.718(5)	1.752(5)	1.720(5)	1.743
	602 - 644	623	1.770(5)	1.725(5)	1.740(5)	1.735(5)	1.743
	652 - 694	673	1.775(5)	1.739(5)	1.725(5)	1.722(5)	1.740
	702 - 744	723	1.778(5)	1.714(5)	1.723(5)	1.736(5)	1.738
	752 -794	773	1.774(5)	1.718(5)	1.734(5)	1.727(5)	1.738
	802 - 844	823	1.752(5)	1.739(5)	1.722(5)	1.724(5)	1.734
	863 - 894	879	1.757(5)	1.731(5)	1.720(5)	1.726(5)	1.734
	902 - 944	923	1.761(5)	1.717(5)	1.733(5)	1.727(5)	1.735

T1m-O bonds (Å)	Binning[1] (K)	Ave (K)[2]	OA1	OBM	OCM	ODM	AVE.
	90 - 152	121	1.603(7)	1.593(6)	1.634(6)	1.613(6)	1.611
	153 - 213	183	1.583(9)	1.599(7)	1.636(7)	1.598(7)	1.604
	214 - 275	244	1.582(9)	1.600(9)	1.634(9)	1.584(9)	1.600
	279 - 336	306	1.568(9)	1.618(9)	1.640(9)	1.583(9)	1.602
	337 - 398	367	1.550(10)	1.623(9)	1.638(9)	1.608(9)	1.605

399 - 459	429	1.574(9)	1.616(9)	1.633(7)	1.589(7)	1.603
460 - 500	480	1.570(9)	1.615(9)	1.640(7)	1.598(7)	1.606
452 - 494	473	1.606(5)	1.594(5)	1.635(5)	1.615(5)	1.613
512 - 544	528	1.596(5)	1.597(5)	1.638(5)	1.604(5)	1.609
552- 594	573	1.586(5)	1.599(5)	1.646(5)	1.602(5)	1.608
602 - 644	623	1.593(5)	1.604(5)	1.646(5)	1.603(5)	1.612
652 - 694	673	1.591(5)	1.589(5)	1.630(5)	1.615(5)	1.606
702 - 744	723	1.584(5)	1.600(5)	1.647(5)	1.590(5)	1.605
752 -794	773	1.584(5)	1.598(5)	1.646(5)	1.603(5)	1.608
802 - 844	823	1.593(5)	1.586(5)	1.632(5)	1.624(5)	1.609
863 - 894	879	1.582(5)	1.583(5)	1.636(5)	1.629(5)	1.608
902 - 944	923	1.590(5)	1.593(5)	1.644(5)	1.613(5)	1.610

T2o-O bonds (Å)	**Binning[1] (K)**	**Ave (K)[2]**	**OA2**	**OBO**	**OCM**	**ODM**	**AVE.**
	90 - 152	121	1.639(6)	1.578(6)	1.600(6)	1.630(7)	1.612
	153 - 213	183	1.641(7)	1.598(9)	1.612(7)	1.647(9)	1.625
	214 - 275	244	1.652(9)	1.590(9)	1.587(9)	1.661(9)	1.623
	279 - 336	306	1.632(9)	1.607(9)	1.596(9)	1.647(9)	1.621
	337 - 398	367	1.642(9)	1.616(10)	1.590(10)	1.637(10)	1.621
	399 - 459	429	1.648(7)	1.602(9)	1.595(9)	1.639(9)	1.621
	460 - 500	480	1.654(7)	1.601(9)	1.605(9)	1.627(9)	1.622
	452 - 494	473	1.648(5)	1.567(5)	1.599(5)	1.642(5)	1.614
	512 - 544	528	1.650(5)	1.571(5)	1.599(5)	1.642(5)	1.616
	552- 594	573	1.656(5)	1.571(5)	1.602(5)	1.643(5)	1.618
	602 - 644	623	1.651(5)	1.575(5)	1.597(5)	1.643(5)	1.617
	652 - 694	673	1.632(5)	1.570(5)	1.599(5)	1.643(5)	1.611
	702 - 744	723	1.646(5)	1.585(5)	1.608(5)	1.650(5)	1.622
	752 -794	773	1.638(5)	1.580(5)	1.600(5)	1.643(5)	1.615

802 - 844	823	1.613(5)	1.573(5)	1.611(5)	1.632(6)	1.607
863 - 894	879	1.605(5)	1.583(5)	1.604(5)	1.632(6)	1.606
902 - 944	923	1.620(5)	1.577(5)	1.604(5)	1.646(5)	1.612

T2m-O bonds (Å)	**Binning[1] (K)**	**Ave (K)[2]**	**OA2**	**OBM**	**OCO**	**ODO**	**AVE.**
	90 - 152	121	1.648(6)	1.621(6)	1.601(6)	1.632(6)	1.626
	153 - 213	183	1.649(7)	1.608(9)	1.600(7)	1.624(9)	1.620
	214 - 275	244	1.632(9)	1.612(9)	1.602(9)	1.643(9)	1.622
	279 - 336	306	1.639(9)	1.602(9)	1.601(9)	1.650(9)	1.623
	337 - 398	367	1.645(9)	1.592(10)	1.592(9)	1.646(9)	1.619
	399 - 459	429	1.637(7)	1.594(9)	1.572(7)	1.641(9)	1.611
	460 - 500	480	1.638(7)	1.587(9)	1.589(7)	1.635(9)	1.612
	452 - 494	473	1.640(5)	1.608(5)	1.594(5)	1.640(5)	1.621
	512 - 544	528	1.637(5)	1.607(5)	1.592(5)	1.646(5)	1.621
	552- 594	573	1.637(5)	1.606(5)	1.582(5)	1.643(5)	1.617
	602 - 644	623	1.630(5)	1.612(5)	1.581(5)	1.633(5)	1.614
	652 - 694	673	1.637(5)	1.612(5)	1.602(5)	1.647(5)	1.625
	702 - 744	723	1.641(5)	1.603(5)	1.595(5)	1.635(5)	1.619
	752 -794	773	1.644(5)	1.609(5)	1.585(5)	1.636(5)	1.619
	802 - 844	823	1.657(5)	1.600(6)	1.617(5)	1.636(5)	1.628
	863 - 894	879	1.662(5)	1.607(6)	1.613(5)	1.634(5)	1.629
	902 - 944	923	1.662(5)	1.597(5)	1.591(5)	1.636(5)	1.622

Na-O bonds (Å)	**Binning[1] (K)**	**Ave (K)[2]**	**NA**	**OA1***	**OA1**	**OA2**	**OBO**	**OCO**	**ODO**	**ODM**	**AVE.**
	90 - 152	121	3.889(9)	2.657(7)	2.523(7)	2.350(6)	2.470(7)	2.953(9)	2.413(7)	2.987(7)	2.780
	153 - 213	183	3.894(10)	2.666(9)	2.517(9)	2.349(9)	2.475(9)	2.955(9)	2.405(9)	2.980(9)	2.780
	214 - 275	244	3.916(11)	2.690(10)	2.526(9)	2.364(9)	2.482(9)	2.937(11)	2.398(10)	2.976(10)	2.786
	279 - 336	306	3.933(12)	2.716(10)	2.540(10)	2.379(9)	2.496(9)	2.939(11)	2.411(10)	2.966(10)	2.798

337 - 398	367	3.948(13)	2.732(11)	2.542(10)	2.371(9)	2.503(10)	2.918(11)	2.427(11)	2.966(11)	2.801
399 - 459	429	3.954(11)	2.713(9)	2.550(9)	2.383(9)	2.498(9)	2.951(9)	2.432(9)	2.983(9)	2.808
460 - 500	480	3.969(11)	2.727(9)	2.575(9)	2.380(9)	2.499(9)	2.937(9)	2.443(9)	2.984(9)	2.814
452 - 494	473	3.984(5)	2.691(5)	2.577(5)	2.360(5)	2.518(5)	2.950(5)	2.428(5)	2.986(5)	2.812
512 - 544	528	3.999(6)	2.709(5)	2.579(5)	2.371(5)	2.528(5)	2.949(5)	2.434(5)	2.995(5)	2.821
552- 594	573	4.019(6)	2.723(5)	2.584(5)	2.363(5)	2.543(5)	2.954(5)	2.432(5)	3.001(5)	2.827
602 - 644	623	4.024(6)	2.726(6)	2.595(5)	2.377(5)	2.538(5)	2.949(6)	2.452(5)	3.001(6)	2.833
652 - 694	673	4.031(6)	2.728(6)	2.605(6)	2.390(5)	2.542(5)	2.956(6)	2.446(5)	2.988(6)	2.836
702 - 744	723	4.049(6)	2.745(6)	2.615(6)	2.371(5)	2.555(5)	2.954(6)	2.467(6)	2.991(6)	2.843
752 -794	773	4.064(7)	2.752(6)	2.631(6)	2.389(5)	2.566(6)	2.946(6)	2.480(6)	2.978(6)	2.851
802 - 844	823	4.056(7)	2.735(6)	2.637(6)	2.417(6)	2.542(6)	2.945(6)	2.497(6)	2.980(6)	2.851
863 - 894	879	4.070(7)	2.755(6)	2.668(6)	2.415(6)	2.563(6)	2.945(6)	2.492(6)	2.982(6)	2.861
902 - 944	923	4.077(7)	2.746(6)	2.664(6)	2.406(5)	2.592(6)	2.955(6)	2.496(6)	2.980(6)	2.865

T-O-T angles (°)	Binning[1] (K)	Ave (K)[2]	T-Oa1-T	T-Oa2-T	T-Obo-T	T-Obm-T	T-Oco-T	T-Ocm-T	T-Odo-T	T-Odm-T
	90 - 152	121	142.0(5)	129.7(4)	140.2(4)	163.1(5)	128.6(4)	136.1(4)	133.6(4)	151.7(4)
	153 - 213	183	141.3(5)	128.7(5)	141.0(5)	163.0(6)	128.4(5)	135.3(5)	132.0(5)	151.7(5)
	214 - 275	244	142.2(6)	130.6(5)	140.3(6)	163.4(7)	127.9(5)	136.2(6)	131.8(6)	152.1(6)
	279 - 336	306	143.5(7)	131.3(5)	141.7(6)	162.3(7)	128.5(6)	134.6(6)	132.8(6)	151.8(6)
	337 - 398	367	143.5(7)	130.9(6)	141.8(6)	161.8(7)	127.8(6)	135.9(6)	133.6(6)	152.0(6)
	399 - 459	429	142.7(6)	131.0(5)	140.8(5)	162.3(6)	130.3(5)	135.7(5)	134.0(5)	151.4(5)
	460 - 500	480	144.1(6)	130.7(4)	140.4(5)	162.3(6)	128.5(5)	134.0(5)	133.8(5)	151.7(5)
	452 - 494	473	141.5(3)	130.4(3)	141.5(3)	161.9(3)	129.2(3)	135.5(3)	132.9(3)	149.7(3)
	512 - 544	528	141.7(4)	131.1(3)	141.9(3)	161.7(4)	129.4(3)	134.5(3)	132.7(3)	150.7(3)
	552- 594	573	142.1(4)	130.7(3)	142.3(3)	161.7(4)	130.2(3)	134.3(3)	132.8(3)	150.7(4)
	602 - 644	623	142.2(4)	131.7(3)	142.5(4)	161.2(4)	130.2(3)	134.0(4)	132.9(3)	150.7(4)
	652 - 694	673	142.2(4)	132.0(3)	141.8(4)	162.3(4)	129.8(3)	135.9(4)	133.1(4)	149.6(4)
	702 - 744	723	143.0(4)	130.8(3)	142.5(4)	162.2(4)	130.4(3)	133.9(4)	133.4(4)	150.3(4)

752 -794	773	143.1(4)	131.8(3)	142.9(4)	161.3(4)	130.1(3)	133.9(4)	134.0(4)	148.6(4)
802 - 844	823	142.7(4)	132.0(4)	142.0(4)	162.8(4)	129.6(4)	135.1(4)	134.2(4)	148.6(4)
863 - 894	879	144.6(4)	132.5(4)	142.7(4)	162.3(4)	129.1(4)	135.3(4)	133.6(4)	148.7(4)
902 - 944	923	143.9(4)	131.7(3)	143.8(4)	161.7(4)	130.1(3)	134.6(4)	134.0(4)	147.7(4)

Notes.

[1]Temperature interval of the binned powder diffraction data

[2]Average temperatures of each temperature interval of 20K binning from 90K - 500K and 5K binning from 452K - 944K.

*The bond length of a the longer of the two OA1 oxygen atoms

Table A.5.2: T-O bond lengths, M-O bond lengths and T-O-T angles for the single-crystal refinement results for An26

T1o-O bonds (Å)	Temp. (K)	OA1	OBO	OCO	ODO	AVERAGE
	100[1]	1.698(3)	1.697(3)	1.685(3)	1.702(3)	1.696
	150[1]	1.696(3)	1.699(3)	1.682(3)	1.700(3)	1.694
	200[1]	1.694(3)	1.696(3)	1.682(3)	1.700(3)	1.693
	250[1]	1.697(3)	1.693(3)	1.683(3)	1.700(3)	1.693
	300[1]	1.699(3)	1.696(3)	1.685(3)	1.696(3)	1.694
	300[1]	1.695(3)	1.695(3)	1.680(3)	1.700(3)	1.693
	303[2]	1.696(3)	1.694(3)	1.683(3)	1.695(3)	1.692
	323[2]	1.695(3)	1.693(3)	1.683(3)	1.696(3)	1.692
	373[2]	1.697(3)	1.690(3)	1.685(3)	1.696(3)	1.692
	423[2]	1.695(3)	1.690(3)	1.682(3)	1.697(3)	1.691
	473[2]	1.696(5)	1.691(5)	1.682(5)	1.696(5)	1.691
	523[2]	1.695(5)	1.689(3)	1.681(3)	1.694(5)	1.690
	573[2]	1.692(5)	1.691(5)	1.681(3)	1.696(5)	1.690
	623[2]	1.694(5)	1.694(5)	1.685(5)	1.690(5)	1.691
	673[2]	1.698(5)	1.688(5)	1.681(5)	1.692(5)	1.690
	723[2]	1.694(5)	1.688(5)	1.683(5)	1.692(5)	1.689
	773[2]	1.696(5)	1.684(5)	1.685(5)	1.695(5)	1.690
	823[2]	1.692(5)	1.688(5)	1.683(5)	1.695(5)	1.690
	873[2]	1.691(5)	1.689(5)	1.681(5)	1.688(5)	1.687
	923[2]	1.693(5)	1.689(5)	1.686(5)	1.693(5)	1.690
	973[2]	1.689(5)	1.687(5)	1.686(5)	1.692(5)	1.689
	1023[2]	1.694(5)	1.689(5)	1.683(5)	1.693(5)	1.690

T1m-O bonds (Å)	Temp. (K)	OA1	OBM	OCM	ODM	AVERAGE
	100[1]	1.641(3)	1.622(3)	1.646(3)	1.634(3)	1.636

150[1]	1.642(3)	1.621(3)	1.644(3)	1.634(3)	1.635
200[1]	1.642(3)	1.622(3)	1.642(3)	1.631(3)	1.634
250[1]	1.639(3)	1.622(3)	1.643(3)	1.634(3)	1.635
300[1]	1.637(3)	1.620(3)	1.642(3)	1.634(3)	1.633
300[1]	1.642(3)	1.622(3)	1.643(3)	1.632(3)	1.635
303[2]	1.645(3)	1.622(3)	1.644(3)	1.634(3)	1.636
323[2]	1.644(3)	1.623(3)	1.642(3)	1.634(3)	1.636
373[2]	1.643(3)	1.621(3)	1.642(3)	1.632(3)	1.635
423[2]	1.645(3)	1.620(3)	1.642(3)	1.633(3)	1.635
473[2]	1.640(5)	1.622(5)	1.643(3)	1.632(5)	1.634
523[2]	1.641(3)	1.617(5)	1.645(3)	1.629(5)	1.633
573[2]	1.641(5)	1.620(5)	1.646(3)	1.630(5)	1.634
623[2]	1.638(5)	1.620(5)	1.644(5)	1.630(5)	1.633
673[2]	1.638(5)	1.617(5)	1.639(3)	1.632(5)	1.632
723[2]	1.639(5)	1.616(5)	1.641(5)	1.628(5)	1.631
773[2]	1.638(5)	1.616(5)	1.640(5)	1.631(5)	1.631
823[2]	1.638(5)	1.617(5)	1.641(5)	1.630(5)	1.632
873[2]	1.641(5)	1.615(5)	1.643(5)	1.632(5)	1.633
923[2]	1.638(5)	1.622(5)	1.642(5)	1.627(5)	1.632
973[2]	1.641(5)	1.616(5)	1.642(5)	1.628(5)	1.632
1023[2]	1.634(5)	1.613(5)	1.639(5)	1.629(5)	1.629

T2o-O bonds (Å)	**Temp. (K)**	**OA2**	**OBO**	**OCM**	**ODM**	**AVERAGE**
	100[1]	1.660(2)	1.633(3)	1.640(3)	1.630(3)	1.641
	150[1]	1.659(3)	1.632(3)	1.639(3)	1.627(3)	1.639
	200[1]	1.654(2)	1.631(3)	1.637(3)	1.632(3)	1.639
	250[1]	1.656(3)	1.632(3)	1.637(3)	1.627(3)	1.638
	300[1]	1.654(3)	1.632(3)	1.635(3)	1.628(3)	1.637

300[1]	1.655(3)	1.628(3)	1.632(3)	1.630(3)	1.636
303[2]	1.653(3)	1.630(3)	1.634(3)	1.631(3)	1.637
323[2]	1.653(3)	1.631(3)	1.633(3)	1.626(3)	1.636
373[2]	1.653(3)	1.634(3)	1.633(3)	1.630(3)	1.638
423[2]	1.652(3)	1.631(3)	1.631(3)	1.629(3)	1.636
473[2]	1.656(3)	1.632(5)	1.635(5)	1.626(5)	1.637
523[2]	1.655(3)	1.628(5)	1.629(5)	1.629(5)	1.635
573[2]	1.657(3)	1.628(5)	1.631(5)	1.626(5)	1.636
623[2]	1.656(3)	1.628(5)	1.630(5)	1.629(5)	1.636
673[2]	1.656(3)	1.628(5)	1.632(5)	1.626(5)	1.636
723[2]	1.655(3)	1.631(5)	1.630(5)	1.629(5)	1.636
773[2]	1.654(3)	1.630(5)	1.631(5)	1.630(5)	1.636
823[2]	1.654(5)	1.628(5)	1.630(5)	1.629(5)	1.635
873[2]	1.654(5)	1.628(5)	1.629(5)	1.630(5)	1.635
923[2]	1.653(5)	1.624(5)	1.628(5)	1.629(5)	1.634
973[2]	1.654(5)	1.628(5)	1.631(5)	1.630(5)	1.636
1023[2]	1.653(5)	1.624(5)	1.630(5)	1.630(5)	1.634

T2m-O bonds (Å)	**Temp. (K)**	**OA2**	**OBM**	**OCO**	**ODO**	**AVERAGE**
	100[1]	1.655(3)	1.631(3)	1.627(3)	1.641(3)	1.639
	150[1]	1.658(3)	1.634(3)	1.625(3)	1.639(3)	1.639
	200[1]	1.658(3)	1.629(3)	1.627(3)	1.639(3)	1.638
	250[1]	1.655(3)	1.629(3)	1.625(3)	1.636(3)	1.636
	300[1]	1.658(3)	1.632(3)	1.622(3)	1.640(3)	1.638
	300[1]	1.656(3)	1.628(3)	1.626(3)	1.634(3)	1.636
	303[2]	1.656(3)	1.627(3)	1.623(3)	1.638(3)	1.636
	323[2]	1.658(3)	1.628(3)	1.621(3)	1.639(3)	1.637
	373[2]	1.657(3)	1.628(3)	1.620(3)	1.637(3)	1.636

423[2]	1.658(3)	1.629(3)	1.622(3)	1.635(3)	1.636	
473[2]	1.655(3)	1.624(5)	1.622(3)	1.635(3)	1.634	
523[2]	1.653(3)	1.629(5)	1.622(3)	1.635(3)	1.635	
573[2]	1.654(5)	1.625(5)	1.624(3)	1.633(5)	1.634	
623[2]	1.652(3)	1.626(5)	1.621(5)	1.635(5)	1.634	
673[2]	1.653(3)	1.629(5)	1.622(3)	1.637(5)	1.635	
723[2]	1.651(5)	1.627(5)	1.622(5)	1.632(5)	1.633	
773[2]	1.651(5)	1.627(5)	1.618(5)	1.631(5)	1.632	
823[2]	1.653(5)	1.626(5)	1.622(5)	1.634(5)	1.634	
873[2]	1.652(5)	1.627(5)	1.625(5)	1.633(5)	1.634	
923[2]	1.651(5)	1.621(5)	1.622(5)	1.631(5)	1.631	
973[2]	1.655(5)	1.625(5)	1.619(5)	1.631(5)	1.633	
1023[2]	1.650(5)	1.630(5)	1.621(5)	1.625(5)	1.632	

Na-O bonds (Å)	**Temp. (K)**	**OA1**	**OA2**	**OBO**	**OBM**	**OCM**	**ODO/ODM**	**OA1***	**AVE**
	100[1]	2.425(3)	2.334(3)	2.440(3)	2.959(5)	2.800(3)	2.469(3)†	2.805(3)	2.605
	150[1]	2.432(3)	2.333(3)	2.449(3)	2.964(5)	2.805(3)	2.472(3)†	2.808(3)	2.609
	200[1]	2.433(3)	2.335(3)	2.453(3)	2.965(5)	2.809(3)	2.473(3)†	2.804(3)	2.610
	250[1]	2.434(3)	2.339(3)	2.459(3)	2.958(5)	2.806(3)	2.479(3)†	2.810(3)	2.612
	300[1]	2.443(3)	2.338(3)	2.460(3)	2.966(5)	2.816(3)	2.479(3)†	2.806(3)	2.615
	300[1]	2.435(3)	2.342(3)	2.463(3)	2.964(5)	2.818(3)	2.481(3)†	2.808(5)	2.616
	303[2]	2.437(3)	2.345(3)	2.469(3)	2.969(5)	2.822(5)	2.480(3)	2.796(5)	2.617
	323[2]	2.439(3)	2.348(3)	2.468(3)	2.970(5)	2.826(5)	2.481(3)	2.796(5)	2.618
	373[2]	2.447(5)	2.352(3)	2.475(3)	2.969(5)	2.832(5)	2.486(3)	2.795(5)	2.622
	423[2]	2.448(5)	2.355(3)	2.486(5)	2.973(5)	2.838(5)	2.485(5)	2.794(5)	2.626
	473[2]	2.454(5)	2.359(5)	2.489(5)	2.971(6)	2.837(5)	2.494(5)	2.802(6)	2.629
	523[2]	2.459(5)	2.364(5)	2.498(5)	2.967(6)	2.845(5)	2.502(5)	2.804(6)	2.634
	573[2]	2.462(5)	2.368(5)	2.505(5)	2.973(6)	2.853(6)	2.500(5)	2.800(6)	2.637

	623[2]	2.467(5)	2.369(5)	2.507(5)	2.960(7)	2.848(6)	2.514(5)	2.815(6)	2.640
	673[2]	2.472(5)	2.370(5)	2.519(5)	2.957(6)	2.857(6)	2.515(5)	2.815(6)	2.644
	723[2]	2.478(5)	2.377(5)	2.527(5)	2.966(7)	2.866(6)	2.523(5)	2.815(6)	2.650
	773[2]	2.480(5)	2.382(5)	2.540(5)	2.964(7)	2.870(6)	2.526(6)	2.815(6)	2.654
	823[2]	2.490(6)	2.385(5)	2.539(6)	2.957(7)	2.877(6)	2.534(6)	2.820(7)	2.657
	873[2]	2.494(6)	2.390(5)	2.547(6)	2.961(9)	2.886(7)	2.542(6)	2.811(7)	2.662
	923[2]	2.501(6)	2.392(5)	2.556(6)	2.968(9)	2.893(6)	2.548(6)	2.819(7)	2.668
	973[2]	2.506(6)	2.398(6)	2.562(6)	2.957(9)	2.895(7)	2.551(7)	2.817(7)	2.669
	1023[2]	2.515(6)	2.401(5)	2.571(6)	2.961(9)	2.912(7)	2.569(6)	2.820(7)	2.678

Ca-O bonds (Å)	**Temp. (K)**	**OA1**	**OA2**	**OBO**	**OCO**	**ODO**	**ODM**	**OA1***	**AVE**
	100[1]	2.394(5)	2.352(5)	2.507(5)	2.971(5)	2.432(5)	2.705(5)	2.845(5)	2.601
	150[1]	2.390(5)	2.362(5)	2.503(5)	2.973(5)	2.445(5)	2.706(5)	2.846(5)	2.604
	200[1]	2.399(5)	2.354(5)	2.514(5)	2.962(5)	2.445(5)	2.701(5)	2.853(5)	2.604
	250[1]	2.401(5)	2.356(5)	2.512(5)	2.954(5)	2.457(5)	2.701(5)	2.859(5)	2.606
	300[1]	2.407(5)	2.351(5)	2.515(5)	2.941(5)	2.465(5)	2.695(5)	2.873(5)	2.607
	300[1]	2.410(5)	2.353(5)	2.521(5)	2.948(5)	2.460(5)	2.698(5)	2.864(5)	2.608
	303[2]	2.406(5)	2.348(5)	2.522(5)	2.930(5)	2.475(5)	2.685(5)	2.878(5)	2.606
	323[2]	2.414(5)	2.347(5)	2.533(5)	2.931(5)	2.467(5)	2.686(5)	2.881(5)	2.608
	373[2]	2.420(5)	2.343(5)	2.534(5)	2.919(5)	2.482(5)	2.685(5)	2.896(5)	2.611
	423[2]	2.420(5)	2.344(5)	2.537(5)	2.911(5)	2.495(5)	2.682(5)	2.903(5)	2.613
	473[2]	2.429(7)	2.346(7)	2.537(7)	2.907(7)	2.504(7)	2.687(7)	2.910(7)	2.617
	523[2]	2.438(7)	2.349(7)	2.556(7)	2.912(7)	2.504(7)	2.686(7)	2.912(7)	2.622
	573[2]	2.444(9)	2.346(9)	2.560(9)	2.902(9)	2.510(9)	2.683(7)	2.919(9)	2.623
	623[2]	2.450(9)	2.357(9)	2.562(9)	2.902(9)	2.517(9)	2.680(9)	2.915(9)	2.626
	673[2]	2.449(9)	2.359(9)	2.566(9)	2.899(9)	2.523(9)	2.680(7)	2.921(9)	2.628
	723[2]	2.459(9)	2.356(9)	2.571(9)	2.882(9)	2.543(9)	2.673(9)	2.939(9)	2.632
	773[2]	2.461(9)	2.361(9)	2.581(9)	2.878(9)	2.549(9)	2.668(9)	2.940(9)	2.634

	823[2]	2.470(9)	2.368(9)	2.592(9)	2.880(9)	2.544(9)	2.663(9)	2.944(9)	2.637
	873[2]	2.476(9)	2.360(9)	2.591(9)	2.866(9)	2.571(9)	2.660(9)	2.958(9)	2.640
	923[2]	2.476(10)	2.377(9)	2.600(10)	2.864(9)	2.571(10)	2.659(9)	2.954(9)	2.643
	973[2]	2.490(11)	2.364(10)	2.609(11)	2.865(10)	2.574(11)	2.666(10)	2.963(10)	2.647
	1023[2]	2.498(10)	2.368(10)	2.616(11)	2.855(10)	2.597(10)	2.660(10)	2.973(10)	2.652

T-O-T angles (°)	**Temp. (K)**	**T-Oa1-T**	**T-Oa2-T**	**T-Obo-T**	**T-Obm-T**	**T-Oco-T**	**T-Ocm-T**	**T-Odo-T**	**T-Odm-T**
	100[1]	141.23(13)	128.35(12)	138.04(13)	159.10(16)	130.43(13)	133.58(13)	133.49(12)	151.19(14)
	150[1]	141.35(14)	128.33(13)	138.22(14)	158.95(17)	130.64(14)	133.73(14)	133.83(14)	151.12(15)
	200[1]	141.35(14)	124.52(12)	138.59(14)	158.93(16)	130.59(13)	133.78(13)	133.75(13)	117.38(13)
	250[1]	141.42(14)	128.49(13)	138.64(14)	158.77(17)	130.71(14)	133.67(14)	133.90(14)	150.86(15)
	300[1]	141.49(14)	124.17(12)	138.59(14)	158.67(17)	130.58(13)	133.76(14)	133.88(13)	150.65(15)
	300[1]	141.29(15)	124.23(13)	138.99(14)	158.66(16)	130.69(14)	134.06(14)	134.09(14)	150.67(16)
	303[2]	141.16(17)	128.64(15)	138.94(16)	158.56(19)	130.59(16)	133.80(16)	134.08(16)	150.34(18)
	323[2]	141.25(17)	128.69(15)	138.90(17)	158.55(19)	130.70(16)	133.78(17)	134.04(16)	150.59(18)
	373[2]	141.38(17)	128.80(15)	139.12(17)	158.4(2)	130.63(17)	133.89(17)	134.20(17)	150.40(19)
	423[2]	141.34(18)	128.74(16)	139.39(18)	158.3(2)	130.86(17)	133.96(18)	134.19(17)	150.4(2)
	473[2]	141.7(2)	128.8(2)	139.4(2)	158.3(3)	130.8(2)	133.6(2)	134.4(2)	150.5(3)
	523[2]	141.8(2)	129.0(2)	139.9(2)	158.2(3)	131.0(2)	134.0(2)	134.5(2)	150.4(3)
	573[2]	141.8(2)	128.9(2)	140.0(2)	158.1(3)	130.9(2)	133.9(2)	134.5(2)	150.3(3)
	623[2]	141.8(3)	129.3(2)	139.9(3)	157.8(3)	130.9(2)	133.8(2)	134.9(2)	149.9(3)
	673[2]	141.8(2)	129.2(2)	140.4(2)	157.7(3)	131.0(2)	134.0(2)	134.6(2)	149.7(3)
	723[2]	142.1(3)	129.4(2)	140.5(3)	157.8(3)	131.0(2)	134.1(3)	135.0(3)	149.8(3)
	773[2]	141.8(3)	129.5(2)	141.0(3)	157.9(3)	131.2(2)	134.1(2)	135.0(3)	149.3(3)
	823[2]	142.2(3)	129.6(2)	140.9(3)	157.5(3)	131.1(3)	134.1(3)	134.8(3)	149.2(3)
	873[2]	142.1(3)	129.6(2)	141.1(3)	157.3(3)	131.1(3)	133.9(3)	135.4(3)	148.6(3)
	923[2]	142.2(3)	129.9(2)	141.3(3)	157.2(3)	131.2(3)	134.1(3)	135.4(3)	149.1(3)
	973[2]	142.4(3)	129.6(2)	141.3(3)	157.2(3)	131.3(3)	134.0(3)	135.4(3)	148.8(3)

	1023[2]	142.6(3)	129.8(2)	141.8(3)	157.2(3)	131.5(3)	134.3(3)	136.0(3)	148.4(3)

Notes.

[1]Results from the data collected at low-temperature on a Gemini diffractometer.

[2]Results from the data collected at high-temperature on a Phillips PW1100 diffractometer.

*The bond length of a the longer of the two OA1 oxygen atoms

† Na-Odo bonds

Table A.5.3: T-O bond lengths, M-O bond lengths and T-O-T angles for the Rietveld refinement results for An27.

T1o-O bonds (Å)	Binning[1] (K)	Ave (K)[2]	OA1	OBO	OCO	ODO	AVE
	90 - 152	121	1.686(5)	1.688(4)	1.693(4)	1.691(4)	1.665
	153 - 213	183	1.693(5)	1.675(4)	1.693(4)	1.704(5)	1.669
	214 - 275	244	1.698(5)	1.669(4)	1.687(4)	1.701(5)	1.664
	279 - 336	306	1.698(5)	1.666(4)	1.692(4)	1.705(5)	1.662
	337 - 398	367	1.697(5)	1.662(5)	1.694(5)	1.703(5)	1.661
	399 - 459	429	1.689(5)	1.666(5)	1.683(5)	1.702(5)	1.670
	460 - 500	480	1.696(5)	1.668(5)	1.690(5)	1.693(5)	1.675
	452 - 494	473	1.687(5)	1.680(5)	1.680(5)	1.689(5)	1.674
	512 - 544	528	1.692(5)	1.673(5)	1.681(5)	1.687(5)	1.670
	552- 594	573	1.692(5)	1.674(5)	1.687(5)	1.699(5)	1.671
	602 - 644	623	1.690(5)	1.670(5)	1.690(5)	1.707(5)	1.667
	652 - 694	673	1.694(5)	1.664(5)	1.686(5)	1.701(5)	1.668
	702 - 744	723	1.693(5)	1.675(5)	1.678(5)	1.693(5)	1.670
	752 -794	773	1.692(5)	1.685(5)	1.674(5)	1.697(5)	1.674
	802 - 844	823	1.687(5)	1.676(5)	1.672(5)	1.692(5)	1.680
	863 - 894	879	1.702(5)	1.681(5)	1.671(5)	1.692(5)	1.658
	902 - 944	923	1.694(6)	1.679(5)	1.674(5)	1.693(5)	1.678

T1m-O bonds (Å)	Binning[1] (K)	Ave (K)[2]	OA1	OBM	OCM	ODM	AVE
	90 - 152	121	1.667(5)	1.612(5)	1.643(4)	1.641(4)	1.650
	153 - 213	183	1.673(5)	1.598(5)	1.637(4)	1.635(4)	1.656
	214 - 275	244	1.668(5)	1.602(4)	1.638(4)	1.643(4)	1.653
	279 - 336	306	1.668(5)	1.606(5)	1.638(4)	1.638(5)	1.650
	337 - 398	367	1.664(5)	1.598(5)	1.644(5)	1.638(5)	1.661
	399 - 459	429	1.660(5)	1.606(5)	1.646(5)	1.638(5)	1.652
	460 - 500	480	1.661(5)	1.606(5)	1.639(5)	1.639(5)	1.657

	452 - 494	473	1.663(5)	1.609(5)	1.636(5)	1.641(5)	1.647
	512 - 544	528	1.660(5)	1.606(5)	1.644(5)	1.637(5)	1.643
	552- 594	573	1.650(5)	1.613(5)	1.654(5)	1.642(5)	1.644
	602 - 644	623	1.665(5)	1.597(5)	1.632(5)	1.629(5)	1.640
	652 - 694	673	1.656(5)	1.599(5)	1.631(5)	1.637(5)	1.646
	702 - 744	723	1.653(5)	1.617(5)	1.635(5)	1.641(5)	1.645
	752 -794	773	1.661(5)	1.623(5)	1.644(5)	1.629(5)	1.644
	802 - 844	823	1.660(5)	1.625(5)	1.640(5)	1.627(5)	1.647
	863 - 894	879	1.644(5)	1.623(5)	1.636(5)	1.636(5)	1.648
	902 - 944	923	1.650(5)	1.623(5)	1.634(5)	1.639(5)	1.651

T2o-O bonds (Å)	**Binning[1] (K)**	**Ave (K)[2]**	**OA2**	**OBO**	**OCM**	**ODM**	**AVE**
	90 - 152	121	1.673(4)	1.620(4)	1.649(4)	1.637(5)	1.650
	153 - 213	183	1.666(4)	1.622(5)	1.641(5)	1.646(5)	1.648
	214 - 275	244	1.664(4)	1.623(5)	1.645(5)	1.634(5)	1.648
	279 - 336	306	1.665(4)	1.626(5)	1.643(5)	1.634(5)	1.652
	337 - 398	367	1.659(5)	1.624(5)	1.634(5)	1.634(5)	1.644
	399 - 459	429	1.662(5)	1.627(5)	1.636(5)	1.633(5)	1.644
	460 - 500	480	1.662(5)	1.631(5)	1.636(5)	1.633(5)	1.651
	452 - 494	473	1.665(5)	1.620(5)	1.649(5)	1.634(5)	1.650
	512 - 544	528	1.663(5)	1.618(5)	1.637(5)	1.641(5)	1.659
	552- 594	573	1.655(5)	1.614(5)	1.635(5)	1.638(5)	1.653
	602 - 644	623	1.656(5)	1.614(5)	1.641(5)	1.648(5)	1.662
	652 - 694	673	1.654(5)	1.613(5)	1.642(5)	1.638(5)	1.655
	702 - 744	723	1.673(5)	1.607(5)	1.639(5)	1.644(5)	1.649
	752 -794	773	1.669(5)	1.605(5)	1.654(5)	1.638(5)	1.646
	802 - 844	823	1.664(5)	1.613(5)	1.652(5)	1.633(5)	1.646
	863 - 894	879	1.661(5)	1.608(5)	1.658(5)	1.624(5)	1.654

	902 - 944	923	1.661(5)	1.616(5)	1.663(5)	1.629(5)	1.649

T2m-O bonds (Å)	Binning[1] (K)	Ave (K)[2]	OA2	OBM	OCO	ODO	AVE
	90 - 152	121	1.673(4)	1.637(5)	1.645(4)	1.665(4)	1.6549
	153 - 213	183	1.664(4)	1.639(5)	1.636(4)	1.662(5)	1.6503
	214 - 275	244	1.664(4)	1.630(5)	1.636(4)	1.658(4)	1.6469
	279 - 336	306	1.667(4)	1.630(5)	1.636(4)	1.649(4)	1.6458
	337 - 398	367	1.669(5)	1.636(5)	1.639(5)	1.653(5)	1.6493
	399 - 459	429	1.668(5)	1.636(5)	1.638(4)	1.647(5)	1.6472
	460 - 500	480	1.663(5)	1.635(5)	1.635(4)	1.653(5)	1.6464
	452 - 494	473	1.665(5)	1.637(5)	1.645(5)	1.659(5)	1.6515
	512 - 544	528	1.667(5)	1.636(5)	1.636(5)	1.660(5)	1.6497
	552- 594	573	1.673(5)	1.627(5)	1.631(5)	1.656(5)	1.6467
	602 - 644	623	1.670(5)	1.633(5)	1.629(5)	1.649(5)	1.6453
	652 - 694	673	1.674(5)	1.637(5)	1.621(5)	1.649(5)	1.6453
	702 - 744	723	1.662(5)	1.626(5)	1.631(5)	1.654(5)	1.9026
	752 -794	773	1.665(5)	1.627(5)	1.636(5)	1.633(5)	1.6402
	802 - 844	823	1.669(5)	1.631(5)	1.623(5)	1.627(5)	1.6375
	863 - 894	879	1.665(5)	1.633(5)	1.631(5)	1.638(5)	1.6417
	902 - 944	923	1.663(5)	1.627(6)	1.627(5)	1.628(5)	1.6363

Na-O bonds (Å)	Binning[1] (K)	Ave (K)[2]	OA1	OA2	OBO	OCO	ODO	ODM	OA1*	AVE
	90 - 152	121	2.417(7)	2.366(7)	2.482(8)	3.035(7)	2.410(8)	2.817(6)	2.725(7)	2.607
	153 - 213	183	2.444(8)	2.365(8)	2.521(8)	3.064(8)	2.394(8)	2.826(5)	2.716(7)	2.619
	214 - 275	244	2.451(7)	2.364(7)	2.515(8)	3.051(7)	2.424(8)	2.837(5)	2.725(7)	2.624
	279 - 336	306	2.444(8)	2.366(8)	2.510(8)	3.036(8)	2.446(8)	2.844(6)	2.729(7)	2.625
	337 - 398	367	2.464(10)	2.365(10)	2.520(11)	3.037(9)	2.448(11)	2.852(7)	2.730(9)	2.631

	399 - 459	429	2.476(10)	2.371(10)	2.517(11)	3.038(10)	2.460(11)	2.838(7)	2.740(9)	2.634
	460 - 500	480	2.480(10)	2.365(10)	2.521(10)	3.027(9)	2.466(10)	2.833(7)	2.755(9)	2.635
	452 - 494	473	2.479(11)	2.386(11)	2.549(13)	3.064(12)	2.426(12)	2.817(7)	2.719(11)	2.634
	512 - 544	528	2.501(14)	2.386(14)	2.579(15)	3.065(14)	2.414(15)	2.821(8)	2.729(14)	2.642
	552- 594	573	2.732(16)	2.150(9)	2.601(19)	NC	2.906(19)	2.499(20)	2.827(14)	2.619
	602 - 644	623	2.466(11)	2.412(11)	2.549(14)	3.035(12)	2.475(14)	2.826(9)	2.743(12)	2.644
	652 - 694	673	2.500(14)	2.399(15)	2.580(16)	3.035(13)	2.470(16)	2.823(9)	2.757(13)	2.652
	702 - 744	723	3.00(8)	1.86(6)	2.74(9)	2.85(9)	2.90(10)	2.64(8)	3.08(7)	2.724
	752 -794	773	2.484(13)	2.416(13)	2.575(16)	3.052(14)	2.492(16)	2.824(9)	2.744(14)	2.655
	802 - 844	823	2.530(23)	2.391(17)	2.561(18)	NC	2.532(17)	NC	2.725(16)	2.548
	863 - 894	879	2.498(18)	2.364(20)	2.591(20)	NC	2.533(20)	NC	2.852(17)	2.568
	902 - 944	923	2.464(16)	2.463(16)	2.502(21)	NC	2.598(21)	NC	2.736(23)	2.553

Ca-O bonds (Å)	**Binning[1] (K)**	**Ave (K)[2]**	**OA1**	**OA2**	**OBO**	**OBM**	**OCM**	**ODO**	**OA1***	**AVE**
	90 - 152	121	2.403(11)	2.281(11)	2.527(11)	2.870(8)	2.674(9)	2.454(11)	2.938(8)	2.592
	153 - 213	183	2.396(11)	2.310(11)	2.492(12)	2.856(7)	2.717(10)	2.500(11)	2.913(9)	2.598
	214 - 275	244	2.392(10)	2.309(10)	2.518(11)	2.859(7)	2.709(9)	2.501(11)	2.933(9)	2.603
	279 - 336	306	2.392(11)	2.315(11)	2.537(12)	2.861(8)	2.714(10)	2.495(12)	2.924(9)	2.605
	337 - 398	367	2.395(14)	2.317(14)	2.553(15)	2.867(10)	2.716(13)	2.497(15)	2.934(12)	2.611
	399 - 459	429	2.400(14)	2.325(15)	2.539(17)	2.865(10)	2.726(13)	2.514(16)	2.942(13)	2.616
	460 - 500	480	2.392(14)	2.343(15)	2.544(16)	2.859(9)	2.740(13)	2.510(15)	2.933(13)	2.617
	452 - 494	473	2.444(16)	2.290(16)	2.521(19)	2.869(12)	2.728(15)	2.551(17)	2.948(14)	2.622
	512 - 544	528	2.462(21)	2.312(21)	2.495(25)	2.867(13)	2.767(22)	2.578(22)	2.922(20)	2.629
	552- 594	573	2.430(21)	2.608(12)	2.483(28)	NC	NC	2.414(29)	2.443(24)	2.476
	602 - 644	623	2.466(17)	2.289(16)	2.611(20)	2.881(14)	2.715(15)	2.527(20)	2.982(14)	2.639
	652 - 694	673	2.432(20)	2.336(20)	2.593(24)	2.858(14)	2.764(20)	2.535(23)	2.954(19)	2.639
	702 - 744	723	1.97(13)	3.13(10)	2.47(14)	2.99(15)	NC	2.45(14)	2.27(15)	2.547
	752 -794	773	2.502(20)	2.283(20)	2.603(25)	2.874(16)	2.725(18)	2.582(23)	2.979(16)	2.650

	802 - 844	823	2.597(17)	2.295(19)	2.603(21)	NC	NC	2.553(22)	2.830(33)	2.576
	863 - 894	879	2.461(30)	2.410(32)	2.595(32)	NC	NC	2.554(31)	2.889(24)	2.582
	902 - 944	923	2.646(33)	2.263(27)	2.730(29)	NC	NC	2.507(33)	2.933(21)	2.616

T-O-T angles (°)	Binning[1] (K)	Ave (K)[2]	T-Oa1-T	T-Oa2-T	T-Obo-T	T-Obm-T	T-Oco-T	T-Ocm-T	T-Odo-T	T-Odm-T
	90 - 152	121	141.9(6)	127.0(5)	139.3(5)	159.4(6)	129.1(5)	133.0(5)	135.9(6)	150.4(6)
	153 - 213	183	142.2(6)	127.4(5)	138.4(5)	158.1(6)	129.7(5)	132.6(5)	135.4(6)	150.9(6)
	214 - 275	244	141.8(6)	127.4(5)	140.3(6)	159.1(6)	129.0(5)	131.8(5)	137.0(6)	150.8(6)
	279 - 336	306	142.4(7)	128.6(5)	139.6(6)	158.7(6)	130.4(6)	132.1(6)	137.0(6)	149.9(6)
	337 - 398	367	142.0(7)	128.7(5)	138.7(7)	156.9(7)	131.2(6)	132.6(6)	137.5(6)	150.4(7)
	399 - 459	429	141.3(8)	127.9(6)	141.5(7)	157.3(7)	130.2(6)	131.1(6)	137.0(7)	151.5(7)
	460 - 500	480	140.4(8)	128.3(6)	139.0(7)	159.0(7)	129.7(6)	130.7(7)	136.8(7)	150.5(8)
	452 - 494	473	140.8(7)	128.1(5)	140.8(6)	158.4(6)	128.9(5)	133.9(6)	136.2(6)	148.6(7)
	512 - 544	528	140.9(7)	128.4(5)	140.8(6)	159.9(7)	128.4(5)	133.3(6)	134.9(6)	147.9(7)
	552- 594	573	141.4(7)	127.3(5)	141.3(7)	159.0(7)	128.5(6)	133.5(6)	135.8(7)	149.6(7)
	602 - 644	623	140.3(7)	128.0(6)	142.3(7)	158.6(7)	128.6(6)	133.1(6)	135.7(7)	147.9(8)
	652 - 694	673	142.1(8)	127.8(6)	141.8(7)	158.8(7)	129.2(6)	133.4(6)	135.8(7)	149.1(8)
	702 - 744	723	141.5(8)	126.3(6)	142.5(7)	158.6(7)	129.6(6)	132.9(7)	136.0(7)	148.9(8)
	752 -794	773	140.9(6)	128.1(5)	143.6(6)	159.7(6)	127.1(5)	133.1(6)	136.1(6)	150.1(7)
	802 - 844	823	138.8(6)	126.0(5)	145.0(6)	157.7(6)	127.9(5)	132.6(6)	138.1(6)	149.6(7)
	863 - 894	879	142.0(7)	128.3(6)	141.7(6)	158.2(7)	128.2(6)	132.8(6)	136.2(7)	148.4(8)
	902 - 944	923	141.3(7)	126.9(6)	142.5(6)	158.1(7)	128.7(6)	133.3(7)	135.4(7)	147.6(8)

Notes.

[1]Temperature interval of the binned powder diffraction data

[2]Average temperatures of each temperature interval of 20K binning from 90K - 500K and 5K binning from 452K - 944K.

*The bond length of a the longer of the two OA1 oxygen atoms

NC: Bonds that were not calculated in that particular refinement.

Table A.5.4: T-O bond lengths, M-O bond lengths and T-O-T angles for the Rietveld refinement results for An35.

T1o-O bonds (Å)	Binning[1] (K)	Ave (K)[2]	OA1	OBO	OCO	ODO	AVERAGE
	90 - 152	121	1.688(9)	1.642(9)	1.698(9)	1.631(9)	1.665
	153 - 213	183	1.690(9)	1.657(9)	1.695(9)	1.634(9)	1.669
	214 - 275	244	1.674(9)	1.666(9)	1.696(9)	1.618(9)	1.664
	279 - 336	306	1.675(10)	1.648(9)	1.688(9)	1.635(9)	1.662
	337 - 398	367	1.677(10)	1.653(9)	1.690(9)	1.624(9)	1.661
	399 - 459	429	1.697(11)	1.647(10)	1.704(10)	1.632(9)	1.670
	460 - 500	480	1.704(11)	1.648(10)	1.709(10)	1.637(9)	1.675
	452 - 494	473	1.713(10)	1.649(9)	1.701(9)	1.634(9)	1.674
	512 - 544	528	1.690(10)	1.652(9)	1.697(9)	1.640(9)	1.670
	552- 594	573	1.690(10)	1.656(9)	1.690(9)	1.648(9)	1.671
	602 - 644	623	1.699(10)	1.647(9)	1.695(9)	1.628(9)	1.667
	652 - 694	673	1.702(10)	1.648(9)	1.700(10)	1.622(9)	1.668
	702 - 744	723	1.695(11)	1.656(10)	1.712(9)	1.617(9)	1.670
	752 -794	773	1.689(9)	1.656(9)	1.710(9)	1.640(9)	1.674
	802 - 844	823	1.717(9)	1.668(9)	1.713(9)	1.620(9)	1.680
	863 - 894	879	1.687(10)	1.640(9)	1.702(9)	1.603(9)	1.658
	902 - 944	923	1.701(10)	1.661(9)	1.704(9)	1.645(9)	1.678

T1m-O bonds (Å)	Binning[1] (K)	Ave (K)[2]	OA1	OBM	OCM	ODM	AVERAGE
	90 - 152	121	1.662(9)	1.611(9)	1.697(9)	1.631(7)	1.650
	153 - 213	183	1.660(9)	1.628(9)	1.688(9)	1.646(7)	1.656
	214 - 275	244	1.668(9)	1.620(9)	1.686(9)	1.638(9)	1.653
	279 - 336	306	1.667(9)	1.619(9)	1.689(9)	1.623(9)	1.650
	337 - 398	367	1.671(9)	1.637(9)	1.705(10)	1.632(9)	1.661

399 - 459	429	1.646(10)	1.626(10)	1.704(10)	1.630(9)	1.652
460 - 500	480	1.655(10)	1.635(10)	1.709(10)	1.628(10)	1.657
452 - 494	473	1.651(9)	1.630(9)	1.692(9)	1.616(9)	1.647
512 - 544	528	1.668(9)	1.607(9)	1.673(9)	1.622(9)	1.643
552- 594	573	1.665(9)	1.609(9)	1.678(9)	1.624(9)	1.644
602 - 644	623	1.662(9)	1.617(10)	1.664(9)	1.616(10)	1.640
652 - 694	673	1.659(9)	1.628(10)	1.694(9)	1.603(10)	1.646
702 - 744	723	1.672(10)	1.612(10)	1.683(10)	1.614(10)	1.645
752 -794	773	1.668(9)	1.603(9)	1.682(9)	1.623(9)	1.644
802 - 844	823	1.654(9)	1.620(9)	1.682(9)	1.630(9)	1.647
863 - 894	879	1.664(9)	1.622(9)	1.693(9)	1.611(9)	1.648
902 - 944	923	1.646(9)	1.627(9)	1.698(9)	1.633(9)	1.651

T2o-O bonds (Å)	**Binning[1] (K)**	**Ave (K)[2]**	**OA2**	**OBO**	**OCM**	**ODM**	**AVERAGE**
	90 - 152	121	1.670(7)	1.668(9)	1.619(9)	1.642(9)	1.650
	153 - 213	183	1.675(7)	1.670(9)	1.624(9)	1.621(9)	1.648
	214 - 275	244	1.669(9)	1.640(9)	1.645(9)	1.636(9)	1.648
	279 - 336	306	1.670(9)	1.654(10)	1.629(9)	1.654(9)	1.652
	337 - 398	367	1.667(9)	1.667(10)	1.605(10)	1.635(9)	1.644
	399 - 459	429	1.673(9)	1.659(11)	1.624(10)	1.618(10)	1.644
	460 - 500	480	1.676(9)	1.660(11)	1.625(10)	1.642(10)	1.651
	452 - 494	473	1.680(9)	1.645(10)	1.589(9)	1.684(9)	1.650
	512 - 544	528	1.692(9)	1.635(10)	1.630(9)	1.677(9)	1.659
	552- 594	573	1.686(9)	1.640(10)	1.621(9)	1.666(10)	1.653
	602 - 644	623	1.680(9)	1.644(11)	1.638(10)	1.684(10)	1.662
	652 - 694	673	1.692(9)	1.629(11)	1.606(10)	1.692(10)	1.655
	702 - 744	723	1.686(9)	1.616(11)	1.621(10)	1.671(10)	1.649
	752 -794	773	1.681(7)	1.614(9)	1.615(9)	1.675(9)	1.646

	802 - 844	823	1.693(9)	1.599(10)	1.615(9)	1.677(9)	1.646
	863 - 894	879	1.695(9)	1.646(10)	1.601(9)	1.673(10)	1.654
	902 - 944	923	1.704(9)	1.628(10)	1.606(10)	1.658(10)	1.649
T2m-O bonds (Å)	**Binning[1] (K)**	**Ave (K)[2]**	**OA2**	**OBM**	**OCO**	**ODO**	**AVERAGE**
	90 - 152	121	1.661(7)	1.650(9)	1.657(7)	1.667(7)	1.659
	153 - 213	183	1.659(7)	1.638(9)	1.648(9)	1.664(9)	1.652
	214 - 275	244	1.658(9)	1.648(9)	1.657(9)	1.668(9)	1.658
	279 - 336	306	1.653(9)	1.651(10)	1.652(9)	1.640(9)	1.649
	337 - 398	367	1.667(9)	1.642(10)	1.632(9)	1.635(9)	1.644
	399 - 459	429	1.661(9)	1.648(11)	1.639(9)	1.637(9)	1.646
	460 - 500	480	1.671(9)	1.627(11)	1.636(9)	1.627(9)	1.640
	452 - 494	473	1.668(9)	1.623(9)	1.656(9)	1.667(9)	1.654
	512 - 544	528	1.654(9)	1.631(10)	1.654(9)	1.683(9)	1.656
	552- 594	573	1.662(9)	1.640(10)	1.654(9)	1.663(9)	1.655
	602 - 644	623	1.655(9)	1.637(10)	1.666(9)	1.672(9)	1.658
	652 - 694	673	1.653(9)	1.612(10)	1.652(9)	1.674(9)	1.648
	702 - 744	723	1.662(9)	1.645(11)	1.651(9)	1.676(9)	1.659
	752 -794	773	1.663(7)	1.643(9)	1.664(7)	1.657(9)	1.657
	802 - 844	823	1.664(7)	1.638(9)	1.657(7)	1.642(9)	1.650
	863 - 894	879	1.662(9)	1.602(10)	1.665(9)	1.698(9)	1.657
	902 - 944	923	1.662(9)	1.597(10)	1.649(9)	1.659(9)	1.642

Na-O bonds (Å)	**Binning[1] (K)**	**Ave (K)[2]**	**OA1**	**OA2**	**OBO**	**OCO**	**ODO**	**ODM**	**OA1***	**AVE**
	90 - 152	121	2.438(18)	2.346(18)	2.537(18)	3.06(3)	2.41(2)	2.754(11)	2.75(2)	2.614
	153 - 213	183	2.41(2)	2.39(3)	2.48(3)	3.10(3)	2.43(3)	2.778(14)	2.71(3)	2.614
	214 - 275	244	2.40(3)	2.39(3)	2.52(3)	3.08(3)	2.45(3)	2.760(15)	2.71(3)	2.616
	279 - 336	306	2.43(3)	2.39(3)	2.52(3)	3.06(3)	2.47(3)	2.734(17)	2.75(3)	2.622
	337 - 398	367	2.46(3)	2.35(3)	2.49(3)	3.04(3)	2.51(3)	2.761(18)	2.77(3)	2.626

	399 - 459	429	2.44(3)	2.37(3)	2.49(3)	3.03(3)	2.54(3)	2.80(3)	2.75(3)	2.631
	460 - 500	480	2.51(4)	2.35(3)	2.50(4)	3.07(4)	2.50(4)	2.86(4)	2.69(4)	2.640
	452 - 494	473	2.43(3)	2.38(3)	2.52(4)	3.08(4)	2.47(4)	2.77(3)	2.71(3)	2.623
	512 - 544	528	2.46(4)	2.33(3)	2.51(3)	3.00(3)	2.51(3)	2.77(3)	2.79(3)	2.624
	552- 594	573	2.49(4)	2.31(4)	2.51(4)	3.02(4)	2.53(4)	2.80(3)	2.77(4)	2.633
	602 - 644	623	2.53(4)	2.28(4)	2.53(4)	3.00(4)	2.55(3)	2.82(4)	2.78(4)	2.641
	652 - 694	673	2.51(4)	2.37(3)	2.59(4)	3.06(4)	2.47(4)	2.76(4)	2.73(4)	2.641
	702 - 744	723	2.53(4)	2.31(3)	2.62(4)	3.04(4)	2.47(4)	2.76(3)	2.76(3)	2.641
	752 -794	773	2.53(3)	2.39(3)	2.686(19)	-	2.40(2)	2.802(19)	2.66(3)	2.578
	802 - 844	823	2.50(3)	2.32(3)	2.64(3)	2.98(3)	2.55(3)	2.741(17)	2.78(3)	2.644
	863 - 894	879	2.53(3)	2.39(3)	2.62(3)	3.09(4)	2.46(3)	2.78(3)	2.72(4)	2.656
	902 - 944	923	2.56(4)	2.43(4)	2.72(4)	-	2.35(5)	2.80(3)	2.63(5)	2.582

Ca-O bonds (Å)	**Binning[1] (K)**	**Ave (K)[2]**	**OA1**	**OA2**	**OBO**	**OBM**	**OCM**	**ODO**	**OA1***	**AVE**
	90 - 152	121	2.406(19)	2.293(18)	2.444(19)	2.835(14)	2.661(18)	2.574(18)	2.920(17)	2.590
	153 - 213	183	2.42(2)	2.281(19)	2.45(3)	2.857(18)	2.659(18)	2.551(19)	2.933(18)	2.593
	214 - 275	244	2.44(2)	2.270(19)	2.47(3)	2.901(18)	2.69(2)	2.573(19)	2.895(19)	2.606
	279 - 336	306	2.42(3)	2.31(3)	2.47(3)	2.871(19)	2.68(3)	2.58(3)	2.91(2)	2.606
	337 - 398	367	2.39(3)	2.34(3)	2.46(3)	2.847(19)	2.70(3)	2.59(3)	2.90(3)	2.604
	399 - 459	429	2.38(3)	2.33(3)	2.54(3)	2.89(3)	2.69(3)	2.53(3)	2.91(3)	2.610
	460 - 500	480	2.43(3)	2.32(3)	2.48(3)	3.00(4)	2.75(4)	2.54(3)	2.83(4)	2.621
	452 - 494	473	2.45(3)	2.25(3)	2.54(4)	2.90(3)	2.66(3)	2.55(3)	2.95(3)	2.614
	512 - 544	528	2.38(3)	2.33(3)	2.58(3)	2.89(3)	2.67(4)	2.48(3)	2.93(3)	2.609
	552- 594	573	2.41(4)	2.30(4)	2.57(4)	2.89(4)	2.68(4)	2.52(3)	2.94(4)	2.616
	602 - 644	623	2.40(4)	2.36(4)	2.55(3)	2.93(4)	2.78(4)	2.51(3)	2.84(4)	2.624
	652 - 694	673	2.48(3)	2.27(3)	2.54(3)	2.95(4)	2.73(4)	2.57(3)	2.93(4)	2.639
	702 - 744	723	2.44(3)	2.30(3)	2.55(4)	2.91(3)	2.74(4)	2.57(3)	2.90(4)	2.630
	752 -794	773	2.54(3)	2.25(3)	2.50(3)	2.90(3)	2.76(3)	2.69(3)	2.90(3)	2.649

	802 - 844	823	2.44(3)	2.28(3)	2.58(3)	2.841(18)	2.70(3)	2.66(3)	2.94(3)	2.634
	863 - 894	879	2.55(4)	2.27(3)	2.52(4)	2.95(4)	2.78(4)	2.63(4)	2.89(4)	2.656
	902 - 944	923	2.69(5)	2.16(4)	2.48(5)	3.03(4)	2.81(5)	2.73(5)	2.90(4)	2.686

T-O-T angles (°)	**Binning[1] (K)**	**Ave (K)[2]**	**T-Oa1-T**	**T-Oa2-T**	**T-Obo-T**	**T-Obm-T**	**T-Oco-T**	**T-Ocm-T**	**T-Odo-T**	**T-Odm-T**
	90 - 152	121	141.9(6)	127.0(5)	139.3(5)	159.4(6)	129.1(5)	133.0(5)	135.9(6)	150.4(6)
	153 - 213	183	142.2(6)	127.4(5)	138.4(5)	158.1(6)	129.7(5)	132.6(5)	135.4(6)	150.9(6)
	214 - 275	244	141.8(6)	127.4(5)	140.3(6)	159.1(6)	129.0(5)	131.8(5)	137.0(6)	150.8(6)
	279 - 336	306	142.4(7)	128.6(5)	139.6(6)	158.7(6)	130.4(6)	132.1(6)	137.0(6)	149.9(6)
	337 - 398	367	142.0(7)	128.7(5)	138.7(7)	156.9(7)	131.2(6)	132.6(6)	137.5(6)	150.4(7)
	399 - 459	429	141.3(8)	127.9(6)	141.5(7)	157.3(7)	130.2(6)	131.1(6)	137.0(7)	151.5(7)
	460 - 500	480	140.4(8)	128.3(6)	139.0(7)	159.0(7)	129.7(6)	130.7(7)	136.8(7)	150.5(8)
	452 - 494	473	140.8(7)	128.1(5)	140.8(6)	158.4(6)	128.9(5)	133.9(6)	136.2(6)	148.6(7)
	512 - 544	528	140.9(7)	128.4(5)	140.8(6)	159.9(7)	128.4(5)	133.3(6)	134.9(6)	147.9(7)
	552- 594	573	141.4(7)	127.3(5)	141.3(7)	159.0(7)	128.5(6)	133.5(6)	135.8(7)	149.6(7)
	602 - 644	623	140.3(7)	128.0(6)	142.3(7)	158.6(7)	128.6(6)	133.1(6)	135.7(7)	147.9(8)
	652 - 694	673	142.1(8)	127.8(6)	141.8(7)	158.8(7)	129.2(6)	133.4(6)	135.8(7)	149.1(8)
	702 - 744	723	141.5(8)	126.3(6)	142.5(7)	158.6(7)	129.6(6)	132.9(7)	136.0(7)	148.9(8)
	752 -794	773	140.9(6)	128.1(5)	143.6(6)	159.7(6)	127.1(5)	133.1(6)	136.1(6)	150.1(7)
	802 - 844	823	138.8(6)	126.0(5)	145.0(6)	157.7(6)	127.9(5)	132.6(6)	138.1(6)	149.6(7)
	863 - 894	879	142.0(7)	128.3(6)	141.7(6)	158.2(7)	128.2(6)	132.8(6)	136.2(7)	148.4(8)
	902 - 944	923	141.3(7)	126.9(6)	142.5(6)	158.1(7)	128.7(6)	133.3(7)	135.4(7)	147.6(8)

Notes.

[1]Temperature interval of the binned powder diffraction data

[2]Average temperatures of each temperature interval of 20K binning from 90K - 500K and 5K binning from 452K - 944K.

*The bond length of a the longer of the two OA1 oxygen atoms

Table A.5.6: T-O bond lengths, M-O bond lengths and T-O-T angles for the Rietveld refinement results for An46.

T1o-O bonds (Å)	Binning[1] (K)	Ave (K)[2]	OA1	OBO	OCO	ODO	AVE
	90 - 152	121	1.685(10)	1.654(9)	1.671(9)	1.655(9)	1.666
	153 - 213	183	1.687(11)	1.664(10)	1.648(10)	1.643(9)	1.661
	214 - 275	244	1.704(12)	1.665(11)	1.674(11)	1.645(10)	1.672
	279 - 336	306	1.698(10)	1.666(9)	1.675(9)	1.639(9)	1.670
	337 - 398	367	1.694(10)	1.657(9)	1.670(9)	1.642(9)	1.666
	399 - 459	429	1.670(10)	1.659(9)	1.681(9)	1.642(9)	1.663
	460 - 500	480	1.696(10)	1.675(9)	1.659(9)	1.630(9)	1.665
	452 - 494	473	1.675(9)	1.648(7)	1.664(7)	1.660(7)	1.662
	512 - 544	528	1.676(9)	1.658(7)	1.676(7)	1.654(6)	1.666
	552- 594	573	1.692(9)	1.658(7)	1.674(7)	1.664(7)	1.672
	602 - 644	623	1.678(9)	1.656(7)	1.675(7)	1.662(7)	1.668
	652 - 694	673	1.673(9)	1.679(7)	1.685(7)	1.652(7)	1.672
	702 - 744	723	1.669(9)	1.666(7)	1.675(7)	1.660(7)	1.668
	752 -794	773	1.693(9)	1.656(9)	1.679(9)	1.640(9)	1.667
	802 - 844	823	1.677(9)	1.657(9)	1.683(9)	1.651(9)	1.667
	863 - 894	879	1.697(9)	1.654(9)	1.680(9)	1.648(9)	1.670
	902 - 944	923	1.674(9)	1.661(9)	1.667(9)	1.644(9)	1.662

T1m-O bonds (Å)	Binning[1] (K)	Ave (K)[2]	OA1	OBM	OCM	ODM	AVE
	90 - 152	121	1.678(9)	1.612(10)	1.668(9)	1.636(9)	1.649
	153 - 213	183	1.672(10)	1.627(11)	1.663(10)	1.625(9)	1.647
	214 - 275	244	1.655(12)	1.626(12)	1.666(12)	1.604(10)	1.638
	279 - 336	306	1.650(10)	1.627(10)	1.679(9)	1.628(9)	1.646
	337 - 398	367	1.670(9)	1.632(9)	1.651(9)	1.636(9)	1.647
	399 - 459	429	1.665(9)	1.609(9)	1.670(9)	1.632(9)	1.644
	460 - 500	480	1.654(9)	1.594(10)	1.646(9)	1.641(9)	1.634

	452 - 494	473	1.671(9)	1.606(9)	1.656(7)	1.625(7)	1.640
	512 - 544	528	1.662(7)	1.618(7)	1.670(7)	1.640(7)	1.648
	552- 594	573	1.660(9)	1.609(9)	1.654(7)	1.634(7)	1.639
	602 - 644	623	1.675(9)	1.603(9)	1.661(7)	1.646(7)	1.646
	652 - 694	673	1.671(9)	1.598(9)	1.676(9)	1.641(9)	1.647
	702 - 744	723	1.679(9)	1.596(9)	1.682(9)	1.625(9)	1.646
	752 -794	773	1.652(9)	1.611(9)	1.677(9)	1.631(9)	1.643
	802 - 844	823	1.673(9)	1.617(9)	1.697(9)	1.630(9)	1.654
	863 - 894	879	1.666(9)	1.630(9)	1.698(9)	1.640(9)	1.659
	902 - 944	923	1.670(9)	1.624(9)	1.687(9)	1.633(9)	1.654

T2o-O bonds (Å)	**Binning[1] (K)**	**Ave (K)[2]**	**OA2**	**OBO**	**OCM**	**ODM**	**AVE**
	90 - 152	121	1.671(9)	1.666(10)	1.643(9)	1.649(9)	1.657
	153 - 213	183	1.656(9)	1.680(11)	1.650(10)	1.663(10)	1.662
	214 - 275	244	1.662(10)	1.677(12)	1.643(12)	1.652(11)	1.659
	279 - 336	306	1.675(9)	1.680(10)	1.631(10)	1.653(9)	1.660
	337 - 398	367	1.647(9)	1.682(10)	1.657(9)	1.644(9)	1.658
	399 - 459	429	1.651(9)	1.684(10)	1.659(9)	1.652(9)	1.662
	460 - 500	480	1.654(9)	1.653(10)	1.657(9)	1.631(9)	1.649
	452 - 494	473	1.661(7)	1.655(9)	1.661(7)	1.664(7)	1.660
	512 - 544	528	1.661(6)	1.649(7)	1.661(7)	1.643(7)	1.654
	552- 594	573	1.671(7)	1.649(9)	1.675(7)	1.642(9)	1.659
	602 - 644	623	1.671(7)	1.651(9)	1.676(7)	1.637(9)	1.659
	652 - 694	673	1.677(7)	1.630(9)	1.657(9)	1.642(9)	1.652
	702 - 744	723	1.674(7)	1.638(9)	1.670(9)	1.654(9)	1.659
	752 -794	773	1.664(9)	1.628(9)	1.646(9)	1.658(9)	1.649
	802 - 844	823	1.683(9)	1.637(9)	1.634(9)	1.649(9)	1.651
	863 - 894	879	1.673(9)	1.649(9)	1.641(9)	1.637(9)	1.650

	902 - 944	923	1.664(9)	1.637(9)	1.647(10)	1.651(9)	1.650

T2m-O bonds (Å)	Binning[1] (K)	Ave (K)[2]	OA2	OBM	OCO	ODO	AVE
	90 - 152	121	1.641(9)	1.664(10)	1.652(9)	1.651(9)	1.652
	153 - 213	183	1.660(9)	1.651(11)	1.675(9)	1.667(9)	1.663
	214 - 275	244	1.664(10)	1.670(13)	1.648(10)	1.666(10)	1.662
	279 - 336	306	1.652(9)	1.657(10)	1.648(9)	1.652(9)	1.652
	337 - 398	367	1.647(9)	1.655(10)	1.660(9)	1.654(9)	1.654
	399 - 459	429	1.670(9)	1.683(10)	1.663(9)	1.671(9)	1.672
	460 - 500	480	1.670(9)	1.662(10)	1.670(9)	1.667(9)	1.667
	452 - 494	473	1.655(7)	1.645(9)	1.675(6)	1.677(7)	1.663
	512 - 544	528	1.666(6)	1.634(9)	1.666(6)	1.690(6)	1.664
	552- 594	573	1.667(7)	1.653(9)	1.656(6)	1.683(7)	1.665
	602 - 644	623	1.664(7)	1.651(9)	1.658(7)	1.669(7)	1.661
	652 - 694	673	1.652(7)	1.657(9)	1.651(7)	1.678(7)	1.660
	702 - 744	723	1.665(7)	1.645(9)	1.662(7)	1.685(7)	1.664
	752 -794	773	1.669(7)	1.645(9)	1.669(7)	1.687(9)	1.668
	802 - 844	823	1.670(7)	1.633(9)	1.665(9)	1.669(9)	1.659
	863 - 894	879	1.681(9)	1.623(9)	1.651(9)	1.679(9)	1.659
	902 - 944	923	1.668(9)	1.626(10)	1.649(9)	1.695(9)	1.660

Na-O bonds (Å)	Binning[1] (K)	Ave (K)[2]	OA1	OA2	OBO	OCO	ODO	ODM	OA1*	AVE
	90 - 152	121	2.35(3)	2.36(3)	2.45(3)	2.95(3)	2.54(3)	2.670(18)	2.89(3)	2.601
	153 - 213	183	2.36(3)	2.34(3)	2.48(3)	2.96(3)	2.51(3)	2.638(18)	2.88(3)	2.595
	214 - 275	244	2.37(4)	2.41(3)	2.57(3)	3.07(4)	2.39(4)	2.64(2)	2.80(4)	2.607
	279 - 336	306	2.36(3)	2.38(3)	2.45(3)	2.98(3)	2.54(3)	2.655(19)	2.88(3)	2.606
	337 - 398	367	2.38(3)	2.52(3)	2.523(25)	2.98(3)	2.50(3)	2.645(18)	2.848(24)	2.628
	399 - 459	429	2.451(18)	2.333(18)	2.479(20)	NC	2.443(20)	2.819(13)	2.731(18)	2.543

	460 - 500	480	2.43(5)	2.43(4)	2.62(4)	NC	2.35(4)	2.715(33)	2.75(4)	2.549
	452 - 494	473	2.40(3)	2.40(3)	2.582(24)	3.04(3)	2.41(3)	2.648(14)	2.827(25)	2.615
	512 - 544	528	2.424(30)	2.394(28)	2.612(30)	3.06(4)	2.38(4)	2.658(18)	2.802(30)	2.619
	552- 594	573	2.387(25)	2.407(26)	2.557(27)	3.031(29)	2.429(29)	2.664(15)	2.812(27)	2.612
	602 - 644	623	2.382(31)	2.448(27)	2.587(34)	NC	2.39(4)	2.704(23)	2.73(4)	2.540
	652 - 694	673	2.411(25)	2.400(23)	2.610(24)	3.009(28)	2.434(27)	2.629(15)	2.845(25)	2.620
	702 - 744	723	2.425(31)	2.396(27)	2.646(29)	3.03(4)	2.39(4)	2.622(20)	2.831(33)	2.620
	752 -794	773	2.390(34)	2.446(30)	2.60(4)	3.05(4)	2.45(4)	2.645(24)	2.80(4)	2.626
	802 - 844	823	2.353(30)	2.461(28)	2.590(35)	3.05(4)	2.46(4)	2.64(3)	2.793(35)	2.621
	863 - 894	879	2.387(34)	2.432(28)	2.58(4)	3.00(4)	2.47(4)	2.62(3)	2.845(34)	2.619
	902 - 944	923	2.47(4)	2.415(35)	2.66(4)	3.04(4)	2.43(4)	2.63(3)	2.82(4)	2.638

Ca-O bonds (Å)	**Binning[1] (K)**	**Ave (K)[2]**	**OA1**	**OA2**	**OBO**	**OBM**	**OCM**	**ODO**	**OA1***	**AVE**
	90 - 152	121	2.406(19)	2.293(18)	2.469(17)	2.880(13)	2.705(15)	2.494(17)	2.839(15)	2.584
	153 - 213	183	2.375(19)	2.358(19)	2.444(18)	2.891(13)	2.722(17)	2.507(18)	2.827(18)	2.589
	214 - 275	244	2.44(2)	2.330(18)	2.42(2)	2.884(17)	2.75(2)	2.558(18)	2.819(19)	2.600
	279 - 336	306	2.44(2)	2.270(19)	2.476(18)	2.869(14)	2.713(15)	2.500(17)	2.858(15)	2.589
	337 - 398	367	2.42(3)	2.31(3)	2.474(17)	2.903(13)	2.743(15)	2.534(15)	2.825(15)	2.601
	399 - 459	429	2.39(3)	2.34(3)	2.49(3)	2.778(18)	2.63(2)	2.55(3)	2.940(19)	2.588
	460 - 500	480	2.38(3)	2.33(3)	2.44(3)	2.95(3)	2.81(4)	2.57(3)	2.80(3)	2.611
	452 - 494	473	2.43(3)	2.32(3)	2.474(18)	2.910(12)	2.755(18)	2.527(15)	2.858(15)	2.611
	512 - 544	528	2.45(3)	2.25(3)	2.47(3)	2.923(14)	2.77(2)	2.537(19)	2.838(19)	2.605
	552- 594	573	2.38(3)	2.33(3)	2.502(19)	2.886(14)	2.738(17)	2.515(18)	2.867(15)	2.603
	602 - 644	623	2.41(4)	2.30(4)	2.49(3)	2.928(19)	2.74(3)	2.56(2)	2.848(18)	2.611
	652 - 694	673	2.40(4)	2.36(4)	2.473(18)	2.885(12)	2.770(18)	2.562(15)	2.829(17)	2.611
	702 - 744	723	2.48(3)	2.27(3)	2.47(3)	2.932(17)	2.78(3)	2.555(19)	2.814(19)	2.614
	752 -794	773	2.44(3)	2.30(3)	2.55(3)	2.947(19)	2.75(3)	2.54(3)	2.88(3)	2.630
	802 - 844	823	2.54(3)	2.25(3)	2.55(3)	2.945(18)	2.734(19)	2.55(2)	2.864(18)	2.633

	863 - 894	879	2.44(3)	2.28(3)	2.55(3)	2.984(19)	2.75(3)	2.52(3)	2.87(3)	2.628
	902 - 944	923	2.55(4)	2.27(3)	2.52(3)	2.935(19)	2.79(3)	2.58(3)	2.86(3)	2.644

T-O-T angles (°)	Binning[1] (K)	Ave (K)[2]	T-Oa1-T	T-Oa2-T	T-Obo-T	T-Obm-T	T-Oco-T	T-Ocm-T	T-Odo-T	T-Odm-T
	90 - 152	121	141.2(7)	128.9(5)	137.7(6)	159.2(7)	131.1(5)	132.2(6)	136.1(6)	150.9(6)
	153 - 213	183	140.7(7)	128.5(6)	137.2(7)	159.4(7)	130.8(6)	132.3(6)	135.5(7)	150.7(7)
	214 - 275	244	141.2(9)	128.9(7)	137.7(8)	157.8(8)	129.9(7)	131.9(7)	135.8(8)	150.3(8)
	279 - 336	306	142.4(7)	129.0(6)	137.6(7)	156.6(7)	131.0(6)	132.1(6)	136.2(7)	149.4(7)
	337 - 398	367	139.7(7)	129.4(5)	138.8(6)	160.0(6)	130.5(5)	133.1(6)	136.8(6)	150.7(6)
	399 - 459	429	141.5(7)	127.2(5)	138.7(7)	158.4(7)	130.2(6)	132.4(6)	135.2(6)	150.6(7)
	460 - 500	480	143.0(7)	128.8(5)	138.7(6)	159.9(7)	131.0(6)	133.4(6)	136.1(6)	150.4(7)
	452 - 494	473	143.5(6)	128.4(4)	139.5(5)	158.9(5)	130.3(5)	132.9(5)	133.9(5)	150.3(6)
	512 - 544	528	142.8(5)	127.7(4)	139.8(5)	159.7(5)	130.0(4)	132.0(5)	134.4(5)	149.7(6)
	552- 594	573	142.1(6)	128.4(4)	139.2(5)	158.8(5)	129.6(5)	131.9(5)	133.4(5)	149.5(6)
	602 - 644	623	141.3(6)	127.8(4)	139.9(5)	158.7(6)	130.0(5)	131.3(5)	134.5(5)	150.4(6)
	652 - 694	673	141.8(6)	128.5(5)	139.4(6)	158.8(6)	129.8(5)	132.2(5)	135.0(5)	149.4(6)
	702 - 744	723	141.8(6)	127.8(5)	139.5(5)	160.5(6)	129.9(5)	131.1(5)	134.3(5)	149.8(6)
	752 -794	773	142.1(6)	128.0(5)	141.6(6)	158.7(6)	130.1(5)	131.9(6)	134.9(6)	149.4(6)
	802 - 844	823	141.6(6)	126.9(5)	140.8(6)	159.0(7)	129.8(5)	131.4(6)	134.6(6)	149.6(7)
	863 - 894	879	142.0(7)	127.0(6)	139.3(6)	157.8(7)	130.4(6)	131.2(6)	133.7(6)	148.8(7)
	902 - 944	923	142.1(7)	128.5(6)	140.6(6)	159.3(7)	131.1(6)	132.0(6)	134.2(6)	148.6(7)

Notes.

[1]Temperature interval of the binned powder diffraction data

[2]Average temperatures of each temperature interval of 20K binning from 90K - 500K and 5K binning from 452K - 944K.

*The bond length of a the longer of the two OA1 oxygen atoms

NC: Bonds that were not calculated in that particular refinement.

Table A.4.6: the four tilting systems for the high-pressure single-crystal refinements of An20.

Tilt systems (°)	Press.†	ϕ1	ϕ2	ϕ3	ϕ4
	0.0001	2.19	10.31	3.71	2.83
	2.149(9)	1.67	9.69	2.92	1.83
	3.764(9)	1.58	9.66	2.38	1.36
	4.341(10)	1.29	9.63	2.15	-1.59
	5.717(10)	1.65	9.57	2.1	-1.7
	6.756(6)	1.96	9.16	1.55	-2.46
	8.144(9)	1.74	9.32	1.68	-4.65
	9.150(10)	2.36	9.52	2.78	-7.06

Notes.

All tilting systems were calculated using cif reader.

Table A.4.7: the four tilting systems for the high-pressure single-crystal refinements of An37.

Tilt systems (°)	Press.†	ϕ1	ϕ2	ϕ3	ϕ4
	0.0001	2.18	9.68	3.71	2.83
	1.92(3)	2.11	9.03	2.92	1.83
	4.18(3)	1.57	8.89	2.38	1.36
	5.967(9)	1.86	8.79	2.15	-1.59
	7.128(9)	1.77	8.76	2.1	-1.7
	8.477(10)	1.73	8.7	1.55	-2.46
	9.457(10)	1.62	8.68	1.68	-4.65

Notes.

All tilting systems were calculated using cif reader.

Table A.5.7: The four tilting systems for the Rietveld refinement results of Albite (An0).

Tilts (°)	Binning[1] (K)	Temp. (K)[2]	ϕ1	ϕ2	ϕ3	ϕ4
	90 - 152	121	1.99	10.16	4.38	3.33
	153 - 213	183	1.79	10.3	4.73	3.82
	214 - 275	244	2.25	10.25	4.53	3.71
	279 - 336	306	2.5	10.56	4.88	3.7
	337 - 398	367	2.48	10.54	4.5	3.6
	399 - 459	429	2.24	10.63	4.44	3.26
	460 - 500	480	2.77	10.82	4.03	3.26
	452 - 494	473	2.08	10.61	5.25	3.31
	512 - 544	528	2.08	10.82	5.11	3.18
	552- 594	573	2.05	10.98	5.19	3.33
	602 - 644	623	2.2	11.15	5.9	3.1
	652 - 694	673	2.59	10.61	5.48	3.27
	702 - 744	723	2.63	10.86	5.37	3.37
	752 -794	773	2.74	11.2	5.73	3.43
	802 - 844	823	2.86	10.91	5.6	3.38
	863 - 894	879	3.65	10.9	6.52	3.26
	902 - 944	923	3.12	11.24	6.52	3.55

Notes.

[1]Temperature interval of the binned powder diffraction data

[2]Average temperatures of each temperature interval of 20K binning from 90K - 500K and 5K binning from 452K - 944K.

All of the tilting systems were calculated with CifReader

Table A.5.8: The four tilting systems for the Rietveld refinement results of An26.

Tilts (°)	Temp. (K)	$\phi 1$	$\phi 2$	$\phi 3$	$\phi 4$
	100[1]	2.13	9.75	3.62	2.12
	150[1]	2.15	9.82	3.63	2.1
	200[1]	2.14	9.85	3.7	2.18
	250[1]	2.17	9.91	3.77	2.14
	300[1]	2.23	9.98	3.87	2.11
	300[1]	2.09	10.03	3.82	2.16
	303[2]	2.11	9.99	3.84	2.16
	323[2]	2.17	10.02	3.85	2.12
	373[2]	2.22	10.08	3.9	2.13
	423[2]	2.15	10.18	4.01	2.17
	473[2]	2.3	10.22	4.04	2.03
	523[2]	2.31	10.33	4.04	2.12
	573[2]	2.33	10.34	4.22	2.11
	623[2]	2.39	10.43	4.14	1.99
	673[2]	2.37	10.42	4.44	2.09
	723[2]	2.44	10.56	4.42	2.06
	773[2]	2.35	10.64	4.6	2.24
	823[2]	2.54	10.64	4.65	2.16
	873[2]	2.5	10.73	4.73	2.12
	923[2]	2.49	10.83	4.89	1.99
	973[2]	2.6	10.92	4.79	2.05
	1023[2]	2.6	11.02	4.9	2.15

Notes.

[1]Results from the data collected at low-temperature on a Gemini diffractometer.

[2]Results from the data collected at high-temperature on a Phillips PW1100 diffractometer.

All of the tilting systems were calculated with CifReader

Table A.5.9: The four tilting systems for the Rietveld refinement results of An27.

Tilts (°)	Binning[1] (K)	Temp. (K)[2]	ϕ1	ϕ2	ϕ3	ϕ4
	90 - 152	121	1.91	9.8	3.76	3.03
	153 - 213	183	1.7	9.83	3.61	3.04
	214 - 275	244	1.58	10.07	3.78	2.83
	279 - 336	306	1.4	10.19	3.57	2.7
	337 - 398	367	1.46	10.23	4.38	2.57
	399 - 459	429	1.86	10.29	4.33	2.42
	460 - 500	480	1.91	10.21	4.26	2.37
	452 - 494	473	2.02	9.9	4.59	2.42
	512 - 544	528	2.03	10.22	4.52	2.72
	552- 594	573	2.21	10.36	4.73	3.02
	602 - 644	623	2.02	10.39	4.46	2.82
	652 - 694	673	2.12	10.39	4.34	2.78
	702 - 744	723	2.18	10.47	4.72	3.01
	752 -794	773	1.94	10.61	4.86	2.46
	802 - 844	823	1.7	10.77	4.92	2.26
	863 - 894	879	1.98	10.7	5.55	2.03
	902 - 944	923	2.09	10.62	5.43	2.2

Notes.

[1]Temperature interval of the binned powder diffraction data

[2]Average temperatures of each temperature interval of 20K binning from 90K - 500K and 5K binning from 452K - 944K.

All of the tilting systems were calculated with CifReader

Table A.5.10: The four tilting systems for the Rietveld refinement results of An35.

Tilts (°)	Binning[1] (K)	Temp. (K)[2]	ϕ1	ϕ2	ϕ3	ϕ4
	90 - 152	121	1.35	10.39	2.67	2.5
	153 - 213	183	1.52	10.33	3.15	1.91
	214 - 275	244	1.17	10.43	3.01	2.21
	279 - 336	306	1.61	10.27	2.74	2.46
	337 - 398	367	1.45	10.39	3.47	1.21
	399 - 459	429	0.99	10.97	3.2	2.26
	460 - 500	480	0.68	11.07	2.67	2.3
	452 - 494	473	1.16	10.35	3.34	2.41
	512 - 544	528	1.17	10.33	3.25	3.23
	552- 594	573	1.44	10.6	3.76	2.52
	602 - 644	623	0.98	10.44	3.6	3.23
	652 - 694	673	1.6	10.9	2.22	3.11
	702 - 744	723	1.02	11.07	4.15	2.72
	752 -794	773	1.24	10.79	3.84	2.93
	802 - 844	823	0.52	11.18	4.88	1.99
	863 - 894	879	1.71	10.78	2.87	2.68
	902 - 944	923	1.5	11.22	3.58	3.09

Notes.

[1]Temperature interval of the binned powder diffraction data

[2]Average temperatures of each temperature interval of 20K binning from 90K - 500K and 5K binning from 452K - 944K.

All of the tilting systems were calculated with CifReader

Table A.5.11: The four tilting systems for the Rietveld refinement results of An46.

Tilts (°)	Binning[1] (K)	Temp. (K)[2]	ϕ1	ϕ2	ϕ3	ϕ4
	90 - 152	121	1.23	10.03	3.09	1.78
	153 - 213	183	1.33	9.48	3.33	1.72
	214 - 275	244	1.38	9.75	2.67	1.84
	279 - 336	306	1.79	9.7	3.16	1.52
	337 - 398	367	0.61	9.92	3.37	2.2
	399 - 459	429	1.71	9.46	4.25	1.85
	460 - 500	480	1.82	9.66	3.64	2.06
	452 - 494	473	2.25	9.71	4.12	2.3
	512 - 544	528	1.96	9.96	3.98	2.55
	552- 594	573	2.1	9.49	3.96	2.54
	602 - 644	623	1.62	9.94	4.33	2.06
	652 - 694	673	1.9	9.93	3.79	2.12
	702 - 744	723	1.64	10.03	3.79	2.65
	752 -794	773	1.8	10.16	4.19	2.54
	802 - 844	823	1.8	10.34	4.05	2.56
	863 - 894	879	2.03	10.44	3.56	2.51
	902 - 944	923	2.13	10.28	4.42	2.68

Notes.

[1]Temperature interval of the binned powder diffraction data

[2]Average temperatures of each temperature interval of 20K binning from 90K - 500K and 5K binning from 452K - 944K.

All of the tilting systems were calculated with CifReader

Appendix B: Unit cell parameters

Table B.5: Unit cell parameters of the high- pressure single-crystal refinements of An20.

Press.†	a (Å)	d(100) (Å)*	b (Å)	c (Å)	α (°)	β (°)	γ (°)	V (Å^3)
0.0001	8.1642(6)	7.309	12.8382(3)	7.1353(4)	93.859(5)	116.448(5)	88.930(5)	668.03(6)
2.149(9)	8.0347(6)	7.183	12.7517(6)	7.0763(6)	93.782(9)	116.603(6)	89.163(6)	646.75(7)
3.764(9)	7.9457(4)	7.1	12.6929(2)	7.0366(4)	93.706(5)	116.653(5)	89.329(3)	632.81(5)
4.341(10)	7.9148(6)	7.072	12.6721(6)	7.0235(6)	93.665(10)	116.665(5)	89.378(9)	628.11(7)
5.717(10)	7.8422(8)	7.006	12.6273(4)	6.9913(6)	93.575(7)	116.665(9)	89.529(5)	617.34(8)
6.756(6)	7.7867(6)	6.957	12.5951(4)	6.9681(4)	93.491(7)	116.656(7)	89.622(5)	609.46(6)
8.144(9)	7.7141(4)	6.891	12.5533(3)	6.9392(3)	93.360(5)	116.674(5)	89.712(3)	599.25(4)
9.150(10)	7.6565(4)	6.838	12.5235(8)	6.9160(3)	93.252(6)	116.699(3)	89.688(7)	591.34(5)

Notes.

* Calculated using CifReader

† Pressures were calculated using the Equation of state for Quartz (Angel *at el.* 1999)

Table B.5: Unit cell parameters of the high- pressure single-crystal refinements of An37.

Press.†	a (Å)	d(100) (Å)*	b (Å)	c (Å)	α (°)	β (°)	γ (°)	V (Å^3)
0.0001	8.1698(4)	7.322	12.8637(8)	7.1180(3)	93.556(6)	116.299(3)	89.768(6)	669.11(6)
1.92(3)	8.0632(3)	7.222	12.7833(9)	7.0620(3)	93.445(5)	116.359(3)	90.004(5)	650.76(6)
4.18(3)	7.9540(4)	7.124	12.7011(8)	7.0030(4)	93.304(6)	116.347(3)	90.262(5)	632.57(6)
5.967(9)	7.8742(6)	7.053	12.6410(4)	6.9612(3)	93.181(5)	116.331(5)	90.393(5)	619.67(5)
7.128(9)	7.8205(7)	7.007	12.6010(4)	6.9328(4)	93.102(6)	116.290(6)	90.505(5)	611.23(7)
8.477(10)	7.7604(4)	6.955	12.5581(3)	6.9033(4)	92.990(5)	116.257(5)	90.627(3)	602.09(5)
9.457(10)	7.7173(4)	6.917	12.5267(3)	6.8805(4)	92.908(5)	116.244(5)	90.696(5)	595.38(5)

Notes.

* Calculated using CifReader

† Pressures were calculated using the Equation of state for Quartz (Angel *at el.* 1999)

Table B.1 Unit cell parameters from the results of the low- and high- temperature Rietveld refinements of albite (An0).

Binning[1] (K)	Ave (K)[2]	a (Å)	d(100) (Å)*	b (Å)	c (Å)	α (°)	β (°)	γ (°)	V (Å^3)
90 - 152	121	8.12812(4)	7.259	12.78649(6)	7.16498(4)	94.2640(3)	116.7272(2)	87.6782(3)	663.235(6)
153 - 213	183	8.13316(5)	7.267	12.78815(7)	7.16393(4)	94.2634(4)	116.6813(3)	87.6821(4)	663.903(9)
214 - 275	244	8.13913(6)	7.275	12.79068(8)	7.16339(5)	94.2552(6)	116.6352(3)	87.6833(6)	664.747(10)
279 - 336	306	8.14539(6)	7.284	12.79378(9)	7.16320(5)	94.2399(6)	116.5918(3)	87.6817(6)	665.667(10)
337 - 398	367	8.15185(6)	7.292	12.79682(9)	7.16306(5)	94.2169(6)	116.5511(3)	87.6770(6)	666.594(11)
399 - 459	429	8.15816(5)	7.3	12.80013(7)	7.16329(4)	94.1919(4)	116.5135(3)	87.6715(4)	667.541(9)
460 - 500	480	8.16387(5)	7.307	12.80338(7)	7.16370(4)	94.1656(4)	116.4833(3)	87.6648(4)	668.413(9)
452 - 494	473	8.16425(3)	7.307	12.80382(4)	7.16384(3)	94.1626(2)	116.4818(1)	87.6644(2)	668.491(5)
512 - 544	528	8.17025(3)	7.315	12.80731(4)	7.16444(3)	94.1305(2)	116.4520(2)	87.6566(2)	669.418(5)
552- 594	573	8.17656(3)	7.322	12.81100(4)	7.16525(3)	94.0940(2)	116.4228(2)	87.6490(2)	670.401(5)
602 - 644	623	8.18309(4)	7.33	12.81498(5)	7.16597(3)	94.0531(2)	116.3935(2)	87.6395(2)	671.412(5)
652 - 694	673	8.18944(4)	7.337	12.81880(5)	7.16698(3)	94.0098(3)	116.3673(2)	87.6313(2)	672.412(5)
702 - 744	723	8.19545(4)	7.344	12.82263(4)	7.16770(3)	93.9662(3)	116.3409(2)	87.6213(2)	673.359(5)
752 -794	773	8.20202(4)	7.351	12.82665(5)	7.16879(3)	93.9166(3)	116.3152(2)	87.6118(3)	674.397(6)
802 - 844	823	8.20825(4)	7.359	12.83025(5)	7.16970(3)	93.8655(3)	116.2902(2)	87.6021(3)	675.366(6)
863 - 894	879	8.21476(4)	7.366	12.83436(5)	7.17074(3)	93.8131(3)	116.2677(2)	87.5922(3)	676.383(6)
902 - 944	923	8.22168(3)	7.374	12.83818(4)	7.17174(3)	93.7544(3)	116.2406(2)	87.5797(2)	677.444(5)

Notes.

[1]Temperature interval of the binned powder diffraction data

[2]Average temperatures of each temperature interval of 20K binning from 90K - 500K and 5K binning from 452K - 944K.

*calculated using CifReader

Table B.2 Unit cell parameters from the results of the low- and high- temperature single-crystal refinements of An26.

Temp. (K)	a (Å)	d(100) (Å)*	b (Å)	c (Å)	α (°)	β (°)	γ (°)	V (Å^3)
100[1]	8.1402(6)	7.289	12.8404(9)	7.1159(7)	93.802(6)	116.411(9)	89.450(6)	664.52(9)
150[1]	8.1466(7)	7.294	12.8411(7)	7.1175(7)	93.789(6)	116.412(9)	89.443(6)	665.23(9)
200[1]	8.1453(6)	7.293	12.8320(7)	7.1168(6)	93.763(6)	116.413(9)	89.422(5)	664.61(8)
250[1]	8.1475(6)	7.296	12.8313(7)	7.1173(7)	93.733(6)	116.403(9)	89.413(5)	664.89(9)
300[1]	8.1520(6)	7.3	12.8320(7)	7.1188(7)	93.719(6)	116.409(9)	89.387(5)	665.42(9)
300[1]	8.1503(6)	7.3	12.8343(8)	7.1148(6)	93.799(5)	116.380(7)	89.359(6)	665.13(8)
303[2]	8.1503(12)	7.298	12.8342(11)	7.1184(18)	93.716(13)	116.412(14)	89.390(10)	665.3(2)
323[2]	8.1525(12)	7.3	12.8344(11)	7.1190(18)	93.716(13)	116.411(14)	89.389(10)	665.6(2)
373[2]	8.1564(9)	7.305	12.8392(8)	7.1200(12)	93.685(9)	116.394(6)	89.375(7)	666.39(14)
423[2]	8.1595(12)	7.309	12.8394(12)	7.1199(16)	93.636(13)	116.376(14)	89.352(10)	666.79(19)
473[2]	8.1633(12)	7.313	12.8432(11)	7.1210(16)	93.620(12)	116.361(13)	89.333(10)	667.50(19)
523[2]	8.1672(11)	7.317	12.8467(11)	7.1232(15)	93.591(11)	116.350(12)	89.325(10)	668.30(18)
573[2]	8.1725(12)	7.323	12.8494(12)	7.1221(18)	93.547(11)	116.345(13)	89.305(11)	668.8(2)
623[2]	8.1765(12)	7.328	12.8501(13)	7.1234(13)	93.506(10)	116.316(11)	89.290(11)	669.53(17)
673[2]	8.1806(13)	7.332	12.8538(13)	7.1246(15)	93.459(12)	116.313(12)	89.271(11)	670.23(19)
723[2]	8.1854(14)	7.337	12.8584(14)	7.1258(15)	93.422(11)	116.297(13)	89.259(12)	671.1(2)
773[2]	8.1914(16)	7.344	12.8597(16)	7.126(3)	93.362(15)	116.276(17)	89.244(14)	671.9(2)
823[2]	8.1956(13)	7.349	12.8647(15)	7.1273(15)	93.317(11)	116.266(12)	89.212(13)	672.68(19)
873[2]	8.1996(15)	7.353	12.8659(14)	7.128(3)	93.257(14)	116.250(17)	89.210(13)	673.3(3)
923[2]	8.2041(18)	7.359	12.8708(16)	7.130(3)	93.218(18)	116.22(2)	89.200(15)	674.3(3)
973[2]	8.2090(18)	7.365	12.8733(16)	7.132(3)	93.152(18)	116.20(2)	89.195(14)	675.2(3)
1023[2]	8.2157(18)	7.371	12.8748(15)	7.134(3)	93.114(18)	116.21(2)	89.163(14)	675.9(3)

Notes.

[1]Results from the data collected at low-temperature on a Gemini diffractometer.

[2]Results from the data collected at high-temperature on a Phillips PW1100 diffractometer.

*calculated using CifReader

Table B.3 Unit cell parameters from the results of the low- and high-temperature Rietveld refinements of An27.

Binning[1] (K)	Ave (K)[2]	a (Å)	d(100) (Å)*	b (Å)	c (Å)	α (°)	β (°)	γ (°)	V (Å^3)
90 - 152	121	8.1603(3)	7.305	12.85100(3)	7.12908(3)	93.78730(10)	116.45070(10)	89.28640(10)	667.768(3)
153 - 213	183	8.1631(3)	7.308	12.85240(3)	7.12905(3)	93.76390(10)	116.43250(10)	89.27560(10)	668.196(3)
214 - 275	244	8.16622(3)	7.312	12.85419(3)	7.12938(3)	93.73860(10)	116.41580(10)	89.26470(10)	668.698(3)
279 - 336	306	8.16984(3)	7.317	12.85638(3)	7.1298(3)	93.70890(10)	116.39730(10)	89.25230(10)	669.284(3)
337 - 398	367	8.17418(3)	7.322	12.85919(3)	7.13055(3)	93.6743(2)	116.37760(10)	89.2374(2)	670.003(3)
399 - 459	429	8.17845(3)	7.327	12.86221(3)	7.13143(3)	93.6415(2)	116.35860(10)	89.2235(2)	670.736(3)
460 - 500	480	8.18196(3)	7.331	12.86473(3)	7.13224(3)	93.61350(10)	116.34370(10)	89.21150(10)	671.343(3)
452 - 494	473	8.18244(3)	7.332	12.86495(4)	7.13229(3)	93.6087(2)	116.34160(10)	89.2096(2)	671.416(5)
512 - 544	528	8.18633(3)	7.336	12.86748(4)	7.13303(3)	93.5765(2)	116.32550(10)	89.1968(2)	672.060(5)
552- 594	573	8.19065(3)	7.341	12.87065(4)	7.13412(3)	93.5415(2)	116.3092(2)	89.1832(2)	672.808(5)
602 - 644	623	8.1952(3)	7.347	12.87384(4)	7.13516(3)	93.5022(2)	116.29020(10)	89.1685(2)	673.593(5)
652 - 694	673	8.19929(3)	7.351	12.87678(4)	7.1362(3)	93.4669(2)	116.27480(10)	89.1548(2)	674.300(5)
702 - 744	723	8.20388(3)	7.357	12.87999(4)	7.1373(3)	93.4237(2)	116.25730(10)	89.1420(2)	675.089(5)
752 -794	773	8.20886(3)	7.362	12.88375(4)	7.13870(3)	93.3787(2)	116.2399(2)	89.1269(2)	675.966(5)
802 - 844	823	8.21370(3)	7.368	12.88737(4)	7.14008(3)	93.3309(2)	116.2227(2)	89.1110(2)	676.826(5)
863 - 894	879	8.21853(3)	7.373	12.89076(4)	7.14128(3)	93.2794(2)	116.2054(2)	89.0953(2)	677.656(5)
902 - 944	923	8.22335(3)	7.379	12.89430(4)	7.14264(3)	93.2308(2)	116.1886(2)	89.0808(2)	678.506(5)

Notes.

[1]Temperature interval of the binned powder diffraction data

[2]Average temperatures of each temperature interval of 20K binning from 90K - 500K and 5K binning from 452K - 944K.

*calculated using CifReader

Table B.4 Unit cell parameters from the results of the low- and high- temperature Rietveld refinements of An35.

Binning[1] (K)	Ave (K)[2]	a (Å)	d(100) (Å)*	b (Å)	c (Å)	α (°)	β (°)	γ (°)	V (Å^3)
90 - 152	121	8.15538(6)	7.304	12.85607(10)	7.11926(5)	93.7276(6)	116.3772(3)	89.7158(6)	667.062(11)
153 - 213	183	8.15790(7)	7.307	12.85739(10)	7.11940(5)	93.7042(6)	116.3649(3)	89.7054(6)	667.446(11)
214 - 275	244	8.16078(7)	7.31	12.85895(10)	7.11974(5)	93.6771(6)	116.3495(3)	89.6908(6)	667.912(12)
279 - 336	306	8.16430(7)	7.315	12.86118(11)	7.12047(6)	93.6473(6)	116.3344(4)	89.6777(6)	668.504(12)
337 - 398	367	8.16811(8)	7.319	12.86391(12)	7.12129(6)	93.6132(6)	116.3199(4)	89.6643(6)	669.154(13)
399 - 459	429	8.17211(8)	7.324	12.86675(12)	7.12214(6)	93.5810(6)	116.3043(4)	89.6496(7)	669.833(14)
460 - 500	480	8.17532(8)	7.327	12.86902(12)	7.12309(6)	93.5533(6)	116.2939(4)	89.6328(6)	670.393(14)
452 - 494	473	8.17585(8)	7.328	12.86922(12)	7.12312(6)	93.5498(6)	116.2905(4)	89.6344(6)	670.471(13)
512 - 544	528	8.17918(8)	7.332	12.87150(12)	7.12396(6)	93.5191(6)	116.2794(4)	89.6210(6)	671.037(13)
552- 594	573	8.18347(8)	7.337	12.87455(12)	7.12517(6)	93.4860(6)	116.2649(4)	89.6060(6)	671.780(14)
602 - 644	623	8.18725(8)	7.341	12.87748(13)	7.12624(6)	93.4527(6)	116.2494(4)	89.5899(7)	672.466(14)
652 - 694	673	8.19116(8)	7.345	12.88039(13)	7.12740(6)	93.4198(6)	116.2397(4)	89.5775(7)	673.137(14)
702 - 744	723	8.19529(8)	7.35	12.88343(13)	7.12856(6)	93.3881(6)	116.2263(4)	89.5607(7)	673.853(14)
752 -794	773	8.19929(7)	7.355	12.88621(10)	7.12957(5)	93.3500(6)	116.2104(3)	89.5469(6)	674.550(12)
802 - 844	823	8.20343(7)	7.359	12.88944(11)	7.13084(5)	93.3087(6)	116.1961(3)	89.5325(6)	675.299(12)
863 - 894	879	8.20824(8)	7.365	12.89293(11)	7.13241(6)	93.2608(6)	116.1844(4)	89.5120(6)	676.139(13)
902 - 944	923	8.21250(8)	7.369	12.89633(12)	7.13369(6)	93.2177(6)	116.1705(4)	89.4963(6)	676.907(13)

Notes.

[1]Temperature interval of the binned powder diffraction data

[2]Average temperatures of each temperature interval of 20K binning from 90K - 500K and 5K binning from 452K - 944K.

*calculated using CifReader

Table B.5: Unit cell parameters from the results of the low- and high- temperature Rietveld refinements of An46.

Binning[1] (K)	Ave (K)[2]	a (Å)	d(100) (Å)*	b (Å)	c (Å)	α (°)	β (°)	γ (°)	V (Å^3)
90 - 152	121	8.16641(8)	7.318	12.86051(12)	7.11503(6)	93.6322(6)	116.2951(4)	89.8363(6)	668.316(13)
153 - 213	183	8.16809(9)	7.321	12.86133(13)	7.11522(6)	93.6133(6)	116.2868(4)	89.8270(7)	668.584(15)
214 - 275	244	8.17108(9)	7.324	12.86338(14)	7.11596(7)	93.5877(7)	116.2741(4)	89.8166(7)	669.104(17)
279 - 336	306	8.17390(8)	7.328	12.86482(12)	7.11617(6)	93.5580(6)	116.2596(4)	89.8068(6)	669.545(13)
337 - 398	367	8.17707(7)	7.331	12.86721(11)	7.11711(6)	93.5283(6)	116.2465(3)	89.7953(6)	670.122(13)
399 - 459	429	8.18035(8)	7.335	12.86989(11)	7.11798(6)	93.5002(6)	116.2331(4)	89.7835(6)	670.719(13)
460 - 500	480	8.18332(8)	7.339	12.87227(11)	7.11886(6)	93.4731(6)	116.2212(4)	89.7753(6)	671.265(13)
452 - 494	473	8.18385(6)	7.339	12.87253(10)	7.11890(5)	93.4681(6)	116.2201(3)	89.7730(6)	671.337(11)
512 - 544	528	8.18685(6)	7.343	12.87440(9)	7.11979(5)	93.4434(6)	116.2101(3)	89.7622(6)	671.847(11)
552- 594	573	8.19005(6)	7.347	12.87741(9)	7.12075(5)	93.4164(6)	116.1961(3)	89.7488(6)	672.466(11)
602 - 644	623	8.19383(6)	7.351	12.88037(10)	7.12197(5)	93.3878(6)	116.1828(3)	89.7369(6)	673.151(11)
652 - 694	673	8.19750(7)	7.355	12.88315(10)	7.12310(5)	93.3566(6)	116.1700(3)	89.7248(6)	673.808(12)
702 - 744	723	8.20174(7)	7.36	12.88634(10)	7.12462(5)	93.3267(6)	116.1599(3)	89.7130(6)	674.554(12)
752 -794	773	8.20556(7)	7.364	12.88940(10)	7.12591(5)	93.2923(6)	116.1468(3)	89.6987(6)	675.259(12)
802 - 844	823	8.20950(7)	7.369	12.89272(10)	7.12701(5)	93.2549(6)	116.1299(3)	89.6828(6)	675.995(13)
863 - 894	879	8.21370(7)	7.373	12.89583(11)	7.12848(6)	93.2163(6)	116.1218(4)	89.6640(6)	676.726(13)
902 - 944	923	8.21794(7)	7.378	12.89899(11)	7.12997(5)	93.1809(6)	116.1093(3)	89.6470(6)	677.488(13)

Notes.

[1]Temperature interval of the binned powder diffraction data

[2]Average temperatures of each temperature interval of 20K binning from 90K - 500K and 5K binning from 452K - 944K.

*calculated using CifReader

Appendix C: Citations

Figure 1.4 [used with permission]
Carpenter, M.A. (1994) Subsolidus phase relations of plagioclase feldspar solid solution. *In* Parsons I. (ed) Feldspars and Their Reactions. Kluwer Academic Publishers, Netherlands: 221-269. Used with permission from Dr. Michael Carpenter (author of the chapter), Dr. Ian Parsons (editor of the book) Will Bruins (editor for Springer); letters are attached.

Chapter 2 [used with permission]
Sochalski-Kolbus, L.M., Angel, R.J., Nestola, F. (2010) The effect of Al/Si disorder on the bulk moduli of plagioclase feldspars. *Mineralogical Magazine*, **vol 74: issue 6**. Pp. 943-950. Used with permission from Dr. Ross J. Angel (co-author), Dr. Fabrizio Nestola (co-author) and Dr. Mark Welch (editor of Mineralogical Magazine); letters are attached.

Chapter 3 [used with permission]
Angel, R.J., Sochalski-Kolbus, L.M., Tribaudino, M. (2012) Tilts and tetrahedra: the origin of the anisotropy in feldspars. *American Mineralogist*, **vol 97: no. 0506**. Pp. 765. Used with permission from Dr. Ross J. Angel (first author), Dr. Mario Tribaudino (co-author), Mrs. Rachel Russel (editor of American Mineralogist); letters are attached.